Universität Rostock Traditio et Innovatio

Aus der Professur für Atmosphärenphysik
der Mathematisch-Naturwissenschaftlichen Fakultät

Modelling of mid-latitude ionospheric trough location and dynamics using multi-frequency radio sounding and in-situ observations

Dissertation
zur Erlangung des akademischen Grades
Doctor rerum naturalium (Dr. rer. nat.)

an der Mathematisch-Naturwissenschaftlichen Fakultät
der Universität Rostock

vorgelegt von
M.Eng. Kateryna Lubyk
aus Neustrelitz

Rostock, 6.11.2025

https://doi.org/10.18453/rosdok_id00005886

Gutachter:

Prof. Dr. Claudia Stolle,	Universität Rostock, Leibniz-Institut für Atmosphärenphysik
PD. Dr. Elena Kronberg,	Ludwig-Maximilians-Universität München Department für Geo- und Umweltwissenschaften
Prof. Dr.-Ing. Andreas Wehrenpfennig,	Hochschule Neubrandenburg, Landschaftswissenschaften und Geomatik

Jahr der Einreichung: 2024

Jahr der Verteidigung: 2025

Declaration of Authorship

I, Kateryna Lubyk, declare that this thesis titled, "Modelling of mid-latitude ionospheric trough location and dynamics using multi-frequency radio sounding and in-situ observations" and the work presented in it are my own. This work was completed at the Faculty of Mathematics and Natural Sciences at the University of Rostock under the supervision of Prof. Dr. Claudia Stolle. I confirm that:

- The opportunity for this PhD project was not communicated to me commercially. In particular I have not engaged any organisation that for money seeks supervisors for the drawing up of dissertations or that performs entirely or partially on my behalf the duties incumbent upon me regarding the examinations.
- I hereby declare under oath that I have completed the work submitted here independently and have composed it without outside assistance. Furthermore, I have not used anything other than the resources and sources stated and where I have taken sections from these works in terms of content or text, I have identified this appropriately.

Signed: _____

Date: _____

"Success is the sum of small efforts - repeated day in and day out."

Robert Collier

Acknowledgements

This PhD thesis is the result of my research conducted at the Institute for Solar-Terrestrial Physics in the German Aerospace Center. I am deeply thankful to the DLR SO Institute for providing me with the job contract that made this work possible. I am deeply grateful for the sincere support of numerous individuals, without whom this work would not have been possible. I extend my heartfelt thanks to all those who contributed to the realization of this thesis.

I would like to express my deepest gratitude to Dr. Mainul Hoque, whose unwavering support, insightful advice, and constant motivation were crucial in the completion of this work. Without his guidance, this thesis would not have been possible.

I am also extremely thankful to prof. Dr. Claudia Stolle for her invaluable involvement in my research, her thoughtful suggestions, and her consistent availability for our regular meetings. Her contributions have greatly enriched my work. I am very grateful to her for her help and support.

I extend my heartfelt thanks to Prof. Dr.-Ing. Andreas Wehrenpfennig for his motivation and support during the final stages of my thesis. His encouragement was crucial in helping me bring this project to fruition.

I am profoundly grateful to all my colleagues for their kindness, positivity, and friendship. A special thank goes to my dear friend and colleague, Marjolijn Adolfs. We embarked on this PhD journey together, and her unwavering support has been a source of strength throughout.

I am also deeply thankful to my colleagues who have become true friends: Dr. Daniela Banys, Galina Voinov, Dr. Sergey Voinov, and Dr. Shradha Fowdur. Your friendship has been a cherished part of this experience. My gratitude extends to Dr. Gerlinde Wauer and Dr. Jochen Wauer for their kindness and immense support, especially during the pandemic. You have become like a second family to me, for which I am forever grateful.

My heartfelt thanks also go to my dear friend Yullia Hresko, whom I met at DLR, for her true friendship and unwavering support. I would also like to thank Olgha Gryshun for her support throughout my PhD journey. My heartfelt thanks also to Natalia Zagorodniuk for her regular yoga classes, which not only kept me calm but also helped me stay in shape throughout this journey.

I would like to express my deepest gratitude to my family, especially my parents, Maryna and Volodumyr Lubyk, and my beloved sisters, Olha and Mariana Lubyk. Thank you for believing in me and supporting me every step of the way.

A special note of gratitude goes to the Armed Forces of Ukraine for protecting my homeland and allowing me to worry less about the safety of my family in Ukraine during these challenging times.

Lastly, I would like to express my profound thanks to my fiancé, Ayham Akesh, for his unwavering support and understanding.

Abstract

The Earth's ionosphere is characterized by seasonal and diurnal variations due to Solar influences. Extreme ultraviolet (EUV) radiation, X-rays, and Lyman-alpha are the main factors affecting the electron density distribution of the ionosphere. In addition, the ionosphere is not homogeneous and has several large-scale features. One of these is the mid-latitude ionospheric trough, which is the main focus of this research. The mid-latitude ionospheric trough (MIT) is a phenomenon of electron density depletion in the nocturnal F region located at subauroral latitudes. Primarily, the MIT is located between the equatorward edge of the auroral oval and the plasmapause or plasmaspheric boundary layer. The MIT has a V-shaped structure and is characterized by a sharp gradient mainly on its poleward side. The sharp density gradients of the low-density ionospheric trough can cause significant signal delays, making it a source of error for trans-ionospheric radio systems used in communications and navigation satellites such as Global Navigation Satellite Systems (GNSS). Additionally, the L-band used by GNSS can experience signal scintillation due to small-scale irregularities at both the poleward and equatorward boundaries of the MIT. Therefore, understanding the relationship between the trough and space weather using both radio signals and in-situ monitoring is crucial.

The objective of this study is to improve our understanding of the MIT phenomenon using new satellite data to identify and describe the mid-latitude ionospheric trough and to develop the MIT model. The statistical analysis of MIT was performed using long-term in-situ electron density measurements from the GRACE (2002-2015) and Swarm (2013-2019) satellites and ground-based measurements such as total electron content (TEC) from the International GNSS Service (IGS) Global Ionosphere Maps (GIMs) (1998-2023). The mid-latitude ionospheric trough in the Northern and Southern Hemispheres was studied in relation to magnetic local time, geographic distribution, seasons, solar activity, and geomagnetic activity conditions such as solar wind plasma speed, interplanetary magnetic field components, and high-resolution geomagnetic indices SYM-H and Hp30. As a function of all these parameters, the main features of the MIT, such as minimum trough position, trough width and depth, and trough occurrence probability, were investigated. The results obtained in this work align with previous publications and, moreover, have some new findings. All dependencies obtained using the MIT detection function were compared with the PRISM ESA product ("Plasmapause Related boundaries in the topside Ionosphere as derived from Swarm Measurements - Earth Online", n.d.), which already contains detected troughs derived from Swarm measurements, but using a different detection algorithm.

Despite its importance, MIT has not yet been included in global empirical models used to correct for ionospheric propagation effects on GNSS signals, such as IRI (Bilitza, 2018), NeQuick-G (ICD, 2010; Nava, Coisson, & Radicella, 2008), and NTCM-G (Hoque et al., 2019), etc. Based on a statistical study of MIT, an empirical MIT model for determining the position, width, and depth of troughs in the Northern and Southern Hemispheres was derived. In the future, our MIT model can be included in and contribute to the improvement of the global TEC models mentioned above.

In addition, the behavior of the troughs during approximately 356 geomagnetic storms in a period from 2002 to 2019 was studied. It was observed that the main ionospheric trough shifts towards the equator with a decreasing Dst index during the main phase of the magnetic storms. As the Dst index increases during the storm

recovery phase, the trough position shifts poleward. The developed trough model is also able to reproduce the storm trend well. During the storm events, different local time groups were analyzed, such as dusk, dawn, and night. As well as different longitudinal sectors, such as the American and European sectors. Finally, the model results and the trough detected by IGS TEC maps were compared for the recent extreme geomagnetic storm event, namely the Mother's Day event from 9 - 15 May 2024. The developed model is also able to show smoothed changes in trough position during such an extreme geomagnetic event.

Keywords: mid-latitude ionospheric trough, Northern and Southern Hemispheres, high and low solar activity, trough detection, trough modeling

Zusammenfassung

Unsere Ionosphäre ist geprägt von jahres- und tageszeitlichen Schwankungen, welche auf solare Einflüsse zurückzuführen sind. Extrem-ultraviolette Strahlung (EUV), Röntgenstrahlung und Lyman-Alpha-Strahlung sind die wichtigsten Faktoren, die die Elektronendichteverteilung in der Ionosphäre beeinflussen. Darüber hinaus ist die Ionosphäre nicht homogen und weist verschiedene großskalige Irregularitäten auf. Eine davon ist der Ionosphärentrog in den mittleren Breiten, der im Mittelpunkt dieser Arbeit steht. Der Ionosphärentrog (engl. mid-latitude ionospheric trough, kurz MIT) ist eine Plasmadichteverringerung in der nächtlichen F-Schicht in subauroralen Breiten. Der MIT befindet sich im Wesentlichen zwischen dem äquatorwärts gerichteten Rand des Polarlichtovals und der Plasmapause bzw. der plasmasphärischen Grenzschicht. Der MIT hat eine V-förmige Struktur und zeichnet sich vor allem durch einen scharfen Gradienten auf seiner polwärts gerichteten Seite aus. Die steilen Dichtegradienten des MIT mit geringer Dichte führen zu erheblichen Signalverzögerungen und stellen somit eine Fehlerquelle für transionosphärische Funksysteme dar, die in Kommunikations- und Navigationssatelliten, wie dem globalen Satellitennavigationssystem (GNSS), eingesetzt werden. Darüber hinaus kann es im L-Band, das von GNSS genutzt wird, aufgrund von kleinskaligen Irregularitäten sowohl an der polwärts als auch an der äquatorwärts gelegenen Grenze des MIT zu Szintillationen führen. Daher ist es von entscheidender Bedeutung, die Beziehung zwischen dem Trog und dem Weltraumwetter anhand von Funksignalen und In-situ-Überwachung zu verstehen.

Ziel dieser Studie ist ein besseres Verständnis des MIT-Phänomens, mithilfe neuer Satellitendaten um den Ionosphärentrog in den mittleren Breiten zu beschreiben und schließlich ein MIT-Modell zu entwickeln. Die statistische Analyse des MIT wurde anhand von Langzeitmessungen der Elektronendichte durch die Satelliten GRACE (2002-2015) und Swarm (2013-2019) sowie anhand von bodengestützten Messungen des International GNSS Service (IGS) in Form von globalen Ionosphärenkarten des Gesamtelektronengehalts (TEC-Karten) (1998-2023) durchgeführt. Der MIT in der nördlichen und südlichen Hemisphäre wurde in Bezug auf die magnetische Lokalzeit, die geografische Verteilung, die Jahreszeiten, die Sonnenaktivität und geomagnetische Aktivitätsbedingungen, wie die Plasmageschwindigkeit des Sonnenwinds, interplanetare Magnetfeldkomponenten und hochauflösende geomagnetische Indizes SYM-H und Hp30, untersucht. In Abhängigkeit von all diesen Parametern wurden MIT-Parameter wie die Position der minimalen Elektronendichte, die Breite und Tiefe des Trogs, sowie die Wahrscheinlichkeit des Auftretens eines solchen untersucht. Die in dieser Arbeit erzielten Ergebnisse stimmen mit früheren Veröffentlichungen überein und enthalten darüber hinaus einige neue Erkenntnisse. Alle Abhängigkeiten, die mit der MIT-Erkennungsfunktion ermittelt wurden, wurden mit dem PRISM-ESA-Produkt („Plasmapause Related boundaries in the topside Ionosphere as derived from Swarm Measurements - Earth Online“, o. D.) verglichen und validiert.

Dieses Produkt enthält bereits Tröge, die aus Swarm-Messungen abgeleitet wurden, jedoch einen anderen Erkennungsalgorithmus verwendet. Trotz seiner Bedeutung wurde der MIT noch nicht in globale empirische Modelle aufgenommen, um ionosphärische Ausbreitungseffekte auf GNSS-Signale zu kompensieren, wie zum Beispiel IRI (Bilitza, 2018), NeQuick-G (ICD, 2010; Nava, Coisson & Radicella, 2008), und NTCM-G (Hoque et al., 2019). Auf Grundlage statistischer Untersuchungen des MIT wurde ein empirisches MIT-Modell zur Bestimmung der Position,

Breite und Tiefe von Trögen auf der Nord- und Südhalbkugel entwickelt. In Zukunft kann unser MIT-Modell in die oben genannten globalen TEC-Modelle integriert werden und zu deren Verbesserung beitragen.

Außerdem wurde das Verhalten der Tröge während etwa 356 geomagnetischer Stürme im Zeitraum von 2002 bis 2019 untersucht. Es wurde beobachtet, dass sich der Ionosphärentrog während der Hauptphase eines geomagnetischen Sturms in Abhängigkeit des steigenden Dst-Index Richtung Äquator verschiebt. In der Erholungsphase des Sturms verschiebt sich der Trog wieder polwärts. Das entwickelte MIT-Modell gibt diesen Trend gut wider. Diese Untersuchungen wurden einzeln für verschiedene Lokalzeiten (Morgen, Abend, Nacht) und geographische Längengradsektoren (Europa, Amerika) durchgeführt. Schließlich wurden die Modellergebnisse und die von IGS-TEC-Karten erfassten Tröge während des jüngsten schweren geomagnetischen Sturmereignisses, dem sogenannten Muttertags-Event vom 9. bis 15. Mai 2024, verglichen. Das Modell ist in der Lage, die Veränderung der Trogposition auch während solcher Extremereignisse mit nur leichter Glättung widerzugeben.

Contents

Declaration of Authorship **iii**

Acknowledgements **vii**

Abstract **ix**

Zusammenfassung **xi**

List of Figures **xxiii**

List of Tables **xxv**

List of Abbreviations **xxvii**

List of Symbols **xxix**

1 Introduction **1**
1.1 Motivation and research objectives 1
1.2 Thesis structure 2

2 Space Weather **3**
2.1 The Sun 3
2.2 The Magnetosphere-Ionosphere-Thermosphere system 5
2.2.1 Magnetosphere 6
2.2.2 Structure and composition of the upper atmosphere and ionosphere 8
2.3 Periodic changes in the ionosphere with time 11
2.4 Total Electron Content 12
2.5 Geomagnetic storms 13

3 Global ionospheric models **17**
3.1 International Reference Ionosphere 17
3.2 NeQuick 18
3.3 NTCM 19
3.4 Comparison of models 20
3.5 Mid-latitude trough in global ionospheric models 21

4 Mid-latitude ionospheric trough **23**
4.1 The Mid-Latitude Trough: Historical Context 23
4.2 Main features of the mid-latitude trough 24
4.3 Formation and physical phenomenon associated with mid-latitude trough 26
4.4 Key Space weather parameters influence MIT dynamics 28
4.4.1 Hp30 and Kp index 28

4.4.2 SYM-H and Dst index . . . 29
4.4.3 F10.7 index . . . 29
4.4.4 Convection electric field . . . 30

5 Database and Method **31**
5.1 Database: Satellite observations (Swarm, GRACE) and IGS maps . . . 31
5.1.1 Swarm . . . 31
5.1.2 PRISM . . . 32
5.1.3 GRACE . . . 34
5.1.4 Global vTEC maps from IGS . . . 35
5.2 Method for detecting mid-latitude trough . . . 36
5.3 Datasets differences and implications on trough detection . . . 42

6 Results of the statistical analysis of the MIT **45**
6.1 MIT and its dependencies on space weather parameters . . . 45
6.1.1 Geographical distribution . . . 45
6.1.2 Solar Cycle dependence . . . 46
6.1.3 Seasonal variation . . . 48
6.1.4 Diurnal variation . . . 49
6.1.5 Dependence on Solar Wind, Flow Pressure and IMF Bx, By, Bz components . . . 56
6.1.6 Dependence on Hp30 Index . . . 61
6.1.7 Dependence on SYM-H Index . . . 63
6.1.8 Trough occurrence dependence on Space Weather Indices . . . 65
6.1.8.1 MIT occurrence dependence on F10.7 . . . 66
6.1.8.2 MIT occurrence dependence on Hp30 index . . . 66
6.1.8.3 MIT occurrence dependence on SYM-H index . . . 68
6.1.8.4 MIT occurrence dependence on SW plasma speed . . . 69
6.1.8.5 MIT occurrence dependence on Flow pressure . . . 69
6.1.8.6 MIT occurrence dependence on IMF Bz . . . 70
6.1.8.7 Main findings about MIT behaviour regarding Space weather indices . . . 71
6.1.9 Trough Slopes . . . 71

7 Modeling of the MIT **77**
7.1 Reasoning of the model . . . 77
7.2 Empirical modeling of MIT parameters . . . 79
7.2.1 Modeling Approach . . . 79
7.2.1.1 MIT location in Northern and Southern Hemispheres 82
7.2.1.2 MIT depth in Northern and Southern Hemispheres . . 83
7.2.1.3 MIT width in Northern and Southern Hemispheres . . 84
7.2.2 Modeling Results . . . 85

8 Analysis of MIT during Geomagnetic storms **93**
8.1 Data and methodology . . . 93
8.2 MIT during Geomagnetic storms using GRACE and IGS data 2002-2015 94
8.3 MIT during Geomagnetic storms 2013-2019 using Swarm, PRISM, IGS data . . . 98
8.4 Case study: Mother's Day Storm 2024 . . . 104
8.5 Model performance during the Mother's Day Storm . . . 105

9 Summary and Outlook **111**

Bibliography **117**

A List of Publications **125**
A.1 Journal publications 125
A.2 Conference publications 125
A.3 Workshops 125

B Geomagnetic Storms **127**
B.1 MIT during Geomagnetic storms using GRACE and IGS 2002-2015 . . 128
B.2 MIT during Geomagnetic storms 2013-2019: Swarm, PRISM and IGS . 131

List of Figures

2.1 The structure of the main regions of the Sun updated by ("The Sun - NASA", n.d.) . . . 4
2.2 An illustration of the spiral shape of the magnetic field lines and the growth of the solar wind from the Sun. Figure modified from Lu et al. (2022). . . . 6
2.3 Distinct regimes are created when the solar wind strikes the Earth's magnetic field (Lang & Lang, 2009). . . . 8
2.4 Typical temperature and ionospheric plasma density profiles of the atmosphere, labeled with the different layers (Kelley, 2009) . . . 9
2.5 Principal neutral and ionic components of the ionosphere (N stands for free electrons) around local noon in summertime during a period of medium solar activity at mid-latitude (Dominici et al., 1998) . . . 10
2.6 Variations in the solar cycle represented by the F10.7 index and sunspot number, using data from ("OMNIWeb Data Explorer", n.d.) . 12
2.7 Illustration of STEC (S line) vs VTEC (V dashed line) (Vierinen et al., 2016) . . . 13
2.8 Illustration of the global TEC distribution obtained from IMPC (German Aerospace Center (DLR), 2024) . . . 14
2.9 SYM-H index, IMF Bz component, solar wind plasma speed, and flow pressure during the geomagnetic storm on 26–27 September 2011. Data from the 1-minute resolution OMNI dataset clearly illustrate the storm's distinct phases: initial, main, and recovery ("OMNIWeb Data Explorer", n.d.). . . . 15

4.1 Schematic Diagram of a model of the mid-latitude ionospheric trough including its basic parameters (Mallis & Essex, 1993) . . . 24
4.2 Diagram of the stagnation mechanism by (Spiro et al., 1978). The magnetospheric electric field dominates plasma flow in region D, whereas the corotation electric field predominates in region A. Due to the combined impacts of the two electric field distributions, the flow reverses from eastward to westward in the intermediate regions (regions B and C). The line that the east-west velocity component approaches 0 is known as the stagnation line. . . . 27

5.1 Timeline of observations from the GRACE and Swarm satellite missions, as well as IGS global vTEC maps and the F10.7 time series from 1998 to 2023 . . . 32
5.2 Evolution of daily minimum, maximum, and mean altitudes for the GRACE and Swarm A and C satellites. Shaded areas represent the range (min-max), and solid lines indicate mean altitudes. . . . 33

5.3 The Swarm satellite's side (top panel) and front (ram-direction) views, together with the locations of its instruments and several onboard systems ("Swarm operations", n.d.). 33
5.4 PRISM example of the MIT structure's characteristic points (a), the related SETE (b). Swarm A observations on January 1, 2015 around 01:20 UT (MLT = 2.5–3.0).The raw and smoothed profiles are shown as gray dots and thick green lines, respectively. The MIT minimum and SETE maximum are shown by a labeled downward/upward triangle, and boundary positions are indicated by labeled vertical lines. (Heilig et al., 2022). 34
5.5 Schematic of the GRACE satellite constellation and its instrumentation. a) with the top view of the satellite, b) the bottom view, c) the interior view ("GRACE (Gravity Recovery And Climate Experiment) - eoPortal", n.d.). 36
5.6 Global distribution of stations of the IGS network ("IGS Network", n.d.). 37
5.7 Illustration of the workflow for the trough detection algorithm. 39
5.8 Diagrammatic representation of the width, depth, and characteristic features of the mid-latitude trough (Lubyk et al., 2022) 40
5.9 Example of the IGS TEC map on 22.12.2008 with the quiet geomagnetic activity. TEC values are shown between 40° and 70° magnetic latitudes in both the Northern and Southern Hemispheres. The black line represents the solar terminator, where the night side is colored with light blue and the day side is shaded with light yellow. The red circles represent the trough position. 40
5.10 Example illustrations of the April 14, 2002 GRACE trajectory between 40° and 70° magnetic latitudes across the Northern (a) and Southern (c) Hemispheres. Plotting of concentric circles occurs at intervals of 10°. The magnetic latitudes of 40° and 70° are represented by the blue lines. The satellite path's footprint is shown by the red line. There is a star to indicate the magnetic pole. Ne profiles that correspond to the identified trough minimum location and trough characteristic points for the Hemispheres of the North (b) and South (d) are plotted below. The upper plots for the Northern (b) and Southern (d) Hemispheres show detrended logs of Ne. The Ne running average is shown as the gray dashed line. The threshold for trough identification is indicated by the red dashed line, whereas the yellow line represents the Ne profile. Reprinted from (Lubyk et al., 2022). 41

6.1 Polar view of the geographic locations of trough minimum locations (marked by red dots) for (A),(E) - Grace, (B),(F) - Swarm, (C),(G) - IGS TEC maps, and (D),(H) - PRISM. The top row shows the Northern Hemisphere, and the bottom row shows the Southern Hemisphere. The geomagnetic pole positions for each plot are indicated by purple stars. 46
6.2 The variations in (A) trough location, (B) trough width, and (C) trough depth of the mid-latitude trough as a function of the F10.7 index for the Northern and Southern Hemispheres. Error bars indicate the STD of the values. 47

6.3 Mean trough minimum position values plotted for Northern (A) and Southern (B) Hemispheres using GRACE, Swarm, IGS, and PRISM data for different seasons: December solstice, June solstice, and the equinoxes. Error bars indicate the STD of the values. 49
6.4 Seasonal differences between the Northern and Southern Hemispheres in the occurrence rate of MIT. Monthly variations of MIT occurrence in the Northern and Southern Hemispheres are shown in (A) and (B), respectively. 49
6.5 The monthly variations in the (A, B) trough location, (C, D) trough width, and (E, F) trough depth of the mid-latitude trough in the Northern and Southern Hemispheres. Error bars indicate the STD of the values. 50
6.6 Changes in the trough position and its width marked by the equatorward and poleward break points throughout the day in the Northern (A) and Southern (B) Hemispheres according to the magnetic local time. 52
6.7 Variation in the trough width (A, B) and depth (C, D) throughout the day according to magnetic local time in the Northern and Southern Hemispheres. Error bars indicate the STD of the values. 53
6.8 Occurrence rates as a function of magnetic local time and magnetic latitude for the December solstice, June solstice, and equinoxes. Corresponding polar views of the trough detected by IGS TEC maps (A-C), GRACE (D-F), Swarm (G-I), and PRISM (J-L) are shown for the Northern hemisphere. 54
6.9 Occurrence rates as a function of magnetic local time and magnetic latitude for the December solstice, June solstice, and equinoxes. Corresponding polar views of the trough detected by IGS TEC maps (A-C), GRACE (D-F), Swarm (G-I), and PRISM (J-L) are shown for the Southern Hemisphere. 55
6.10 Variations in the (A, B) - trough location, (C, D) - trough width, and (E, F) trough depth of the mid-latitude trough depending on solar wind plasma speed in the Northern and Southern Hemispheres. Error bars indicate the STD of the values. 57
6.11 Variations in the (A, B) - trough location, (C, D) - trough width, and (E, F) trough depth of the mid-latitude trough depending on flow pressure in the Northern and Southern Hemispheres. Error bars indicate the STD of the values. 58
6.12 Variations in the (A, B) - trough location, (C, D) - trough width, and (E, F) trough depth of the mid-latitude trough depending on IMF Bx component in the Northern and Southern Hemispheres. Error bars indicate the STD of the values. 59
6.13 Variations in the (A, B) - trough location, (C, D) - trough width, and (E, F) trough depth of the mid-latitude trough depending on IMF By component in the Northern and Southern Hemispheres. Error bars indicate the STD of the values. 60
6.14 Variations in the (A, B) - trough location, (C, D) - trough width, and (E, F) trough depth of the mid-latitude trough depending on IMF Bz component in the Northern and Southern Hemispheres. Error bars indicate the STD of the values. 61

6.15 The trough minimum location (A, B), trough width (C, D), and trough depth (E, F) as a function of the Hp30 index for the Northern and Southern Hemispheres. Error bars indicate the STD of the values. . . . 63
6.16 The trough minimum location (A, B), trough width (C, D), and trough depth (F, F) as a function of the SYM-H index for the Northern and Southern Hemispheres. Error bars indicate the STD of the values. . . . 65
6.17 Northern (A) and Southern (B) Hemisphere scatter plots of the monthly averaged trough occurrence rate against its F10.7 index. Additionally displayed for each panel are the correlation coefficient and the linear fitted line. 66
6.18 Northern (A) and Southern (B) Hemisphere bar plots of the trough occurrence rate against Hp30 index. 68
6.19 Northern (A) and Southern (B) Hemisphere bar plots of the trough occurrence rate against SYM-H index. 69
6.20 Northern (A) and Southern (B) Hemisphere bar plots of the trough occurrence rate against solar wind plasma speed. 69
6.21 Northern (A) and Southern (B) Hemisphere bar plots of the trough occurrence rate against flow pressure. 70
6.22 Northern (A) and Southern (B) Hemisphere bar plots of the trough occurrence rate against IMF Bz component. 70
6.23 F10.7 index dependence of the trough poleward slope (top plot) and equatorward (bottom plot) for the calm period (Kp index$<$ 3) in Northern Hemisphere. 72
6.24 F10.7 index dependence of the trough poleward slope (top plot) and equatorward (bottom plot) for the storm period (Kp index $>$ 3) in Northern Hemisphere. 73
6.25 F10.7 index dependence of the trough poleward slope (top plot) and equatorward (bottom plot) for the calm period (Kp index $<$ 3) in Southern Hemisphere. 73
6.26 F10.7 index dependence of the trough poleward slope (top plot) and equatorward (bottom plot) for the storm period (Kp index $>$ 3) in Southern Hemisphere. 74
6.27 Kp index dependence of the trough poleward slope (top plot) and equatorward (bottom plot) in Northern Hemisphere. 75
6.28 Kp index dependence of the trough poleward slope (top plot) and equatorward (bottom plot) in Southern Hemisphere. 75

7.1 An example of the high values of the trough depth in the Northern Hemisphere in the American sector during the Halloween solar storm on the 29th of October 2003, where Dst was -268 nT at 21 UT. The blue line represents the TEC profile, and the orange line is the running average. The red dots represent the detected Tm position and the breakpoints Be and Bp. 79
7.2 Correlation of MIT parameters - such as trough minimum position, width, depth - with space weather parameters for both (A) Northern and (B) Southern Hemispheres. Positive correlations are shown in red and negative correlations are shown in blue. 80

7.3 Trough-location model prefit, represented by the red dashed curve, and trough-averaged data, represented by the blue curve, as a function of (A) day of the year, (B) Dst index, (C) F10.7 index, (D) Kp index and (E) local time. 87
7.4 Trough-location model fit (see continuation on the next page). 88
7.4 Final full trough-location model fit (red dashed curves) with the coefficients given in Table 7.2 and trough-averaged data (blue line) as a function of (from top to bottom): (A, B) day of the year, (C, D) Dst index, (E, F) F10.7 index, (G, H) Kp index, and (I, J) local time. Each row compares the Northern Hemisphere (left) and Southern Hemisphere (right). 89
7.5 Final full trough depth model fit (red dashed curves) with the coefficients given in Table 7.3 and trough-averaged data (blue curves) for Northern (left column) and Southern Hemispheres (right column) as functions of (A, B) day of the year, (C, D) Dst index, (E, F) F10.7 index, and (G, H) Kp index. 90
7.6 Final full trough width model fit (red dashed curves) with the coefficients given in Table 7.4 and trough-averaged data (blue curves) for Northern (left column) and Southern Hemispheres (right column) as functions of (A, B) Dst index, (C, D) F10.7 index, and (E, F) Kp index. . 91
7.7 Histograms of Trough Model residuals (input data minus model values) for the Northern Hemisphere (left column) and Southern Hemisphere (right column), showing (A, B) trough location, (C, D) trough depth, and (E, F) trough width. 92

8.1 The distribution of the storms that have been used in this research as well as the data groups that have been used are marked. 94
8.2 Mean and median trough position during storms in the night magnetic local time sector (22 - 2 MLT) for the European (left column) and American (right column) sectors separately in the Northern Hemisphere for GRACE, IGS TEC map observations and model values. The storm minimum is marked with a red dashed line and set to 0 epoch hour. 96
8.3 Mean and median trough position during storms in the dusk magnetic local time sector (18 - 21 MLT) for the European (left column) and American (right column) sectors separately in the Northern Hemisphere for GRACE, IGS TEC map observations and model values. The storm minimum is marked with a red dashed line and set to 0 epoch hour. 97
8.4 Mean and median trough position during storms in the dawn magnetic local time sector (3 - 7 MLT) for the European (left column) and American (right column) sectors separately in the Northern Hemisphere for GRACE, IGS TEC map observations and model values. The storm minimum is marked with a red dashed line and set to 0 epoch hour. 98
8.5 The trough minimum location (A) and trough width (B) mean plotted for different MLT sectors and for Europe and American sector separately using GRACE, IGS TEC maps and Model data. 100

8.6 The trough minimum location (A) and trough width (B) mean plotted for different MLT sectors and for Europe and American sector separately using Swarm, IGS TEC maps, PRISM and Model data. 101
8.7 Mean and median trough position during storms in the night magnetic local time sector (22 - 2 MLT) for the European (left column) and American (right column) sectors separately in the Northern Hemisphere for PRISM, Swarm, IGS TEC map observations and model values. The storm minimum is marked with a red dashed line and set to 0 epoch hour. 102
8.8 Mean and median trough position during storms in the dusk magnetic local time sector (18 - 21 MLT) for the European (left column) and American (right column) sectors separately in the Northern Hemisphere for PRISM, Swarm, IGS TEC map observations and model values. The storm minimum is marked with a red dashed line and set to 0 epoch hour. 103
8.9 Mean and median trough position during storms in the dawn magnetic local time sector (3 - 7 MLT) for the European (left column) and American (right column) sectors separately in the Northern Hemisphere for PRISM, Swarm, IGS TEC map observations and model values. The storm minimum is marked with a red dashed line and set to 0 epoch hour. 104
8.10 Epochal analysis of the trough position in NH during the Mother's Day storm event at different local times, such as dusk (green color), night (blue color), and dawn (red color). The top plot shows the trough position determined from the IGS UQRG maps, and the second plot below shows the trough position using the model values. The third plot displays the Dst index values, and the last plot shows the Kp index during the 24 hours before the storm peak, which occurred on 11.05.2024 at 02:00:00 (marked with a gray dashed line indicating the epoch time set to 0 hours) and 72 hours after. 106
8.11 Epochal analysis of the trough position in SH during the Mother's Day storm event at different local times, such as dusk (green color), night (blue color), and dawn (red color). The top plot shows the trough position determined from the IGS UQRG maps, and the second plot below shows the trough position using the model values. The third plot displays the Dst index values, and the last plot shows the Kp index during the 24 hours before the storm peak, which occurred on 11.05.2024 at 02:00:00 (marked with a gray dashed line indicating the epoch time set to 0 hours) and 72 hours after. 107
8.12 3-Dimensional plot of trough profiles in NH detected during Mother day storm from IGS TEC maps (left column) and trough profiles derived using model (right columns). 108
8.13 3-Dimensional plot of trough profiles in SH detected during Mother day storm from IGS TEC maps (left column) and trough profiles derived using model (right columns). 109

8.14 Model performance during the Mother's Day Storm event. Bar plots show the Pearson correlation between the observed trough minimum location from IGS TEC maps and our model predictions for geomagnetic latitude. Correlation in the Northern Hemisphere is marked with blue color, and the Southern Hemisphere is marked with yellow; results are separated by local time sectors (night, dusk, dawn). 110

B.1 Mean and median trough position during storms in the night magnetic local time sector (22 - 2 MLT) for the European (left column) and American (right column) sectors separately in the Southern Hemisphere for GRACE, IGS TEC map observations and model values. The storm minimum is marked with a red dashed line and set to 0 epoch hour. 128
B.2 Mean and median trough position during storms in the dusk magnetic local time sector (18 - 21 MLT) for the European (left column) and American (right column) sectors separately in the Southern Hemisphere for GRACE, IGS TEC map observations and model values. The storm minimum is marked with a red dashed line and set to 0 epoch hour. 129
B.3 Mean and median trough position during storms in the dawn magnetic local time sector (3 - 7 MLT) for the European (left column) and American (right column) sectors separately in the Southern Hemisphere for GRACE, IGS TEC map observations and model values. The storm minimum is marked with a red dashed line and set to 0 epoch hour. 130
B.4 Mean and median trough position during storms in the night magnetic local time sector (22 - 2 MLT) for the European (left column) and American (right column) sectors separately in the Southern Hemisphere for PRISM, Swarm, IGS TEC map observations and model values. The storm minimum is marked with a red dashed line and set to 0 epoch hour. 131
B.5 Mean and median trough position during storms in the dusk magnetic local time sector (18 - 21 MLT) for the European (left column) and American (right column) sectors separately in the Southern Hemisphere for PRISM, Swarm, IGS TEC map observations and model values. The storm minimum is marked with a red dashed line and set to 0 epoch hour. 132
B.6 Mean and median trough position during storms in the dawn magnetic local time sector (3 - 7 MLT) for the European (left column) and American (right column) sectors separately in the Southern Hemisphere for PRISM, Swarm, IGS TEC map observations and model values. The storm minimum is marked with a red dashed line and set to 0 epoch hour. 133

List of Tables

2.1 Common vertical attributes of the ionosphere observed during daytime. 9

3.1 Overview of selected ionosphere models and their characteristics. . . . 18
3.2 Comparison of Ionospheric Models 20

5.1 Comparison of Swarm, GRACE, and IGS TEC Data for Trough Detection 43

6.1 Mean trough minimum position values (MLAT, [deg]) reprinted in the Northern Hemisphere using GRACE, Swarm, IGS, and PRISM data for different seasons: December solstice, June solstice, and the equinoxes. The corresponding standard deviation follows the sign ±. . 49
6.2 Mean trough minimum position values (MLAT, [deg]) reprinted in the Southern Hemisphere using GRACE, Swarm, IGS, and PRISM data for different seasons: December solstice, June solstice, and the equinoxes. The corresponding standard deviation follows the sign ±. . 51
6.3 Main findings about trough behaviour regarding Space weather indices 71

7.1 GPS/Galileo/GLONASS L1 range error 78
7.2 Optimal set of model coefficients of MIT location in the Northern and Southern Hemispheres 83
7.3 Optimal set of model coefficients of MIT depth in the Northern and Southern Hemispheres 84
7.4 Optimal set of model coefficients of MIT width in the Northern and Southern Hemispheres 85

8.1 NH Comparison of trough minimum position and width for Europe and American sectors, during different MLT sectors using GRACE and IGS TEC data 95
8.2 NH Comparison of trough minimum position and width for Europe and American sectors, during different MLT sectors using Swarm, PRISM, IGS TEC and model data. 99

List of Abbreviations

CODE	**C**enter for **O**rbit **D**etermination in **E**urope
CME	**C**oronal **M**ass **E**jection
DLR	German Aerospace Center
DMSP	**D**efense **M**eteorological **S**atellite **P**rogram
DOY	**D**ay **O**f the **Y**ear
EC	**E**uropean **C**ommission
EUV	**E**xtreme **U**ultraviolet light
ESA	**E**uropean **S**pace **A**gency
JPL	**J**et **P**ropulsion **L**aboratory
GFZ	German Research Centre for Geosciences
GIM	**G**lobal **I**onosphere **M**ap
GPS	**G**lobal **P**ostitioning **S**ystem
GNSS	**G**lobal **N**avigation **S**atellite **S**ystems
GRACE	**G**ravity **R**ecovery and **C**limate **E**xperiment sattelite
GSE	**G**eocentric **S**olar **E**cliptic coordinates
IGS	**I**nternational **G**NSS **S**ervice
IMAGE	**I**mager for **M**agnetopause-to-**A**urora **G**lobal **E**xploration
IMF	**I**nterplanetary **M**agnetic **F**ield
IMPC	**I**onosphere **M**onitoring and **P**Prediction **C**enter
IONEX	**ION**osphere Map **E**xchange
IRI	**I**nternational **R**eference **I**onosphere
KBR	**K**-**B**and **R**anging System
LT	**L**ocal **T**ime
MIT	**M**id-latitude **I**onospheric trough
MLAT	**M**agnetic **L**atitude
MLT	**M**agnetic **L**ocal **T**ime
NASA	**N**ational **A**eronautics and **S**pace **A**dministration
NH	**N**orthern **H**emisphere
NOAA	**N**ational **O**ceanic and **A**tmospheric **A**dministration
NEDM	**N**eustrelitz **E**lectron **D**ensity **M**odel
NTCM	**N**eustrelitz **T**TE**C** **M**odel
PP	**P**lasmapause **P**osition
PRISM	**P**lasmapause **R**elated boundaries in the topside **I**onosphereas derived from **S**warm **M**easurements
SAPS	**S**ubauroral **P**olarization **S**tream
SETE	**S**ubauroral **E**lectron **T**emperature **E**nhancement
RE	**E**arth's **R**adius
SH	**S**outhern **H**emisphere
SP	**S**torm **P**eak
SSC	**S**udden **S**torm **C**ommencement
STD	**S**tandard **D**eviation
SW	**S**olar **W**ind

SWe	**S**pace **W**eather
UPC	**U**niversitat **P**olitècnica de **C**atalunya
UT	**U**niversal **T**ime
UV	**U**ultraviolet light
VHF	**V**ery **H**igh **F**requency

List of Symbols

Be	Break point eqwatorward	
Bp	Break point poleward	
$\overrightarrow{B_{sw}}$	interplanetary magnetic field vector	[nT]
Dst	Disturbance Storm Time	[nT]
E	Electric field	[V/m]
E_{conv}	Convection electric field	[mV/m]
EW	Equatorward slope	
$F10.7$	Solar radio flux at 10.7 cm	[sfu]
He	Equatorward half point	
Hp	Poleward half point	
$Hp30$	Kp-like index with a time resolution of half an hour	
Kp	Geomagnetic index	
L	Rate of loss via recombination	
N	Electron density	
PW	Poleward slope	
q	production rate	
$STEC$	Slant Total electron content	[TECU]
$SYM\text{-}H$	Longitudinally Symmetric Disturbance Field in Horizontal Direction	[nT]
SW	Solar Wind	
TEC	Total electron content	[TECU]
Tm	Trough minimum position	
Te	Electron temperature	[K]
Ne	Electron density	[electrons/m^3]
$NmF2$	Peak electron density	[electrons/m^3]
v	Mean drift velocity of electrons	[m/s]
$\overrightarrow{v_{sw}}$	solar wind bulk flow speed	[km⁄s]
$VTEC$	Vertical Total electron content	[TECU]
λ	Wavelength	[m]

Chapter 1

Introduction

1.1 Motivation and research objectives

The phenomenon referred to as the main ionospheric trough, or mid-latitude trough (MIT) is characterized by a significant decrease in plasma density in the nighttime F region and topside ionosphere at subauroral latitudes. Predominantly situated between the equatorward boundary of the auroral oval and the footprints of the plasmapause or plasmaspheric boundary layer (Heilig et al., 2022; Pierrard & Voiculescu, 2011), the main ionospheric trough typically spans several degrees of latitude. It appears as a longitudinally extended band, persisting for multiple hours of local time (LT).

The mid-latitude ionospheric trough manifests as a distinctive V-shaped structure within the ionosphere, characterized by a steep gradient on its poleward side during nighttime and a noticeable transition from darkness to dawn along its equatorward boundary (Liu & Xiong, 2020). Additionally, the equatorward wall of the MIT corresponds to the ionospheric footprint of the plasmapause (Rodger et al., 1992; Zou et al., 2011), while its poleward wall is linked to the equatorward boundary of the auroral precipitation zone (Rodger, 2008).

The steep density gradients within the low-density ionospheric trough cause considerable signal delays, posing a significant error source for trans-ionospheric radio systems utilized in communication and navigation satellites, such as Global Navigation Satellite Systems (GNSS). Additionally, small-scale irregularities at both the poleward and equatorward boundaries induce signal scintillation in the L-band used by GNSS and very high frequencies (VHF) signals. Hence, it is crucial to comprehend the connection of the trough and space weather through both radio signals and in-situ measurements.

Since 1965, when the trough was first identified (Muldrew, 1965), several observational techniques, including satellite and ground-based methods, have been used to observe and study the MIT (Aa et al., 2020; He et al., 2011; Krankowski et al., 2009; Lee et al., 2011). There are already many climatological results presented in the literature, as well as trough formation and physical phenomena associated with the mid-latitude trough. However, there are still inconsistencies in the MIT climatology and MIT has not yet been integrated into global empirical models such as International Reference Ionosphere (IRI) (Bilitza et al., 2022), NeQuick-G (Nava, Coisson, & Radicella, 2008; Union, 2010), and NTCM-G (Hoque et al., 2019), which provide corrections for ionospheric propagation effects on GNSS signals.

The primary objective of this study is to perform a statistical analysis of MIT using data from different data sources like satellite and ground-based data and to construct an ionospheric model that accurately depicts the ionospheric trough alongside density irregularities at its boundaries. We will utilize multi-frequency

data obtained from long-term global ionosphere monitoring at various altitudes, employing global ionospheric TEC maps. Additionally, high-resolution in-situ GRACE and Swarm constellations measurements will be utilized. This data will be employed to detect and model the mid-latitude ionospheric trough.

1.2 Thesis structure

This thesis is organized to provide a comprehensive understanding of the mid-latitude trough phenomenon. It begins with an introductory section that outlines the motivation and research objectives and lays the foundation for the following chapters. Chapter 2 covers the basics of space weather, including the influence of the Sun, the structure of the magnetosphere-ionosphere-thermosphere system, periodic ionospheric changes, total electron content, and geomagnetic storms. Chapter 3 introduces global ionospheric models, including the IRI, NeQuick and NTCM. Chapter 4 describes the mid-latitude ionospheric trough and its initial discovery. It also describes the formation mechanisms of the mid-latitude trough and the critical space weather parameters that influence it. Chapter 5 outlines the methodology for data collection and analysis, including satellite observations and ground-based maps, and the technique for detecting the mid-latitude trough. Chapter 6 presents the results of statistical analyses of the mid-latitude ionospheric trough, investigating its dependence on various space weather parameters. Moving to the modeling aspect, Chapter 7 discusses the rationale behind the proposed model, its empirical formulation, and modeling results. Chapter 8 analyzes the mid-latitude ionospheric trough during geomagnetic storms. Additionally, in Chapter 8 is a comparison of the modeling results with the trough detected from IGS TEC maps during the extreme geomagnetic storm of 2024 - the Mother's Day storm event. Finally, Chapter 9 summarizes the results obtained in this thesis, presents the conclusions and provides an outlook for future work.

Chapter 2

Space Weather

In the last 50 years the investigations into Space Weather (SWe) has become more and more intensively studied by many scientists and research institutions due to its profound impact on modern technological systems. Space weather is a developing discipline in space sciences that explores the effects of the Sun on Earth's space environment. This field investigates the consequences of such interactions, including potential harm to or loss of Earth-orbiting satellites. It also addresses concerns related to astronaut safety, as well as the potential risks to the dependability and precision of global communication and navigation systems.

This chapter presents the overview of topic of space weather, as well describes the Sun, which is its primary source of energy, the solar wind, the Magnetosphere-Ionosphere-Thermosphere system, and geomagnetic and ionospheric disturbances.

2.1 The Sun

The Milky Way galaxy has an estimated 100 billion stars, including our Sun. The Sun is Earth's main energy source, and this energy comes from thermonuclear reactions in its core. During this process, energy is released, some of which reaches the surface and travels into space as electromagnetic radiation. On average, roughly 150,000,000 kilometers separate the Sun from Earth. This distance is defined as 1 astronomical unit (AU). The mass of the Sun is 1.9×10^{30} kg. The estimated radius of the Sun is 696,000 km. It consists of the five most abundant elements, and their relative amounts are as follows: hydrogen(H)- 92.1%, helium (He)- 7.8%, oxygen (O)- 0.061%, carbon (C)-0.030%, nitrogen (N)- 0.0084%. There are other elements and heavy metals, but they compose less than 2% of the overall number of elements (Davies, 1990).

The inner part of the Sun is structured with three main regions: the convection zone, the radiation zone, and the core. Figure 2.1 depicts the Sun's structure, components and layers. In the core of the Sun, thermonuclear processes take place. The Sun is powered by these reactions, which release enormous amounts of energy every second. The solar constant, which measures how much energy is intercepted from the Sun per square meter per second, is roughly 1400 W m^{-2}. Another parameter of the Sun is luminosity, which is the total amount of energy that the Sun emits in a second. The luminosity of the Sun is equal to $3,86 \times 10^{26}$ W (Moldwin, 2008).

The core of the Sun is where all of its energy is generated by nuclear fusion. The material that composes the core is particularly dense because of the extremely high pressure and very high temperature of the core. This allows the nuclear reactions in the core of the Sun to occur. Radiation transfer moves energy from the Sun's core, where it is generated, to the surrounding areas. The term "radiative zone" refers

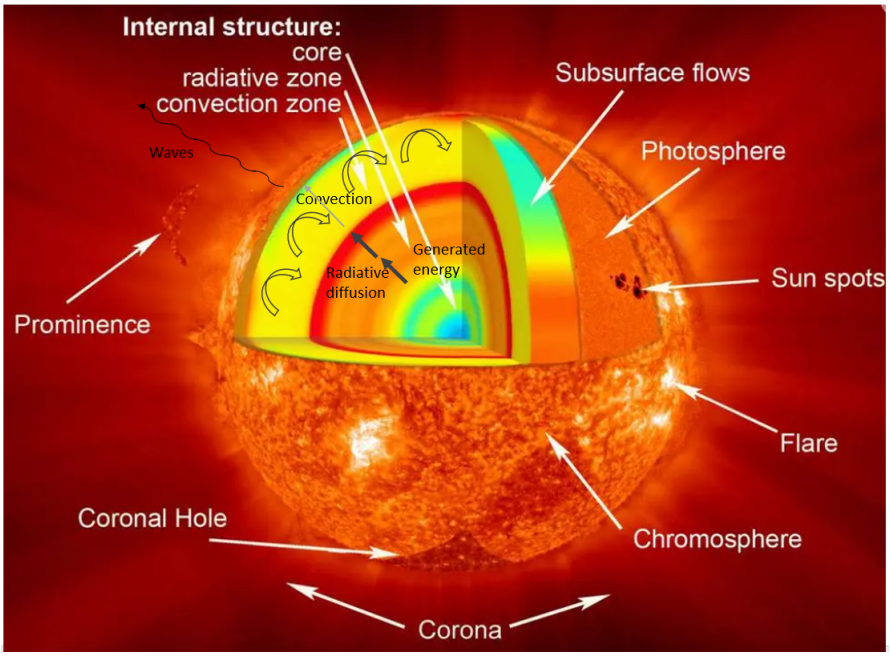

FIGURE 2.1: The structure of the main regions of the Sun updated by ("The Sun - NASA", n.d.)

to the path from the Sun's center to its outer regions. Here, energy, in the form of radiation, interacts with particles in the Sun's interior. The temperature drops steadily from near 15,600,000°C at the core of the Sun to around 1,500,000°C at the outer edge of the radiative zone, where the energy transfer across this zone can take as long as 170,000 years. The following layer, known as the convection zone, is where particles and atoms in the plasma absorb the energy and rise through the layer, enabling the transfer of heat to the surface (ESA, 2023).

What appears to be the surface of the Sun (a yellow disc) when seen from the Earth is actually the photosphere. This layer is extremely thin, roughly 500–700 kilometers thick (Thomas & Weiss, 2012). Visible radiation is released by the photosphere, which has a temperature range of 4500 K at the outer edge to around 6000 K near the convective zone. Above the photosphere is located another layer - the chromosphere. The temperature of this layer rises rapidly, reaching up to 20,000 K. Also, it is thicker and is less dense than the photosphere.

The corona refers to the outermost layer of the Sun, encompassing it entirely. It's the largest and least dense part of the Sun, composed of plasma with temperatures soaring up to 1,000,000 Kelvin, and it's even less dense than the chromosphere. Material from the corona is carried into space by the solar wind (ESA, 2023).

Each layer of the Sun not only differs in temperature and composition but also hosts unique phenomena, offering a variety of processes and features to observe. These include sunspots, prominences, Coronal Mass Ejections (CMEs), and flares. Large-scale electromagnetic radiation eruptions that take place in an active zone are known as solar flares. They can last from a few minutes to many hours, with an average duration of thirty minutes (Davies, 1990). It is common to associate flares or prominence eruptions with sporadic geomagnetic storms (Foukal, 2008). In Figure 2.1, can be seen the photosphere, featuring visible dark regions known as sunspots. These sunspots typically appear between latitudes 40° North and

40° South, although they can sometimes cluster together. Due to their lower temperature of around 4,000 degrees, they appear darker than the surrounding photosphere because they emit less light. Sunspots can have diameters exceeding 300,000 kilometers and boast significantly stronger magnetic fields, ranging from 100 to 5,000 times stronger than the surrounding field. While clusters of sunspots may persist for up to 100 days, individual sunspots typically form within a few days (Lilensten & Bornarel, 2005). Prominences are extensive structures composed of magnetic fields and plasma that extend outward from the Sun's surface, often forming loop shapes. Unlike the corona's hot plasma, prominences consist of colder plasma, similar to that found in the chromosphere. These formations develop over about a day and can persist in the corona for weeks or even months, stretching across vast distances into space. Certain prominences have the potential to trigger coronal mass ejections or flares (ESA, 2023). While flares release light, CMEs release material. These ejections typically last for several hours until all the twisted magnetic field lines are rearranged. When a CME occurs, it releases a significant amount of matter and electromagnetic energy. If directed towards Earth, a surge of particles can reach our planet within 2 to 5 days. Additionally, the CME brings along twisted magnetic fields that can interact with Earth's magnetic field, leading to geomagnetic storms (ESA, 2023). Apart from the above features, coronal holes are also of great importance. They are associated with regions of unipolar, open magnetic field lines that stream high-speed solar wind. The solar wind is the fast-moving stream of particles that constantly emerges from the solar corona and travels well beyond Earth's orbit into interplanetary space (Baumjohann & Treumann, 2012).

During calm times, the average solar wind speed is 400 km/s, while during disturbed times, it rises to roughly 1000 km/s. (Davies, 1990). The biggest structures of the solar wind in the interplanetary medium are caused by the Sun's spin. Solar wind particles are radially ejected, and the interplanetary magnetic field carried with them is shaped into an Archimedean spiral pattern due to the rotation of the Sun. According to authors in Baumjohann and Treumann (2012), the solar wind typically near the Earth has electron density of 5 cm^{-3} and electron temperature of 10^5 K. The solar wind has a low speed near the Sun, but it grows faster as one moves farther away from it. At a critical distance, roughly five solar radii above the photosphere, the wind reaches supersonic speed. Reaching the vicinity of the Earth, the solar wind comprises fully ionized plasma, which includes electrons, protons, and alpha particles (Baumjohann & Treumann, 2012).

The portion of the Sun's magnetic field that is carried outward into interplanetary space by the solar wind is known as the interplanetary magnetic field (IMF). The IMF takes the form of a spiral due to the Sun's rotation, and its intensity decreases with distance. When it reaches the vicinity of the Earth, the intensity of the IMF varies from 1 to 37 nT. It has 3 components, such as Bz, which is perpendicular to the ecliptic plane, and Bx and By in the ecliptic plane (Zolesi & Cander, 2014). Figure 2.2 shows schematically the solar wind and the IMF.

2.2 The Magnetosphere-Ionosphere-Thermosphere system

The Magnetosphere-Ionosphere-Thermosphere system is a dynamic and interconnected region of Earth's upper atmosphere that plays a crucial role in various geophysical processes, space weather phenomena, and interactions with the solar wind. This complex system encompasses the interactions between Earth's magnetic field, the ionized gases in the ionosphere, and the neutral gases in the thermosphere,

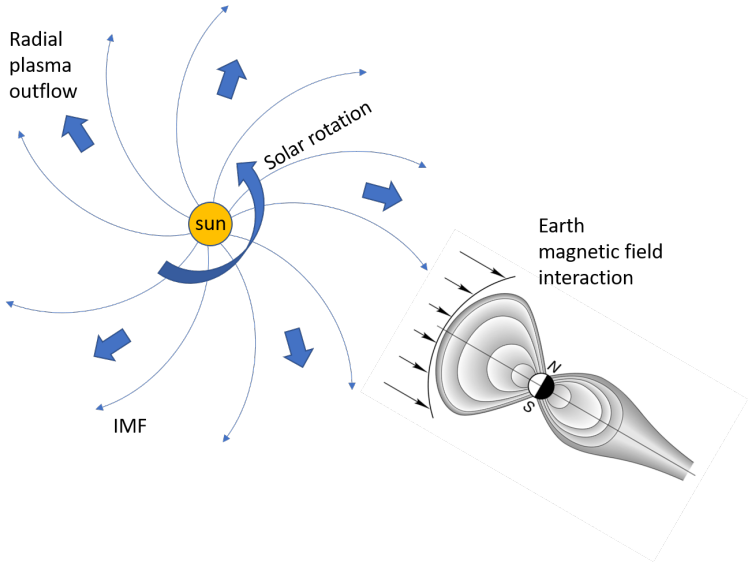

FIGURE 2.2: An illustration of the spiral shape of the magnetic field lines and the growth of the solar wind from the Sun. Figure modified from Lu et al. (2022).

creating a highly dynamic environment that undergoes significant changes in response to external influences such as solar activity and geomagnetic disturbances. Understanding the magnetosphere-ionosphere-thermosphere system is vital for several reasons:

1. It protects against the solar wind and particle radiation, safeguarding life on Earth and preserving the atmosphere.

2. The magnetosphere-ionosphere-thermosphere system influences technological systems such as satellite communications, navigation, and power grids, making it crucial for modern society's functioning.

3. Studying the magnetosphere-ionosphere-thermosphere system provides insights into fundamental plasma physics processes and contributes to our understanding of similar systems in other planets and celestial bodies.

This chapter examines the basic components and interactions within the Magnetosphere-Ionosphere-Thermosphere system.

2.2.1 Magnetosphere

The magnetosphere and atmosphere protect Earth's surface from harmful electromagnetic and particle radiation from the Sun. Therefore, the link between the magnetosphere and the Sun is a core topic of space weather. The region of space surrounding Earth that is in control of the Earth's magnetic field is known as the magnetosphere. The Earth's magnetosphere develops its current form due to solar wind blow. Figure 2.3 shows the main elements of the magnetosphere. The plasma carried by the solar wind interacts with the magnetosphere and creates a bow shock. The bow shock is always on the sunward side of the magnetosphere, and its location is quite changeable but typically it is approximately the size of 15 Earth's radii

(Lang & Lang, 2009). Next there is a boundary between the magnetosphere and the surrounding plasma which is called magnetopause. The equilibrium between the solar wind's dynamic pressure and the Earth's magnetic field's dynamic pressure defines the magnetopause's location. The magnetopause can move inward and outward in response to variations in the solar wind pressure. The space area between Earth's magnetopause and magnetosphere's bow shock is known as the magnetosheath.

The shocked solar wind plasma can not simply pass through the terrestrial magnetic field. It bows around the Earth and pulls the terrestrial magnetic field into extended magnetotail on the night side much beyond the lunar orbit (Baumjohann & Treumann, 2012). In the magnetosphere, protons and electrons compose most of the plasma. These particles originate from the terrestrial ionosphere and the solar wind. He^{++} ions received from the solar wind and smaller quantities of O^{+} and He^{+} ions from the ionospheric region are also present (Baumjohann & Treumann, 2012). Nonetheless, the plasma in magnetosphere is not evenly spread out. It is broken down into several areas with different temperatures and densities: radiation belt, plasmasphere, plasmasheet, and magnetotail lobe. The plasma in the magnetosphere also moves in response to external forces. Ions and electrons move together in the solar wind, but they move apart in other regions of the plasma, producing an electric current. The ring current, magnetopause current, field-aligned currents, and tail current are some examples of these electric currents in the magnetosphere. These currents have a significant impact on the dynamics of the plasma environment around Earth. They move energy, mass, charge, and momentum.

A key aspect in our understanding of the dynamics of the magnetosphere and geomagnetic storms is the ring current. The ring current is an electric current that circles around the Earth in the equatorial plane at a distance of around three to five Earth's radii from the center of the planet (Baumjohann & Treumann, 2012). When viewed from the Earth's north pole, the ring current travels clockwise and is carried by ions and electrons that are moving in opposing directions. Originating in the Earth's plasma sheet, the ring current particles travel earthward under the influence of our planet's electric and magnetic fields from dawn to sunset. The so-called Dst effect occurs during the main phase of geomagnetic storms when the ring current weakens and increases the Earth's magnetic field.

A fraction of Earth's neutral atmosphere is ionized by solar ultraviolet light, forming the ionosphere at altitudes above 80 km, where collisions are too rare for rapid recombination to occur. In the mid-latitude ionosphere, typical values for temperature are $T_e \approx 10^3$K and for electron density are $n_e \approx 10^5 cm^{-3}$ (Baumjohann & Treumann, 2012). The ionosphere expands at high altitudes and gradually merges with the plasmasphere at low and middle latitudes. As can be seen in the figure, the plasmasphere is located within the radiation belt and has a toroidal shape. In plasmasphere the thicker and colder plasma corotates with the Earth. The plasmasphere broadens to around 4 Earth radii (RE) (in the equatorial plane) to its limit called plasmapause (Baumjohann & Treumann, 2012).

The signature of the exiting coupling between the magnetosphere and the ionosphere is the auroral emission. Typically, auroras occur at high latitudes within the auroral oval. It occurs when plasma sheet electrons fall down magnetic field lines into the ionosphere, ionizing neutral particles and generating photons (Baumjohann & Treumann, 2012).

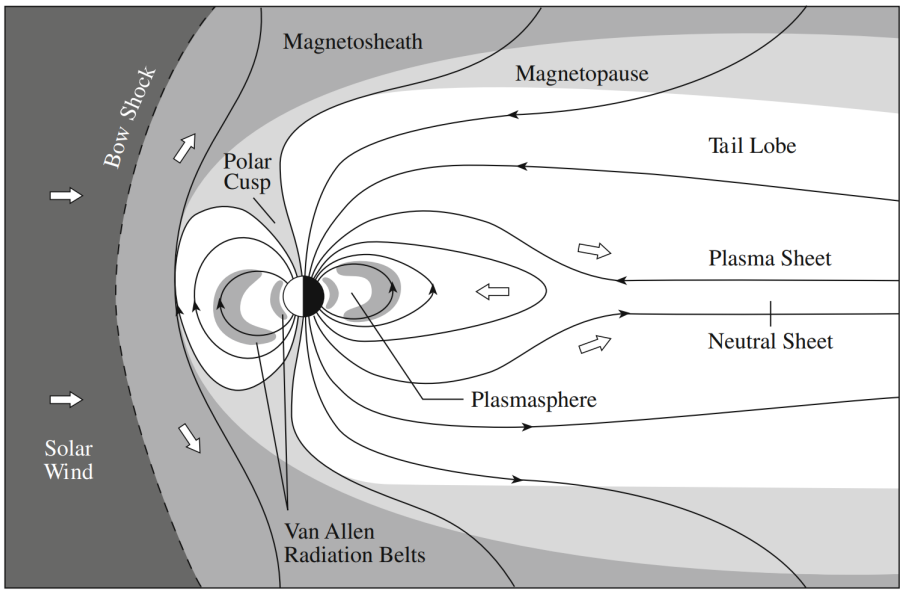

FIGURE 2.3: Distinct regimes are created when the solar wind strikes the Earth's magnetic field (Lang & Lang, 2009).

2.2.2 Structure and composition of the upper atmosphere and ionosphere

Typically, the area over 80 km is considered to be the upper atmosphere. The upper atmosphere primarily comprises neutral atoms and molecules called the thermosphere. Temperature profiles represent the atmosphere structure; however, the number density of the plasma is used to represent the ionosphere. Figure 2.4 provides typical temperature and plasma density profiles in the mid-latitudes. The thermosphere absorbs the sun's UV (ultraviolet) and EUV (extreme ultraviolet) light and is responsible for the rise in temperature there. EUV radiation plays a crucial role in generating plasma within the sunlit hemisphere by its ability to ionize the neutral atmosphere through the energetic solar photons it emits (Kelley, 2009).

The amount of ionized gas increases significantly within the thermosphere, forming the ionosphere. The ionosphere is a higher, ionized region of the Earth's atmosphere, located between roughly 60 and 1000 km.

There is an observed shift in the Earth's ionosphere's plasma parameters concerning altitude, latitude, longitude, season, solar cycle, and universal time. Solar EUV, UV, and x-ray radiation are the main sources of plasma and energy for the ionosphere; however, magnetospheric electric fields and particle precipitation also significantly impact the ionosphere. The IMF orientation and solar wind dynamic pressure, or the state of the interplanetary medium, are the primary determinants of the magnetospheric effect's strength and form. The global distributions of the plasma densities, temperatures, and drifts are determined by various external driving mechanisms combined with the radiative, chemical, dynamical, and electrodynamical processes that function in the ionosphere (Schunk & Nagy, 2004).

The Figure's 2.4 right-hand section displays two plasma density profiles, one representative of mid-latitude daytime conditions and the other nighttime. The primary regions are labeled as D, E, F1, and F2 regions, each exhibiting distinct daytime characteristics represented in the Table 2.1 (Hargreaves, 1992).

TABLE 2.1: Common vertical attributes of the ionosphere observed during daytime.

Region	Height (km)	Electron density (cm^{-3})
D	60 - 90	$10^2 - 10^4$
E	105 - 160	several 10^5
F_1	160-180	several $10^5 - 10^6$
F_2	maximum variable around 300	up to several 10^6

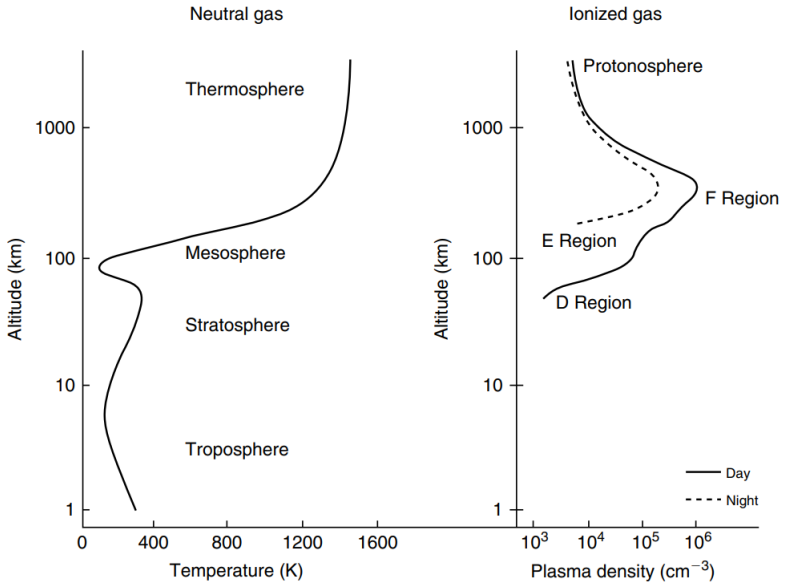

FIGURE 2.4: Typical temperature and ionospheric plasma density profiles of the atmosphere, labeled with the different layers (Kelley, 2009)

Primarily, the lower ionosphere (up to 100 km) is predominantly influenced by photochemical processes governing its formation and ionization balance. The transition to the middle ionosphere (100–170 km) delineates the boundary where ionization-recombination processes coincide with thermal and dynamic processes. The upper ionosphere, known as the F region, is characterized by the movement of charged particles within plasma through ambipolar diffusion, thermospheric winds, and interactions between the ionosphere and the magnetosphere. The actual altitudes of the ionospheric layers vary based on factors such as solar zenith angle, time of day, season, solar cycles, and solar activity (Zolesi & Cander, 2014).

From the radio communications and navigation systems perspective, the F region is the most crucial region of the terrestrial ionosphere. Its height ranges from 140 to 600 km, sometimes reaching as high as the uppermost boundaries of the ionosphere. Solar radiation causes the F region to split into two distinct layers, known as F1 and F2, as a result of the intricate physical processes involved in its development.

The principal positive charge carriers in the ionized component of the F1 layer are mostly O+ (see Figure 2.5). EUV solar radiation with wavelengths between

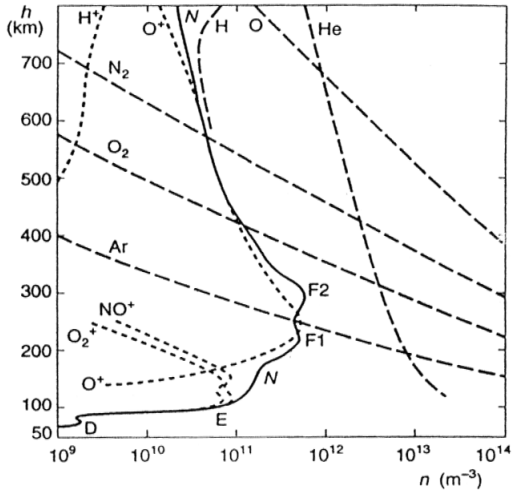

FIGURE 2.5: Principal neutral and ionic components of the ionosphere (N stands for free electrons) around local noon in summertime during a period of medium solar activity at mid-latitude (Dominici et al., 1998)

λ = 58.4 and 30.4 nm is the primary cause of ionization here. The F2 layer is the most important layer of the ionosphere as it is present 24 hours in all solar-terrestrial conditions. O+ ions, with secondary H+ and He+, are the predominant charge carriers in the F2 layer (see Figure 2.5). The photo-ionisation process by EUV light in the wavelength range of 5 to 102.7 nm is the primary source of electron-ions in the F region (Zolesi & Cander, 2014).

The ionospheric regions described above are all very fluctuating, and the difference between day and night can be significant. At night, the E zone becomes significantly weaker, and the D and F1 regions disappear. On the other hand, the F2 region usually remains, although with less intensity.

In the ionosphere, there is a dynamic equilibrium. After the ionization of atmospheric gases, the electrons and ions have a tendency to recombine and react with other gaseous species to create more ions. The relative speeds of the production and loss processes determine the net concentration of free electrons (or electron density). Predominantly, the continuity equation can be used to express the rate of change of electron density (Eq. 2.1) (Hunsucker & Hargreaves., 2003):

$$\frac{dN}{dt} = q - L - \nabla \cdot (N\mathbf{v}) \tag{2.1}$$

where $-\nabla \cdot (N\mathbf{v})$ reflects the loss of electrons by movement (i.e. transport processes), $\mathbf{v}$ being their mean drift velocity, and q is the plasma production rate (per unit volume), L is the rate of loss via recombination, which can be expressed as $L = \alpha N^2$ where α is the recombination coefficient.

In the F region, the dynamics of plasma density, can be described by the continuity equation, where the rate of change of electron density results from the relation between plasma production, recombination losses, and transport processes. During daytime due to strong solar illumination, q is large. Around local noon, the plasma density builds up until production and losses nearly balance ($q \approx L$), so that the rate of change $\frac{dN}{dt}$ is being small at noon. On large seasonal and spatial

scales, the transport processes $-\nabla \cdot (N\mathbf{v})$ can often be neglected, and the system approaches photo-chemical equilibrium. On smaller time scales, transport-induced density variations need to be considered — for example, neutral winds or $\mathbf{E} \times \mathbf{B}$ drifts.

At night, solar photoionization vanishes ($q \approx 0$). The plasma density then decays due to recombination ($\frac{dN}{dt} \approx -L$) or through transport ($\frac{dN}{dt} \approx -\nabla \cdot (N\mathbf{v})$), depending on the further conditions. At night, the dominance of loss and transport processes is essential for the formation of large-scale depletions such as the mid-latitude trough.

The geomagnetic field has a significant impact on charged particles in the upper ionosphere, which are guided along the field lines. The ionization level rises at low latitudes because sunlight strikes the Earth's surface roughly orthogonally. Near the geomagnetic equator, the so-called ionospheric fountain—or equatorial anomaly—is created when the electric field in the E region, which is directed from east to west, causes an electromagnetic drift ($\mathbf{E} \times \mathbf{B}$) that raises the equatorial hmF2 (Davies, 1990).

At high latitude, plasma is transported away from Earth at high latitudes by vertical diffusion and the anti-solar convection plasma flow. Contrary to the equatorial region, the ionisation is low due to the large solar zenith angle. Even though the polar cap remains continuously illuminated for half of the year and is not affected by the typical 24-hour day-night cycle, diurnal variations are still observable. This results from the convection of plasma through electromagnetic transport and neutral winds.

In the mid-latitudes, horizontal neutral winds are mainly the means of transport. An equatorward wind elevates the plasma, while a poleward wind reduces it because neutral winds cannot transport ions across the geomagnetic field lines (Davies, 1990).

Plasma density drops at night due to the absence of solar ionization, which is most pronounced in the equatorial region. In this way, ionisation undergoes significant changes, leading the ionosphere to exhibit pronounced diurnal and seasonal variations, as well as variations driven by the solar cycle and short-term solar disturbances.

2.3 Periodic changes in the ionosphere with time

The Sun experiences an 11-year solar cycle marked by fluctuations in sunspot numbers. These sunspots signify solar activity, including flares and intense energy releases that can heat localized regions of the Sun's atmosphere to millions of degrees Kelvin. Thus, the solar cycle reflects the Sun's activity and variability. Figure 2.6 depicts the number of sunspots on the Sun. Sunspots are areas with strong magnetic fields. When the number of sunspots changes, the Sun's magnetic field also changes. The Sun's magnetic field undergoes a 22-year cycle, shifting in structure and orientation, with its polarity reversing during this period. The frequency of solar disturbances that affect Earth also follows a cycle, with solar minimum often presenting quiet space weather and solar maximum demonstrating a high possibility of severe space weather (Moldwin, 2008).

Another aspect is the rotation of the Sun which has a period of approximately 27 day period, which also cause some periodic variations in the ionosphere. Research by Coley and Heelis (2012) has indicated that there are changes of 27 days periodicity in the temperature and plasma density in the ionosphere at an altitude of 400-500 km. There is also a seasonal variation of the F2 layer (its peak NmF2) of the

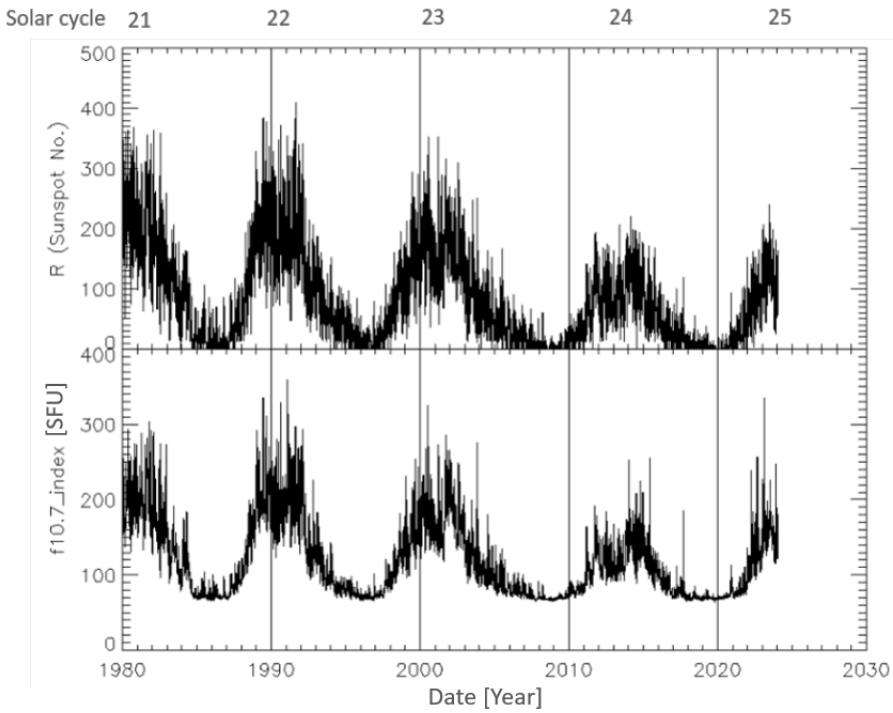

FIGURE 2.6: Variations in the solar cycle represented by the F10.7 index and sunspot number, using data from ("OMNIWeb Data Explorer", n.d.)

ionosphere. These seasonal fluctuations, which have been called "anomalies," significantly deviate from the "normal" seasonal pattern that the Chapman theory predicts if the solar zenith angle is the primary factor controlling the ionosphere. These anomalies include the semiannual anomaly, which shows that NmF2 is highest at equinox, the winter anomaly, which shows that NmF2 is bigger in winter than in summer, and the annual anomaly, which shows that the worldwide NmF2 is greater in December than in June (Rishbeth & Müller-Wodarg, 2006; Yu et al., 2004).

2.4 Total Electron Content

The state of the ionosphere or potential ionospheric space weather effects can be monitored using electron density (Ne) or TEC (Total electron content). The quantity of free electrons per unit volume is known as electron density. The entire number of electrons along a channel between a radio transmitter and receiver is known as the total electron content. TEC is measured in TEC units, namely TECU, where 1 TECU equals 10^{16} free electrons/m^2 which is equal to 16, 24 cm delay at the GPS L1 frequency. TEC can be defined by integrating along the path ds through the ionosphere with the location-dependent electron density $n_e(s)$ using the following equation:

$$\mathrm{TEC} = \int n_e(s)\, ds\,. \tag{2.2}$$

The integrated electron density along the line-of-sight signal path connecting a satellite to a receiver determines the overall impact on radio waves. Therefore, TEC

is a crucial factor that characterizes the main influence of the ionized atmosphere on radio wave propagation.

The electron density can be integrated perpendicular to the ground standing route, resulting in the vertical TEC (VTEC), whereas any straight path can be used to integrate to obtain the slant TEC (STEC). STEC is highly dependent on the geometry, especially the elevation angle. Comparisons between different satellite-receiver pairs are complicated by the longer path through the ionosphere at lower elevation angles, resulting in a larger STEC. Thus, it is used VTEC measurements. VTEC is typically estimated from STEC using a "mapping function". The most popular method relies on the mapping function only on the elevation angle by assuming the ionosphere as a thin shell at a set height. Figure 2.7 demonstrates the concept of converting STEC to VTEC. At the same time, the height of the pierce point might range between 450 km for multiple IGS global ionosphere maps (GIMs) and 400 km for the global maps from the Ionosphere Monitoring and Prediction Center (IMPC) at DLR. Different analysis centers release various GIM solutions, such as final or quick solutions, with varying temporal resolutions, such as hourly, bi-hourly, or 15-minute intervals. Figure 2.8 illustrates the TEC's geographic distribution, which was taken from IMPC (German Aerospace Center (DLR), 2024).

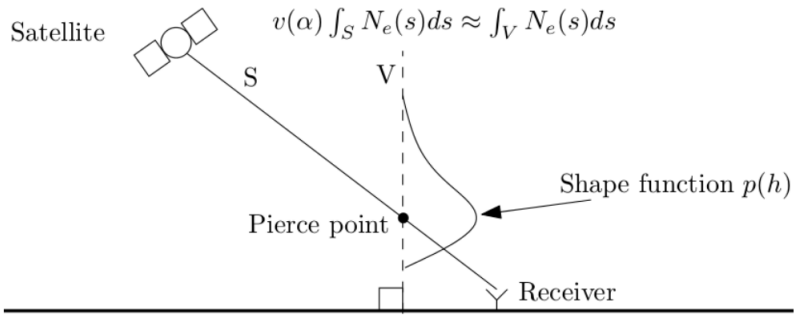

FIGURE 2.7: Illustration of STEC (S line) vs VTEC (V dashed line) (Vierinen et al., 2016)

2.5 Geomagnetic storms

Geomagnetic storms can occur when there is a significant, rapid change in solar wind dynamic pressure, which happens when a coronal mass ejection or material from a solar flare hits the magnetopause. If there is a significant southward component of the IMF and increased solar wind pressure, the storms can be more severe (Schunk & Nagy, 2004). When the southward Interplanetary Magnetic Field connects with Earth's northward field, it boosts the energy and momentum flowing into the magnetosphere, speeding up convection. This extra energy strengthens the ring current, leading to a quick drop in the SYM-H index.

Geomagnetic storms typically consist of three phases: sudden storm commencement (SSC), main phase, and recovery. Figure 2.9 shows a time history of SYM-H index and IMF Bz component during the storm that occurred on 26 September 2011 and the corresponding typical phases of the storm. The Earth's geomagnetic response, characterized as a jump in the horizontal field component known as the storm sudden commencement. The SSC caused by the starting compression of the

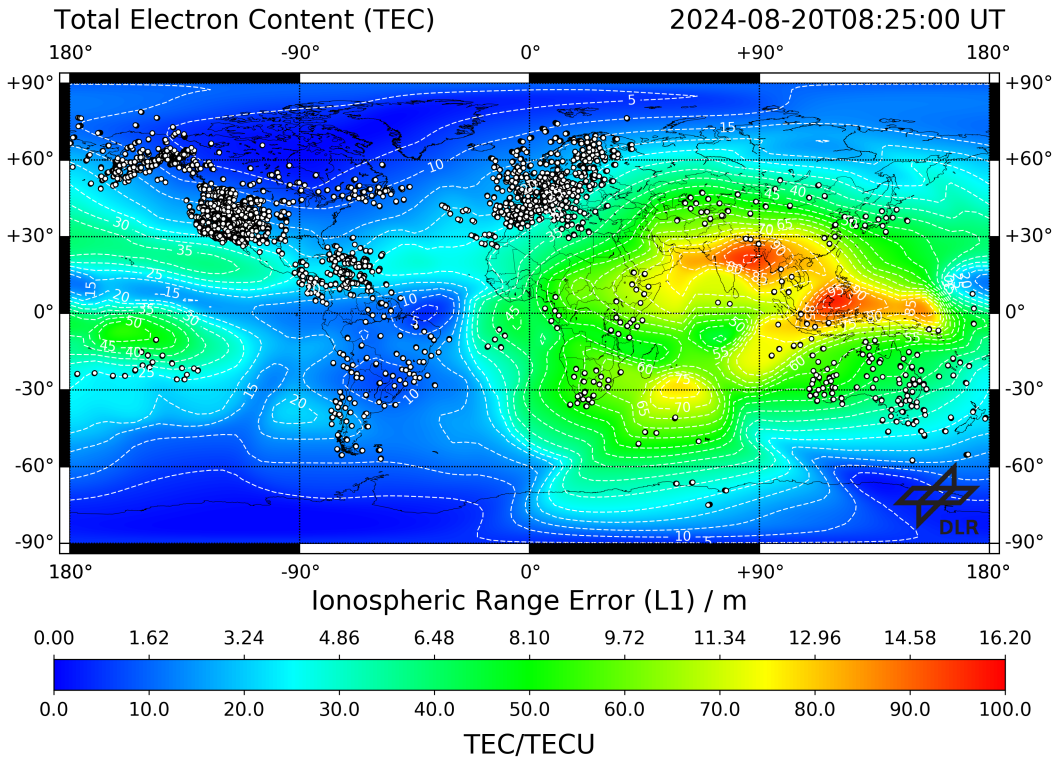

FIGURE 2.8: Illustration of the global TEC distribution obtained from IMPC (German Aerospace Center (DLR), 2024)

magnetosphere when collision with a solar plasma cloud and current intensification near the magnetopause. This initial compression is accompanied by rapid increases in solar wind plasma speed and dynamic flow pressure. The ring current's geomagnetic effect is indicated by a drop in the field's H-component at the equator of tens to hundreds of nT. At other latitudes, there is also an increase in geomagnetic activity. This rapid drop in the SYM-H index is the storm's main phase. This drop usually lasts for hours before the SYM-H index slowly returns to normal over several days, marking the recovery phase. The frequency of storms varies throughout the solar cycle, typically occurring a few times per month, peaking in number and intensity during solar maximum. Also typically during solar maximum occurs more severe storms which lasting one to two days and with a sharp SSC. Each storm is accompanied by a rapid expansion of the auroral oval in both hemispheres, and in many cases, the radiation belts strengthen, and the inner edge of the outer belt moves closer to Earth. In major storms, the slot region may fill completely, and the inner belt intensifies significantly. Another measure of geomagnetic activity, the Kp index, also rises during storms, indicating increased variability in Earth's magnetic field at mid-latitudes. The Kp scale spans from 0 indicating no activity to 9 which represents a major storm, with an average or most likely level of about 3 (Moldwin, 2008).

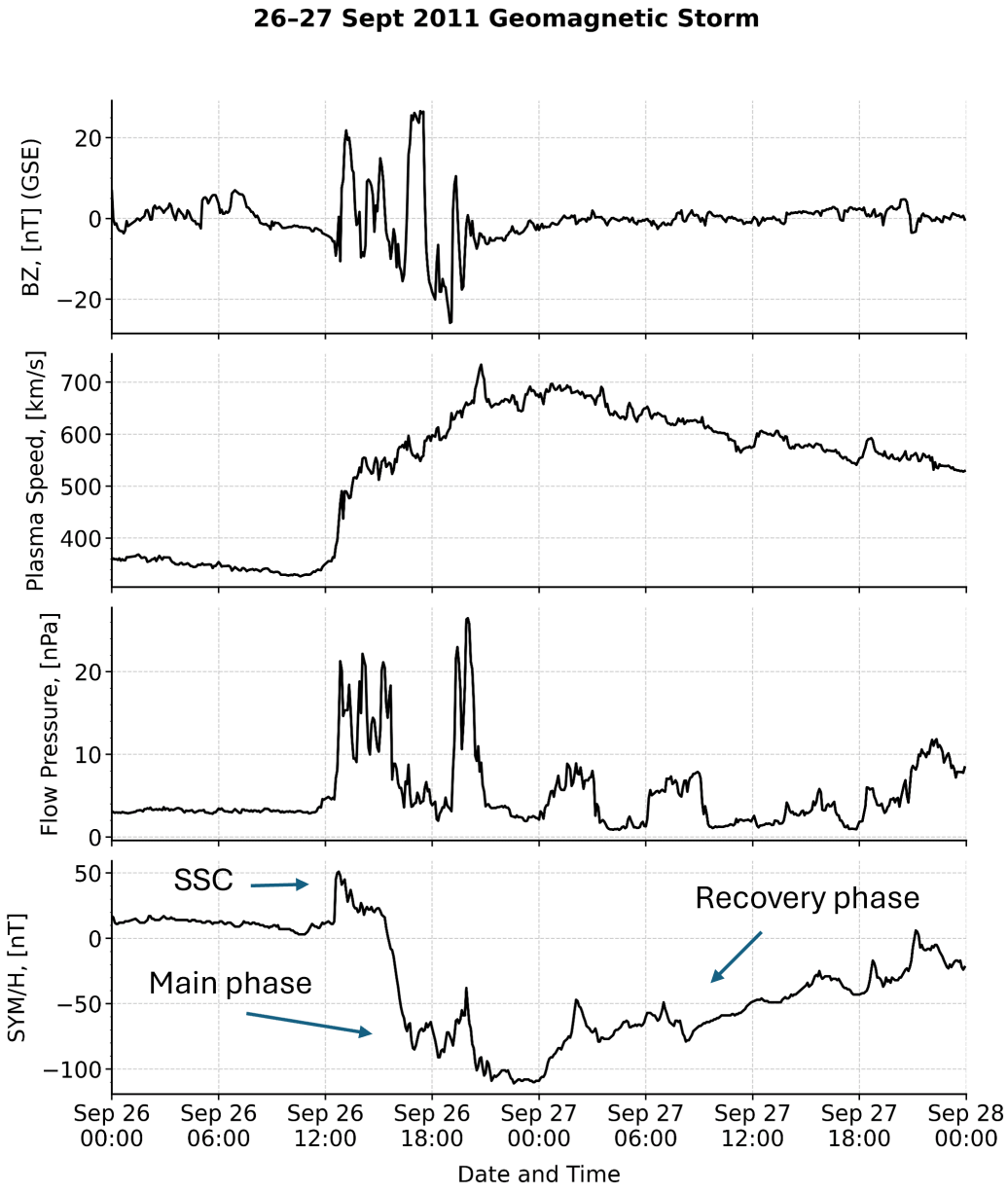

FIGURE 2.9: SYM-H index, IMF Bz component, solar wind plasma speed, and flow pressure during the geomagnetic storm on 26–27 September 2011. Data from the 1-minute resolution OMNI dataset clearly illustrate the storm's distinct phases: initial, main, and recovery ("OMNIWeb Data Explorer", n.d.).

Chapter 3

Global ionospheric models

Global ionospheric models play a crucial role in various GNSS applications by significantly improving positioning accuracy and reliability. Such models are particularly valuable in single-frequency GNSS processing, where direct ionospheric corrections are essential due to the lack of dual-frequency measurements. Moreover, during periods characterized by pronounced ionospheric gradients or scintillation events, these models help mitigate adverse effects on positioning performance. They also expedite the ambiguity resolution process in Precise Point Positioning (PPP) and enhance positioning results in medium- and long-baseline network solutions.

Numerous research groups and institutes across the globe are working on ionospheric modeling, and various models have been developed to improve understanding of the ionosphere's complex behavior. Ionospheric models are used to calculate a range of plasma parameters and can be applied to forecasting, ionospheric specification, or gaining a deeper comprehension of the different physical processes. The three primary categories of ionospheric models are data assimilation, physics-based, and empirical. In the physics-based models, the behavior of the ionosphere is determined by fundamental physical laws. Meanwhile, the uncertainties in the physical understanding are overcome by the empirical models. They rely entirely or partially on observational data to determine the variation in the ionosphere's electron density. Since they are empirical, they are just as accurate and representative as the data used to design the model. The empirical models are built by binning the data according to time of day, month, season, altitude, latitude, longitude, and solar and geomagnetic activity. The data are then fitted using a variety of analytical expressions or orthogonal functions. This makes it possible to estimate the parameters of the ionosphere beyond time or space measurements.

In this chapter, we provide an overview of global ionosphere models such as the IRI, NeQuick, and NTCM. Table 3.1 summarizes selected ionosphere models along with their main characteristics.

3.1 International Reference Ionosphere

A well-known empirical ionospheric model that is widely used is the International Reference Ionosphere (IRI) (Bilitza, 2018; Bilitza et al., 1990, 2011, 2014, 2022). This model contains information from incoherent scatter radars (Jicamarca, Arecibo, Millstone Hill, Malvern, St. Santin), the ISIS and Alouette topside sounders, a global network of ionosondes, and in-situ data from rockets and satellites. Every year, during special IRI Workshops, IRI is updated. IRI is a complex model that provides information for the provided coordinate time and date on the :

1. electron density, in the height range of 65 - 30,000 km,

TABLE 3.1: Overview of selected ionosphere models and their characteristics.

Model	Category	Characteristics
IRI	Empirical	Represent average conditions: ionosphere "climate"
NeQuick	Empirical	Represent average conditions: ionosphere "climate"
NTCM	Empirical	Climatological TEC model derived from GNSS observations
NeQuick-G	Broadcasted Empirical	Simple, corrects ∼70% of ionosphere error in Galileo
NTCM-G	Broadcasted Empirical	Simple, GNSS-adapted climatological TEC, Galileo-specific

2. the ion composition (O+, H+, He+, N+, NO+, O2+, Cluster ions),
3. temperatures of the electrons and ions in the altitude range of 60 - 2,000 km,
4. the vertical total electron content (vTEC) from the lower border to an upper boundary that the user specifies,
5. occurrence probability of an F1 layer, of spread-F, and of sporadic-E,
6. auroral boundaries,
7. effects of ionospheric storms on F and E peak densities,
8. ratio of plasma frequency to electron gyro frequency ("IRI, International Reference Ionosphere", n.d.).

The main driving parameters for the model are

1. solar indices (F10.7 daily, 81-day, and 12-month running mean; sunspot number 12-month running mean),
2. ionospheric index (ionosonde-based IG index 12-month running mean),
3. magnetic index (3-h ap, daily ap) ("IRI, International Reference Ionosphere", n.d.).

In addition, a storm model included in recent versions of IRI enhances modeling outcomes during ionospheric storms as compared to the traditional climatology approach. The planetary geomagnetic Kp index drives the storm model. The IRI model has been modified throughout the years due to the efforts of the international scientific community and is updated on a regular basis. The IRI model can be accessed from the following official source: https://irimodel.org/.

3.2 NeQuick

Another global empirical model for the ionosphere is the NeQuick model (Nava, Coisson, & Radicella, 2008). NeQuick is a fast-run ionospheric electron density model specifically developed for trans-ionospheric propagation applications. This

model was developed at the Aeronomy and Radiopropagation Laboratory (now T/ICT4D Laboratory) of the Abdus Salam International Centre for Theoretical Physics (ICTP) - Trieste, Italy, with the collaboration of the Institute for Geophysics, Astrophysics and Meteorology of the University of Graz, Austria (Nava, Coïsson, & Radicella, 2008). NeQuick is a monthly median 3D ionospheric model that provides an analytic function describing the ionospheric electron density distribution by summing Epstein layers. The electron density profile is constructed using anchor points associated with standard ionospheric properties (for example, foF2, M(3000)F2, foF1, and foE). The electron density profile and its first derivative are always continuous due to its design.

This model provides the ionospheric electron density as a function of time and space. Position, time, and solar flux are the three main inputs of the NeQuick model, and the output is the electron concentration at the specified location in space and time. The latest version of NeQuick is NeQuick 2. The NeQuick package has methods to determine electron density along any direct ground-to-satellite ray path and to calculate the appropriate Total Electron Content (TEC) using numerical integration. One important variant of the NeQuick model is the NeQuick-G model. The European GALILEO satellite navigation system uses the NeQuick-G model for ionospheric corrections in the single frequency operation. The effective ionization level (Az), which is derived using Galileo broadcast coefficients, is the only input parameter that drives NeQuick G. NeQuick G, however, requires a lot of processing power and time to run computationally (Hoque et al., 2019).

The different versions of the NeQuick model can be accessed from the following official sources:

1. NeQuick: https://www.itu.int/rec/R-REC-P.531-14-201908-I/en,
2. NeQuick-G: https://www.gsc-europa.eu/support-to-developers/ionospheric-correction-algorithms/galileo-nequick-g-source-code,
3. NeQuick 2: https://t-ict4d.ictp.it/nequick2/source-code.

3.3 NTCM

An empirical model which provides a useful and efficient way to determine global TEC is the Neustrelitz Total Electron Content Model (NTCM). The NTCM model uses 12 model coefficients, few empirically fixed parameters, and the solar radio flux F10.7 index. The data and coefficients are connected via a nonlinear system of equations provided by

$$\mathrm{VTEC}_{\mathrm{NTCM\text{-}GL}} = F_{\mathrm{LT}}\, F_{\mathrm{seas}}\, F_{\mathrm{mag}}\, F_{\mathrm{crest}}\, F_{\mathrm{sol}}\,. \tag{3.1}$$

Using an iterative nonlinear least-squares method, the 12 coefficients have been identified. The individual terms represent distinct approaches for modeling variations in TEC associated with local time (F_{LT}), seasonal (F_{seas}), and geomagnetic field (F_{mag}) influences. The terms F_{crest} and F_{sol} represent longitudinal variations associated with low-latitude ionospheric crest features and variations due to solar activity, correspondingly. The diurnal, semi-diurnal, and ter-diurnal harmonic functions primarily characterize the local time variation. The latitudinal variation is modeled using a dipole-based approach dependent on geomagnetic latitude, along with a specific formulation addressing the ionization crests on either side of the

geomagnetic equator. The solar radio flux at 10.7 cm wavelength is used to measure the degree of solar activity (Jakowski et al., 2011).

For model development were used extensive VTEC database from CODE. The initial NTCM-GL approach's high-quality TEC dataset includes information from over 130 IGS stations spanning more than half a solar cycle from 1998 to 2007.

An empirical model called NTCM-G performs similarly to NeQuick-G, however, with a lower complexity. The European Commission (EC) has recommended to use DLR's NTCM-G as a NeQuick-G substitute for single-frequency Galileo services since May 2022. The NTCM model, which was created at DLR, is accessible in multiple versions (Hoque & Jakowski, 2015; Hoque et al., 2017, 2018, 2019; Jakowski et al., 2011). It can also be driven by GPS or Galileo coefficients. Moreover, the NTCM model can also be driven by the solar flux index F10.7.

The NTCM model can be accessed from the following official source: https://impc.dlr.de/products/modelling.

3.4 Comparison of models

IRI is a complex and globally recognized ionosphere model. It works well for case studies and research. Furthermore, a storm model included in the latest version of IRI strengthens modeling performance during ionospheric storms as compared to the traditional climatology approach. However, the computation time of TEC is not optimal and requires more time due to the computation of other parameters like ion composition and electron temperature, which are not needed for TEC computations. Moreover, IRI is limited by the height at 2000 km restricts the applicability of IRI in GNSS-based TEC monitoring.

IRI and NeQuick can provide a three-dimensional electron density (Ne) distribution, whereas NTCM model can only provide TEC distribution. However, the NTCM model runs quickly and is simple to use in operational systems because of its simple methodology. Despite its simplicity, the NTCM model practically performs the same as NeQuick, which uses a more complex electron density model (Nava, Coisson, & Radicella, 2008). While NTCM performs well under regular conditions, it may struggle under extreme ionospheric conditions.

Table 3.2 is summarising the main strengths and weaknesses of the models.

TABLE 3.2: Comparison of Ionospheric Models

Model	Strengths	Weaknesses
IRI	Global, widely accepted, comprehensive electron density, & TEC, can serve as background for data assimilation	Not data-driven; smooths out small-scale variations; input based on indices like F10.7 or Kp
NTCM	Optimized for TEC, GNSS data-based, computationally efficient	Only provide TEC, no electron density information, very smooth, not suitable under extreme conditions
NeQuick	3D electron density, used in Galileo, considers solar activity, can be assimilated as background	Not data-driven, similar complexity to IRI, does not resolve small-scale variability

3.5 Mid-latitude trough in global ionospheric models

In the studies by Yang et al. (2015) and Yang et al. (2018), the trough was investigated using the International Reference Ionosphere models IRI-2007 and IRI-2012, respectively. The study by Yang et al. (2015) investigated the variations of the trough-minimum position (Tm) delivered by the IRI-2007 model and compared them with the variations of the GPS-TEC Tm with respect to MLT (magnetic local time) and the F10.7 index. The diurnal variation in the IRI-TEC trough was similar to that of the GPS TEC trough. However, the IRI-TEC trough was located at higher latitudes. The GPS-TEC trough minimum position changed little with F10.7 index, whereas the IRI-TEC trough minimum position showed a strong F10.7 index dependence. The IRI-TEC did not show any response to geomagnetic activity. The study by Yang et al. (2015) suggested that the IRI-2007 model needs to be further corrected.

Later in the study Yang et al. (2018) troughs detected from DMSP satellites (Defense Meteorological Satellite Program) were compared with trough detected using the IRI-2012 model in a quiet period. The findings show that the model trough position and longitudinal changes in the model electron density match the observed values in the Northern and Southern Hemispheres only in December, whereas the results for the September equinox and summer deviate significantly or the trough structure can not be identified at all. Based on these studies, we can conclude that the IRI model does not accurately represent the mid-latitude trough, and the IRI would benefit by including the MIT model in it. Currently, there is no dedicated MIT model inside IRI or NeQuick. Both models use a set of spherical harmonic maps to represent the global foF2 or NmF2 distribution. These maps may inherit some MIT-like signatures by chance, but the MIT is not explicitly modeled.

In the literature, there was no study found about the investigation of the trough in the NTCM or NeQuick model. However, we can make assumptions based on the models' constellations that neither the NTCM nor the NeQuick model can represent trough features well. As discussed before, troughs appear more frequently during increasing geomagnetic activity. The NTCM model performs well in quiet geomagnetic activity; however, during storm periods, it may encounter some issues, which can significantly impact trough representation. In quiet conditions, NTCM may exhibit a general decrease in TEC around the expected MIT latitudes during the local night, but only if the location, depth, and width are correct. It is important to note that NTCM is not based on a physical ionospheric model but is constructed from only 12 model coefficients. Therefore, MIT cannot be represented in NTCM at all.

Similar to NTCM limitations, the NeQuick model also has limitations. Both models, IRI and NeQuick use a number of spherical harmonics maps for global foF2/NmF2 distribution. The maps may inherit some signature of MIT by chance. That is why it is crucial to develop a trough model and integrate it into models like IRI, NTCM, or NeQuick.

Chapter 4

Mid-latitude ionospheric trough

The mid-latitude is the area of the ionosphere that spans the Northern and Southern Hemispheres between 25° and 65° latitudes. The ionosphere in the mid-latitude area is generally benign in comparison to the equatorial or polar ionosphere. The movement of ionospheric plasma is controlled by winds in the neutral atmosphere and the Earth's magnetic field in the mid-latitude region (Acharya, 2017). One of the important features observed in the mid-latitude ionosphere is the mid-latitude ionospheric trough. The mid-latitude ionospheric trough, also called the "Main ionospheric Trough", is determined as the depletion of plasma in the nighttime F region. Since 1965 (Muldrew, 1965), this phenomenon has been investigated through a variety of methods. During this period, a lot of research has been done about the mid-latitude ionospheric trough, its morphology, and its dynamics. Nonetheless, the results diverge in some cases, and till now, MIT has not yet been included in global empirical models for correcting ionospheric propagation effects on GNSS signals. This chapter will present the literature review and the main properties and behavior of the mid-latitude trough so far.

4.1 The Mid-Latitude Trough: Historical Context

The ionospheric mid-latitude trough is a phenomenon that occurs when the electron density of the F-layer of the ionosphere is significantly depleted in the sub-auroral zone. The main ionospheric trough is a large-scale spatial depletion, which is located on the border between the high- and mid-latitude ionosphere. In 1927, the existence of the ionosphere was proven, and it began being the topic of research for many scientists and research centers. Decades later, on September 28, 1962, the first artificial satellite dedicated to studying the ionosphere was launched. This allowed Muldrew to be the first who detected the mid-latitude ionospheric trough as a local depletion in electron density when the satellite crossed the border between Canada and the USA by the topside sounder Alouette 1 (Muldrew, 1965).

First, as it was discovered, it was known as the Canadian-border effect. After that, it was researched from the ground using various methods, including ionosondes, incoherent-scatter radar (Zou et al., 2011), and electron content measurement. Since then, numerous studies have been conducted to investigate the formation and distribution of the mid-latitude trough. These studies have revealed important insights into the characteristics of the trough, such as its diurnal and seasonal variations and its dependence on solar and geomagnetic activities. Research has also pointed out that despite progress, various critical issues regarding the mid-latitude trough need further investigation. For instance, the complexities of the trough morphology in a three-dimensional space and the role of interrelated dynamic, energetic, and chemical processes in its formation require continued exploration.

The main obstacle in MIT research is to define uniform and robust criteria for identifying the trough due to its highly dynamic nature.

One of the first programs to identify the troughs was developed by Tulunay and Sayers (1971). Their algorithm attempted to identify troughs from electron density profiles based on limiting the search area to 30° - 70° latitudes, then checking the electron density ratio and the logarithmic electron density gradients on either side of the trough minimum. Later on, the authors in Ishida et al. (2014) used for identification trough plausible background electron density, and the electron density should have decreased by at least 20% compared to the background electron density to be identified as the trough region.

4.2 Main features of the mid-latitude trough

The mid-latitude ionospheric trough is a V-shaped ionosphere structure of the F2 layer electron density. MIT is composed phenomenologically of three elements: the equatorward electron density wall, the trough minimum, and the poleward electron density wall; as is shown in Figure 4.1, it is the function of latitude versus electron density (Mallis & Essex, 1993). The trough equatorward boundary shows a significant change from dusk to dawn, and its poleward wall has a very steep gradient during the night (Liu & Xiong, 2020). Additionally, MIT's equatorward wall aligns with the ionospheric footprint of the plasmapause (Rodger et al., 1992; Zou et al., 2011), and its poleward wall is linked to the equatorward border of the auroral precipitation zone (Rodger, 2008).

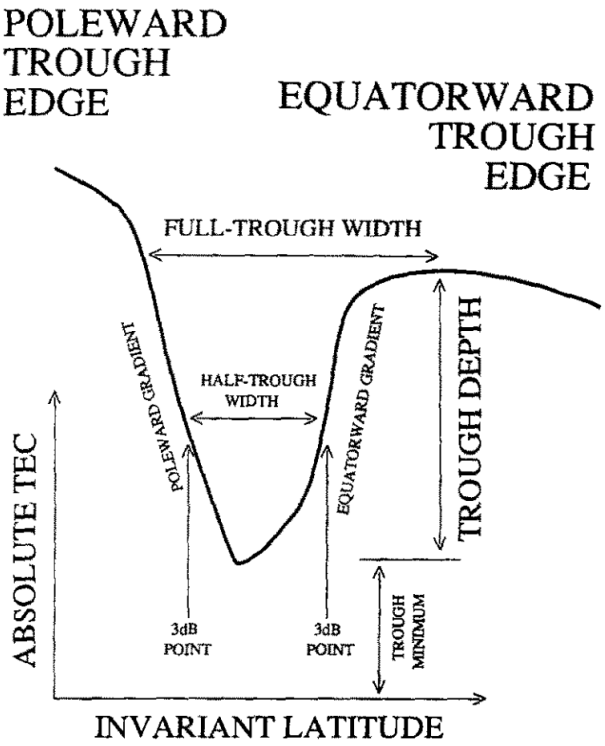

FIGURE 4.1: Schematic Diagram of a model of the mid-latitude ionospheric trough including its basic parameters (Mallis & Essex, 1993)

The minimum point of electron concentration, also known as the trough minimum, is located between the poleward and equatorward slopes. Besides, important factors like the trough minimum position, trough width, and trough depth can be used to define the MIT. Based on the results of a large number of previous studies, there are some agreed-upon morphological characteristics of the mid-latitude trough:

1. Local time variation

   MIT is primarily a nighttime phenomenon, extending consistently from dusk to dawn at geomagnetic latitudes of 50°–70°. The most common magnetic local time to detect the MIT is at night, between 18:00 and 06:00. The MIT has a location at higher latitudes during the afternoon and moves equatorward during later local time (Deminov & Shubin, 2018; Karpachev, 2003, 2019; Krankowski et al., 2009; Mallis & Essex, 1993; Oksman, 1982; Parker et al., 2018; Rodger, 2008; Werner & Prölss, 1997).

2. Seasonal and hemispheric variation

   In comparison to the Southern Hemisphere, the Northern Hemisphere has a more pronounced seasonal dependence on MIT. MIT occurs less in the summer (May–August) months and is mainly observed in the equinox and winter months (Nov–Feb) (Aa et al., 2020; Lee et al., 2011; Voiculescu et al., 2006). Troughs are narrow in summertime, while winter sees the widest troughs. Although the summertime trough is only 0.5°–3° wide, it frequently reaches a width of 10° or more in the winter (Voiculescu et al., 2006). In the Southern Hemisphere, the trough is deeper in the local winter months than it is in the summer, whereas in the Northern Hemisphere, the trough width behaves differently (Matyjasiak et al., 2016). During the local winter, the trough minimum appears at higher latitudes, while in the local summer it moves more to lower latitudes (Aa et al., 2020).

3. Longitudinal variation

   MIT location was observed to change depending on the longitude. The trough location typically occurs at a greater latitude in the longitudinal sector containing the magnetic pole during the winter and equinoxes. For the Northern Hemisphere, this is the western longitudinal sector, while for the Southern Hemisphere, it is the eastern longitudinal sector (Aa et al., 2020; Yang et al., 2018).

4. Geomagnetic activity dependence

   The trough typically deepens and moves toward lower latitudes as geomagnetic activity increases (Karpachev, 2003; Le et al., 2017; Prölss, 2007; Werner & Prölss, 1997; Yang et al., 2016).

5. Solar activity dependence

   The trough location moves slightly (1° - 2°) poleward when solar activity is low and equatorward when solar activity is high (Aa et al., 2020; Le et al., 2017). The dependence on the solar cycle is particularly noticeable in the Northern Hemisphere. In the Northern Hemisphere, the trough minimum is found at a latitude that is around 2-4 degrees higher than in the Southern Hemisphere. During times of strong solar activity, the trough often has a deeper and narrower form (Aa et al., 2020; Ishida et al., 2014).

6. Interplanetary magnetic field dependence

   When Bz is negative, more daytime troughs are detected, and more nighttime troughs when By is negative (Voiculescu et al., 2006; Voiculescu & Nygrén, 2007).

Numerous investigations have estimated linear models that relate MIT's latitude to different magnetic activity measurements. Examples include the time-averaged auroral electrojet index (Werner & Prölss, 1997) and the Dst index (Karpachev et al., 1995); however they are less common. The Kp index is one of the parameters that have been used by many researchers (Collis & Häggström, 1988; Deminov & Shubin, 2018; Dudeney et al., 1983; Yang et al., 2015). Here is a current formula (Eq. 4.1) from Aa et al. (2020) of the the trough minimum position:

$$Tm = 65.8^{\circ} - 1.7Kp. \tag{4.1}$$

4.3 Formation and physical phenomenon associated with mid-latitude trough

So far, numerous mechanisms that may be responsible for the trough formation have been investigated and suggested. The stagnation mechanism is the one that is most frequently brought up. The stagnation theory, first proposed by Knudsen, considers the conflicting effects of the Earth's rotation and auroral electric field-induced convection (Knudsen, 1974). The plasma flow is corotational, or antisunward, in the evening side ionosphere close to the equator, while it is sunward in the higher latitudes in the return flow of the dusk convection cell. These two flows have to counterbalance each other out and produce a stagnation zone at some latitude between them. Having recently corotated from the dayside, plasma equatorward of the stagnation zone would have a rather high electron density. In the same way, auroral precipitation would result in higher electron density in plasma poleward of the zone. On the other hand, plasma that ends up in the stagnation zone would stay there for a long time before recombining. Figure 4.2 depicts the scenario schematically. In areas B and C, there is a reversal of flow and a state of stagnation, while region A is primarily influenced by corotation, and region D is characterized by convection (Spiro et al., 1978). This theory was examined, validated through comparisons with measurements, and found to be reasonable in studies conducted by Spiro et al. (1978) and Nilsson et al. (2005). Furthermore, recent research has demonstrated a strong correlation between the stagnation mechanism and the plasmapause position (PP) dynamics, especially during periods of geomagnetic disturbance (Kp > 1.5), when the MIT coincide with the location of the PP on the night side, thus confirming the connection between ionospheric and magnetospheric processes (Heilig et al., 2022). On the other hand, morning and postmidnight troughs cannot be explained by the stagnation mechanism. Only evening and premidnight troughs can.

Another mechanism that can be responsible of the trough formation is increased recombination rate due to enhanced ion temperature. During times of geomagnetic activity, changes in the main trough are influenced by electric fields near the subauroral ionosphere and the presence of SAPS (subauroral polarization stream). SAPS-driven ion velocities are much faster than neutral wind velocities, leading to increased ion temperatures through frictional heating (Zhang et al., 2017).

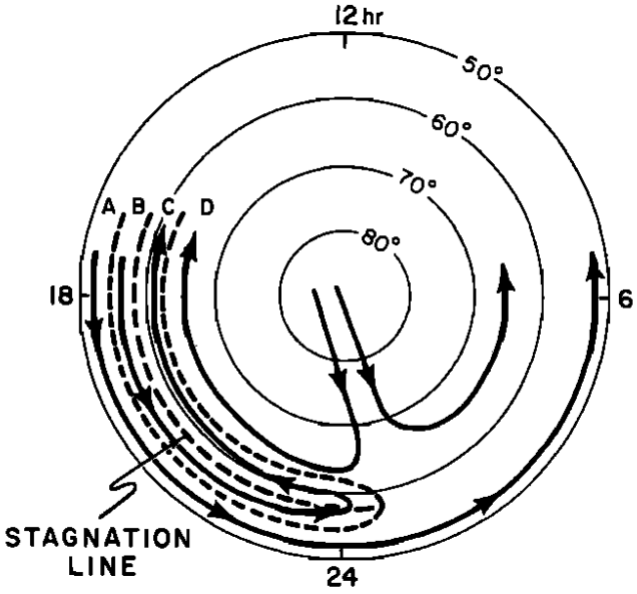

FIGURE 4.2: Diagram of the stagnation mechanism by (Spiro et al., 1978). The magnetospheric electric field dominates plasma flow in region D, whereas the corotation electric field predominates in region A. Due to the combined impacts of the two electric field distributions, the flow reverses from eastward to westward in the intermediate regions (regions B and C). The line that the east-west velocity component approaches 0 is known as the stagnation line.

Consequently, the ion loss process speeds up through the next charge exchange reaction (Schunk et al., 1976), described by (Eq. 4.2):

$$N_2 + O^+ = NO^+ + N \tag{4.2}$$

where the molecular ion that is produced, NO^+, recombines with electrons far more quickly than O^+ (Schunk & Nagy, 2000). This rapid loss of ions results in a deepening of the trough. This plasma loss process can be significantly nonlinear, with higher ion-neutral velocities significantly increasing the rate of ion loss. Additionally, the increased frictional heating causes plasma thermal expansion and field-aligned plasma upflow, further contributing to trough formation (Anderson et al., 1991; Ishida et al., 2014; Voiculescu & Roth, 2008). Global in-situ observations have further validated this process, especially with respect to SAPS, and confirmed its importance as a major mechanism in trough formation under a range of geomagnetic conditions (Heilig et al., 2022).

Another process that could contribute to the formation of the trough is the precipitation and transportation mechanism. Rodger explained that the trough in the ionosphere is like its "normal" state between its northern and southern walls (Rodger et al., 1992). The northern wall is mainly shaped by auroral particle precipitation and sometimes by dense plasma moving across the polar cap from the daytime, known as boundary blobs (Rodger et al., 1986). The southern wall is formed by plasma replenishment from the nighttime plasmasphere (Yizengaw & Moldwin, 2005) and by sunlit plasma due to corotation (Voiculescu et al., 2010). Furthermore, because of their common origin in electric field-driven convection, it has been proposed that the mid-latitude trough can be an effective marker

for tracking plasmaspheric plume trajectories, particularly in the afternoon sector (Heilig et al., 2022). This link provides new ways to study and predict trough behavior based on plasmaspheric dynamics, further highlighting MIT's connection to magnetospheric processes (Heilig et al., 2022).

It should be pointed out that a variety of mechanisms, each with varying significance based on geomagnetic activity conditions, probably contributed to the creation of the trough. Moreover, a trough may be formed in the daylight sector by the convection flow that transports depleted plasma there (Pryse et al., 1998; Rodger et al., 1992; Whalen, 1989). Remarkably, it has been shown that understanding the dynamics of the MIT depends on the continuous observation of the small-scale field-aligned currents (SSB) and their relation to the PP, especially when reconstructing the dayside PP position from the night-side observations (Heilig et al., 2022).

4.4 Key Space weather parameters influence MIT dynamics

Ionospheric space weather refers to the constantly changing state of Earth's upper atmosphere, influenced by disturbances caused by electromagnetic energy and plasma ejected from the Sun. To understand and predict ionospheric space weather, it's crucial to define and quantify its causes. Solar and geomagnetic activity indices are commonly used metrics for this purpose, aiding in research, modeling, real-time monitoring, and forecasting (Cander, 2019).

4.4.1 Hp30 and Kp index

Changes in the solar wind lead to fluctuations in electric currents within the magnetosphere and ionosphere, affecting the magnetic field. Ground-based magnetometers detect these magnetic field variations (Mayaud, 1980). Geomagnetic indices, such as the Kp index, are utilized to measure the intensity of geomagnetic disturbances caused by solar wind variations. The Kp index is used to track subauroral geomagnetic disturbance globally (Matzka et al., 2021a). K indices (Bartels et al., 1939) assessed at 13 subauroral observatories in the Northern and Southern Hemispheres are the source of Kp. At each observatory, a K index represents geomagnetic activity on a scale of 0 to 9 during a certain 3-hourly window of the UT day (00–03, 03–06,..., 21–24 UT). Geomagnetic pulsations, bays or substorms, sudden commencements, geomagnetic storms, and other geomagnetic disturbances resulting from quick variations in the ring-current and other magnetospheric and ionospheric currents are all included in the K-variation (Matzka et al., 2021a). The K index is standardized to ensure uniform distribution across observatories, making it independent of latitude. K indices are converted to standardized Ks indices to adjust for seasonal and UT biases. Kp represents planetary geomagnetic activity, calculated as the average of 13 Ks indices. Definitive Kp index time series since 1932 and nowcast indices are available on the Kp website at German Research Centre for Geosciences (GFZ) (Matzka et al., 2021b). However, Kp has two main limitations. Firstly, its temporal resolution is limited to 3 hours, meaning it may not accurately capture short-term variations in geomagnetic disturbance onset. This can be problematic for geospace models as conditions in the magnetosphere, ionosphere, and thermosphere can change significantly within this timeframe. Secondly, Kp has an upper limit of 9, meaning it cannot quantify geomagnetic activity beyond this threshold. However, extreme geomagnetic storms with Kp = 9 may vary in intensity

(Matzka et al., 2021a). Alternatively, there is another high-resolution geomagnetic index named the Hpo index. The Hp30 index, similar to Kp but with higher time resolution (half an hour for Hp30 and one hour for Hp60), is not capped at 9 like Kp. Instead, it provides a more detailed description of the strongest geomagnetic storms (Yamazaki et al., 2022).

4.4.2 SYM-H and Dst index

Chapman's work in 1919 established a solid foundation for understanding global storms (Chapman, 1918). By analyzing data from ground magnetometers, he showed that following intense geomagnetic disturbances and auroral activity, the Earth's magnetic field experiences a significant reduction in its horizontal component. This research ultimately contributed to the creation of the Disturbance Storm Time Index (Dst), a key statistical measure of space storm activity. Dst index is a quantitative measure of the magnetospheric ring current. The Dst index, developed by Sugiura in 1964, describes the progression and intensity of geomagnetic activity (Sugiura, 1963).

The Dst index is computed hourly using data from the horizontal component of geomagnetic measurements obtained from four observatories situated at middle latitudes. These observatories include Honolulu (HON, 68.45°, 270.735°), San Juan (SJG, 62.31°, 6.87°), Hermanus (HER, 123.99°, 85.14°), and Kakioka (KAK, 62.31°, 209.58°). They are strategically positioned to be sufficiently distant from both auroral and equatorial electrojets and are evenly spread across different longitudes (Sugiura, 1991).

The longitudinally symmetric (SYM) disturbance index was introduced and derived for the H component, representing the horizontal direction (directed positively towards the geomagnetic dipole pole in the Northern Hemisphere), to characterize symmetric disturbance fields in mid-latitudes with high time resolution (i.e., 1 minute) (SYM-H).

The primary distinction between the hourly Dst index and the SYM-H index is the time resolution. The hourly Dst index is not as effective at displaying the effects of rapid variations in solar wind parameters, such as dynamic pressure, the southward component of the interplanetary magnetic field, or the effect of substorm onset, compared to the minutely SYM-H index (Mandea & Korte, 2010). According to Wanliss and Showalter (2006), the SYM-H index is reliable and would benefit to be implemented in upcoming studies.

4.4.3 F10.7 index

Southworth was the first to record solar radio emissions at centimeter wavelengths (Southworth, 1945), although radio experiments to detect the Sun began as early as the late 1800s. The 10.7 cm solar radio flux (F10.7) is a commonly used measure of solar activity. It's used to indicate solar activity levels and as a substitute for more complex measurements of solar emissions or quantities. Every F10.7 value is the total emission, measured over a 1-hour period centered on the specified epoch, at a wavelength of 10.7 cm from all sources on the solar disk. It is actually a flux density, even though it is referred to as a flux. Furthermore, since emissions at this wavelength are very sensitive to conditions in the upper chromosphere and the base of the corona, the 10 cm wavelength range is perfect for tracking solar activity (Tapping, 2013). The 10.7 cm solar flux measurement provides the intensity of solar radio emissions across a 100 MHz bandwidth centered on 2800 MHz (corresponding

to a 10.7 cm wavelength). Solar flux units (sfu) are used to measure it; 1 sfu is equivalent to $10^{-22} Wm^{-2} Hz^{-1}$. Up to three primary emission mechanisms are dynamically combined in this measurement, and they can fluctuate over time and throughout the solar disk. These mechanisms include concentrations of plasma maintained by active region magnetic fields, as well as thermal free-free emissions from the corona and chromosphere. Especially above sunspots where magnetic fields are strong emission intensity can greatly increase. As was shown in Figure 2.6 monthly-average F10.7 the solar activity cycles are very easily traced. There is also notable variations at peak periods that are linked to the rise and fall of active zones. Every cycle of solar activity has a unique peak value, shape, and length (Tapping, 2013).

4.4.4 Convection electric field

Convection electric field (E_{conv}) (mV/m) magnitude describes the interaction between the solar wind and the magnetosphere and can be used as a direct measure of solar wind parameters. This electric field originates from the interaction between the solar wind and the magnetosphere, and it provides the source driving force for large-scale plasma convection throughout the coupled magnetosphere-ionosphere system. In particular, magnetic field lines in the ionosphere connect to the interplanetary magnetic field when it is directed southward, defining an area referred to as the polar cap. Since it does not collide, the solar wind plasma spreads outward from the Sun in all directions. Despite the electric field being minor in the reference frame of the solar wind, it becomes significant in the Earth's magnetospheric context, where it drives convection and other critical space weather phenomena (Kelley, 2009).

In this work was calculated the convection electric field's magnitude (Eq. 4.3) using the solar wind speed vector $\overrightarrow{v_{sw}}$ (km/s) (Eq. 4.4) and the interplanetary magnetic field vector $\overrightarrow{B_{sw}}$ (nT) and get the absolute value using a formula provided by Kelley (2009):

$$E_{conv} = \left|\overrightarrow{E_{conv}}\right| = \left|-\overrightarrow{v_{sw}} \times \overrightarrow{B_{sw}}\right| \tag{4.3}$$

$$\vec{v}_{sw} = \begin{pmatrix} -v_{sw} \cdot \cos(\mathrm{Lat}_{sw}) \cdot \cos(\mathrm{Lon}_{sw}) \\ v_{sw} \cdot \cos(\mathrm{Lat}_{sw}) \cdot \sin(\mathrm{Lon}_{sw}) \\ v_{sw} \cdot \sin(\mathrm{Lat}_{sw}) \end{pmatrix} \tag{4.4}$$

where the bulk flow speed of solar wind is indicated by v_{sw} (km/s). The vector of the interplanetary magnetic field vector is denoted by B_{sw} (nT). The bulk flow latitude is Lat_{sw} (degrees). The bulk flow longitude is Lon_{sw} (degrees). Both Lat_{sw} and Lon_{sw} are measured in geocentric solar ecliptic (GSE) coordinates.

Chapter 5

Database and Method

This chapter introduces the satellite data and ground-based data used in this thesis. It also provides a brief overview of the scientific instruments on board each of the Swarm and GRACE satellites. The global vTEC maps from the IGS are also described. Finally, the technique used to identify mid-latitude troughs is explained.

5.1 Database: Satellite observations (Swarm, GRACE) and IGS maps

In this work, satellite data from the Swarm and GRACE missions and global vTEC maps from IGS were used to investigate the probability and characteristics of MIT. This research is based on an extensive database that has been built up from 1998 to 2023, including the entire solar cycles 23 and 24, using global vTEC maps from the IGS. The GRACE satellite constellation provides data from 2002 to 2015. In addition, data from the Swarm satellites have been analysed from 2013 to 2021. Figure 5.1 shows a timeline of the observational data and the F10.7 solar radio flux, which indicates periods of high and low solar activity. An overview of the evolution of altitudes in the time frame of the GRACE and Swarm satellites is shown in Figure 5.2.

5.1.1 Swarm

On November 22, 2013, three identical Swarm satellites (A, B, and C) from the European Space Agency (ESA) mission were placed into a near-polar low-Earth orbit from the Plesetsk Cosmodrome (Olsen et al., 2013). With an inclination angle of 87.35° and an altitude of around 460 km, A and C constitute the lower pair of satellites, flying side by side (1.4° longitude separation). In comparison, Swarm B flies in a higher orbit of approximately 520 km with an inclination angle of 87.75°.

Every Swarm satellite is equipped with an identical set of scientific instruments:

- Absolute Scalar Magnetometer (ASM),
- Vector Field Magnetometer (VFM),
- Star Tracker (STR),
- Electric Field Instrument (EFI),
- Global Positioning System (GPS),
- Receiver (GPSR),
- Laser Retro-Reflector (LRR),

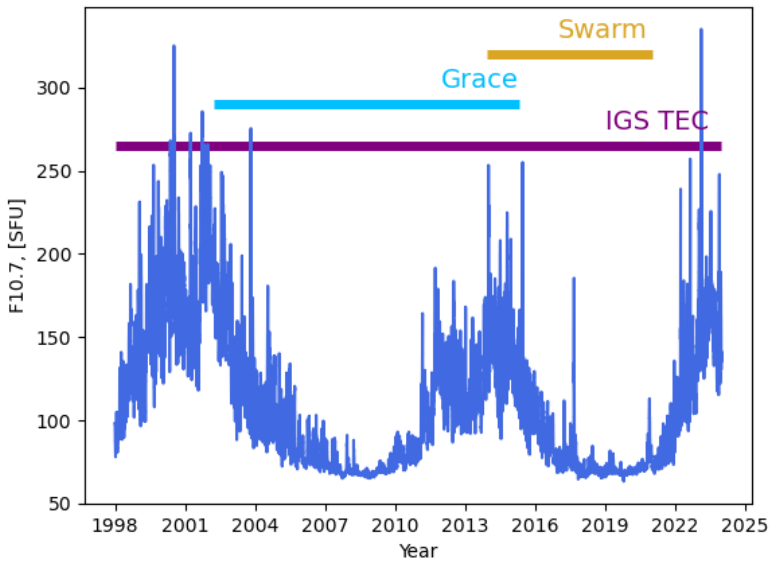

FIGURE 5.1: Timeline of observations from the GRACE and Swarm satellite missions, as well as IGS global vTEC maps and the F10.7 time series from 1998 to 2023

- Accelerometer (ACC).

Figure 5.3 displays schematics of the Swarm satellite's front and side views, showing where specific onboard systems and equipment are located.

The ASM detects the intensity of the magnetic field while the VFM (connected to a star tracker camera) tracks the direction and magnitude of the magnetic field components in space (Fratter et al., 2016). The primary application of GPSR is Precise Orbit Determination (POD); however, interference with these signals can be utilized to deduce whether ionospheric structures are present along the ray path from the transmitter to the receiver (Xiong et al., 2018). On top of the satellite, the GPS antenna is installed. The satellite's internal ACC can determine the thermospheric density. The EFI is situated in the ram direction and is consists of two Langmuir probes (LPs) and thermal ion imagers (TIIs) (see Figure 5.3). TIIs intended to provide data regarding the kinetic temperature and ion bulk drift throughout the satellite's orbit (Knudsen et al., 2017). Ionospheric temperature and electron density are measured by LPs at a frequency of two hertz (Hz).

In this work, only observations from satellites A and C have been combined, as they fly at the same altitude. The Swarm data were downloaded using FTP server (European Space Agency, 2022).

5.1.2 PRISM

PRISM (the Plasmapause Related boundaries in the topside Ionosphere as derived from Swarm Measurements) is a collaborative ESA project between Helmholtz Centre Potsdam - GFZ, Germany and the Mining and Geological Survey of Hungary (Magyar Bányászati és Földtani Szolgálat, MBFSZ), Hungary ("Plasmapause Related boundaries in the topside Ionosphere as derived from Swarm Measurements

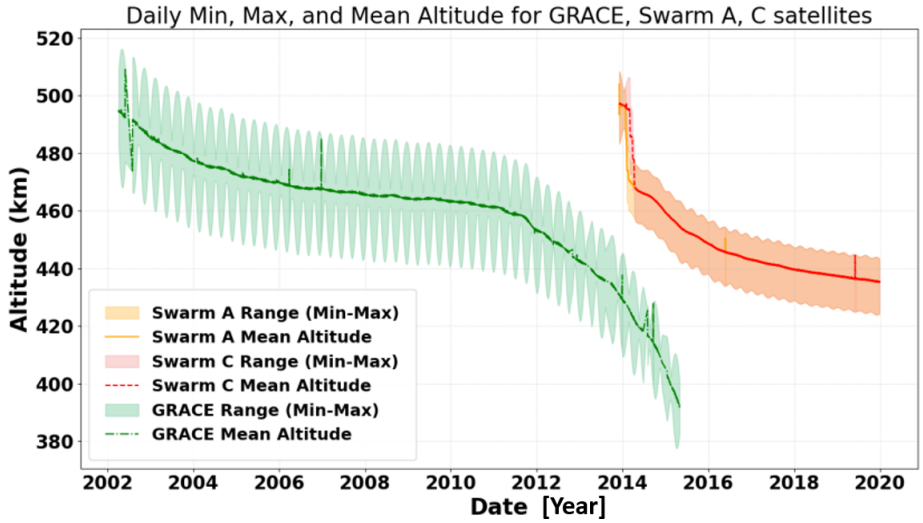

FIGURE 5.2: Evolution of daily minimum, maximum, and mean altitudes for the GRACE and Swarm A and C satellites. Shaded areas represent the range (min-max), and solid lines indicate mean altitudes.

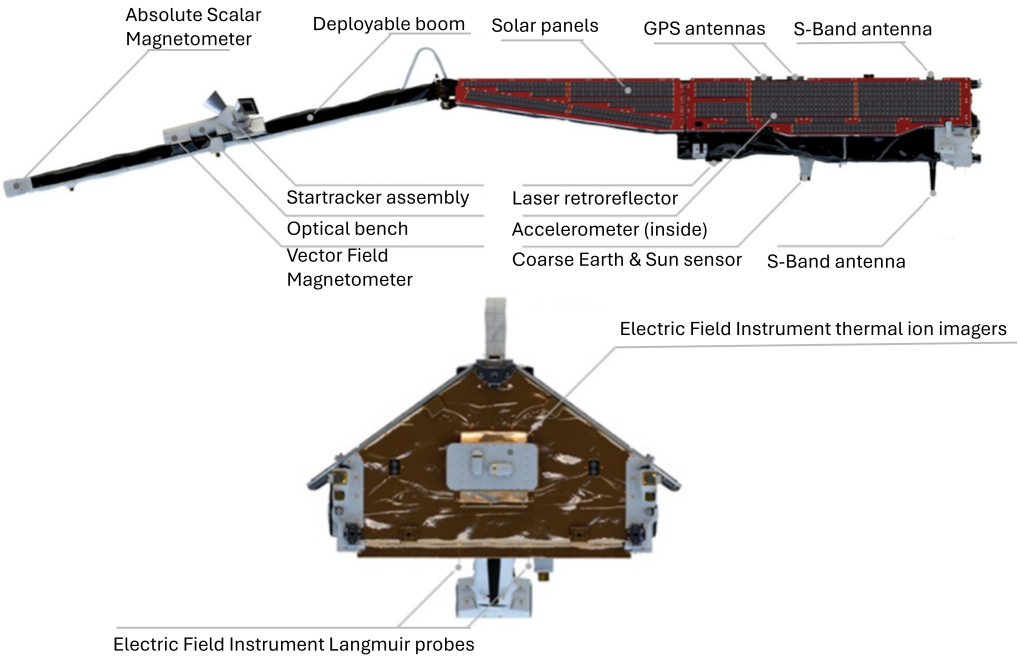

FIGURE 5.3: The Swarm satellite's side (top panel) and front (ram-direction) views, together with the locations of its instruments and several onboard systems ("Swarm operations", n.d.).

- Earth Online", n.d.). PRISM's concept is founded on research findings published in Heilig and Lühr (2013, 2018). Besides the plasmapause, this project also provides the related phenomena such the mid-latitude ionospheric trough. The MIT is determined by electron density and temperature measurements of the Langmuir probe onboard and additionally from GPS TEC estimates. The MIT product contains

all necessary information about MIT observed at ∼ 500 km altitude, such as trough position, its MLT, width, and depth. The algorithm used to identify the MIT product is based on identifying slopes in the log10(Ne) profile within a specific latitude range, indicating the limits of the trough and estimating the trough's position. In order to precisely determine the lowest point of the trough, the edges (or boundaries) are then fine-tuned by looking at the density profiles' second derivatives. Furthermore, by pinpointing a region of elevated electron temperature within the trough range, the Sub Auroral Electron Temperature Enhancement (SETE) is linked to the trough, further defining its bounds. Figure 5.4 depicts one example of the characteristic points of the MIT structure and the associated SETE.

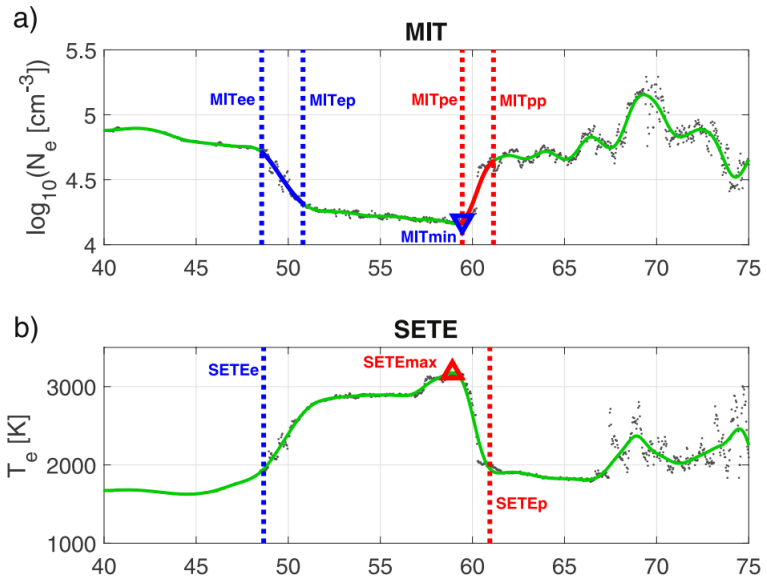

FIGURE 5.4: PRISM example of the MIT structure's characteristic points (a), the related SETE (b). Swarm A observations on January 1, 2015 around 01:20 UT (MLT = 2.5–3.0).The raw and smoothed profiles are shown as gray dots and thick green lines, respectively. The MIT minimum and SETE maximum are shown by a labeled downward/upward triangle, and boundary positions are indicated by labeled vertical lines. (Heilig et al., 2022).

The MIT determined from the PRISM product is used for comparison with the results obtained using the detection function described later in Section 5.2. As mentioned for the Swarm data, this product will only be used for observations from satellites A and C. Also, each trough identified in the PRISM project has a quality flag of the product. The flags are as follows: 3: highest quality, 2: fair quality, 1: uncertain detection, 0: no quality information available, -1: likely false positive detection. In this work, only the highest quality(3) of trough detection was used. The time frame of the PRISM data was chosen in the same way as the detected Swarm data (2013-2019).

5.1.3 GRACE

The GRACE mission - "Gravity Recovery And Climate Experiment" - is a scientific satellite jointly developed by the National Aeronautics and Space Administration

(NASA) and the German Aerospace Agency (Deutsches Zentrum für Luft- und Raumfahrt (DLR)). The worldwide geodetic mission GRACE aimed to collect long-term data for global (high-resolution) models of the mean and time-variable components of the Earth's gravitational field.

The two satellites that constitute the GRACE constellation, GRACE-A, and GRACE-B, were launched into a near-circular polar orbit on March 17, 2002, with an initial altitude of roughly 490 km. In a sequential manner, the two GRACE satellites flew at an orbit inclination angle of 89° and a separation distance of approximately 220 km ±50 km between each other. Near the end of the mission, the orbit altitude decayed to 300 km.

The following scientific instruments are used to accomplish the GRACE mission aims:

- SuperSTAR Accelerometer (ACC),
- Global Positioning System Receiver Assembly (GPS),
- Star Camera Assembly (SCA),
- K-Band Ranging System (KBR),
- Laser Retro Reflector (LRR).

The accurate attitude references for the satellites during science measurements were provided by the two star cameras (SCA). Also, GRACE carried a unique K-Band Ranging System, which was used to precisely measure the relative position change between two satellites using phase tracking of K- and Ka-band signals sent between the two satellites (Case et al., 2002)

GRACE data were downloaded from the GFZ archive (Xiong et al., 2021). GRACE data is stored in ASCII format, and each file contains data for an entire day with a 5-second resolution. Over the course of a day, each GRACE satellite circles the Earth roughly 15 times, with an orbital period of roughly 94.5 minutes.

5.1.4 Global vTEC maps from IGS

GNSS can measure the ionospheric total electron content (TEC), which is a vital parameter for representing ionospheric variations. A worldwide initiative to compute various GIMs using GPS data on a daily basis was initiated by the International GNSS Service (IGS) in June 1998 (Feltens & Schaer, 1998). The centers that provide a computation of GIMs are called Ionosphere Associate Analysis Centers (IAACs). There are five such centers: CODE, ESA, JPL, NRCan, and UPC. These centers provide global ionospheric maps using different ground stations and various generation approaches. The ground GNSS stations in the International GNSS Services (IGS) networks account for over 500 stations (see Figure 5.6).

The IGS product is obtained from solutions provided by analysis centers, encompassing both rapid and final. These ionosphere products are accessible in rapid solutions, delivered within a latency period of less than 24 hours, and final solutions with a latency period of approximately 11 days. Additionally, predicted solutions are available one and two days prior. Ionosphere products are distributed in the IONEX (Ionosphere Exchange) format.

Different modeling approaches and datasets are used by each center, which produces several different levels of GIM accuracy. It has been confirmed that the

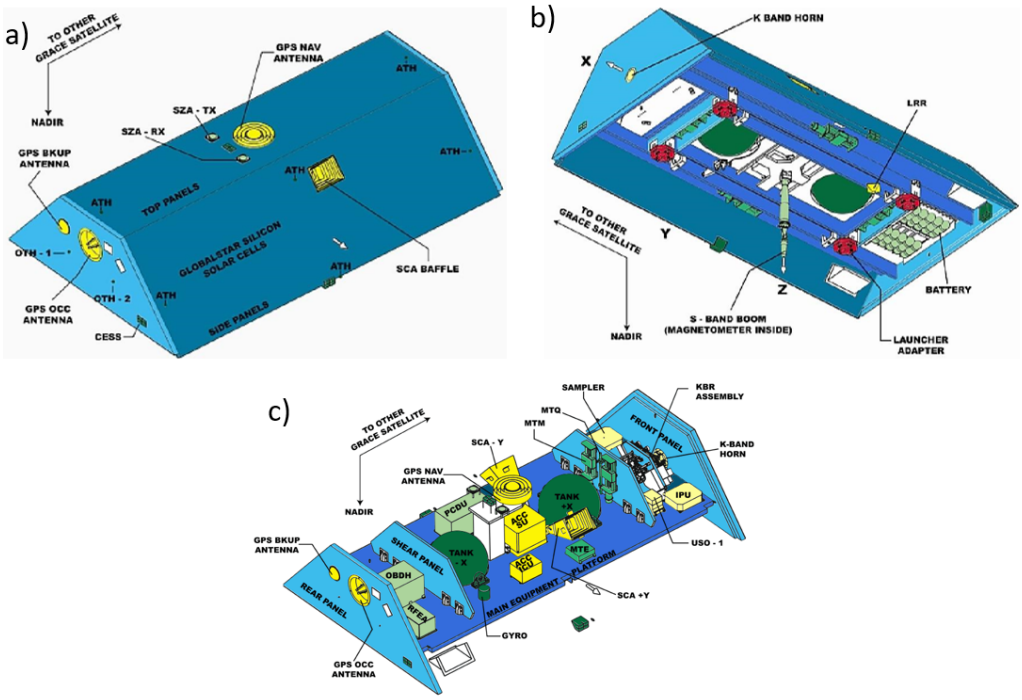

FIGURE 5.5: Schematic of the GRACE satellite constellation and its instrumentation. a) with the top view of the satellite, b) the bottom view, c) the interior view ("GRACE (Gravity Recovery And Climate Experiment) - eoPortal", n.d.).

UQRG GIMs show the best performance (Hernández-Pajares et al., 2017). Specifically, in problematic polar areas with only a few GNSS stations and observations that make VTEC estimation challenging, UQRG can depict realistic VTEC structures (Hernández-Pajares et al., 2020). The UQRG provides the estimated VTEC from slant GNSS observation as a tomographic two-layer voxel-based model in a sun-fixed geomagnetic reference frame. The VTEC of each voxel is computed on a global scale every 15 minutes using the Kriging interpolation technique (Orús et al., 2005). UQRG high-resolution maps provided by the Technical University of Catalonia (UPC) with a 5° longitude and 2.5° latitude spatial resolution.

Relying on the accuracy and characteristics of the UQRG GIMs, they were chosen for this investigation of MIT characteristics. UQRG product in IONEX format containing ionosphere VTEC maps was obtained using the NASA CDDIS FTP server ("CDDIS | | archive | gnss | products |", n.d.).

5.2 Method for detecting mid-latitude trough

In this work was implemented an automatic trough identification algorithm based on the fundamental properties of troughs to detect mid-latitude troughs automatically from the extensive measurement data (Swarm, GRACE, IGS TEC maps). The MIT research focuses on the 40° – 70° magnetic latitude (MLAT) areas, covering all longitudes in both the Northern and Southern Hemispheres, as this region commonly includes MIT occurrences. An approach for identifying MIT occurrences using in situ electron density data from the three Swarm satellites was presented by

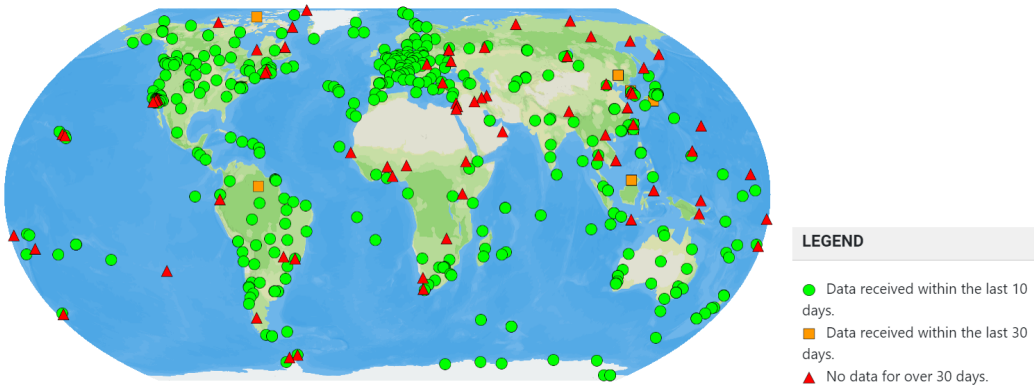

FIGURE 5.6: Global distribution of stations of the IGS network ("IGS Network", n.d.).

Aa et al. (2020). In this work, a similar method was used to create the MIT database and obtain MIT signatures.

The MIT detection method consists of the following steps:

1. Satellite profiles that consist of data from satellites traveling from the geomagnetic equator to the pole or the other way around were handled as a single profile. The satellite profiles have been split to ensure that they consist of data between the 40°-70° magnetic latitude regions in both Hemispheres, as this is an area where the MIT can be observed.

   IGS TEC profiles were constructed similarly using a latitude of 40° - 70° magnetic latitude and the step of 0.37° latitude using one longitude for each profile. The Python-based *getIONEX* software, which includes the `compute_tec_interpol` function, was used to interpolate the IGS TEC maps (Mevius, 2018). This function produces interpolated TEC values for an array of times, latitudes, and longitudes. It uses a complex interpolation method over four latitude and longitude points and two points of time. The function's inputs are latitude, longitude, and time arrays, along with TEC map information. It returns an array of interpolated TEC values.

2. The Ne is averaged across a 48-point sliding window to determine the background electron density. The window size is determined based on a data resolution that corresponds to a distance of around 1800 km on a horizontal plane. It has been proved that this window size is optimal for the investigation. Certain minor anomalies can be seen by a smaller window size, whereas troughs cannot be accurately identified by a bigger window.

3. The trough detection was accomplished within the detrended logarithmic electron density using the formula: $\log_{10}(Ne) - \log_{10}(Ne_{mm})$, where (Ne_{mm}) is the moving average with a window size of 48 points.

   MIT profile was recognized if any profile data values were below the -0.2 (for satellite data) or -0.1 (for IGS TEC data) detrended $log_{10}(Ne)$. The threshold value of -0.2 corresponds to a decrease of about 37% in background electron density and -0.1 level of about 15%. The threshold level was carefully selected to achieve a balance between reliable detection quality and quantity.

4. Once an MIT event has been identified in a profile, the next step is to identify the MIT characteristic points. The location of the minimum density or trough minimum (Tm), the equatorward breakpoint (Be), the poleward breakpoint (Bp), the equatorward halfpoint (He) and the poleward halfpoint (Hp) have all been identified by analysing the Ne profile data. The breakpoints Be and Bp are determined by identifying the intersections between the detrended $log_{10}(Ne)$ values and the profile values. The example of identified points are shown in Figure 5.10 (b,d).

5. The reliability of trough identification was assessed by implementing a trough width filter, with the threshold criterion set within a range determined to be between 1° to 17° (Karpachev, 2003).

Trough width and depth were calculated by using identified characteristic points (see Figure 5.8). The trough width was calculated like $Bp - Be$. Trough depth was calculated like $\frac{(Bp+Be)}{2} - Tm$. The characteristic points, as well as depth and width, are represented in Figure 5.8. The workflow illustrating the trough detection process is presented in Figure 5.7. The workflow represents the main processing steps of trough detection algorithm used in this work: 1) data preparation and profile construction, 2) background electron density or TEC calculation as a running average, 3) application of threshold criteria, 4) identification of trough characteristic points (Tm, Be, Bp, He, Hp), and 5) filtering non-troughs by width criteria.

After applying the trough detection algorithm, approximately 45,000 Ne profiles with trough signatures were detected using GRACE satellite data for both the Northern and Southern Hemispheres. Using Swarm satellite data, 36,000 trough profiles were detected. Using IGS TEC data, the most extensive database has been compiled, containing approximately 20 million trough profiles. The example of trough detection using the GRACE satellite is shown in Figure 5.10. This is example of the trough detection in quiet geomagnetic conditions, where the Kp index was equal to 2 and the Dst index was -9 nT. Figure 5.9 illustrates how troughs were detected using IGS TEC maps in the quiet geomagnetic conditions (Kp index of 2 and Dst index of -5 nT). The IGS TEC map provides a comprehensive view of the ionosphere represented by TEC values between 40° and 70° magnetic latitudes in both the Northern and Southern Hemispheres (see Figure 5.9). In Figure 5.9, the black line on the map represents the solar terminator, which is the boundary between the day (light yellow) and night (light blue) sides of the Earth. The position of the terminator shows very well the diurnal variations of the TEC and the dynamics of the mid-latitude trough. The identified position of the trough is indicated by the red circles on the map. Figures 5.9 and 5.10 visually support the methodology by showing how TEC values vary geographically and over time.

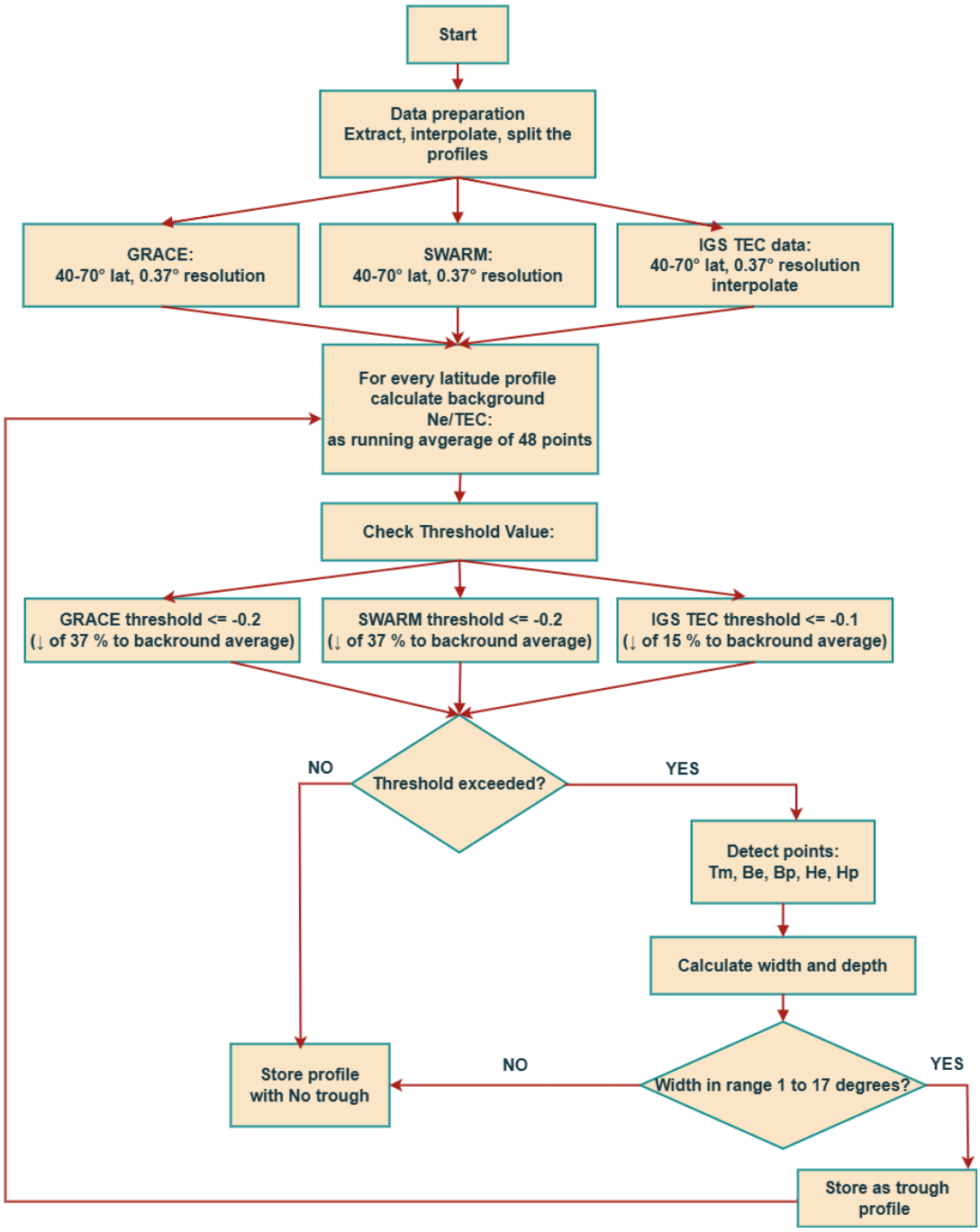

FIGURE 5.7: Illustration of the workflow for the trough detection algorithm.

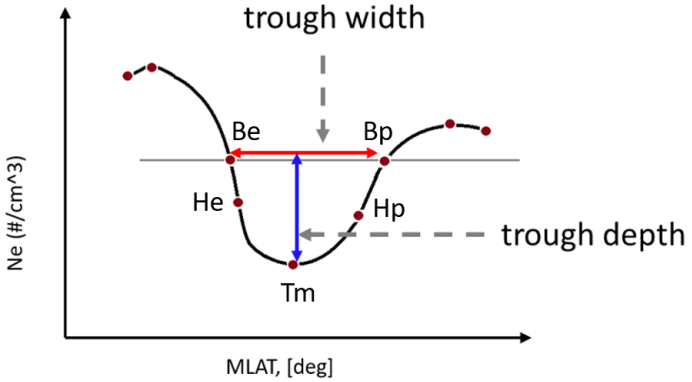

FIGURE 5.8: Diagrammatic representation of the width, depth, and characteristic features of the mid-latitude trough (Lubyk et al., 2022)

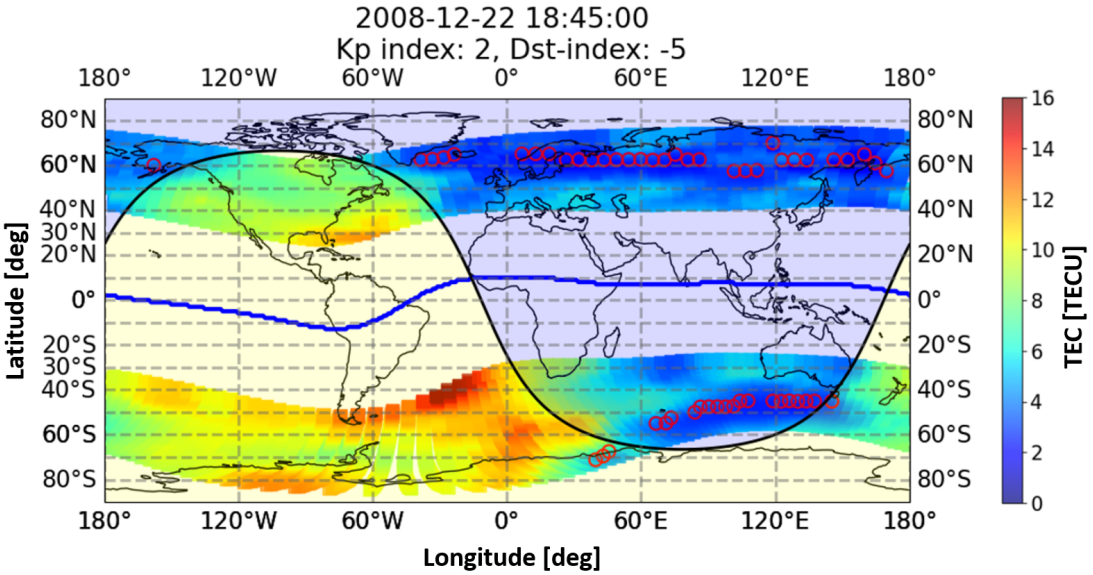

FIGURE 5.9: Example of the IGS TEC map on 22.12.2008 with the quiet geomagnetic activity. TEC values are shown between 40° and 70° magnetic latitudes in both the Northern and Southern Hemispheres. The black line represents the solar terminator, where the night side is colored with light blue and the day side is shaded with light yellow. The red circles represent the trough position.

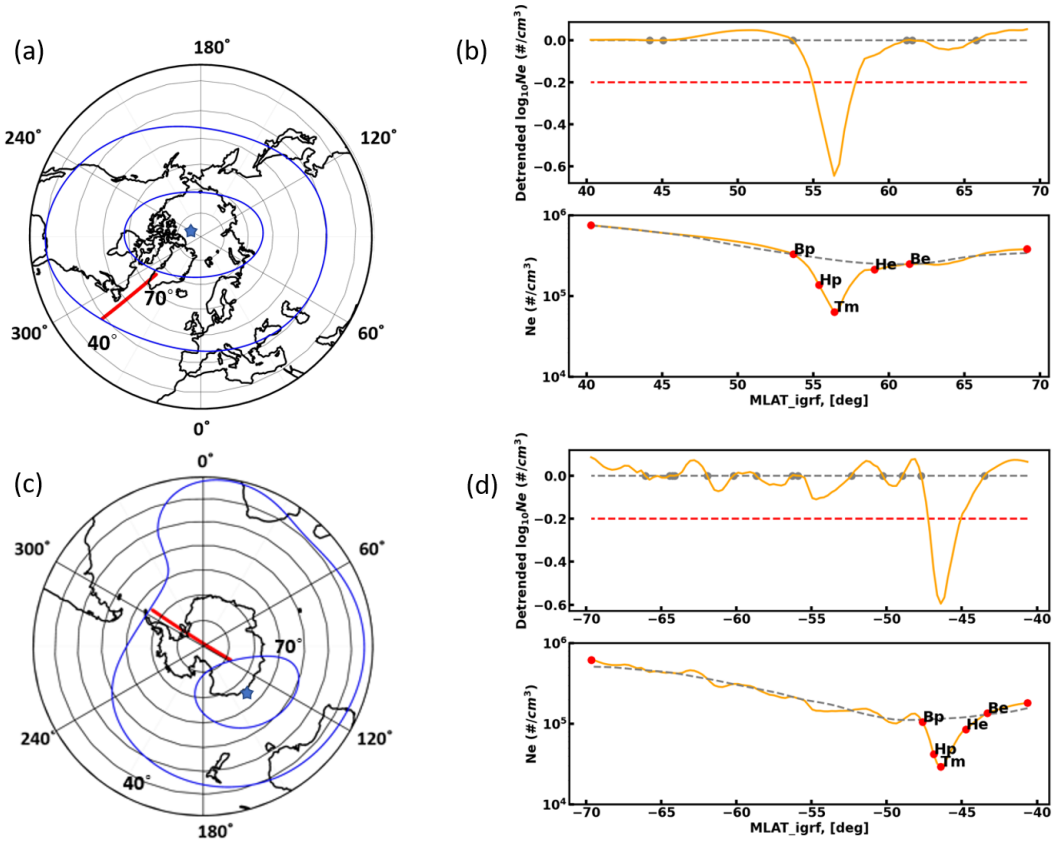

FIGURE 5.10: Example illustrations of the April 14, 2002 GRACE trajectory between 40° and 70° magnetic latitudes across the Northern (a) and Southern (c) Hemispheres. Plotting of concentric circles occurs at intervals of 10°. The magnetic latitudes of 40° and 70° are represented by the blue lines. The satellite path's footprint is shown by the red line. There is a star to indicate the magnetic pole. Ne profiles that correspond to the identified trough minimum location and trough characteristic points for the Hemispheres of the North (b) and South (d) are plotted below. The upper plots for the Northern (b) and Southern (d) Hemispheres show detrended logs of Ne. The Ne running average is shown as the gray dashed line. The threshold for trough identification is indicated by the red dashed line, whereas the yellow line represents the Ne profile. Reprinted from (Lubyk et al., 2022).

5.3 Datasets differences and implications on trough detection

In this work, we have used different datasets such as Swarm, GRACE, and IGS TEC maps. The accuracy of trough detected from these datasets relies on the characteristics of the observational datasets used. Each data source has different measurement techniques, spatial and temporal resolutions, and altitudinal differences, which all affect the trough detection.

The differences of datasets are summarized in Table 5.1. This demonstrates the difficulties and factors to be taken into account when employing multi-source observations for trough detection. Although Swarm and GRACE are in situ electron density measurements, their coverage is limited by orbital characteristics, resulting in gaps in temporal and geographical sampling. This makes them less appropriate for researching global patterns, but especially helpful for identifying distinct and localized trough features. IGS TEC maps, on the other hand, provide constant worldwide coverage, making it possible to examine long-term and large-scale patterns in the MIT. However, the fine-scale latitudinal structure of the trough can be smoothed out because of the vertical integration of TEC. GRACE and Swarm observe electron densities at different heights within the F-region, which affects the trough detection and may complicate the comparison between these datasets. Furthermore, both Swarm and GRACE exhibit quick latitudinal movements of the trough during geomagnetic storms, but TEC maps smoothing may not show so strong trough movements during geomagnetic active periods. Lastly, additional variability is introduced by variations in data processing techniques, such as the calibration uncertainties in GRACE or the interpolation and mapping functions in IGS TEC maps. When comparing observations across datasets, these distinctions need to be considered.

TABLE 5.1: Comparison of Swarm, GRACE, and IGS TEC Data for Trough Detection

Reason	Swarm	GRACE	IGS TEC Maps	Influence on Trough Detection
Measurement Technique	In situ electron density (400–500 km altitude)	In situ electron density (300–500 km altitude)	Ground-based, vertically integrated TEC	TEC maps smooth vertical features; satellites detect trough directly at measurement altitude.
Altitude Dependence	Fixed altitude (400–500 km)	Slightly lower altitude (300–500 km)	Integrated across all altitudes	Altitude differences shift observed trough position vertically and horizontally.
Spatial and Temporal Resolution	High spatial resolution; limited global coverage; orbital gaps	High spatial resolution; limited global coverage; orbital gaps	Global coverage; lower spatial (2.5°–5°) and temporal (15-minutes) resolution	TEC maps lose fine-scale features; satellites detect narrow structures but intermittently.
Data Quality & Processing	Satellite-specific calibration; plasma irregularities	Calibration uncertainties; orbit-related biases	Bias estimation; interpolation; mapping-function errors	Processing differences affect precise trough detection.
Geomagnetic Activity Sensitivity	Sensitive to rapid MIT shifts during storms	Sensitive to rapid MIT shifts during storms	Less sensitive due to smoothing effects	Larger discrepancies during disturbed conditions.
Local Time Coverage	Limited local-time sampling (orbital constraints)	Limited local-time sampling (orbital constraints)	Temporal averaging over local-time variations	Diurnal variation introduces differences unless synchronized.

Chapter 6

Results of the statistical analysis of the MIT

6.1 MIT and its dependencies on space weather parameters

Using data from Swarm, GRACE, and IGS TEC maps, we created a database of MIT characteristics, including MIT minimum, width, depth, and occurrence rate for the Northern (NH) and Southern (SH) Hemispheres. Trough was detected using the method described in Section 5.2. In addition, the product results from ESA's PRISM project are included for independent validation of MIT occurrences. This section presents a statistical analysis of the MIT as a function of space weather parameters such as solar radio flux index F10.7, the flow pressure, the solar wind (SW) plasma speed, the interplanetary magnetic field components Bx, Bz, and By, SYM-H, and Hp30. An analysis of the dependence of the MIT parameters on several geophysical parameters, including geographic and magnetic location, magnetic local time, and seasonal variations, was also performed.

6.1.1 Geographical distribution

The trough minimum position for the Northern and Southern Hemispheres is displayed separately on globe maps in Figure 6.1. Each position of the trough minimum is marked with red color. The distribution of the trough minimum position forms an approximately elliptical shape around the magnetic pole, which is indicated in Figures 6.1 by a magenta star symbol. The results of the trough location distribution in the Northern Hemisphere are consistent across GRACE, Swarm, IGS TEC maps, and Swarm PRISM. However, the Southern Hemisphere's results differ slightly, especially from those obtained from the IGS TEC maps. This result is not surprising since it is well known that IGS TEC maps have much fewer observing stations in the Southern Hemisphere. Therefore, the results for the IGS TEC maps in the Southern Hemisphere may be different and not as accurate. Nevertheless, each dataset varies in its temporal and spatial coverage (see Section 5.3). Comparing all of these data sources increases confidence in the results.

In the earlier studies of Karpachev and Afonin (1999) and Karpachev (2003) found that Northern and Southern Hemispheres exhibit different behaviors for longitudinal variation. More recently, Karpachev (2019) discovered that the longitudinal variation of the nighttime trough position is primarily determined by the longitudinal variation of auroral particle precipitation, neutral atmosphere composition, and electric field. Additionally, the MIT longitudinal difference in NH and SH could be attributed to the geomagnetic declination angle and the thermospheric wind (Zhang et al., 2011, 2012). Early in the evening, the dominant neutral wind

in the mid-latitude F region is eastward. The eastward wind drives the plasma downward in regions where the magnetic declination is westward in the Southern Hemisphere and eastward in the Northern Hemisphere - areas located west of their respective geomagnetic poles. The resulting downward plasma drift lowers the F2 peak altitude and enhances recombination, thereby intensifying plasma depletion within the MIT region (He et al., 2011). These interactions highlight the complex relationship between thermospheric dynamics and the geomagnetic field in shaping the morphology of the trough.

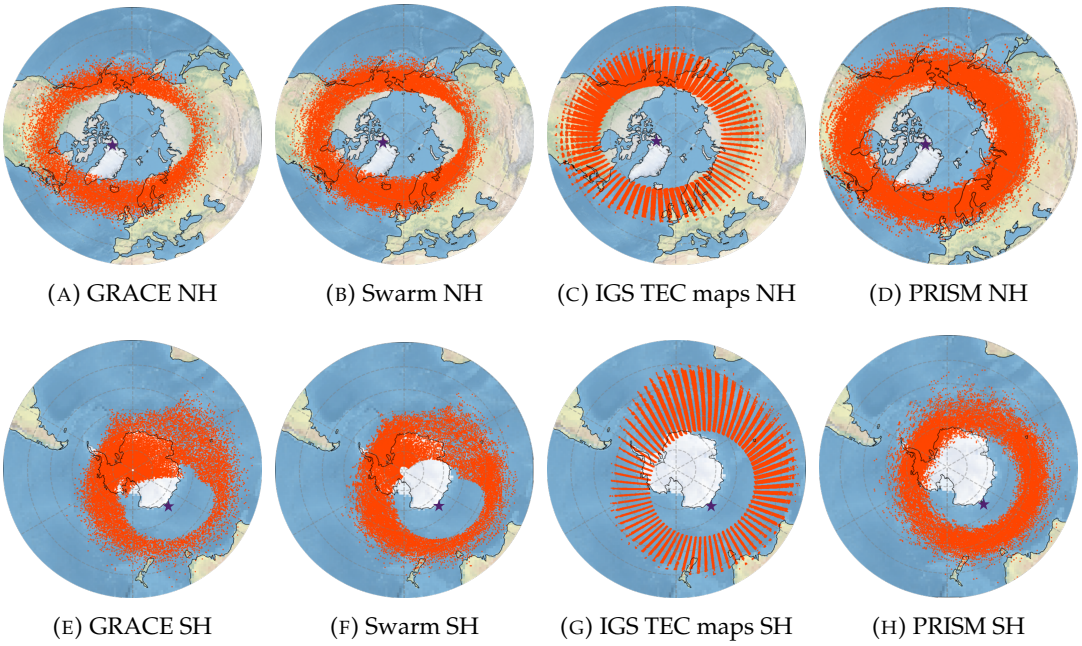

(A) GRACE NH (B) Swarm NH (C) IGS TEC maps NH (D) PRISM NH

(E) GRACE SH (F) Swarm SH (G) IGS TEC maps SH (H) PRISM SH

FIGURE 6.1: Polar view of the geographic locations of trough minimum locations (marked by red dots) for (A),(E) - Grace, (B),(F) - Swarm, (C),(G) - IGS TEC maps, and (D),(H) - PRISM. The top row shows the Northern Hemisphere, and the bottom row shows the Southern Hemisphere. The geomagnetic pole positions for each plot are indicated by purple stars.

6.1.2 Solar Cycle dependence

Solar activity conditions are represented by the solar radio flux index F10.7. Figure 6.2 compare the mean and standard deviation of trough minimum position, width and depth and F10.7 in the Northern and Southern Hemispheres, respectively. The data were binned into intervals containing equal numbers of measurements. Figures 6.2a and 6.2b show how, in both Hemispheres, the position of the trough minimum shifts slightly equatorward during high solar activity and poleward during low solar activity. These dependencies are consistent with the results published by Karpachev et al. (2016). Figures 6.2c and 6.2d show the mean trough width, which remains become slightly narrow with increasing F10.7 in NH, while in the SH only Swarm and PRISM show this trend. However, there is a positive correlation between trough depth and F10.7 increase, as shown in Figures 6.2e and 6.2f. This positive correlation between trough depth and F10.7 index increase was also discovered by Ishida. This correlation can be explained by the cause of

dissociative recombination induced by high ion temperature, which correlates with rising F10.7 levels (Ishida et al., 2014).

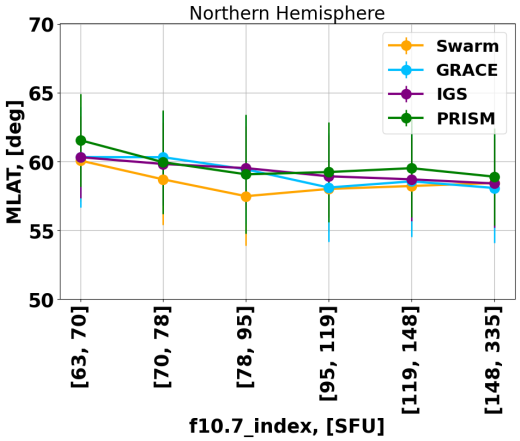

(A) Northern Hemisphere: Trough location

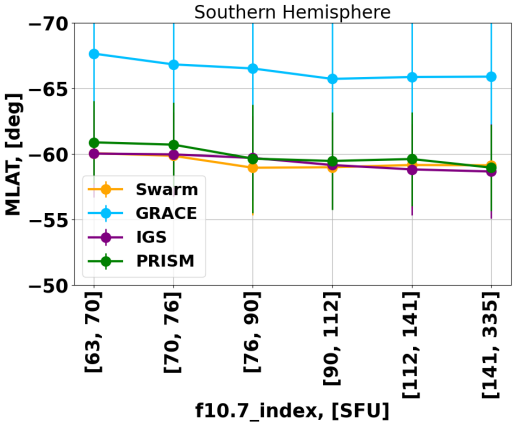

(B) Southern Hemisphere: Trough location

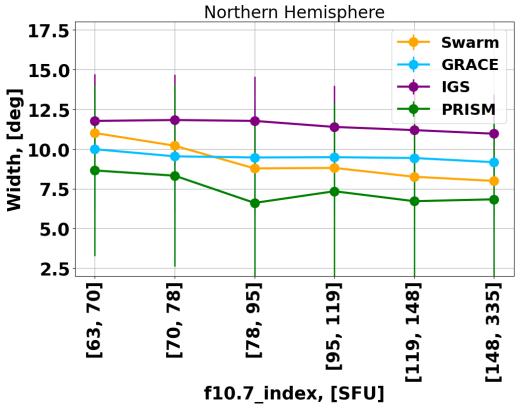

(C) Northern Hemisphere: Width

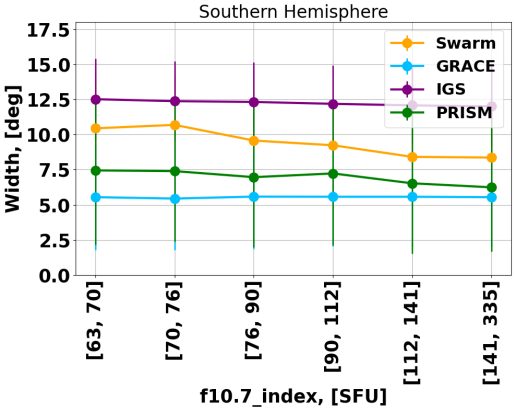

(D) Southern Hemisphere: Width

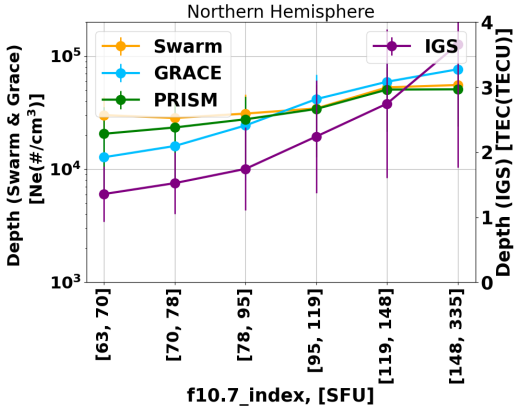

(E) Northern Hemisphere: Depth

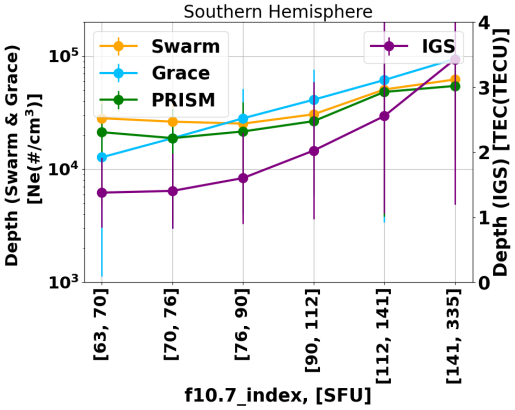

(F) Southern Hemisphere: Depth

FIGURE 6.2: The variations in (A) trough location, (B) trough width, and (C) trough depth of the mid-latitude trough as a function of the F10.7 index for the Northern and Southern Hemispheres. Error bars indicate the STD of the values.

6.1.3 Seasonal variation

Each month's percentage occurrence of the MIT in the Northern and Southern Hemispheres is displayed individually in Figure 6.4a and 6.4b. In Figure 6.4, data were grouped by month. Within each bin, the trough occurrence rate (%) was computed as 100× the ratio of detected troughs to the total number of available observations — satellite passes (Swarm, GRACE, PRISM) or TEC profiles (IGS TEC maps). Analyzing trough monthly occurrence in the Northern Hemisphere shows that troughs more frequently occur during the equinoxes and winter months (Nov–Feb) than during the summer (May–Aug). The overall trend in the southern plot is similar, mainly opposite, since the Northern and Southern Hemispheres have opposite seasons. However, seasonal dependency in the Southern Hemisphere is less apparent than in the Northern Hemisphere. The higher auroral activity in the vicinity of the equinoctial months might be the reason for the increased MIT occurrence during equinoxes. Enhanced auroral activity promotes the formation of the poleward wall of the main trough, making it more straightforward to identify trough footprints near equinoxes.

Seasonal fluctuation patterns are more noticeable in the Northern Hemisphere than in the Southern Hemisphere. This indicates hemispheric asymmetry, namely with the geographic and magnetic poles' offset (Aa et al., 2020).

Tables 6.1 and 6.2 demonstrate the spatial distribution of the MIT minimum over the Northern and Southern Hemispheres during different seasons: December solstice (Nov-Feb), June solstice (May-Aug), and the equinoxes (Mar, Apr, Sep, Oct). The computed mean and corresponding standard deviation are presented using different data sources such as GRACE, Swarm, IGS TEC maps, and PRISM data. We found out that the season has a negligible impact on the mean trough minimum position. In the Northern Hemisphere, the trough position is more consistent through all data sources; however, the results are more deviating in the Southern Hemisphere. Figure 6.3 visually represents the values from the corresponding tables.

Figure 6.5 demonstrate monthly mean and STDs of trough minimum position width and depth for Northern and Southern Hemispheres. The data in Figure 6.5 were binned into intervals with equal numbers of measurements. The trough minimum location moves during winter months at slightly higher latitudes compared to summer months (see Figure 6.5a). In the Southern Hemisphere (see Figure 6.5b) MIT is situated at a higher latitude during the summer. The width varies from 5 to 12 degrees. The trough detected by IGS TEC shows constant width during all months. Swarm and GRACE show a width decrease in summer in the Northern Hemisphere and an increase in the Southern Hemisphere. PRISM data show the same trend in the Southern Hemisphere, but in the Northern, it shows the opposite trend from Swarm and GRACE. The equinox seasons show intermediate width values, but the largest trough width occurs in winter and the narrowest ones in summer, which was also seen in our plots and is in agreement with research by Karpachev (2003) and Voiculescu et al. (2016). Such trough width behavior can be explained by the ionosphere's poleward extension during the winter months as a result of Earth's tilting axial rotation (Aa et al., 2020). Also, the depth of the trough changes accordingly so that in the Northern Hemisphere in spring-summer, it becomes more profound, and in the Southern Hemisphere, in Summer, it becomes more shallow (see Figures 6.5e, 6.5f).

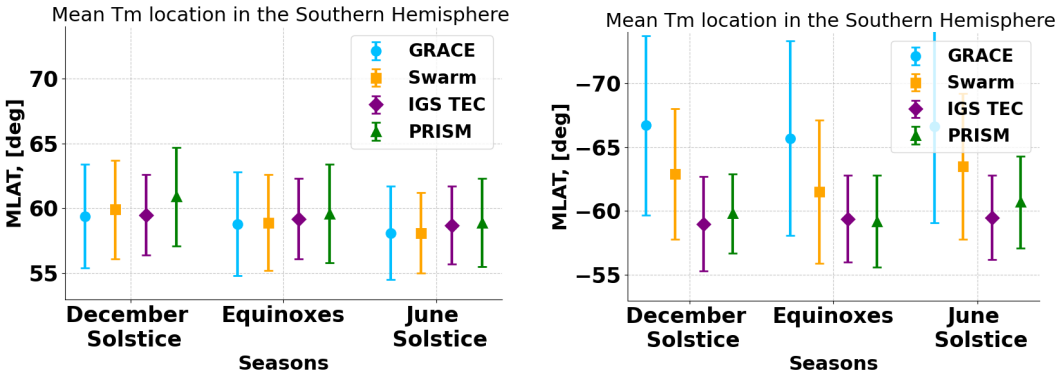

(A) (B)

FIGURE 6.3: Mean trough minimum position values plotted for Northern (A) and Southern (B) Hemispheres using GRACE, Swarm, IGS, and PRISM data for different seasons: December solstice, June solstice, and the equinoxes. Error bars indicate the STD of the values.

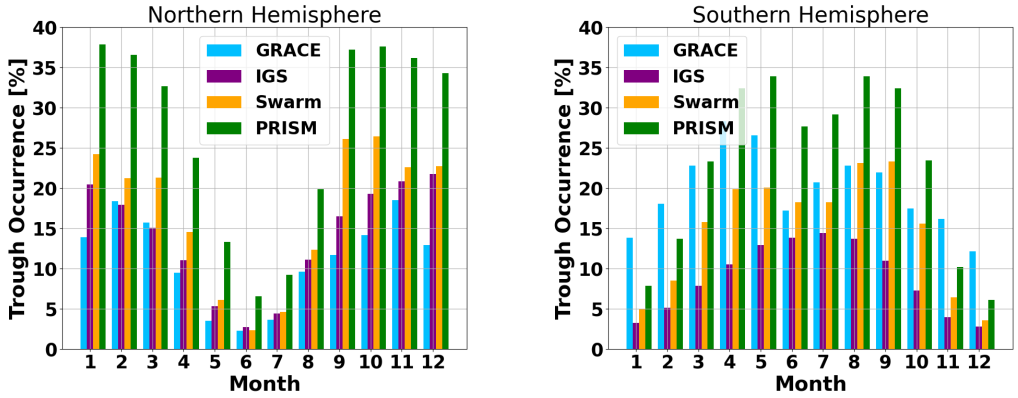

(A) (B)

FIGURE 6.4: Seasonal differences between the Northern and Southern Hemispheres in the occurrence rate of MIT. Monthly variations of MIT occurrence in the Northern and Southern Hemispheres are shown in (A) and (B), respectively.

	December Solstice	Equinoxes	June Solstice
GRACE	59.4 ± 4.0	58.8 ± 4.0	58.1 ± 3.6
Swarm	59.9 ± 3.8	58.9 ± 3.7	58.1 ± 3.1
IGS TEC	59.5 ± 3.1	59.2 ± 3.1	58.7 ± 3.0
Prism	60.9 ± 3.8	59.6 ± 3.8	58.9 ± 3.4

TABLE 6.1: Mean trough minimum position values (MLAT, [deg]) reprinted in the Northern Hemisphere using GRACE, Swarm, IGS, and PRISM data for different seasons: December solstice, June solstice, and the equinoxes. The corresponding standard deviation follows the sign $\pm$.

6.1.4 Diurnal variation

Figures 6.8 and 6.9 show a polar view of the trough occurrence for the Northern and Southern Hemispheres based on the magnetic local time (MLT) and magnetic

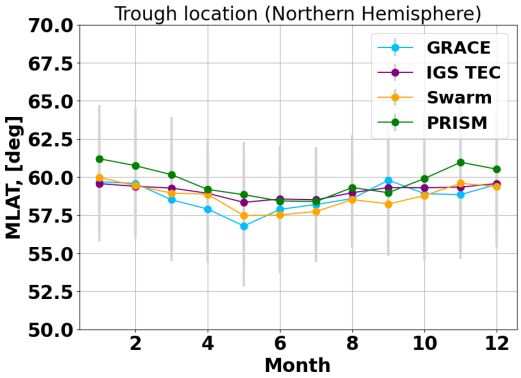

(A) Northern Hemisphere: Trough location

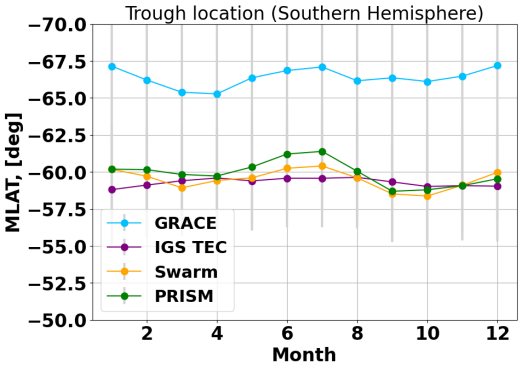

(B) Southern Hemisphere: Trough location

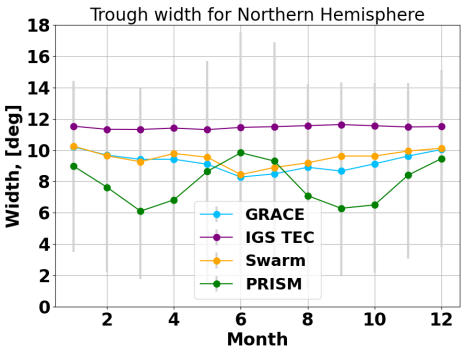

(C) Northern Hemisphere: Width

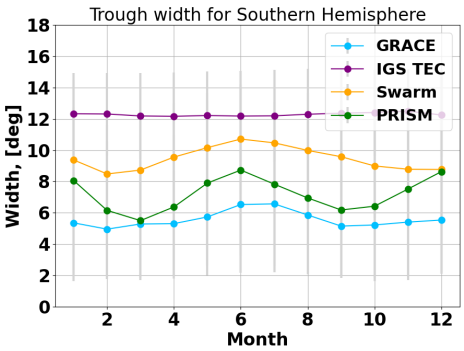

(D) Southern Hemisphere: Width

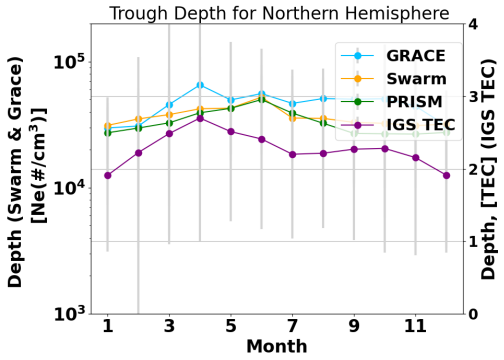

(E) Northern Hemisphere: Depth

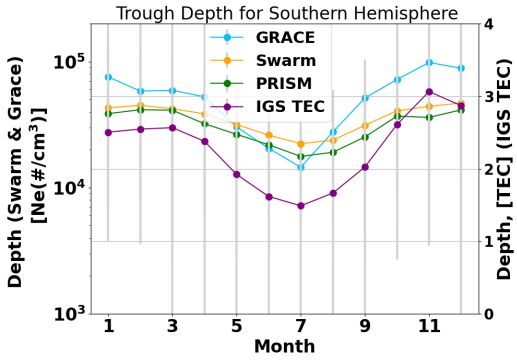

(F) Southern Hemisphere: Depth

FIGURE 6.5: The monthly variations in the (A, B) trough location, (C, D) trough width, and (E, F) trough depth of the mid-latitude trough in the Northern and Southern Hemispheres. Error bars indicate the STD of the values.

	December Solstice	Equinoxes	June Solstice
GRACE	-66.7 ± 7.0	-65.7 ± 7.6	-66.6 ± 7.5
Swarm	-62.9 ± 5.1	-61.5 ± 5.6	-63.5 ± 5.7
IGS TEC	-59.0 ± 3.7	-59.4 ± 3.4	-59.5 ± 3.3
PRISM	-59.8 ± 3.1	-59.2 ± 3.6	-60.7 ± 3.6

TABLE 6.2: Mean trough minimum position values (MLAT, [deg]) reprinted in the Southern Hemisphere using GRACE, Swarm, IGS, and PRISM data for different seasons: December solstice, June solstice, and the equinoxes. The corresponding standard deviation follows the sign $\pm$.

latitude. A resolution of 2° latitude $\times$ 1 h was used to bin the trough minimum position. By dividing each sector's trough minimum position by the total number of profiles that are available there and then multiplying the result by 100, the percentage occurrence was determined. Figures 6.8 and 6.9 illustrate that each season's trough polar plot elongates from dusk to dawn and widens in latitude from 60° to 50° MLAT. At night and in the morning, it is observed more frequently. Due to distinct flow regimes, Rodger et al. proposed that there should be a boundary between the morning trough and dusk trough (Rodger et al., 1992). The trough is more common in the Northern Hemisphere during the December equinoxes and solstices. As was covered in the preceding section, MIT happens more frequently in the Southern Hemisphere on equinoxes and the June solstice.

The particular mechanism is unclear yet to describe the troughs at different MLTs. In the literature it was suggested that different physical processes may be the cause of troughs at different MLTs. Aa et al. suggested that one of the primary mechanisms could be that ionospheric plasma is being steadily depleted by the chemical loss process in the post-midnight sector (Aa et al., 2020).

The variation of the mean trough minimum position (represented by dots of different colors according to the data source) as a function of magnetic local time (MLT) is shown in Figure 6.6. In this figure, the data were grouped into 2-hour MLT bins. Error bars represent the corresponding mean trough widths on the graph. Equatorward and poleward trough breakpoints define the boundaries of the trough width (see Figure 6.6). In the Northern Hemisphere, a steep slope or high gradient is indicated by mean trough widths that are narrower poleward. Toward the equator, the trough widths are relatively wider, indicating a less steep slope. The Southern Hemisphere shows a similar pattern but relatively more minor widths in both directions.

Figure 6.7 show the trough depth and width variations throughout the day. The data in Figure 6.7 were binned into intervals with equal numbers of measurements. The mean width of the troughs in all datasets was between 6 and 13 degrees in the Northern Hemisphere and between 5 and 12 degrees in the Southern Hemisphere. It can be also observe a slight increase in trough width from 7 to 14 MLT, which is also consistent with Mallis and Essex (1993). This coincides with the peak of photoionisation. The daylight trough tends to recede poleward, narrowing in width. The mean trough is deeper in the Northern Hemisphere. The Hemispheres are clearly distinguished, with the Northern Hemisphere showing more pronounced variations in trough depth and width.

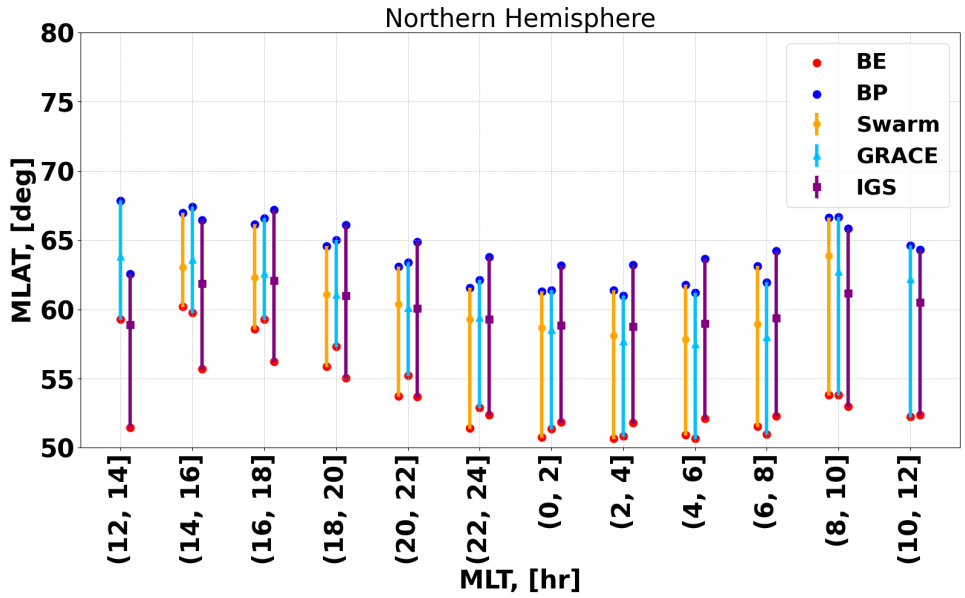

(A)

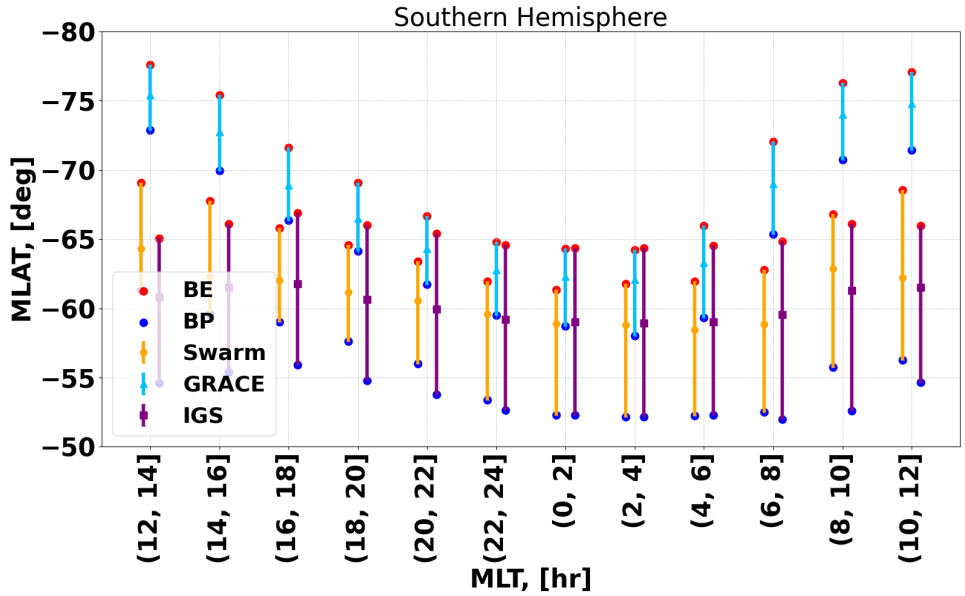

(B)

FIGURE 6.6: Changes in the trough position and its width marked by the equatorward and poleward break points throughout the day in the Northern (A) and Southern (B) Hemispheres according to the magnetic local time.

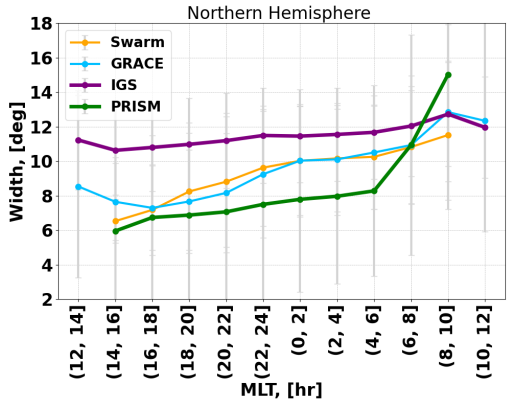

(A) Northern Hemisphere: Width

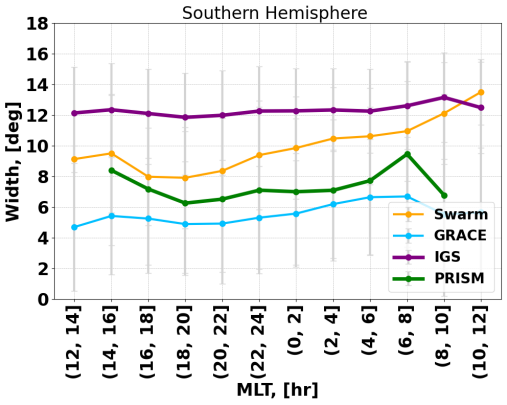

(B) Southern Hemisphere: Width

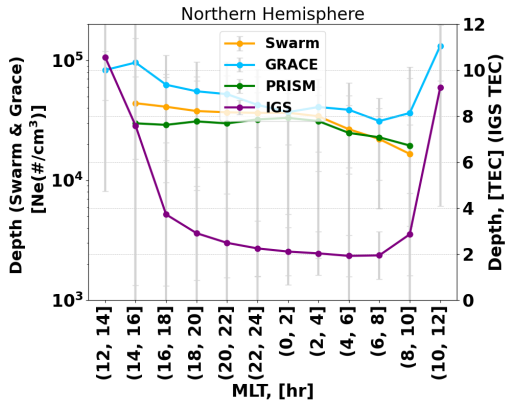

(C) Northern Hemisphere: Depth

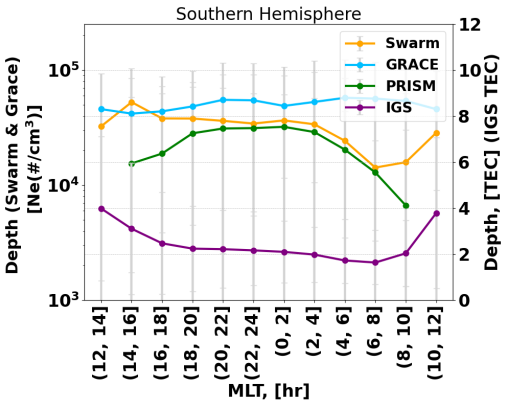

(D) Southern Hemisphere: Depth

FIGURE 6.7: Variation in the trough width (A, B) and depth (C, D) throughout the day according to magnetic local time in the Northern and Southern Hemispheres. Error bars indicate the STD of the values.

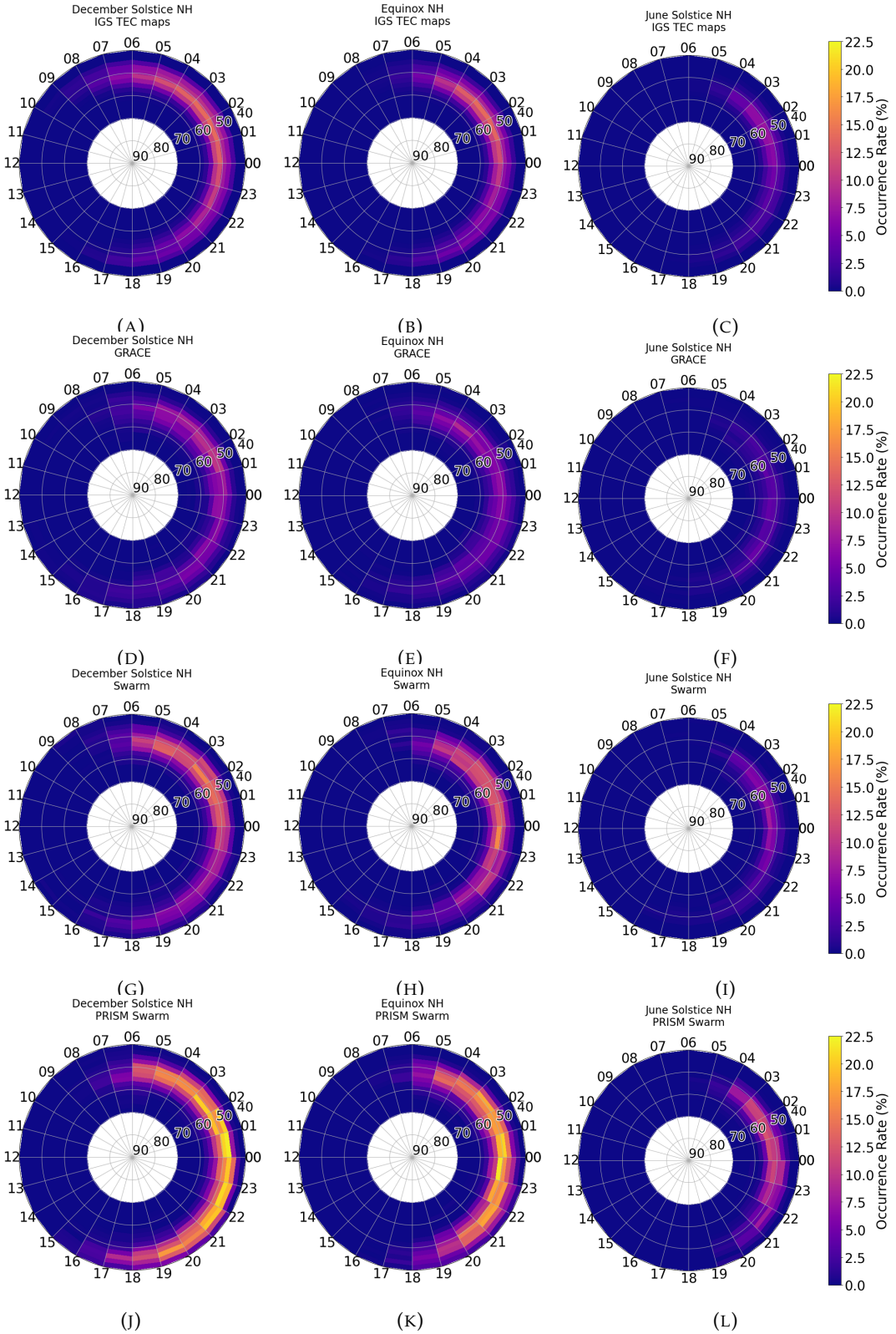

FIGURE 6.8: Occurrence rates as a function of magnetic local time and magnetic latitude for the December solstice, June solstice, and equinoxes. Corresponding polar views of the trough detected by IGS TEC maps (A-C), GRACE (D-F), Swarm (G-I), and PRISM (J-L) are shown for the Northern hemisphere.

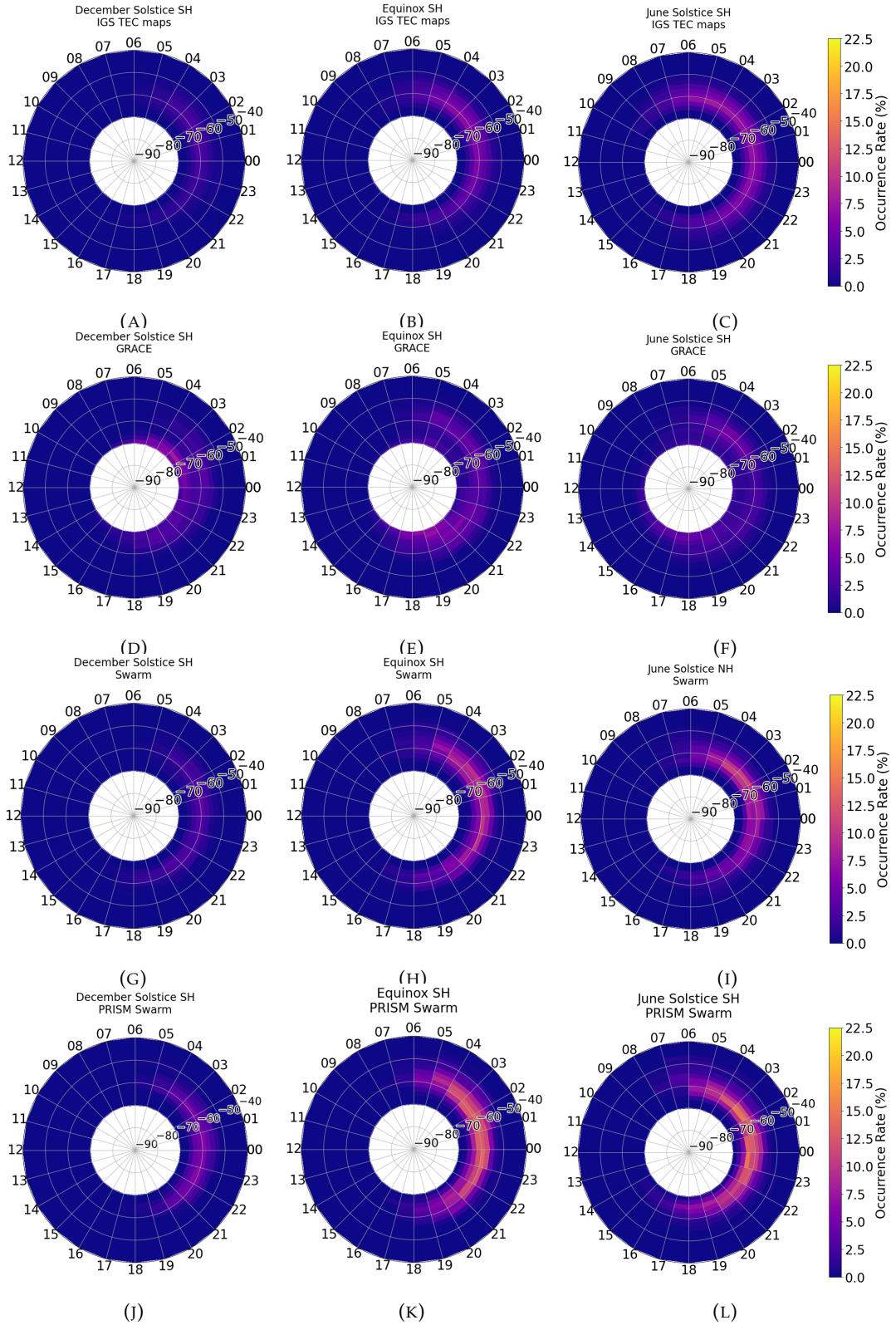

FIGURE 6.9: Occurrence rates as a function of magnetic local time and magnetic latitude for the December solstice, June solstice, and equinoxes. Corresponding polar views of the trough detected by IGS TEC maps (A-C), GRACE (D-F), Swarm (G-I), and PRISM (J-L) are shown for the Southern Hemisphere.

6.1.5 Dependence on Solar Wind, Flow Pressure and IMF Bx, By, Bz components

The interplanetary magnetic field and the dynamic pressure of the solar wind both significantly impact the earth's ionosphere-magnetosphere dynamic and structure. Since MIT is connected to ionospheric and magnetospheric processes, the influence of solar wind, flow pressure, and IMF Bx, By, Bz components on trough position, width, and depth will be investigated here.

Solar wind speed has significant effects on the space weather conditions on Earth. In addition to constricting the Earth's magnetosphere, faster solar winds can also introduce energetic particles that intensify auroral displays and magnetospheric disruption. The data for Figures 6.10 – 6.14 were binned into intervals with equal numbers of measurements. Figure 6.10 shows the trough main parameters correlation with solar wind plasma speed. Both Figures 6.10a and 6.10b show a negative correlation between the solar wind and trough minimum location. High-speed solar wind with speed > 500 km/s enhance the potential for geomagnetic storms. Figures 6.10a and 6.10b illustrate how the trough position clearly responds to rising solar wind speeds. In particular, trough position moves around 3 degrees equatorward when solar wind plasma speed becomes higher then 500 km/s, indicating increased geomagnetic activity. This movement toward the equator is probably caused by increased energy deposition and magnetospheric convection at lower latitudes. He et al. also found a negative connection between solar wind speed and the MIT latitude (He et al., 2011). Figures 6.10c and 6.10d show that for the Swarm and GRACE datasets trough width decreases slightly about 1-2 degrees of latitude with increased solar wind plasma speed. In contrast, IGS and PRISM datasets do not show any changes in width with solar wind plasma speed. However Prism for example have large error bars, meaning that the variation is not statistically significant. Hense, the evidence for a narrowing trough with solar wind speed should be interpreted with caution. Figures 6.10e and 6.10f show that depth is slightly increasing with increased solar wind plasma speed.

Figure 6.11 shows a correlation with flow pressure. With an increase of flow pressure trough was observed to shift a bit to lower latitudes (see Figures 6.11a, 6.11b). The trough develops to be narrower with flow pressure increase for most datasets (see Figures 6.11c, 6.11d). However, large error bars make the variation not statistically significant. Also, the trough becomes deeper with flow pressure increase (see Figures 6.11e, 6.11f).

The variation that occurs in the trough minimum location with respect to the Bx, By, and Bz components is depicted in Figures 6.12, 6.13, and 6.14. Every IMF component displays a similar pattern, and the trough parameters vary very little. However, there is a tendency of the trough depth to increase and become narrower with the increase of the absolute value of Bx, By and mostly Bz IMF component. However we still have large error bars but at least these tendencies are physically reasonable, since stronger IMF components enhance the coupling between the solar wind and the magnetosphere, which in turn can deepen and narrow the trough.

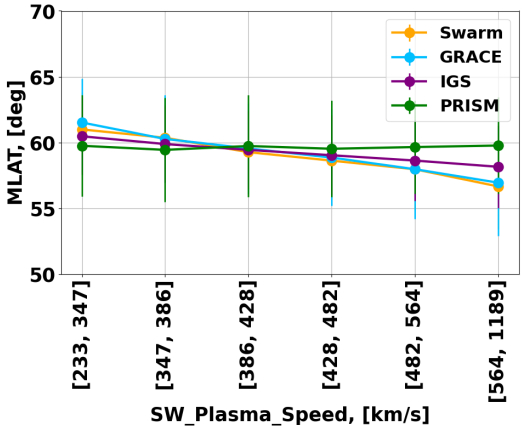

(A) Northern Hemisphere: Trough location

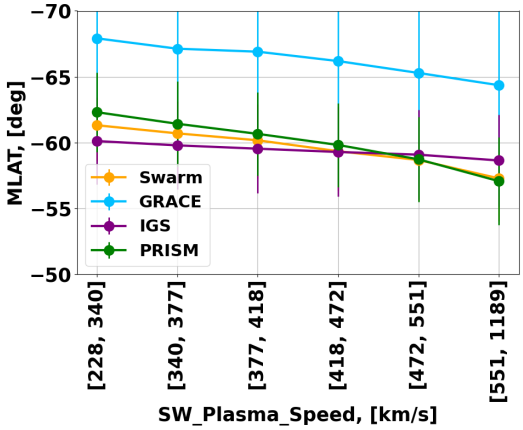

(B) Southern Hemisphere: Trough location

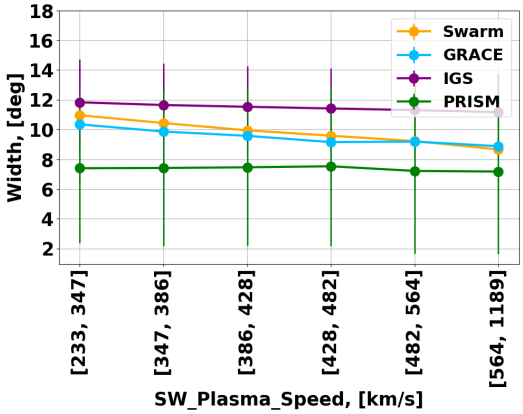

(C) Northern Hemisphere: Width

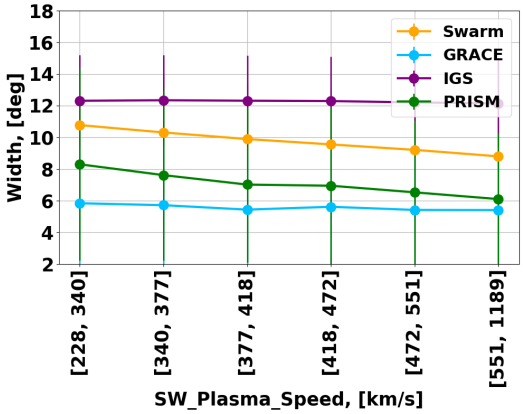

(D) Southern Hemisphere: Width

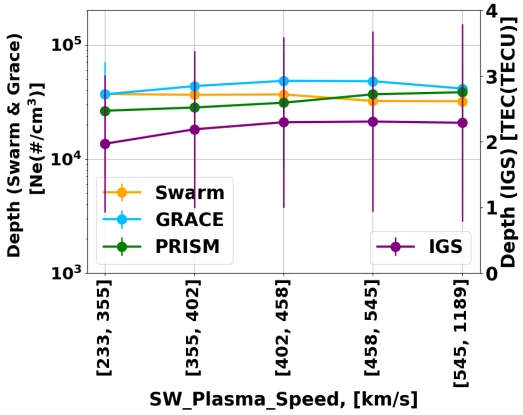

(E) Northern Hemisphere: Depth

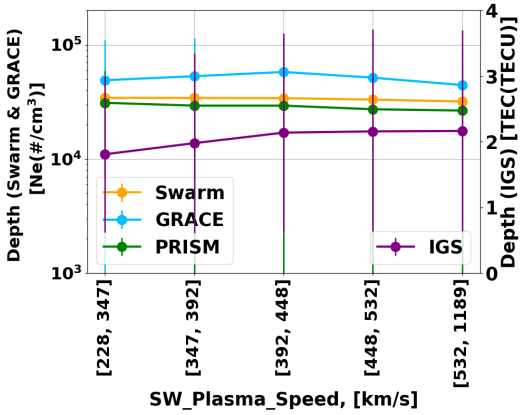

(F) Southern Hemisphere: Depth

FIGURE 6.10: Variations in the (A, B) - trough location, (C, D) - trough width, and (E, F) trough depth of the mid-latitude trough depending on solar wind plasma speed in the Northern and Southern Hemispheres. Error bars indicate the STD of the values.

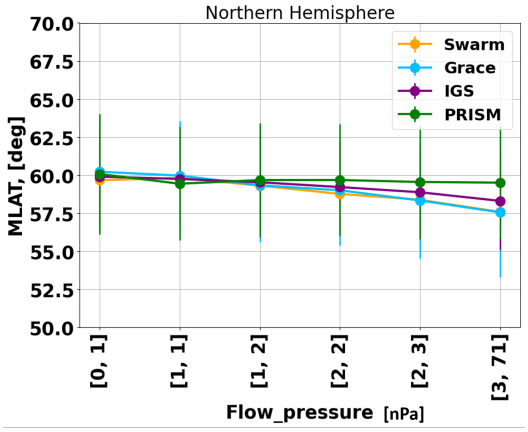

(A) Trough location NH

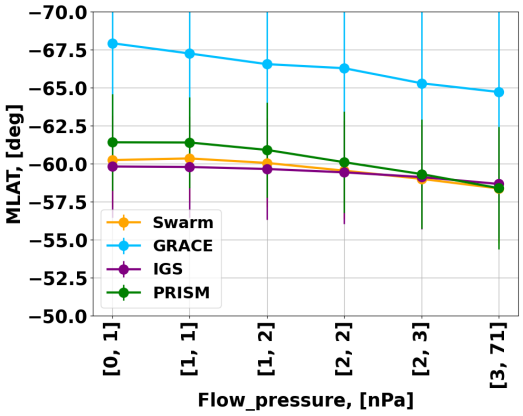

(B) Trough location SH

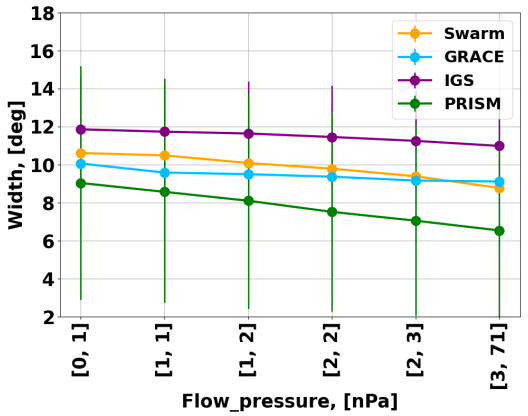

(C) Width NH

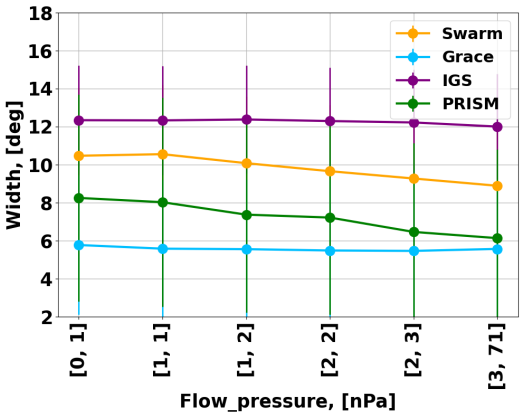

(D) Width SH

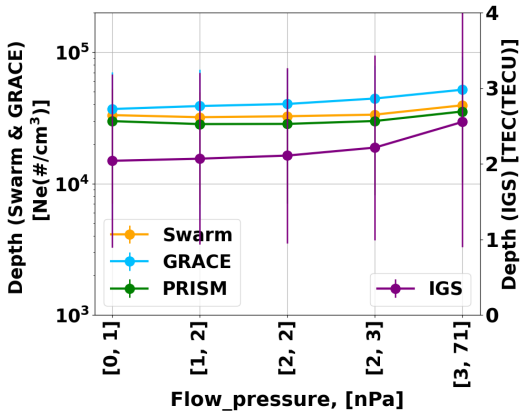

(E) Depth NH

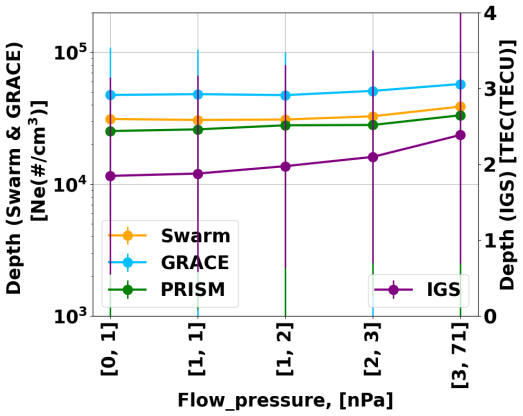

(F) Depth SH

FIGURE 6.11: Variations in the (A, B) - trough location, (C, D) - trough width, and (E, F) trough depth of the mid-latitude trough depending on flow pressure in the Northern and Southern Hemispheres. Error bars indicate the STD of the values.

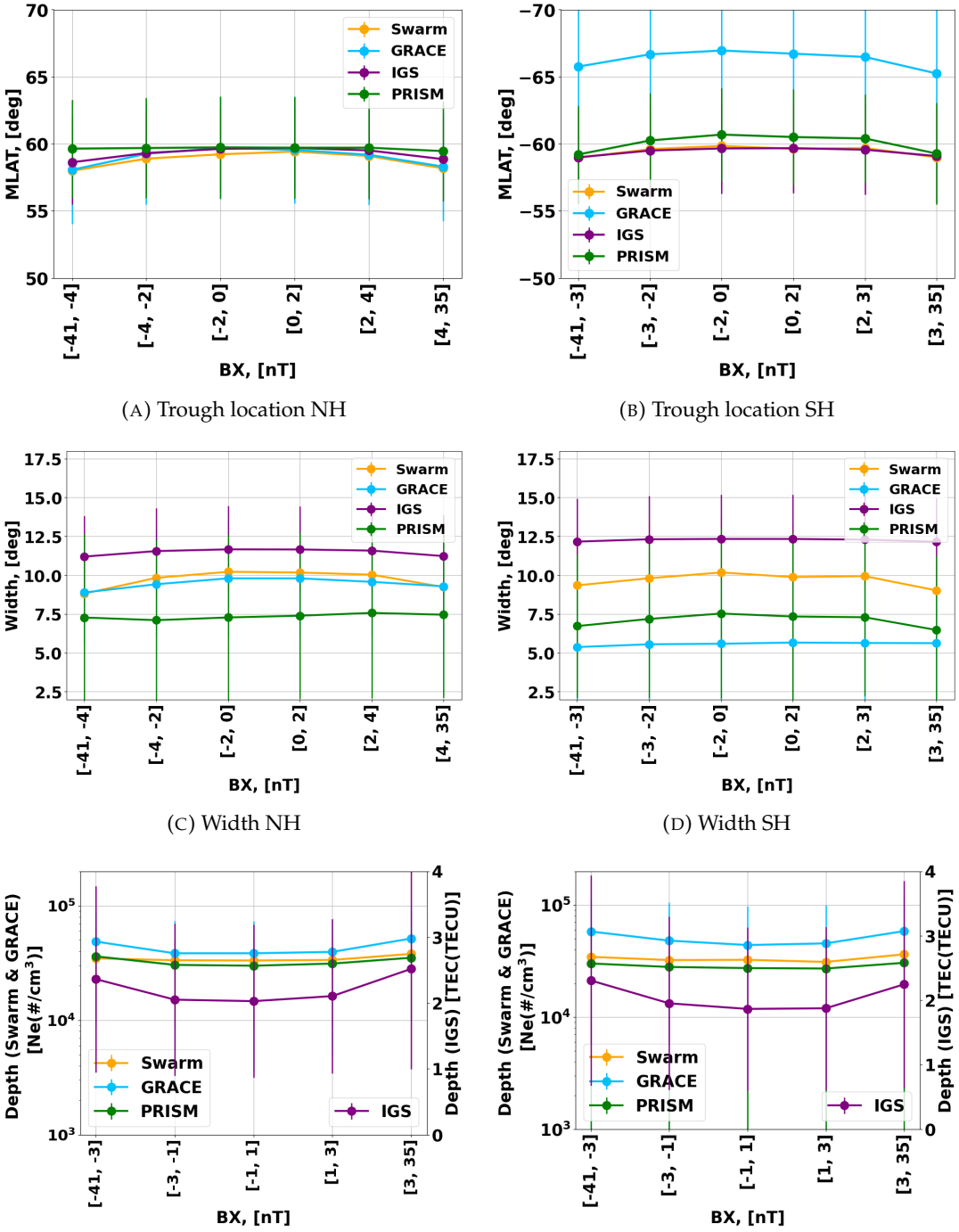

(A) Trough location NH

(B) Trough location SH

(C) Width NH

(D) Width SH

(E) Depth NH

(F) Depth SH

FIGURE 6.12: Variations in the (A, B) - trough location, (C, D) - trough width, and (E, F) trough depth of the mid-latitude trough depending on IMF Bx component in the Northern and Southern Hemispheres. Error bars indicate the STD of the values.

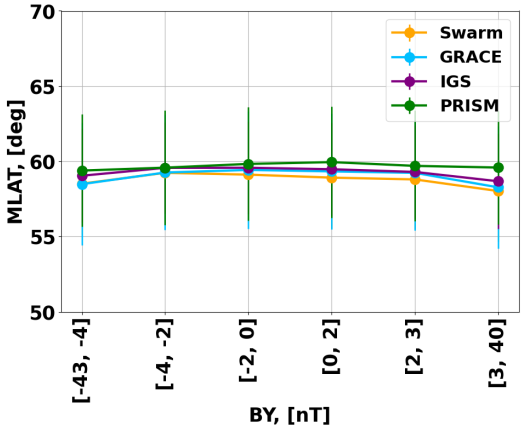

(A) Trough location NH

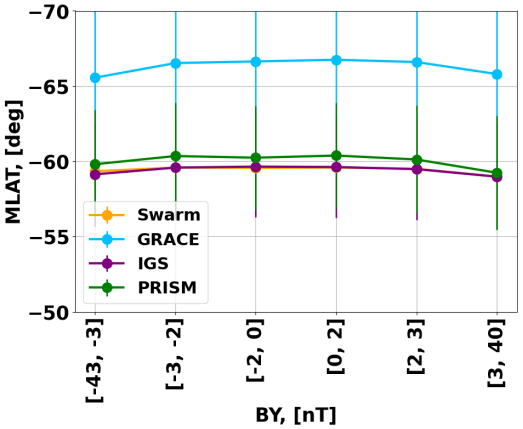

(B) Trough location SH

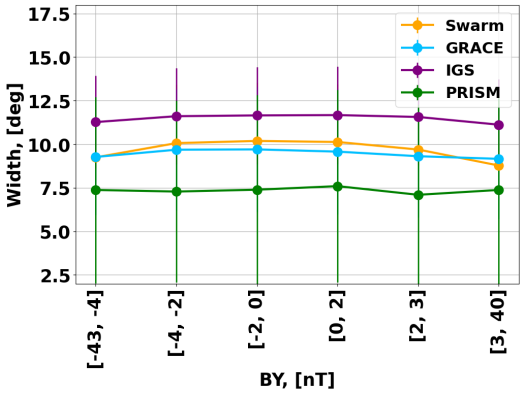

(C) Width NH

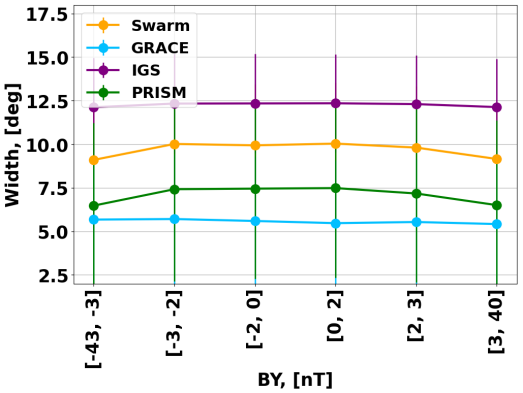

(D) Width SH

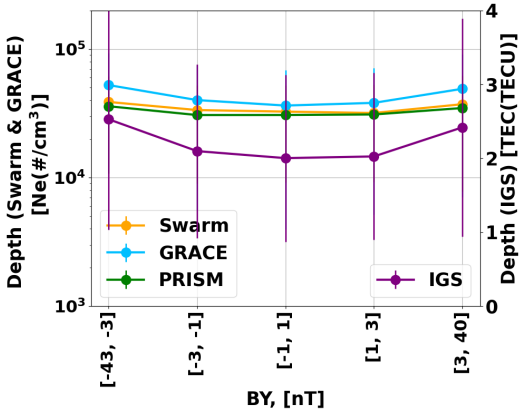

(E) Depth NH

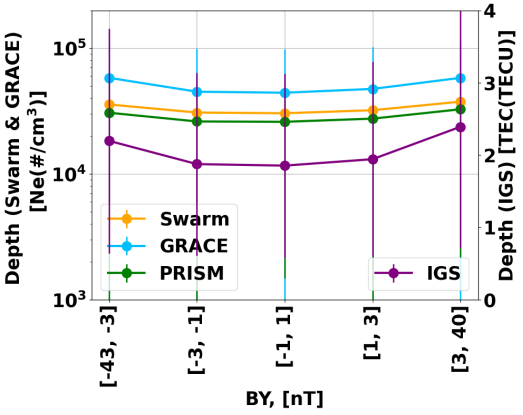

(F) Depth SH

FIGURE 6.13: Variations in the (A, B) - trough location, (C, D) - trough width, and (E, F) trough depth of the mid-latitude trough depending on IMF By component in the Northern and Southern Hemispheres. Error bars indicate the STD of the values.

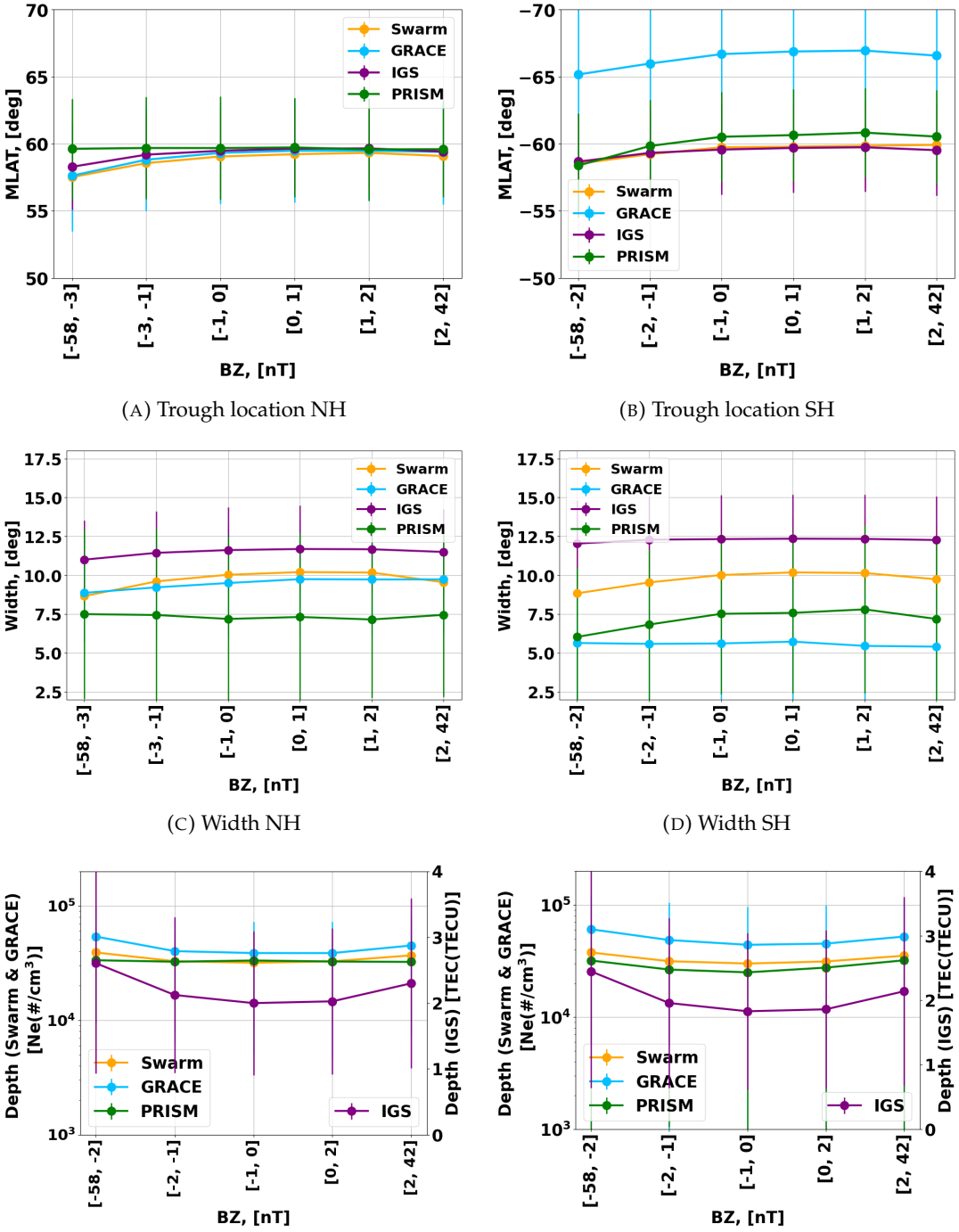

(A) Trough location NH

(B) Trough location SH

(C) Width NH

(D) Width SH

(E) Depth NH

(F) Depth SH

FIGURE 6.14: Variations in the (A, B) - trough location, (C, D) - trough width, and (E, F) trough depth of the mid-latitude trough depending on IMF Bz component in the Northern and Southern Hemispheres. Error bars indicate the STD of the values.

6.1.6 Dependence on Hp30 Index

The trough parameters dependence with a high-cadence Hp30 index are presented in Figure 6.15. The data in Figure 6.15 were binned into intervals with equal numbers of measurements. Figures 6.15a and 6.15b shows that trough minimum

location moves equatorward with an increasing Hp30 index in both Hemispheres. The trough position can move in average up to 6 degrees latitude in equatorward direction. Trough movement to the equatorward with increasing geomagnetic activity also agree with other studies (Karpachev, 2003; Le et al., 2017; Prölss, 2007; Werner & Prölss, 1997; Yang et al., 2016).

The magnetosphere is first compressed by increasing in solar wind pressure. Increased energy is transferred into the magnetosphere by interactions between the Earth's magnetic field and the magnetic field of the solar wind. Both interactions result in an increase in electric current in the magnetosphere and ionosphere as well as an increase in plasma movement through the magnetosphere (caused by increasing electric fields inside the magnetosphere). During periods of high geomagnetic activity, the auroral oval expands equatorward, driven by enhanced particle precipitation and field-aligned currents. The mid-latitude trough, which forms just equatorward of the auroral oval due to ionospheric plasma depletions, follows this movement, shifting to lower magnetic latitudes under disturbed conditions.

Figures 6.15c and 6.15d shows that trough width changes with Hp30 index, mainly trough is becoming narrow with the increase of Hp30 index. Trough can become narrower for up to 3 degrees latitude. Figures 6.15e and 6.15f shows that trough becomes deeper with the increasing of Hp30 index. Almost all data shows consistent results. Trough width and depth variations with increased geomagnetic activity are in agreement with previous studies (Aa et al., 2020).

The relationship of trough and geomagnetic activity level can be explained by SAID or SAPS, which in turn evidently also rely on the degree of geomagnetic activity. With the increasing geomagnetic activity, in the subauroral ionosphere stronger electric fields develop. These fields push ionospheric plasma westward at high speeds, creating SAPS and SAID. These fast flows increase the number of ion-neutral particle collisions, which accelerates electron-ion recombination and causes frictional heating. This causes a deeper trough to appear as the plasma in this area is greatly depleted.

The trough is narrower because the plasma depletion is restricted to a smaller latitudinal band due to the intense and narrow nature of these fluxes. Additionally, the trough moves with SAPS and SAID as they move to lower latitudes during geomagnetic active conditions.

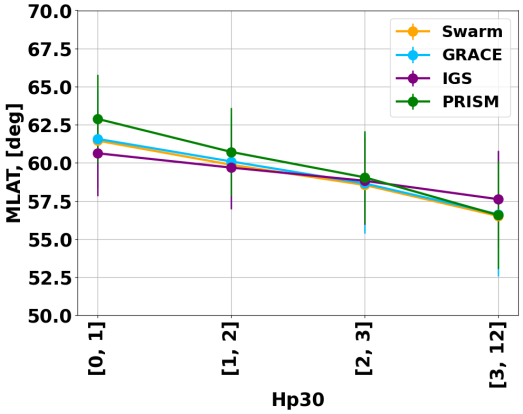

(A) Northern Hemisphere: Trough location

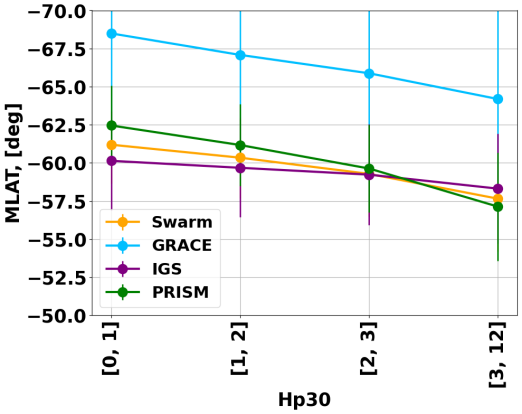

(B) Southern Hemisphere: Trough location

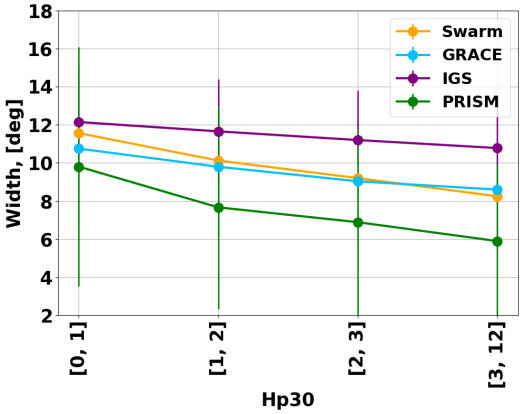

(C) Northern Hemisphere: Width

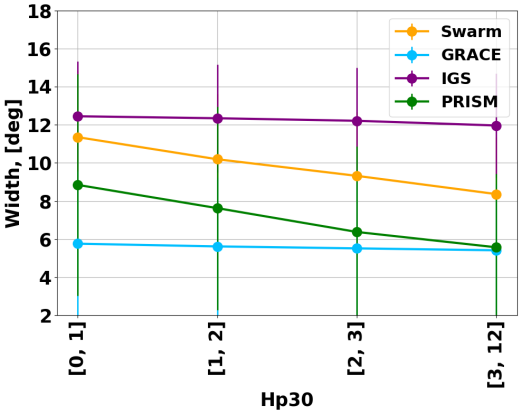

(D) Southern Hemisphere: Width

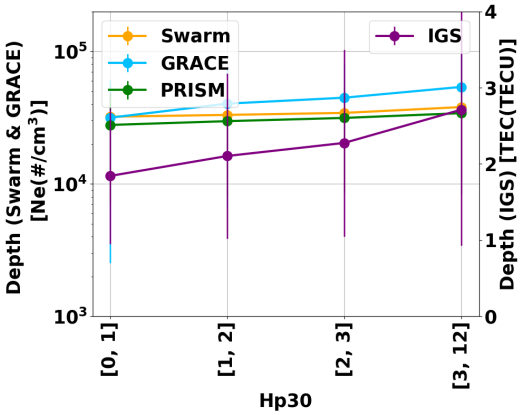

(E) Northern Hemisphere: Depth

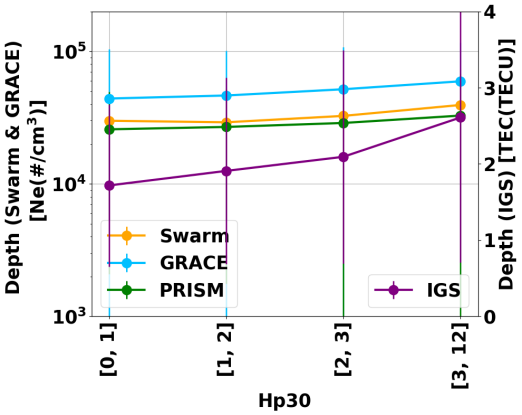

(F) Southern Hemisphere: Depth

FIGURE 6.15: The trough minimum location (A, B), trough width (C, D), and trough depth (E, F) as a function of the Hp30 index for the Northern and Southern Hemispheres. Error bars indicate the STD of the values.

6.1.7 Dependence on SYM-H Index

The dependence of Tm, width, and depth on the SYM-H index is displayed in Figure 6.16. The data in Figure 6.16 were binned into intervals with equal numbers of measurements. The development of a ring current in the inner magnetosphere is

indicated by the SYM-H index (Iyemori, 1990). The main trough characteristics have a significant relationship with the SYM-H index, which measures the strength of the symmetric ring current and is thus a good indicator of the intensity of geomagnetic storms. This correlation is more pronounced in the Northern Hemisphere than in the Southern Hemisphere. With the SYM-H index decreases during increase of geomagnetic activity and the trough position reacts with shift to equatorward, become narrow and deep. The equatorward movement of the trough is due to the expansion of auroral oval during storms, which moves the trough and the subauroral zone toward lower latitudes(Prölss, 2007; Zou et al., 2011). As the SYM-H index decreases (i.e., increasing geomagnetic activity), the trough gets deeper and narrower due to the enhancement of subauroral electric field and associated plasma heating (Nishimura et al., 2021). Our findings support the findings presented by Yang et al. (2016), who demonstrated that trough dynamics vary based on the type of magnetic storm and that trough position shifts during magnetic storms are symmetrical in both the Northern and Southern Hemispheres.

The trough can shift equatorward by up to 9 degrees in magnetic latitude (see Figures 6.16a, 6.16b). The width of trough can become narrower for up to 3 degrees during periods of increased geomagnetic activity (see Figures 6.16c, 6.16d).

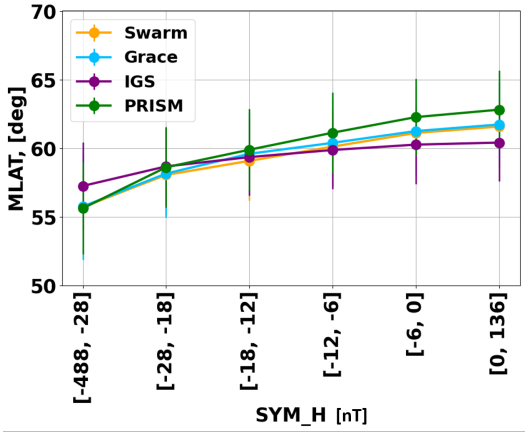

(A) Northern Hemisphere: Trough location

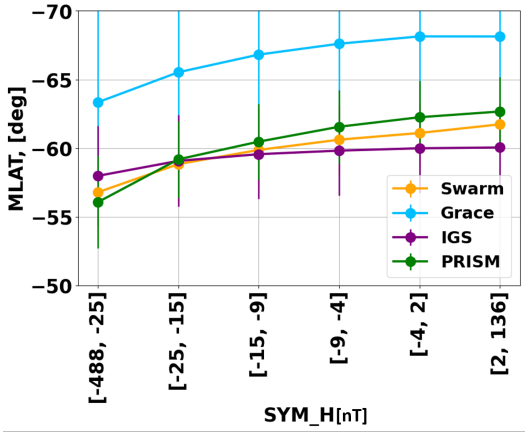

(B) Southern Hemisphere: Trough location

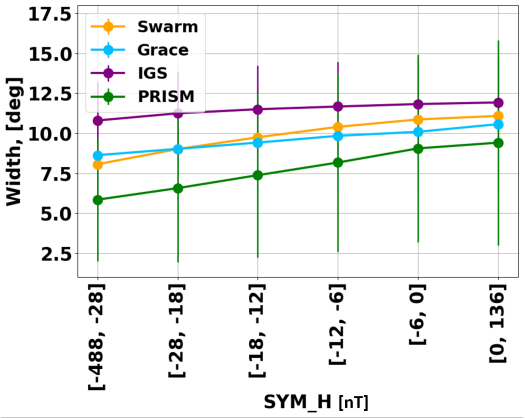

(C) Northern Hemisphere: Width

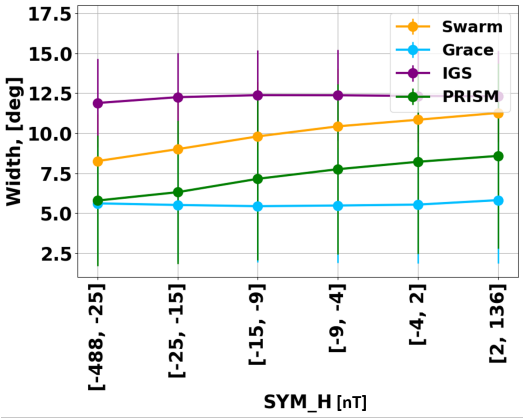

(D) Southern Hemisphere: Width

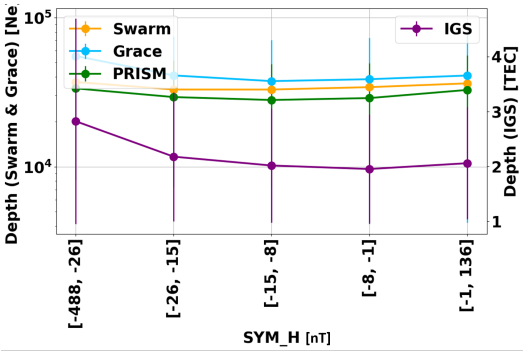

(E) Northern Hemisphere: Depth

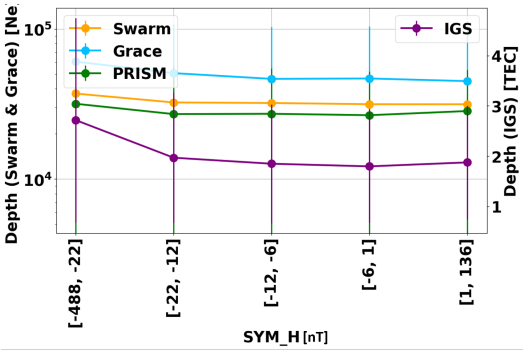

(F) Southern Hemisphere: Depth

FIGURE 6.16: The trough minimum location (A, B), trough width (C, D), and trough depth (F, F) as a function of the SYM-H index for the Northern and Southern Hemispheres. Error bars indicate the STD of the values.

6.1.8 Trough occurrence dependence on Space Weather Indices

The relationship between the trough occurrence and space weather indices such as F10.7, Hp30, SYM-H was examined in this section.

6.1.8.1 MIT occurrence dependence on F10.7

This investigation uses data from Swarm, PRISM, GRACE and IGS, including periods of high and low solar activity (see Figure 5.1 showing the data distribution). GRACE data were not taken for the entire mission period, but the dataset was taken from 2004 to 2012. At the beginning of the GRACE mission, the satellite operated at higher altitudes, reaching up to 520 km. Towards the end of the GRACE mission, the altitude decreased significantly from about 460 km to 380 km (see Figure 5.2). This influenced the results of the occurrence rate published in 2022 (Lubyk et al., 2022). In this publication, GRACE was used for the entire period of GRACE observations (2002 - 2015) and it shows that as the F10.7 index increases, so does the occurrence of MIT. After investigating other data sources, we found that this result is not consistent with other data sources such as Swarm and IGS TEC maps, where the occurrence decreases slightly as F10.7 increases. For this investigation the F10.7 index range was limited to 180 sfu only. Figure 6.17 shows scatter plots of the occurrence rate as a function of the F10.7 index. The data points for the plot were derived as follows: first the data were calculated as monthly means and then binned into bins in the range 60 - 180 sfu with 10 sfu steps for each bin; median F10.7 index and occurrence rate were calculated. In this way, all the data show a negative correlation between the occurrence rate and the F10.7 index. This is logical as the decrease in the trough occurrence rate results from an increase in the ionisation production rate, driven by the enhanced solar extreme ultraviolet radiation associated with high solar activity. The result is also consistent with the results published by Aa et al. (2020).

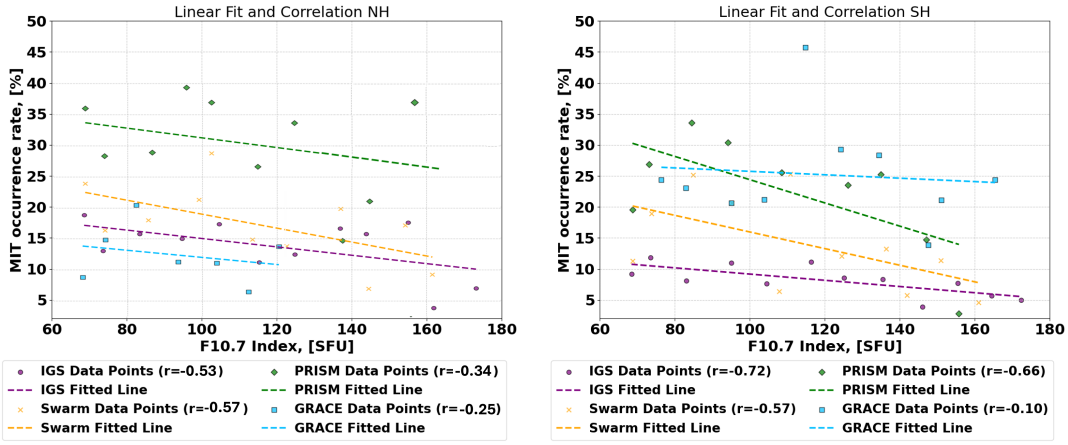

(A) (B)

FIGURE 6.17: Northern (A) and Southern (B) Hemisphere scatter plots of the monthly averaged trough occurrence rate against its F10.7 index. Additionally displayed for each panel are the correlation coefficient and the linear fitted line.

6.1.8.2 MIT occurrence dependence on Hp30 index

The results of the MIT occurrence dependence on the Hp30 index are shown in Figure 6.18. In Figure 6.18, Hp30 index values were binned into intervals containing equal numbers of measurements. Within each bin, the trough occurrence rate (%) was computed as 100× the ratio of detected troughs to the total number of available observations — satellite passes (Swarm, GRACE, PRISM) or TEC profiles (IGS TEC maps). The bar plots shows that the trough occurred more frequently

with increasing geomagnetic activity, as indicated by the Hp30 index, in both Hemispheres. The occurrence rate in the Northern Hemisphere (Figure 6.18a) increases from around 15% in the lowest Hp30 bin [0,1] to more than 40% in the highest bin [3,12]. GRACE dataset shows the strongest increase of trough occurrence. In the Southern Hemisphere, a similar trend is seen (Figure 6.18b). The GRACE dataset shows a trough detection rate approaching 50% in the [3,12] bin and is roughly 10% under quiet conditions.

The trough occurrence trend with respect to the Hp30 index is consistent across all datasets (GRACE, IGS, Swarm, and PRISM). Among them, GRACE shows always more occurrence rate, meaning the trough detection has the highest percentage. This is followed by trough occurrence derived using Swarm data and PRISM trough product, where the PRISM shows constantly around 8% higher occurrence rates than Swarm across all Hp30 bins. However Swarm and PRISM data set have the same original data provided by Swarm mission, but it is used different detection algorithms (see Chapter 5).

The percentage of occurrence by Swarm using our detection algorithm is around 10% in the lowest Hp30 bin [0,1] and around 30% in the highest bin [3,12]. In contrast, PRISM have around 18% in the lowest Hp30 bin [0,1], and 35% in the highest bin [3,12], indicating the impact of algorithmic differences. IGS TEC maps shows the lowest percentage of trough occurrence, where in the lowest Hp30 bin [0,1] in the NH occurrence is about 10% and 20% in the highest bin [3,12]. In the SH IGS TEC maps shows almost no variation in the trough occurrence rate being around 10%. As was mentioned before this is related to the fact that the IGS TEC maps are smoothed and in the SH having sparse station coverage, which may be a reason for such low occurrence rate.

The observed increase in trough occurrence with rising Hp30 index aligns well with previous findings reported by Aa et al. (2020) and Voiculescu et al. (2006). This dependency may be partially explained by the existence of storm-time SAPS/SAID flow channels, which similarly exhibit a distinct Hp30 index dependence. Strong poleward electric fields drive these westward flows, which decrease plasma in the subauroral zone through ion-neutral interactions and frictional heating (Nishimura et al., 2021). The mid-latitude trough thereby becomes deeper, particularly at night, when recombination increases. Higher Hp30 values are linked to stronger plasma depletion and, as a result, more frequent and noticeable trough detection since SAPS/SAID intensity correlates with the Hp30 index.

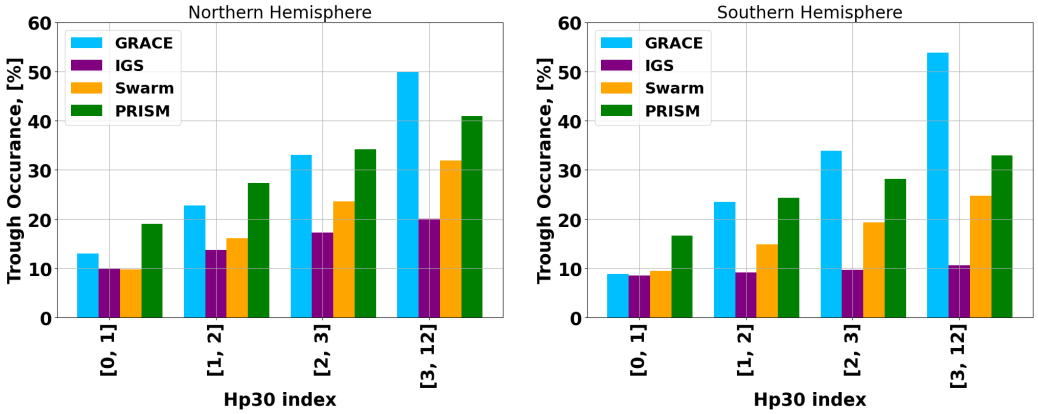

(A) (B)

FIGURE 6.18: Northern (A) and Southern (B) Hemisphere bar plots of the trough occurrence rate against Hp30 index.

6.1.8.3 MIT occurrence dependence on SYM-H index

The results of the MIT occurrence dependence on the SYM-H index are shown in Figure 6.19. In Figure 6.19, SYM-H index values were binned into intervals containing equal numbers of measurements. Within each bin, the trough occurrence rate (%) was computed as 100× the ratio of detected troughs to the total number of available observations — satellite passes (Swarm, GRACE, PRISM) or TEC profiles (IGS TEC maps). The SYM-H index dependence shows that the trough occurred more frequently with increasing ring current intensity during geomagnetic storms in both Hemispheres. The data were divided into 5 bins, the last bin [-488, -26] nT represents highly disturbed conditions. Figure 6.19 clearly shows that MIT occurrence rates rise, as geomagnetic activity intensifies, demonstrated by more negative SYM-H values. The highest trough occurrence rate correspond with the most negative SYM-H bin [- 488, - 26] nT. The GRACE dataset exhibits the largest trough occurrence in the Northern Hemisphere (Figure 6.19A), at around 50%. This is followed by PRISM (∼35%) and Swarm (∼28%). In a similar manner GRACE leads the Southern Hemisphere (Figure 6.19B) with almost 45%, followed by Swarm and PRISM with roughly 30% and 25%, respectively. On all datasets, the occurrence rates sharply decline as geomagnetic conditions become quieter (moving to the right in the SYM-H bins). For instance, GRACE shows around 15% occurrence in both Hemispheres in the quietest SYM-H range [1, 136] nT, whereas Swarm and PRISM show even lower rates, around 10%.

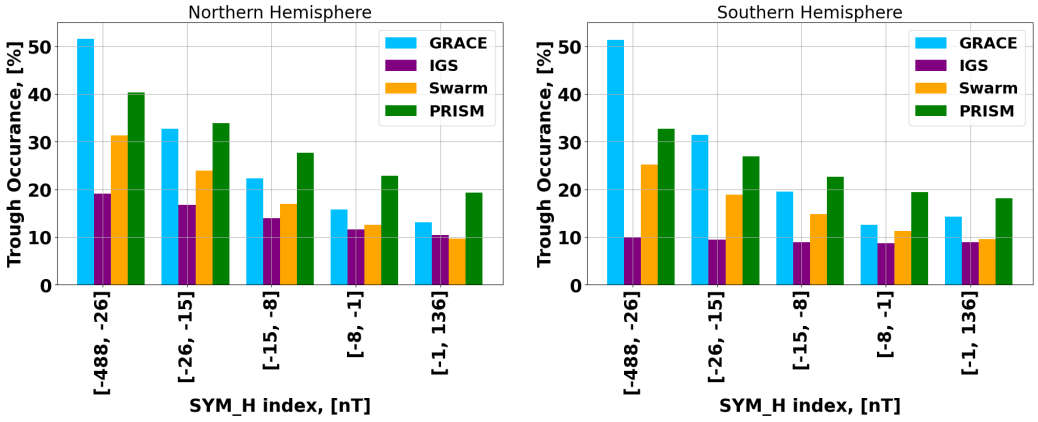

(A) (B)

FIGURE 6.19: Northern (A) and Southern (B) Hemisphere bar plots of the trough occurrence rate against SYM-H index.

6.1.8.4 MIT occurrence dependence on SW plasma speed

The results of the MIT occurrence dependence on the SW plasma speed are shown in Figure 6.20. In Figure 6.20, SW plasma speed index values were binned into intervals containing equal numbers of measurements. Within each bin, the trough occurrence rate (%) was computed as 100× the ratio of detected troughs to the total number of available observations — satellite passes (Swarm, GRACE, PRISM) or TEC profiles (IGS TEC maps). The SW plasma speed dependence shows that the trough occurred more frequently with increasing SW plasma speed in both Hemispheres. High speed solar winds bring geomagnetic storms pointing out again that trough is occurring more during high geomagnetic activity.

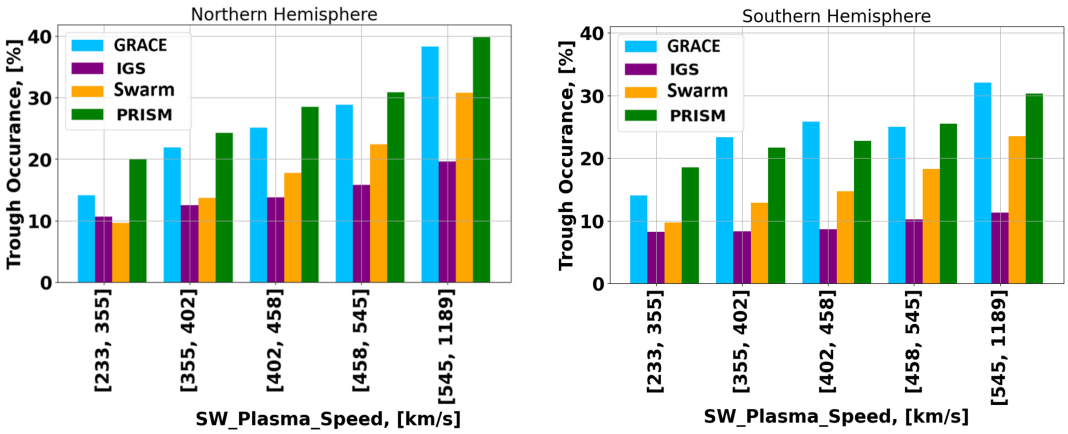

(A) (B)

FIGURE 6.20: Northern (A) and Southern (B) Hemisphere bar plots of the trough occurrence rate against solar wind plasma speed.

6.1.8.5 MIT occurrence dependence on Flow pressure

The results of the MIT occurrence dependence on the flow pressure are shown in Figure 6.21. In Figure 6.21, flow pressure index values were binned into intervals containing equal numbers of measurements. Within each bin, the trough occurrence

rate (%) was computed as 100× the ratio of detected troughs to the total number of available observations — satellite passes (Swarm, GRACE, PRISM) or TEC profiles (IGS TEC maps). The flow pressure dependence shows that the trough occurred more frequently with increasing of flow pressure in both Hemispheres.

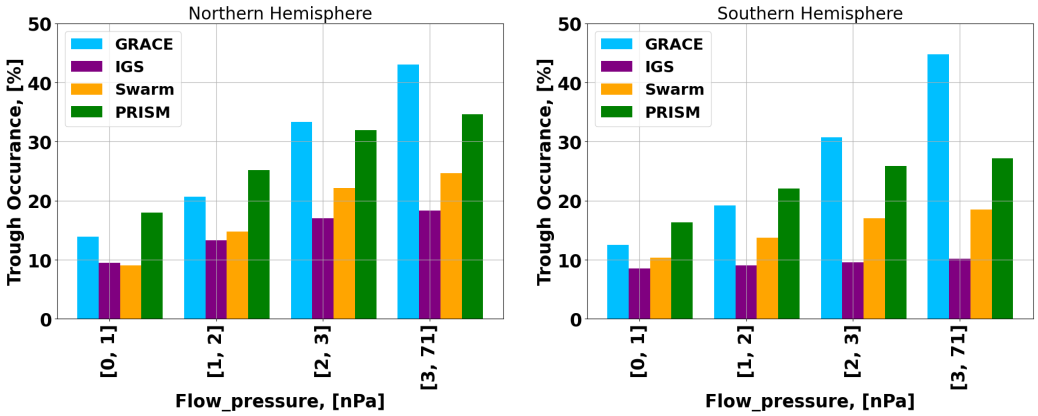

(A) (B)

FIGURE 6.21: Northern (A) and Southern (B) Hemisphere bar plots of the trough occurrence rate against flow pressure.

6.1.8.6 MIT occurrence dependence on IMF Bz

The results of the MIT occurrence dependence on the Bz component of the IMF are shown in Figure 6.22. In Figure 6.22, IMF Bz component values were binned into intervals containing equal numbers of measurements. Within each bin, the trough occurrence rate (%) was computed as 100× the ratio of detected troughs to the total number of available observations — satellite passes (Swarm, GRACE, PRISM) or TEC profiles (IGS TEC maps). Geomagnetic activity is controlled by the Bz component of the IMF. The dependence on the IMF Bz component shows that the trough occurred more frequently in both Hemispheres when the Bz component was negative, indicating periods of intense geomagnetic activity. This is also consistent with Figure 6.18, which shows the increasing dependence of the Hp30 index, as the probability of a high Hp30 index increases during the southward IMF.

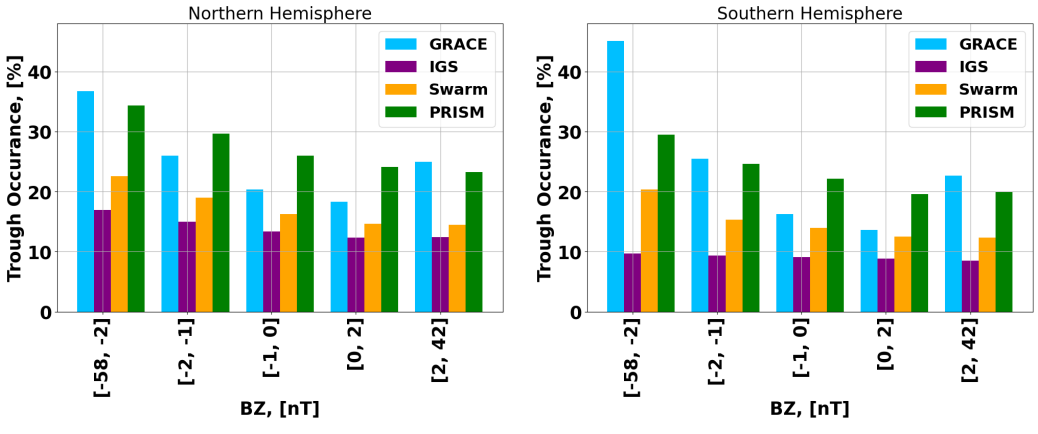

(A) (B)

FIGURE 6.22: Northern (A) and Southern (B) Hemisphere bar plots of the trough occurrence rate against IMF Bz component.

6.1.8.7 Main findings about MIT behaviour regarding Space weather indices

All main findings about trough location, width, depth and occurrence rate behaviour regarding space weather indices is summarised and presented in Table 6.3

SW Index/Trough	Tm location (MLAT)	Width (deg)	Depth (Ne or TEC)	MIT Occurrence (%)
F10.7 index ↑	shifts equatorward	Gets narrow	Gets deeper	decrease
SW plasma speed ↑	shifts equatorward	Gets narrow	Gets deeper	increase
Flow pressure ↑	shifts equatorward	Gets narrow	Gets deeper	increase
IMF BZ ↑	shifts poleward	Gets wider	Gets shallow	decrease
Hp30 index ↑	shifts equatorward	Gets narrow	Gets deeper	increase
SYM-H index ↓	shifts equatorward	Gets narrow	Gets deeper	increase

TABLE 6.3: Main findings about trough behaviour regarding Space weather indices

6.1.9 Trough Slopes

The mid-latitude ionospheric trough, known for its V-shaped appearance, exhibits sharp transitions in electron densities that vary in space and time. These abrupt shifts in electron densities within the trough area create variations in plasma characteristics, subsequently causing instability within the region.

Our analysis of the trough slopes, both the equatorward and poleward slopes, is contingent on the Kp and F10.7 indices. The calculation of the slopes is based on the trough half width and depth. Equation 6.1 was used to calculate the EW slope, and Equation 6.2 was used to calculate the PW slope.

$$\text{slope}_{EW} = \frac{\left(\frac{N_{e_bp}+N_{e_be}}{2} - N_{e_tm}\right)}{\text{latt}_{tm} - \text{latt}_{be}} \tag{6.1}$$

$$\text{slope}_{PW} = \frac{\left(\frac{N_{e_bp}+N_{e_be}}{2} - N_{e_tm}\right)}{\text{latt}_{bp} - \text{latt}_{tm}} \tag{6.2}$$

We have computed both equatorward (EW) and poleward (PW) slopes for Swarm (A, C), GRACE, and IGS TEC maps. Overall, the poleward slope is consistently sharper than the equatorward slope. Figures 6.23 - 6.26 show the dependence on the F10.7 index with the slopes. EW and PW slopes were binned into 20-SFU F10.7 index intervals (e.g., 80–100, 100–120, 120–140, etc). The mean slope was calculated for each bin separately for each data source: Swarm, GRACE, and IGS TEC. The data were analised for NH and SH separatly and divided into the calm period, where the Kp index was equal to or below 3 (see Figures 6.23, 6.25), and the storm period, where the Kp index was more than 3 (see Figures 6.24, 6.26). Both EW and PW slopes become linearly sharper as the F10.7 index increases. The F10.7 index and the trough slope are positively correlated across all datasets, suggesting that more solar activity causes MIT to have steeper slopes. Moreover, we can observe that the poleward slope is constantly steeper than the equatorward slope. Figures 6.24, 6.26 show that the trough slopes become even sharper during the increased geomagnetic activity period. However, the Southern Hemisphere's slopes show slightly more deviating results than the Northern Hemisphere.

Figures 6.27 and 6.28 show more detailed geomagnetic activity influence. Figures show the dependence of the EW and PW slopes on the Kp index for the Northern and Southern Hemispheres. For these figures, EW and PW slopes were grouped

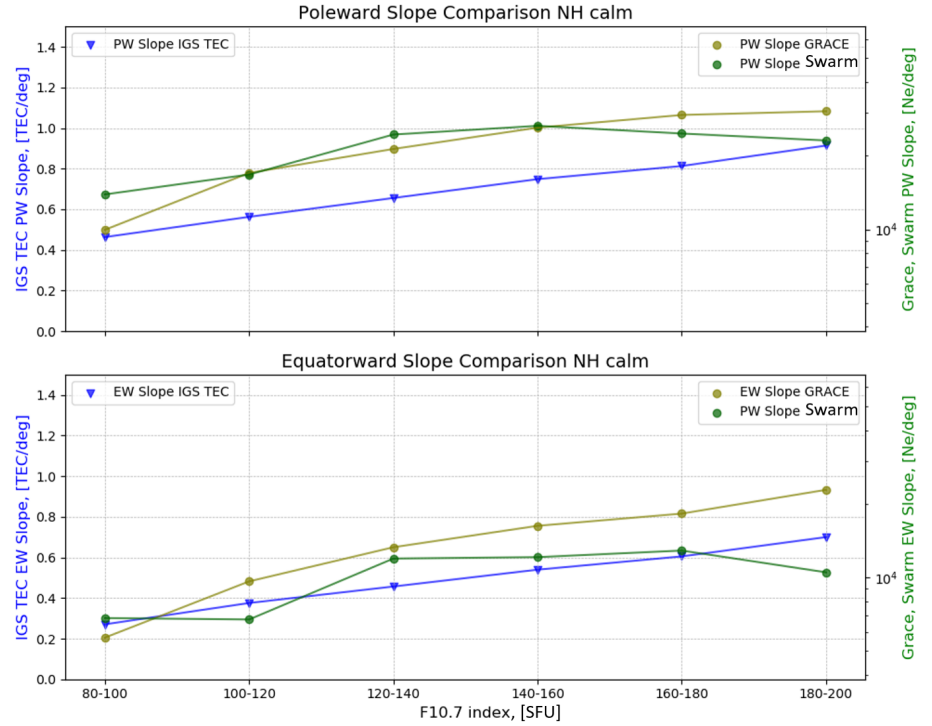

FIGURE 6.23: F10.7 index dependence of the trough poleward slope (top plot) and equatorward (bottom plot) for the calm period (Kp index$<$ 3) in Northern Hemisphere.

into Kp bins (0, 1, 2, etc.), for each bin separately the mean slope was calculated for each data source: Swarm, GRACE, and IGS TEC. Both slopes become exponentially sharper as the Kp index increases. However, the PW slope becomes significantly sharper during strong and extreme geomagnetic activity (8-9 Kp index). All three types of data show similar behavior. Different geomagnetic activity shows different slope behavior. A low Kp index (0-3) indicates that the PW slope remains the same and the EW slope changes slightly. As the Kp index becomes moderate (4-6), the PW slope still shows no significant change, while the EW slope gradually increases. With high geomagnetic activity (7-9), both EW and PW slopes show very steep and very high slope increases. So, as we can see, the ionospheric response may vary regionally, showing differences in behavior between Northern and Southern Hemispheres, especially during periods of high geomagnetic activity. It emphasizes again that trough is influenced by hemispheric asymmetry.

This study comprehensively examines the impact of geomagnetic storms on the mid-latitude ionospheric trough and the influence of increased solar activity on the steepness of the trough walls. The analysis reveals the mid-latitude trough's high sensitivity to geomagnetic conditions and solar activity. Each dataset, closely captured and analyzed, effectively demonstrates the complex dynamics of the slopes.

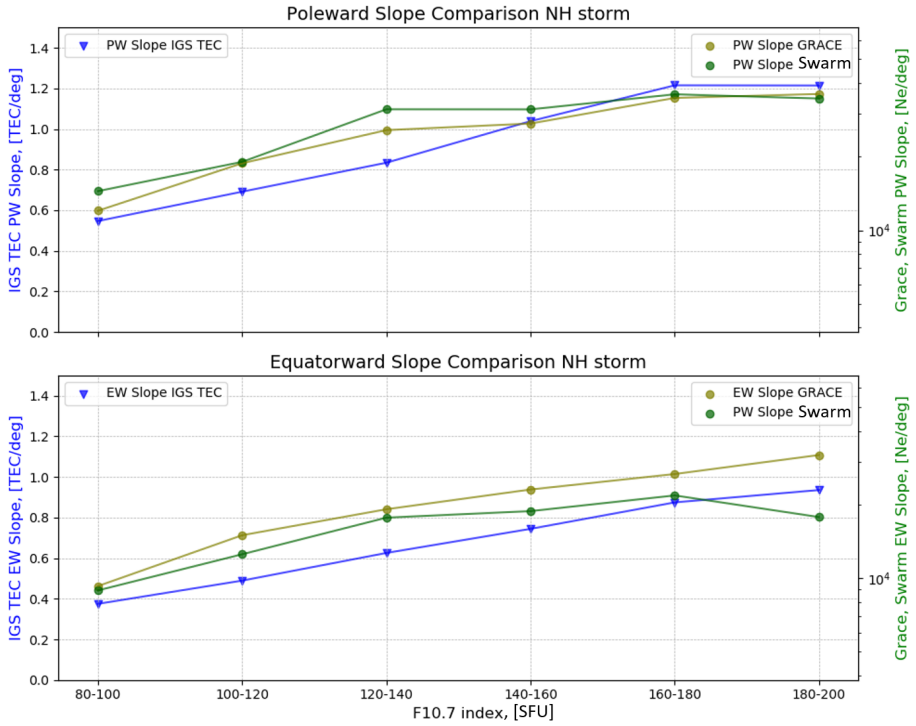

FIGURE 6.24: F10.7 index dependence of the trough poleward slope (top plot) and equatorward (bottom plot) for the storm period (Kp index $>$ 3) in Northern Hemisphere.

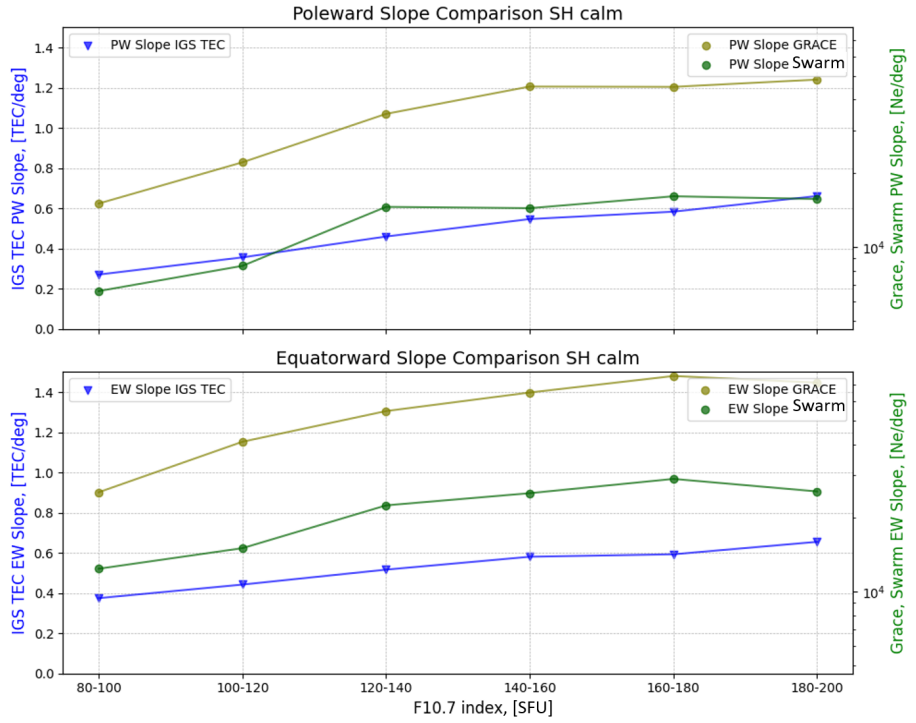

FIGURE 6.25: F10.7 index dependence of the trough poleward slope (top plot) and equatorward (bottom plot) for the calm period (Kp index $<$ 3) in Southern Hemisphere.

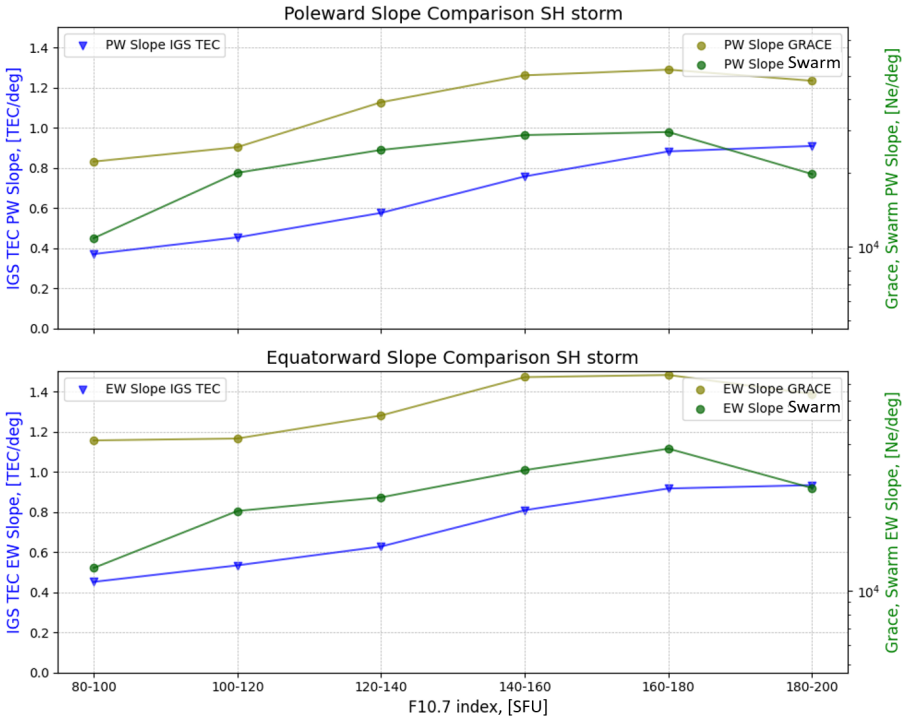

FIGURE 6.26: F10.7 index dependence of the trough poleward slope (top plot) and equatorward (bottom plot) for the storm period (Kp index > 3) in Southern Hemisphere.

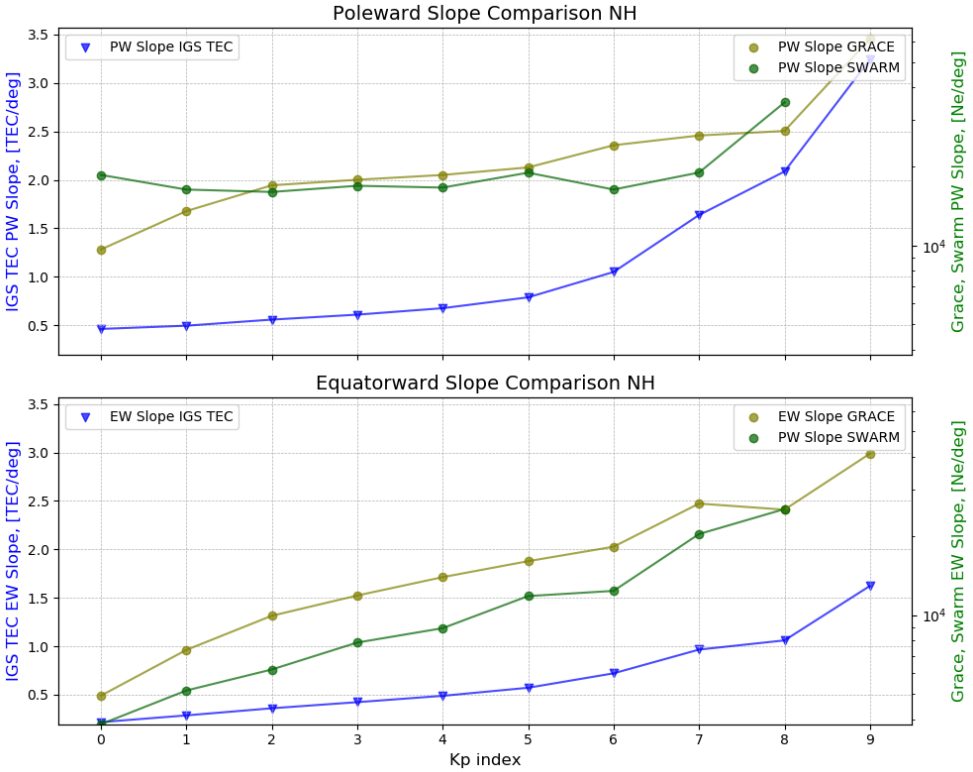

FIGURE 6.27: Kp index dependence of the trough poleward slope (top plot) and equatorward (bottom plot) in Northern Hemisphere.

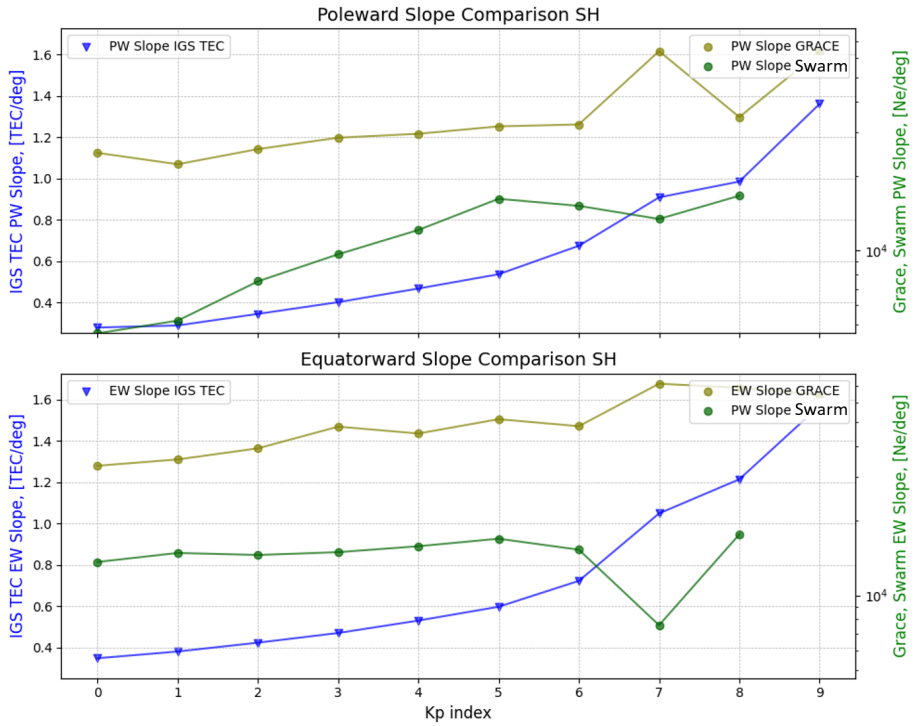

FIGURE 6.28: Kp index dependence of the trough poleward slope (top plot) and equatorward (bottom plot) in Southern Hemisphere.

Chapter 7

Modeling of the MIT

7.1 Reasoning of the model

The Earth's ionosphere has a major effect on the transmission of GNSS signals. GNSS L-band signals have a delay while traveling through the ionosphere.The primary sources of inaccuracy for satellite-based navigation and communication systems, such as GPS, are the dynamics and fluctuations of the ionospheric plasma. The changes in ionospheric density structures are caused mostly by space weather, highly affecting GPS applications. Up to 100 meters of location error can occur due to delays caused by the ionosphere. The positioning error d_I can be estimated by the following in first order (Eq. 7.1): it is proportional to the integral of the electron density along the ray path (TEC):

$$^{d_I} \approx \frac{K}{f^2} \int n_e ds = \frac{K}{f^2} TEC^{slant} \tag{7.1}$$

where the slant TEC (TEC^{slant}) is defined by the integral of the electron density n_e along the ray path s and $K = 40.3\ m^3 s^{-2}$.

The calibration of the TEC measurements is necessary due to instrumental signal delays at receivers and satellites. In dual-frequency measurements, errors due to ionosphere can be corrected by combining the L1 and L2 phases linearly. In order to reduce the ionospheric error in single-frequency measurements, ionospheric information is required. Model values or TEC maps inferred from comparable GNSS observations can supply this information. Because of this, single-frequency systems—like those used in remote sensing radars and positioning—depend on ionospheric models, which offer a climatological estimate of the ionospheric influence. There are currently multiple ionospheric models available for predicting the ionosphere and thereby reducing errors. Examples of models include IRI, NeQuick, NTCM, etc. (see Chapter 3). However, precisely determining the location and characteristics of the anomalies of the ionosphere is crucial for the accuracy of ionospheric models. The mid-latitude ionospheric trough is one of the phenomenon of the F-layer ionosphere that influences radio wave transmission. Because of the large electron density gradients on the equatorward and poleward sides of the mid-latitude trough radio wave propagation can be affected. The mid-latitude ionospheric trough presents difficulties for empirical modeling of the ionosphere. MIT is required to be correctly represented in ionospheric models. Scientific research on modeling the mid-latitude trough is still ongoing. Due to the complex dynamics of the ionospheric trough and the uneven coverage of available observations, it is challenging to develop precise models of this region. Despite these obstacles, it is essential to enhance the models that represent the ionosphere irregularities. Improved models with a more realistic representation of the trough can reduce the

effect of GNSS signals in middle latitudes. Predicting trough dynamics will become increasingly useful for different GNSS-dependent applications as studies progress. The depth of the trough was examined to gain insight into the overall effect of the trough on the GPS L1 range error. For this analysis, the troughs detected on the IGS TEC maps over a period from 2002 to 2015 were used. The effect of 1 TECU on GPS accuracy is determined by its correspondence to a pseudorange delay of 16.2 cm in the GPS L1 frequency band, which was calculated using Formula 7.1:

$$\text{delay_GPS} = \frac{40.3 \times 10^{16}}{(1575.42 \times 10^{6})^2} = \frac{40.3 \times 10^{16}}{2.480 \times 10^{15}} = 0.1624 \text{ meters} = 16.24 \text{ cm} \quad (7.2)$$

The single-user frequency of Galileo is similar to GPS L1 and is E1 = 1575.42 MHz. So, the delay for Galileo will be the same value as for GPS users. Unlike GPS and Galileo, which employ Code Division Multiple Access (CDMA), GLONASS uses a Frequency Division Multiple Access (FDMA) system. This indicates that each satellite uses an individual frequency for transmission. The main frequencies for civilian use (similar to GPS L1 and Galileo E1) are 1598.0625 – 1605.375 MHz. The mean frequency will be around 1602 MHz. The delay for GLONASS will be the following:

$$\text{delay_GLONASS} = \frac{40.3 \times 10^{16}}{(1602 \times 10^{6})^2} = \frac{40.3 \times 10^{16}}{2.5632 \times 10^{15}} = 0.1572 \text{ meters} = 15.72 \text{ cm} \quad (7.3)$$

Assuming that one vertical TEC unit (VTEC) can reach up to 3 slant TEC units (STEC) at low elevation, the minimum, maximum, and average impact on GPS measurement accuracy can be calculated.

TABLE 7.1: GPS/Galileo/GLONASS L1 range error

	Minimum	Maximum	Mean
VTEC	0.2 TEC	51.1 TEC	2.2 ± 1.27 TEC
STEC	0.6 TEC	154.5 TEC	6.6 ± 3.81 TEC
GPS/Galileo L1 range error	0.1 meters	25.09 meters	1.07 ± 0.62 meters
GLONASS mean range error	0.09 meters	24.29 meters	1.04 ± 0.6 meters

The results are shown in Table 7.1. The minimum GPS /Galileo L1 error that can cause the trough is 0.1 meters, and the maximum is about 25 meters. And for GLONASS, the mean minimum frequency error that can cause the trough is 0.09 meters, and the maximum is about 24.29 meters. This high error can occur during enormous geomagnetic activity, as, for example, such a high depth occurred during the so-called enormous Halloween solar storms. The trough on 29th October 2003 at 20:45 and 21:45 UT with very high depth values is presented in Figure 7.1. On 29th October 2003 at 21:00 UT, the Kp index was 9, and the Dst index = -268 nT, causing a large response in TEC values.

This result emphasises the need for continued study and development of accurate ionospheric models of the trough and its inclusion in global ionospheric models. Ongoing research in this area will improve the accuracy and reliability of GNSS, enabling a wide range of useful applications.

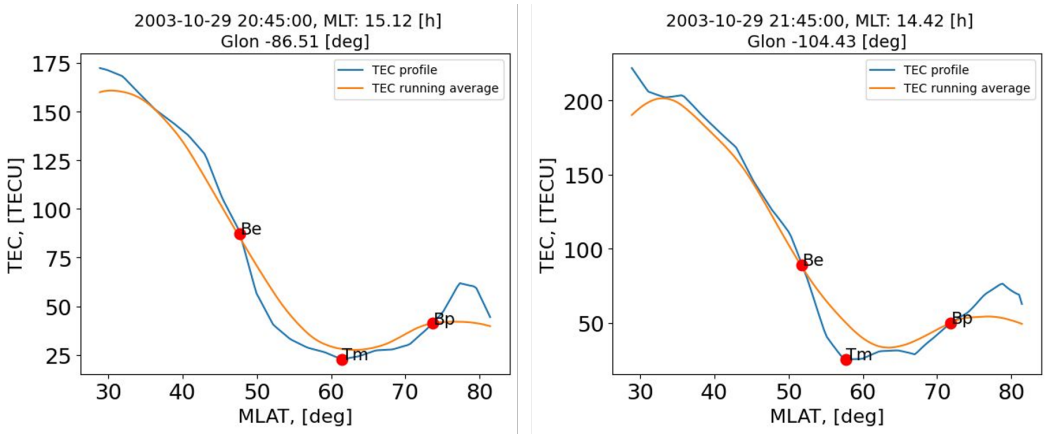

FIGURE 7.1: An example of the high values of the trough depth in the Northern Hemisphere in the American sector during the Halloween solar storm on the 29th of October 2003, where Dst was -268 nT at 21 UT. The blue line represents the TEC profile, and the orange line is the running average. The red dots represent the detected Tm position and the breakpoints Be and Bp.

7.2 Empirical modeling of MIT parameters

7.2.1 Modeling Approach

For the development of the empirical model of the MIT parameters, the trough parameters were derived from the IGS high-resolution vTEC global maps - UQRG in a period of 1998-2023 ("CDDIS | | archive | gnss | products |", n.d.). It was considered to take IGS TEC trough database for modeling since it has the longest time period and is well suited for being implemented for integration in the NTCM model, which is also IGS TEC based. The database for modeling the MIT parameters consists of about 20 million profiles with MIT signatures, which include parameters such as trough minimum, trough width, and trough depth. The IGS TEC data for modeling were taken with a time resolution of 1 hour. The developed MIT (parameters) models are mean/median models representing the climatology of the MIT characteristics. Therefore, the model formulas are trained, and coefficients are derived based on conventional Dst and Kp indices. Our dependency analysis shows that both the Dst and Kp indices have a high correlation with MIT parameters. It is worth mentioning that although the model coefficients are obtained based on Dst and Kp indices, the models can be run/operated with the new high-resolution equivalent indices, such as SYM-H and Hp30, respectively. For this reason, we have also chosen to use model-driven parameters with lower time resolutions, such as the Kp and Dst indices, instead of the high-resolution Hp30 and SYM-H indices. The purpose of taking both the Kp and Dst index for trough modeling is to provide complementary insights into geomagnetic conditions. Using only the Dst index is an insufficient predictor identifier of high-speed-stream-driven storms and of other types of geospace storms (Borovsky & Shprits, 2017). Using both the Kp and Dst indices enables a comprehensive representation of trough dynamics across different geomagnetic activities, thereby improving the accuracy in predicting trough behavior under varying conditions.

The concept of modeling the MIT parameters is based on the NTCM (Neustrelitz

TEC Model) modeling approach (Hoque & Jakowski, 2012; Hoque & Jakowski, 2011; Jakowski et al., 2011). The empirical modeling is based on the nonlinear least squares technique. The model was implemented using the Matlab function *nlinfit* ("nlinfit", n.d.). This function estimates the parameters of nonlinear regression models by minimizing the sum of squared residuals between observed and model-predicted values. It employs iterative algorithms (typically the Levenberg-Marquardt method) to find the best-fit solution, providing parameter estimates along with their associated uncertainties. Using this approach, nonlinear equations with polynomial coefficients were derived to describe the location, width, and depth of the trough minimum separately for the Northern and Southern Hemispheres. The functions representing the MIT parameters depend on the F10.7 index, the Dst index, the Kp index, the day of the year (DOY), and the local time. The correlation of the relevant trough parameters with the space weather indices, as well as the spatial and temporal distribution correlation for both the Northern and Southern Hemisphere, can be seen in Figure 7.2. The local time variation of the trough minimum position model is described by diurnal, semi-diurnal, and ter-diurnal variations. The database contains a variety of data combinations, including high, medium, and low solar and geomagnetic activity conditions, as well as day and night, summer, winter, and equinox periods. Additionally, it encompasses all longitudinal globe distributions and the geomagnetic latitude sector between 40 and 70 degrees. The F10.7 variation, Kp and Dst variations, seasonal variation (i.e., DOY variation), local time variation, and geomagnetic latitude and longitude variations were the criteria used to sort the database.

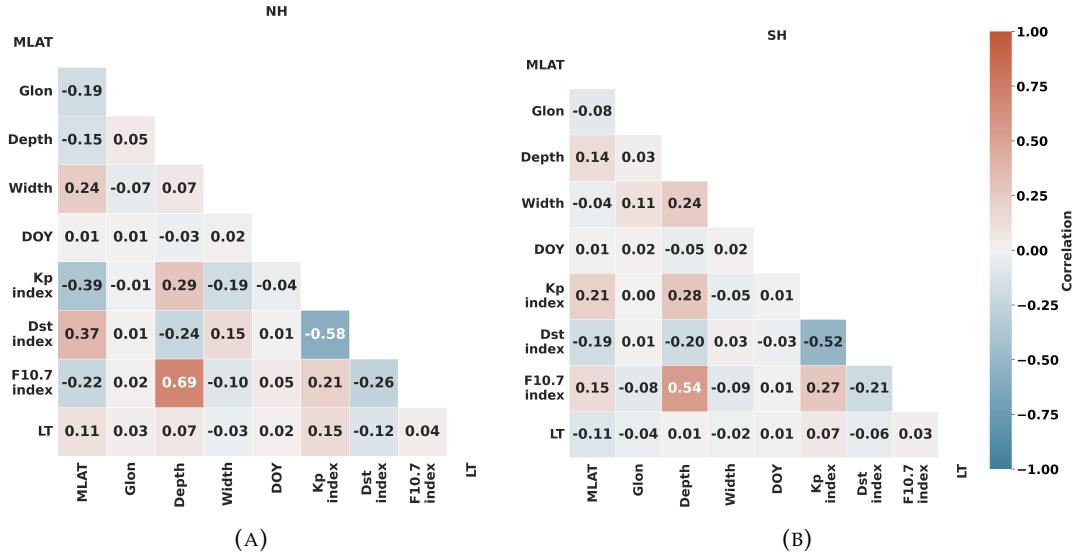

(A) (B)

FIGURE 7.2: Correlation of MIT parameters - such as trough minimum position, width, depth - with space weather parameters for both (A) Northern and (B) Southern Hemispheres. Positive correlations are shown in red and negative correlations are shown in blue.

The dependence of trough minimum location is described by a set of nonlinear equations:

$$\mathrm{MLAT}_{\mathrm{tm}} = F_1 F_2 F_3 F_4 F_5, \tag{7.4}$$

where the factors F_{1-5} explicitly contain the model functions, including model coefficients that describe five main dependencies of trough location. The factor F1

describes the daily variation with local time (LT in hours) as:

$$F_1 = c_1 + c_2 * cos(V_D) + c_3 * cos(V_{SD}) + c_4 * cos(V_{TD}), \tag{7.5}$$

where V_D, V_{SD}, and V_{TD} are the angular phases of the diurnal, semi-diurnal, and terdiurnal harmonic components, respectively. The individual phases (e.g., 14, 14.3, and 23.8) are derived by fitting the F1 formulation to the averaged MIT location variation with LT considering the whole datasets. V_D, V_{SD} and V_{TD} are represented as following:

$$V_D = 2\pi\frac{\text{LT} - 14}{24}, \quad V_{SD} = 2\pi\frac{\text{LT} - 14.3}{12}, \quad V_{TD} = 2\pi\frac{\text{LT} - 23.8}{8}. \tag{7.6}$$

The factor F_2 describes the annual (A) and the semi-annual (SA) variation of trough minimum as given by:

$$F_2 = 1 + c_5 * cos(V_A) + c_6 * cos(V_{SA}), \tag{7.7}$$

where

$$V_A = 2\pi\frac{\text{DOY} - 350.42}{365.25}, \quad V_{SA} = 4\pi\frac{\text{DOY} - 352.14}{365.25}. \tag{7.8}$$

The individual phases (e.g., 350.42 and 352.14) in the equation V_A and V_{SA} are derived by fitting F2 formulation to the averaged MIT location variation with DOY considering the whole datasets.

The factor F_3 describes the solar activity dependence as following :

$$F_3 = 1 + c_7 * exp(-\frac{\text{F10.7}}{10}). \tag{7.9}$$

The slope (e.g., 10 or 200) in F3 or F5 are derived by fitting F3 or F5 formulation to the averaged MIT location variation with F10.7 or Dst considering the whole datasets.

The factor F_4 describes the geomagnetic activity dependence using the Kp index as follows:

$$F_4 = 1 + c_8 * \text{Kp}. \tag{7.10}$$

The factor F_5 describes the geomagnetic activity dependence using Dst index as following

$$F_5 = 1 + c_9 * exp(\frac{\text{Dst}}{200}). \tag{7.11}$$

As described above, the basic modeling approach includes five major dependencies of Tm on the local time, day of the year or season, solar flux index F10.7, disturbance ionosphere index Dst and geomagnetic activity index Kp. Now, the basic model approach has been applied to observation data sets for determining the 9 model coefficients using nonlinear least square squares methods. The coefficients and data are related through the nonlinear system of Equations 7.4 - 7.11. Our goal is to find the values of the coefficients that best fit the data, in the sense of minimizing the sum of squares of the residual errors. In this way, we have obtained a set of 9 model coefficients. In Figure 7.3, the prefit of the Tm variations with local time, day of the year, F10.7, Dst, and Kp indices are plotted from the original input datasets and the model results. These subplots in Figure 7.3 represent individual fitting of parameters (DOY, LT, F10.7, Dst, and Kp) to the average trough-location data, which was used for determining the phases and functional dependencies of the factors F_1–F_5 in the model formulation.

SubFigure 7.3a shows the annual and semi-annual Tm variations, with equatorward trough positions in summer and poleward in winter. SubFigure 7.3b illustrates the strong equatorward shift of Tm during geomagnetic storms. SubFigure 7.3c indicate small poleward shift of Tm with decrease of F10.7 index. SubFigure 7.3d shows linear equatorward shift with increasing Kp index. SubFigure 7.3e indicate diurnal variation of Tm with the Tm most equatorward in the midnight. With a similar approach, the MIT width and depth were modeled for both Hemispheres. The following sub-chapters present the formulas of the modeled MIT location, width and depth together with their corresponding coefficients.

7.2.1.1 MIT location in Northern and Southern Hemispheres

Figure 7.2 shows several important parameters for modeling the position of the MIT in the Northern and Southern Hemispheres.

NH There is a moderate negative correlation (-0.39) between the MLAT in NH and the Kp index, indicating that higher geomagnetic activity (represented by the Kp index) tends to lower the latitude of the MIT. The positive correlation is found with the Dst index (0.37) in NH, indicating that a lower latitude of the MIT is associated with stronger geomagnetic storms. A weak negative correlation (-0.22) is found with the F10.7 index in NH, which also represents a relatively small influence on changing the position of the MIT to lower latitudes. The position of the MIT is also influenced by a positive correlation (0.11) with local time in NH, which leads to a shift of the trough position towards the higher geomagnetic latitudes as local time increases.

SH In most cases, the correlation values of the parameters for modeling in the Southern Hemisphere are lower than in the Northern Hemisphere. Geomagnetic latitude and the Kp index have a weak positive correlation (0.21), indicating that the latitude of MIT tends to decrease with decreasing geomagnetic activity. The Dst index shows an inverse negative correlation (-0.19), indicating that larger geomagnetic storms are associated with a lower latitude of MIT. The F10.7 index shows a weak positive correlation (0.15), which also indicates a rather small influence on moving MIT to higher latitudes. A negative correlation (-0.11) between the local time and the position of MIT results in a shift of the trough position to lower latitudes as the local time increases.

Equation The location of the trough minimum in the Northern and Southern Hemispheres is described in Equation 7.12. Table 7.2 shows the 9 coefficients that determine the MIT MLAT of the trough for NH and SH. Figure 7.4 shows how well the model describes the observed variations in MIT latitude with respect to various parameters, including DOY variation, Dst index, F10.7 index, Kp index, and local time variations, respectively. Subfigures 7.4a and 7.4b show the final full trough-location model fit (red dashed line) and trough-averaged data (blue line) the annual and semi-annual variations for NH and SH, with equatorward trough positions in summer and poleward in winter. Subfigures 7.4c and 7.4d illustrate the strong equatorward shift of Tm during geomagnetic storms in NH and poleward shift in SH. Subfigures 7.4e and 7.4f indicate poleward shift in NH and eqatorward shift in SH of Tm with decrease of F10.7 index. Subfigures 7.4g and 7.4h show a nearly linear equatorward in NH and poleward in SH and shift with increasing Kp index. Subfigures 7.4i and 7.4j indicate diurnal variation of Tm

with the Tm most equatorward around midnight in NH and poleward in SH. In all subplots the averaged data and model fit align very well, the apparent deviations in Subfigures 7.4i and 7.4j are due to the small y-axis range, with absolute differences not exceeding about 1,2 degree MLAT.

$$\begin{aligned} MLAT_tm = (c_1 + c_2 * cos(2\pi \frac{\mathrm{LT} - 14}{24}) + c_3 * cos(2\pi \frac{\mathrm{LT} - 14.3}{12}) + c_4 * cos(2\pi \frac{\mathrm{LT} - 23.8}{8})) \\ * (1 + c_5 * cos(2\pi \frac{\mathrm{DOY} - 350.42}{365.25}) + c_6 * cos(4\pi \frac{\mathrm{DOY} - 352.14}{365.25})) \\ * (1 + c_7 * exp(-\frac{\mathrm{F10.7}}{10}))(1 + c_8 * \mathrm{Kp})(1 + c_9 * exp(\frac{\mathrm{Dst}}{200})) \end{aligned} \tag{7.12}$$

TABLE 7.2: Optimal set of model coefficients of MIT location in the Northern and Southern Hemispheres

Model Coefficients	Northern Hemisphere	Southern Hemisphere
c_1	53.5156	-55.8609
c_2	2.9371	-1.8996
c_3	0.2362	-0.1024
c_4	0.1433	-0.1305
c_5	0.0007	-0.0010
c_6	-0.0060	-0.0047
c_7	10.2496	9.8599
c_8	-0.0121	-0.0064
c_9	0.1890	0.0986

7.2.1.2 MIT depth in Northern and Southern Hemispheres

Many important features for simulating the depth of the trough in the Northern and Southern Hemispheres are shown in Figure 7.2.

NH There is a moderate positive correlation (0.29) between the depth of the trough and the Kp index in NH. This indicates that higher geomagnetic activity (represented by the Kp index) tends to be associated with deeper troughs. A moderate negative correlation (-0.24) between the Dst index and depth in NH also suggests that more intense geomagnetic storms are associated with deeper troughs. There is a strong positive correlation (0.69) between the F10.7 index and depth in NH. This indicates that higher solar radio flux at 10.7 cm, which is indicative of solar activity, is associated with deeper troughs.

SH A moderately positive correlation (0.28) was found between the Kp index and the depth of the trough in SH. This suggests that deeper troughs are typically associated with stronger geomagnetic activity. The Dst index and depth have a negative correlation (-0.2) in SH, indicating that shallower troughs are associated with stronger geomagnetic storms. The F10.7 index and depth have a high positive correlation (0.54) in SH. This suggests that deeper troughs are associated with stronger solar activity.

Equation Equation 7.13 defines the depth of the trough minimum in the Northern and Southern Hemispheres. Table 7.3 lists the 6 coefficients that determine the depth of the trough. The ability of the model to explain the observed variations in the MIT depth with respect to various factors, including variations in the Dst index, such as DOY, the F10.7 index, and the Kp index, is shown in Figure 7.5. Subfigures 7.5a and 7.5b show the final full trough depth model fit (red dashed line) and trough depth averaged data (blue line) the annual and semi-annual variations for NH and SH, with trough depth larger in summer and smaller in winter in NH, in SH it is opposite. Subfigures 7.5c and 7.5d illustrate that the trough becomes deeper during geomagnetic storms in NH and SH. Subfigures 7.5e and 7.5f indicate nearly linear increase of trough depth with increasing F10.7 index in NH and SH. Subfigures 7.5g and 7.5h show a nearly linear increase of trough depth in NH and SH. In all subplots the averaged data and model fit align very well, the apparent deviations in SubFigure 7.5b are due to the small y-axis range, with absolute differences not exceeding about 0,8 TECU.

$$MIT_depth = (c_1 + c_2 * cos(2\pi\frac{\text{DOY} - 320.2}{365.25}) + c_3 * cos(4\pi\frac{\text{DOY} - 9.3}{365.25})) * (1 + c_4 * exp(-\frac{\text{F10.7}}{200})) * (1 + c_5 * exp(\frac{\text{Kp}}{3})) * (1 + c_6 * \exp\left(\frac{|\text{Dst}|}{200}\right)) \tag{7.13}$$

TABLE 7.3: Optimal set of model coefficients of MIT depth in the Northern and Southern Hemispheres

Model Coefficients	Northern Hemisphere	Southern Hemisphere
c_1	3.6237	4.6321
c_2	-0.5528	0.8043
c_3	-0.3318	-0.9412
c_4	-1.1195	-1.1432
c_5	0.0709	0.0571
c_6	0.5446	0.2810

7.2.1.3 MIT width in Northern and Southern Hemispheres

Figure 7.2 illustrates some key features for modeling the width of the trough in the Northern Hemisphere.

NH Trough width has a positive correlation (0.15) with the Dst index, indicating that stronger geomagnetic storms result in wider troughs. There is also a weak negative correlation (-0.19) between the Kp index and width. This suggests that higher geomagnetic activity is associated with narrower troughs, although the effect is stronger compared to the Dst index. There is a weak positive correlation (0.15) between the F10.7 index and width. This suggests that higher solar activity is associated with wider troughs.

SH The Dst index and trough width have a positive but weak correlation (0.03), suggesting that geomagnetic storms influence troughs to become narrow. There is also a weak negative correlation (-0.05) between width and the Kp index. The F10.7 index and width have a negative correlation (-0.09). This suggests that wider troughs are associated with a decrease in solar activity in the Southern Hemisphere.

Equation The width of the trough in the Northern and Southern Hemispheres is modeled by Equation 7.14. The 4 coefficients that are used in the trough width equation are given in Table 7.4. Figure 7.6 illustrates the ability of the model to capture the observed variations in MIT width as a function of several factors, such as the Dst index, the F10.7 index, and the Kp index. Subfigures 7.6a and 7.6b show the final full trough width model fit (red dashed line) and trough-averaged data (blue line) Dst index variations for NH and SH, with width becoming narrower during geomagnetic storms in NH and SH. Subfigures 7.6c and 7.6d indicate that the trough becomes wider with decreasing F10.7 index. Subfigures 7.6e and 7.6f show a nearly linear narrowing of the trough width with increasing Kp index in NH and SH. In all subplots the averaged data and model fit align very well, the apparent deviations in some Subfigures are due to the small y-axis range, with absolute differences not exceeding about 1 degree MLAT.

$$MIT_width = (c_1 + c_2 * exp(-\frac{\text{F10.7}}{200})) * (1 + c_3 * exp(-\frac{\text{Kp}}{3})) * (1 + c_4 * exp(\frac{\text{Dst}}{200})) \quad (7.14)$$

TABLE 7.4: Optimal set of model coefficients of MIT width in the Northern and Southern Hemispheres

Model Coefficients	Northern Hemisphere	Southern Hemisphere
c_1	8.5374	9.9797
c_2	1.3063	2.2077
c_3	0.1702	0.0314
c_4	0.1132	0.0056

7.2.2 Modeling Results

After calculating the model residuals - i.e., the deviations between the model values and the input data - the corresponding histograms for the Northern and Southern Hemispheres are shown in Figure 7.7. These histograms shows the residuals for three modeled parameters: trough location, trough depth, and trough width for NH and SH. The important statistical measures for the histograms, such as mean deviation, standard deviation (std), and root mean square (RMS) values of the model residuals, are shown in the corresponding histograms in Figure 7.7.

Subfigures 7.7a and 7.7b present the residuals for trough location in NH and SH. Both are centered around 0, with RMS values of 2.54° and 3.27°, respectively, indicating slightly higher scatter in SH. Subfigures 7.7c and 7.7d show the residuals for trough depth, with means close to 0 TECU and RMS values of 0.81 TECU and 1.06 TECU, respectively, confirming very good agreement between model and data. Subfigures 7.7e and 7.7f illustrate the residuals for trough width, with RMS values of 2.44° in NH and 2.72° in SH, again centered at zero but with slightly broader distributions compared to depth.

For all histograms, the distribution of the residuals is centered around 0, indicating that there is no consistent bias in the model in either direction. The standard deviation of the residuals is consistent with the standard deviation. In most cases, the residuals appear to follow a normal distribution, as indicated by the roughly symmetric bell-shaped curve centered around zero. This indicates that the model fits the data well without significant bias.

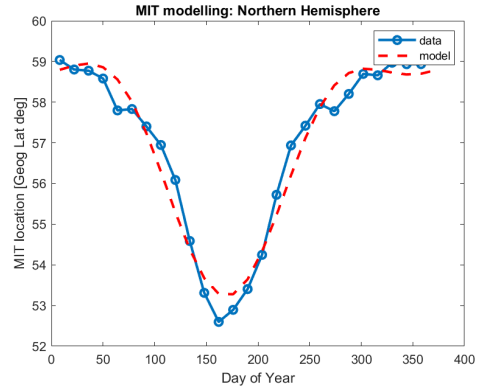

(A)

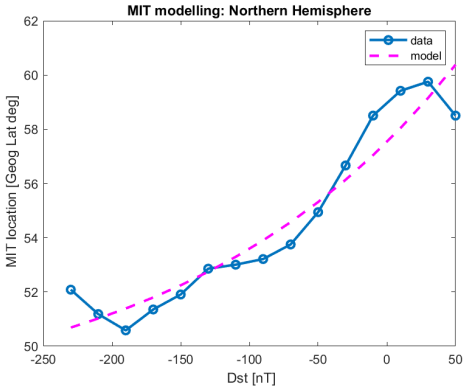

(B)

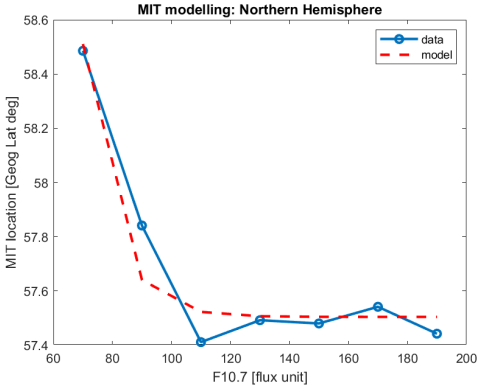

(C)

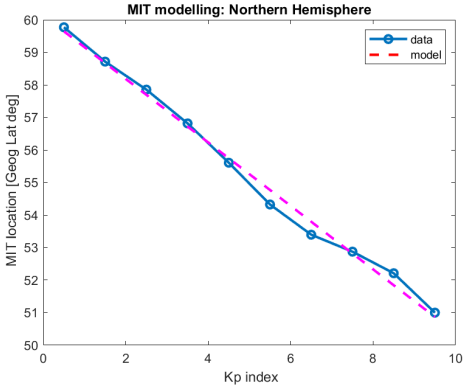

(D)

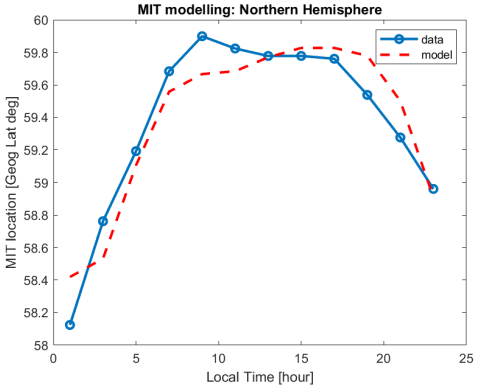

(E)

FIGURE 7.3: Trough-location model prefit, represented by the red dashed curve, and trough-averaged data, represented by the blue curve, as a function of (A) day of the year, (B) Dst index, (C) F10.7 index, (D) Kp index and (E) local time.

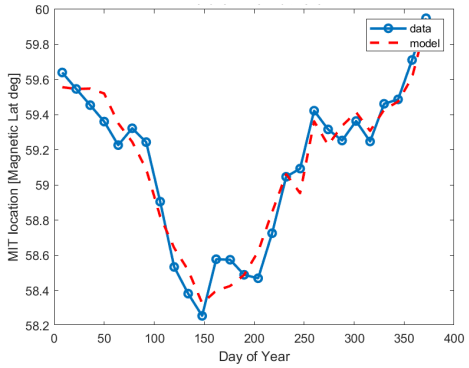

(A) Northern Hemisphere: DOY

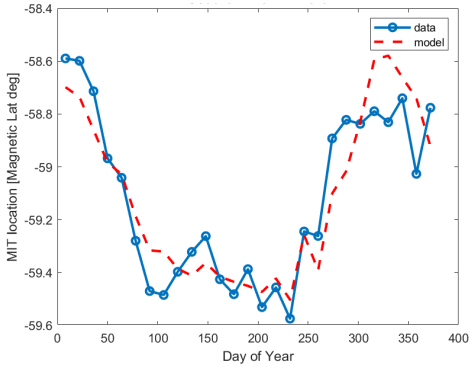

(B) Southern Hemisphere: DOY

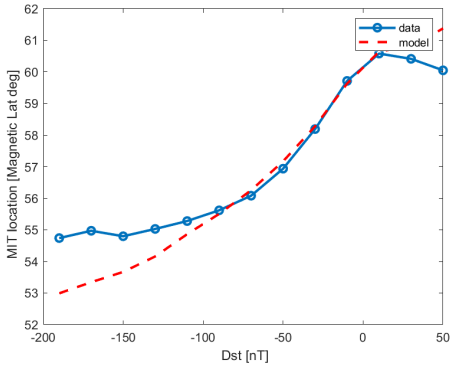

(C) Northern Hemisphere: Dst

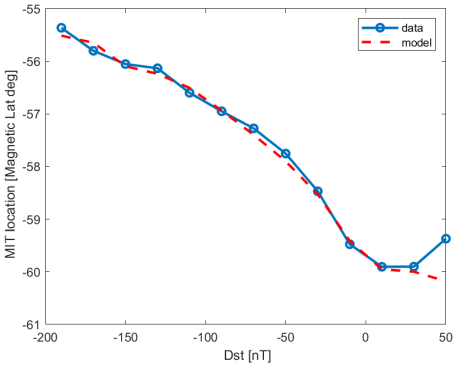

(D) Southern Hemisphere: Dst

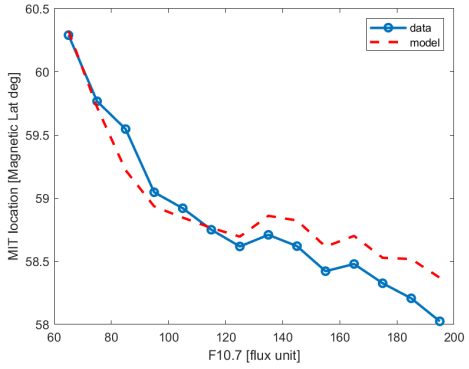

(E) Northern Hemisphere: F10.7

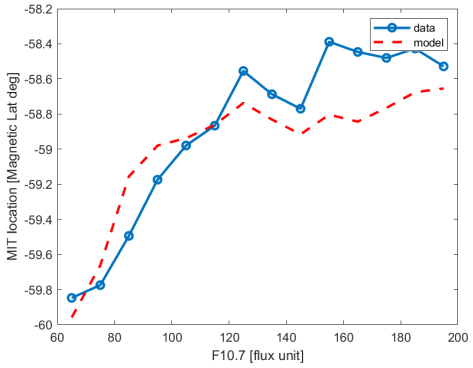

(F) Southern Hemisphere: F10.7

FIGURE 7.4: Trough-location model fit (see continuation on the next page).

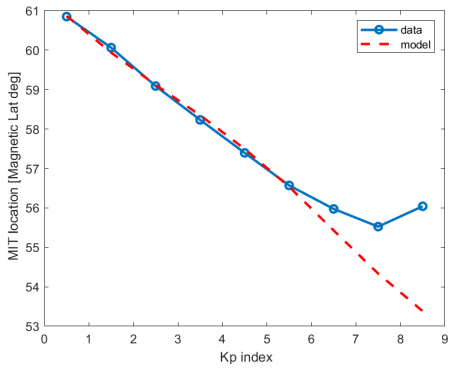

(G) Northern Hemisphere: Kp

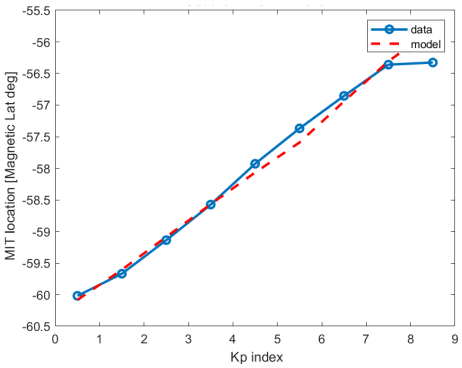

(H) Southern Hemisphere: Kp

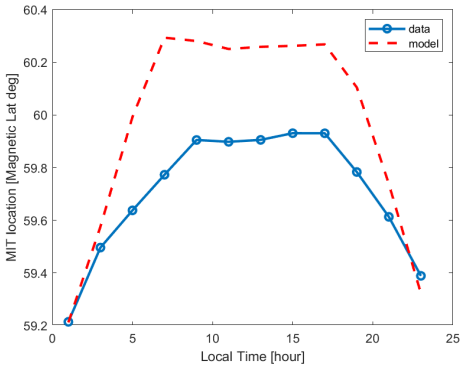

(I) Northern Hemisphere: LT

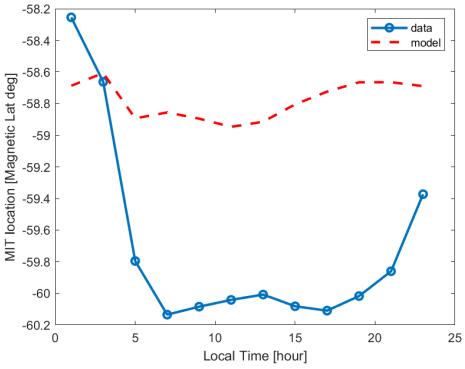

(J) Southern Hemisphere: LT

FIGURE 7.4: Final full trough-location model fit (red dashed curves) with the coefficients given in Table 7.2 and trough-averaged data (blue line) as a function of (from top to bottom): (A, B) day of the year, (C, D) Dst index, (E, F) F10.7 index, (G, H) Kp index, and (I, J) local time. Each row compares the Northern Hemisphere (left) and Southern Hemisphere (right).

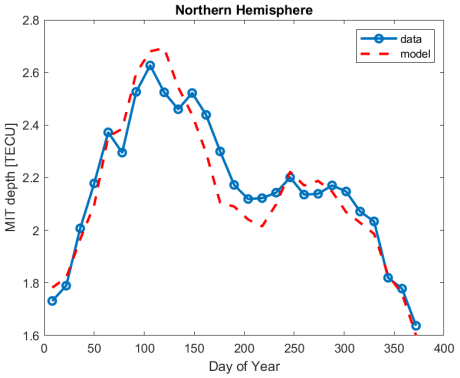

(A) Northern Hemisphere: Day of the Year

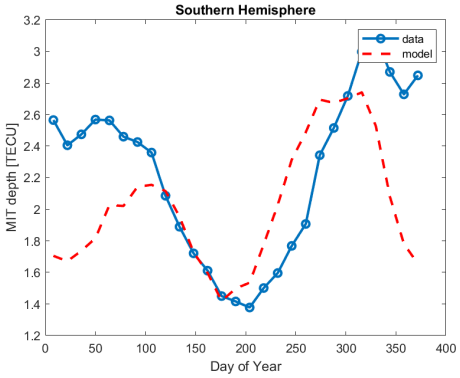

(B) Southern Hemisphere: Day of the Year

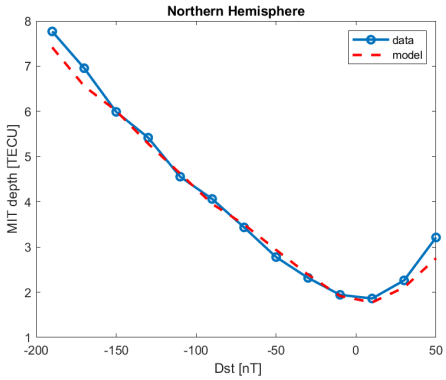

(C) Northern Hemisphere: Dst index

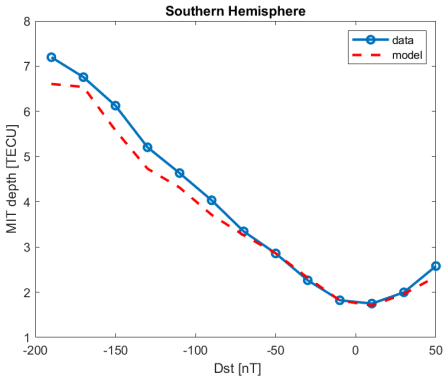

(D) Southern Hemisphere: Dst index

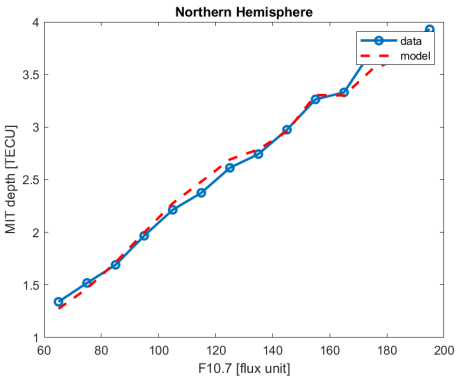

(E) Northern Hemisphere: F10.7 index

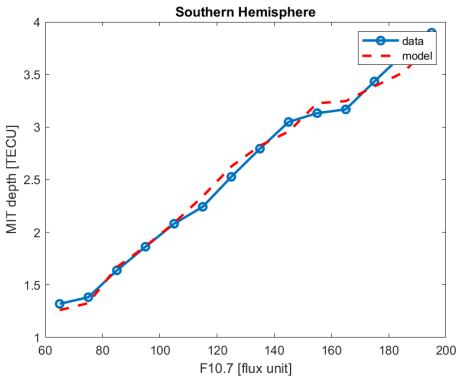

(F) Southern Hemisphere: F10.7 index

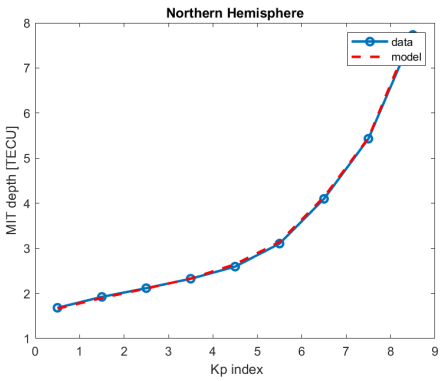

(G) Northern Hemisphere: Kp index

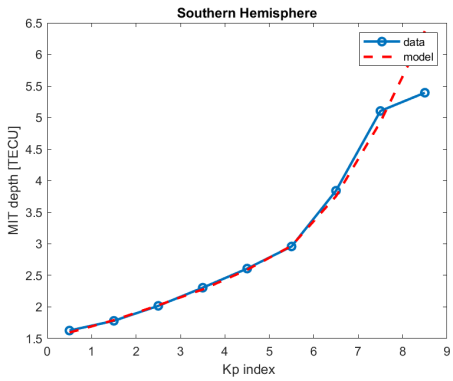

(H) Southern Hemisphere: Kp index

FIGURE 7.5: Final full trough depth model fit (red dashed curves) with the coefficients given in Table 7.3 and trough-averaged data (blue curves) for Northern (left column) and Southern Hemispheres (right column) as functions of (A, B) day of the year, (C, D) Dst index, (E, F) F10.7 index, and (G, H) Kp index.

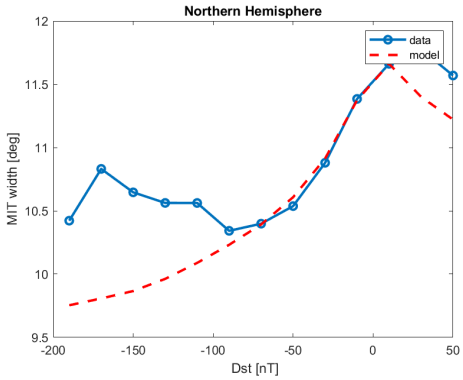

(A) North Hemisphere: Dst index

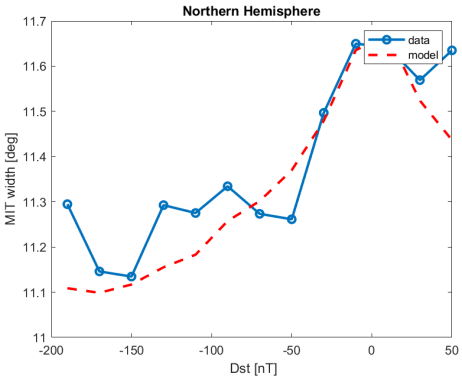

(B) South Hemisphere: Dst index

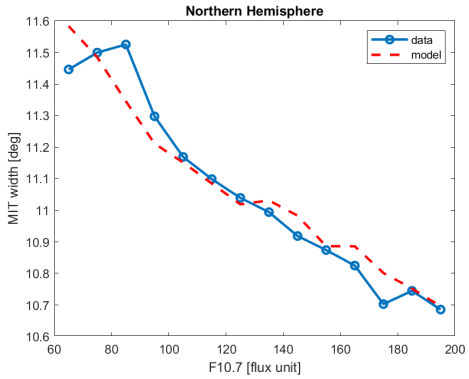

(C) North Hemisphere: F10.7 index

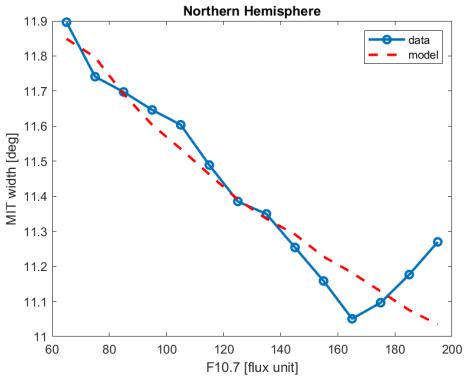

(D) South Hemisphere: F10.7 index

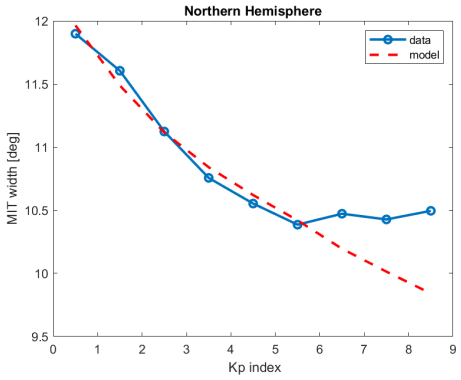

(E) North Hemisphere: Kp index

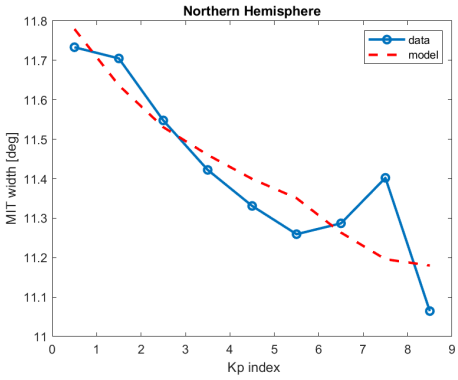

(F) South Hemisphere: Kp index

FIGURE 7.6: Final full trough width model fit (red dashed curves) with the coefficients given in Table 7.4 and trough-averaged data (blue curves) for Northern (left column) and Southern Hemispheres (right column) as functions of (A, B) Dst index, (C, D) F10.7 index, and (E, F) Kp index.

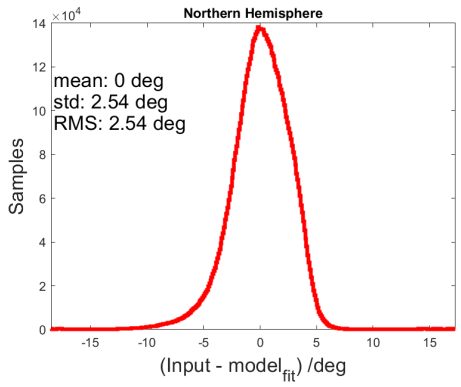

(A) Northern Hemisphere: Trough location

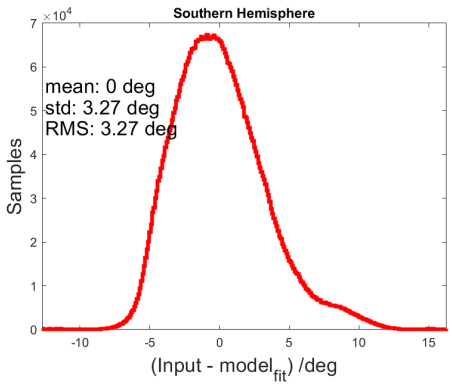

(B) Southern Hemisphere: Trough location

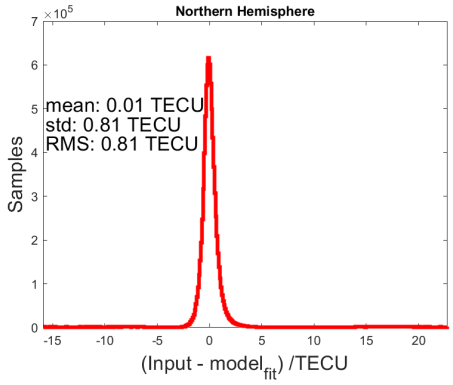

(C) Northern Hemisphere: Trough depth

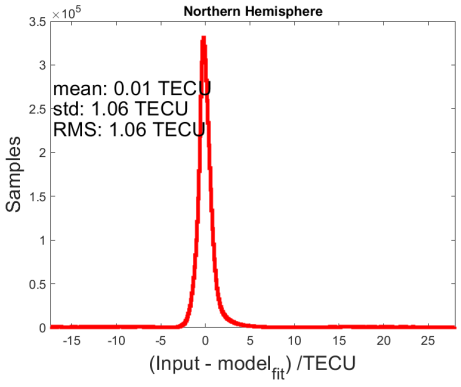

(D) Southern Hemisphere: Trough depth

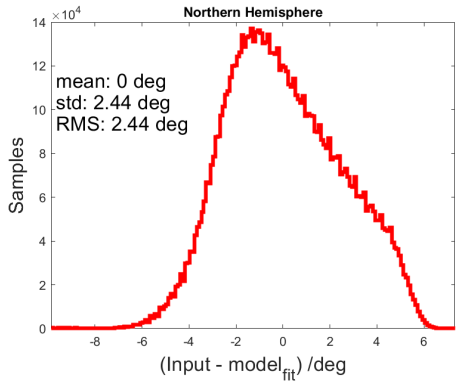

(E) Northern Hemisphere: Trough width

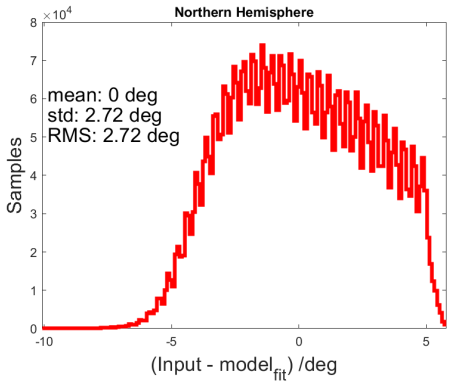

(F) Southern Hemisphere: Trough width

FIGURE 7.7: Histograms of Trough Model residuals (input data minus model values) for the Northern Hemisphere (left column) and Southern Hemisphere (right column), showing (A, B) trough location, (C, D) trough depth, and (E, F) trough width.

Chapter 8

Analysis of MIT during Geomagnetic storms

In this section, a superposed epoch analysis of the position of the mid-latitude trough during various geomagnetic storms is performed. Two data sets periods are examined in this chapter. First, the GRACE and IGS data from the period 2002–2015 are analysed, also the results are compared with trough parameters delivered from our developed MIT model which was introduced in the previous Chapter 7. Second, data from Swarm, PRISM, and IGS covering the period 2013–2019 are used and also compared with the results from our developed MIT model. Finally, a case study is performed using the extreme geomagnetic storm of the last decade, the Mother's Day event. During this event, troughs detected from IGS TEC maps were compared with the troughs derived from our model, as represented in Chapter 7.

8.1 Data and methodology

The storm events are taken from the geomagnetic storms catalog containing storms with Dst index ≤ -50 nT in period from 1996 till 2019 (Miteva & Samwel, 2023). The catalog also provides the origin of the storms. Figure 8.1 displays the storms distribution and associated minimum Dst index for every event. It is evident that most severe storms occur close to the solar maximum, and it also accounts for more storms in general in this period.

In total, it accounted for 356 storms from 2002 to 2019. Each storm was set to 0 epoch in its minimum "peak" of the Dst value. Twenty-four hours before and after each storm have been taken into account. For each analysis group, such as GRACE, IGS data group or Swarm, PRISM, and IGS data group, only data from the same orbital passes were used. This means that the time stamp and longitude should overlap. The data was then grouped into two longitude sectors: Europe ($20°\text{W} <$ longitude $< 60°\text{E}$), which also contain African land part, but for simplicity it will be named just Europe sector and the American sectors ($130°\text{W} <$ longitude $< 30°\text{W}$). The data are also grouped into three local time bins: dusk hours (18 - 21 MLT), night hours (22 - 2 MLT), and dawn hours (3 - 7 MLT). This separation of local time bins was done to eliminate the local time effect of the trough position. The corresponding data were grouped into 2-hour bins, and the mean, median, and standard deviation of each bin were calculated.

The purpose of this investigation is to see a global long-term trend in the ionospheric trough characteristics during the main phase of a geomagnetic storm.

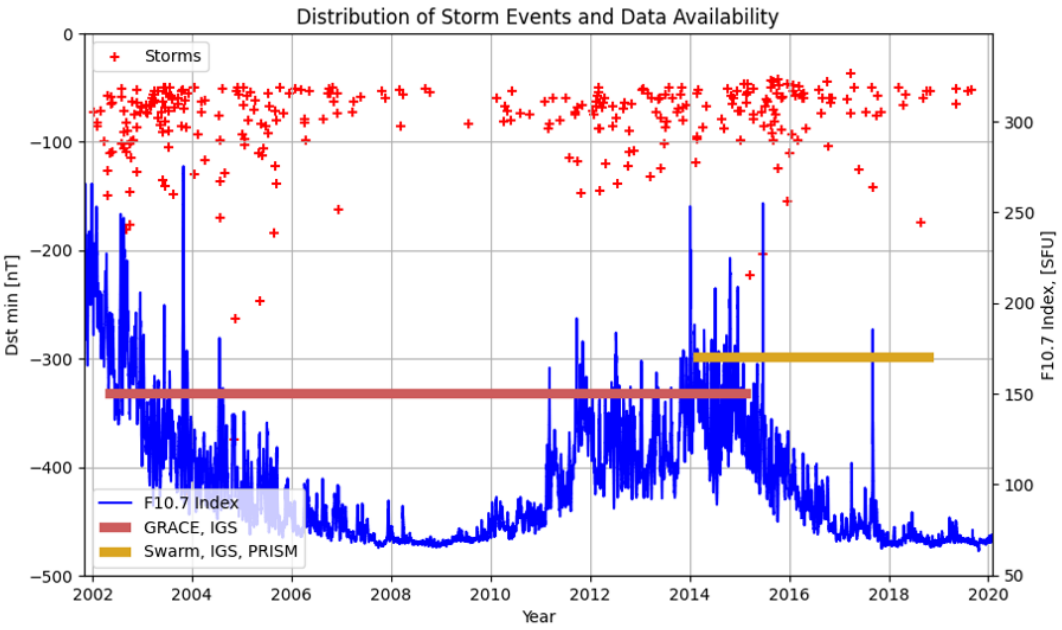

FIGURE 8.1: The distribution of the storms that have been used in this research as well as the data groups that have been used are marked.

8.2 MIT during Geomagnetic storms using GRACE and IGS data 2002-2015

For the first analysis, the period from April 2002 to March 2015 was chosen. Figures 8.2, 8.3, 8.4 show the mean and median trough position for GRACE, IGS TEC map observations and model values during storms in the dawn, dusk and night magnetic local time sectors for the European and American sectors separately in the Northern Hemisphere. A red dashed line indicates the storm minimum, set at 0 epoch hour. The two lower plots represent the Dst index and the Econv mean reconstruction. The Dst index represents the typical signature of geomagnetic storms. Econv represents the energy input to the magnetosphere and ionosphere.

In general, the mean and median trough positions show a clear equatorward movement during the storm main phase, followed by a gradual recovery, consistent with the storm dynamics.

Table 8.1 shows the comparison of trough minimum position and width for the European and American sectors during different MLT sectors. These values are also plotted in the Figure 8.5. It can be seen that in both sectors the data from different observations show a similar trend. The trough is located more equatorward during the dawn hours, then slightly moving poleward during the night, reaching its higher poleward value in the dusk sector. It can also be seen that the same storms in different longitude sectors have different mean trends.

In the European sector, the model deviates from the mean trough position by about 2-3 degrees MLAT in all local time sectors (see Table 8.1). In the American sector, the trough detected from the IGS TEC data and the trough derived from the model are mostly in agreement, deviating only in the dawn sector by 2 degrees

MLAT. In Table 8.1, the width is in the range of 9 - 11 degrees of the trough detected from the IGS TEC data and the trough derived from the model. GRACE shows width in the range of 7 to 9 degrees. In the American longitude sector the width is more consistent with the IGS TEC data. In general, the model performs better in the American longitude sector during the storm period.

The results obtained from the Southern Hemisphere are shown in the appendix (see Figures B.1, B.2, B.3). In general, the results obtained from IGS TEC data in the Southern Hemisphere are not so good, as the IGS TEC maps are very smoothed due to the very sparse GNSS coverage there.

NH		**Europe sector**			**American sector**		
Data source	**Parameter**	**dawn**	**night**	**dusk**	**dawn**	**night**	**dusk**
GRACE	TM	50.9	51.4	54.9	49.9	50.9	57.2
	width	9.4	8.2	7.2	7.3	8.9	8
IGS TEC	TM	50.5	53.3	56.6	52.8	55.2	57.1
	width	9.5	9.0	10.1	9.93	9.9	9.6
Model	TM	54.3	55.4	58.2	55.2	55	57.5
	width	10.2	10.3	10.5	10.5	10.3	10.3

TABLE 8.1: NH Comparison of trough minimum position and width for Europe and American sectors, during different MLT sectors using GRACE and IGS TEC data

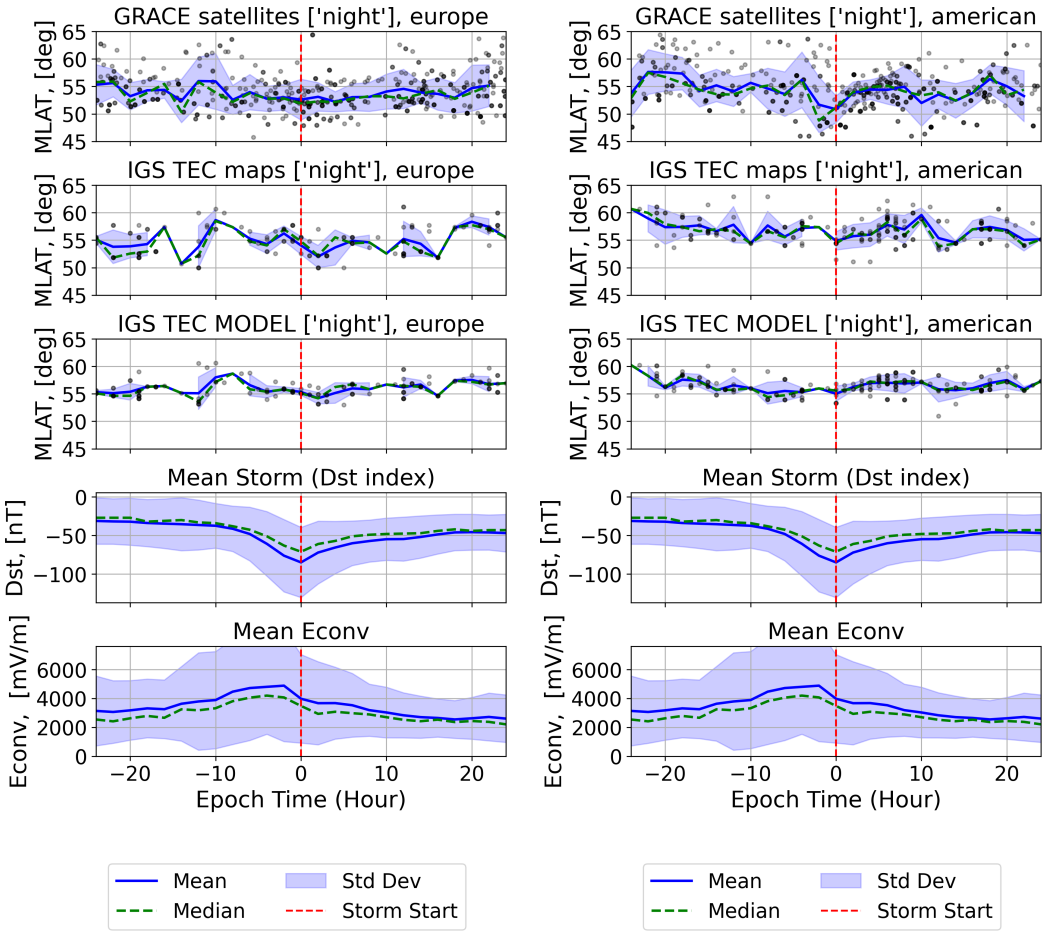

(A) European sector

(B) American sector

FIGURE 8.2: Mean and median trough position during storms in the night magnetic local time sector (22 - 2 MLT) for the European (left column) and American (right column) sectors separately in the Northern Hemisphere for GRACE, IGS TEC map observations and model values. The storm minimum is marked with a red dashed line and set to 0 epoch hour.

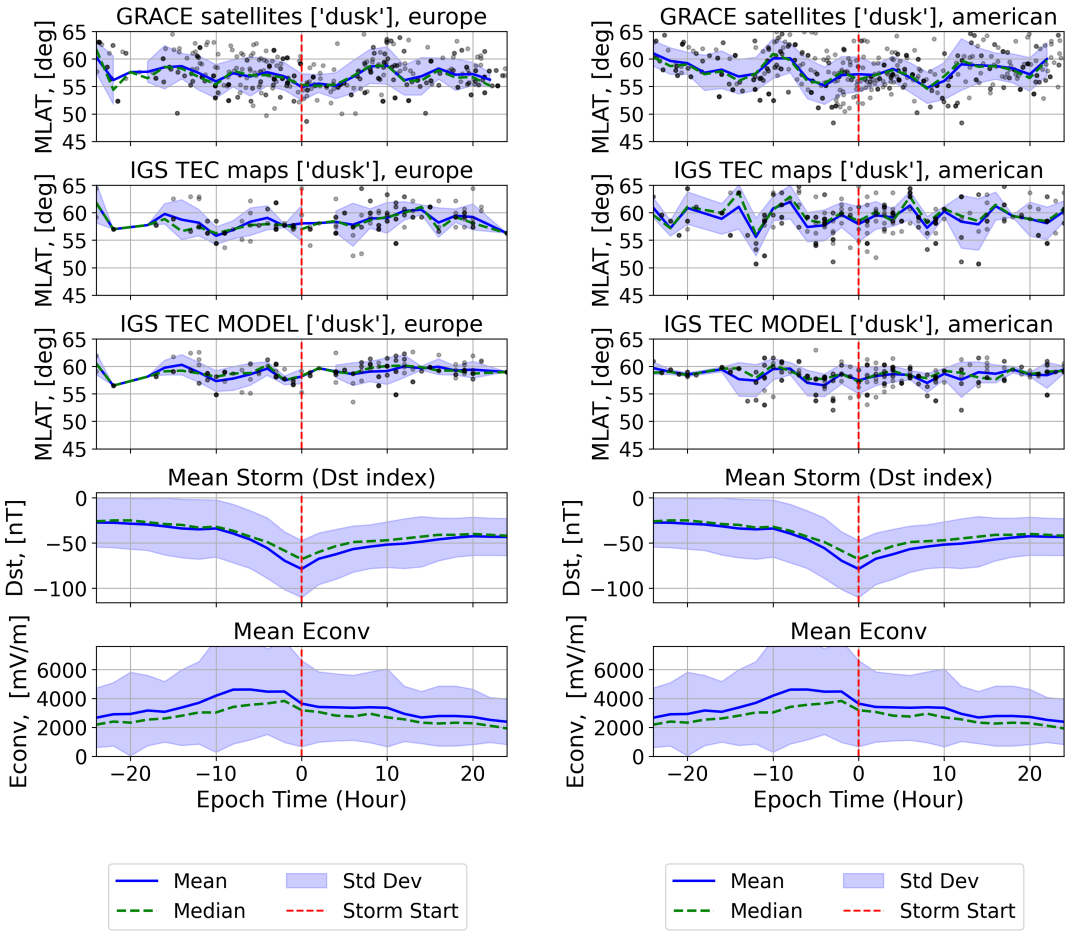

(A) European sector

(B) American sector

FIGURE 8.3: Mean and median trough position during storms in the dusk magnetic local time sector (18 - 21 MLT) for the European (left column) and American (right column) sectors separately in the Northern Hemisphere for GRACE, IGS TEC map observations and model values. The storm minimum is marked with a red dashed line and set to 0 epoch hour.

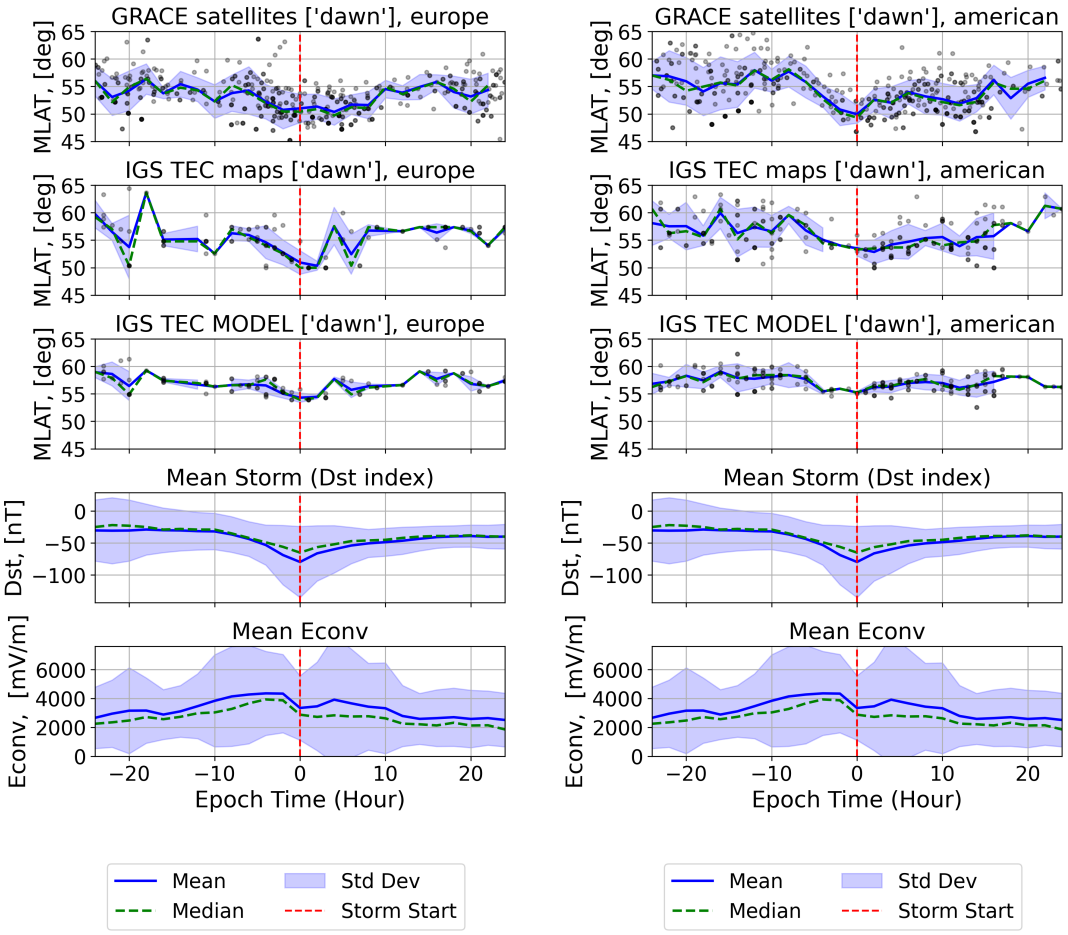

(A) European sector

(B) American sector

FIGURE 8.4: Mean and median trough position during storms in the dawn magnetic local time sector (3 - 7 MLT) for the European (left column) and American (right column) sectors separately in the Northern Hemisphere for GRACE, IGS TEC map observations and model values. The storm minimum is marked with a red dashed line and set to 0 epoch hour.

8.3 MIT during Geomagnetic storms 2013-2019 using Swarm, PRISM, IGS data

For the second analysis of the geomagnetic storms and MIT, the period from December 2013 to January 2019 was chosen. Figures 8.7, 8.8, 8.9 show the mean and median trough position for Swarm, PRISM, IGS TEC map observations and model values during storms in the dawn, dusk and night magnetic local time sectors for the European and American sectors separately in the Northern Hemisphere. A red dashed line indicates the storm minimum, set at 0 epoch hour. The two lower plots represent the Dst index and the Econv mean reconstruction. In general, the mean and median trough positions show a very clear equatorward movement during the storm main phase, followed by a gradual recovery, consistent with storm dynamics and in agreement with the results presented in the previous section.

Table 8.2 shows the comparison of trough minimum position and width for the European and American sectors during different MLT sectors. These values are

also plotted in the Figure 8.6. It can be seen that in both sectors the data from different observations show a similar trend. The trough is located more poleward during the dusk hours, then more equatorward during the night, reaching its higher equatorward value in the dawn sector. It can also be seen that the same storms in different longitude sectors have different mean trends.

In the European sector, the largest deviation between the model and IGS TEC trough minimum positions occurs in the night sector, where the model shows the trough overestimated by about 4 degrees MLAT more poleward. In contrast, in the American sector, the trough detected from the IGS TEC data and the trough derived from the model are more consistent, with a maximum deviation of 2 degrees MLAT in the dawn sector. The width is in the range of about 9 to 11 degrees of the trough detected from the IGS TEC data and around 10 degrees width of the trough derived from the model. Swarm and PRISM show width in range of 4 to 9 degrees. In the American sector we can see a very clear width trend where the trough is narrow at dusk local time sector and then widens at night and reaches its maximum at dawn. In the European sector we can still see this trend with the width of the trough detected by Swarm and PRISM, but not as pronounced. Overall, in terms of trough width and trough position, the model aligns more closely with the IGS TEC observations in the American sector.

The results obtained from the Southern Hemisphere are located in the appendix (see Figures B.4, B.5, B.6). As was already mentioned before, due to the very low GNSS coverage in the Southern Hemisphere, the IGS TEC maps are extremely smoothed, which generally results in poorer IGS TEC data outputs.

NH		**Europe sector**			**American sector**		
Data source	**Parameter**	**dawn**	**night**	**dusk**	**dawn**	**night**	**dusk**
Swarm	TM	52.6	50.2	56	50	51	56.7
	width	7.2	7.2	6.1	7.9	6.7	5.2
PRISM Swarm	TM	52.2	50.5	55.4	49	53	54.6
	width	6	4.8	4.2	9.3	6.3	5
IGS TEC	TM	52.7	51.1	59.4	53.4	54.4	57.5
	width	9.3	10	10.1	11.2	9.6	10.1
Model	TM	55	55.5	58	56	54.3	56.7
	width	10.4	10.5	10.6	10.7	10.3	10.4

TABLE 8.2: NH Comparison of trough minimum position and width for Europe and American sectors, during different MLT sectors using Swarm, PRISM, IGS TEC and model data.

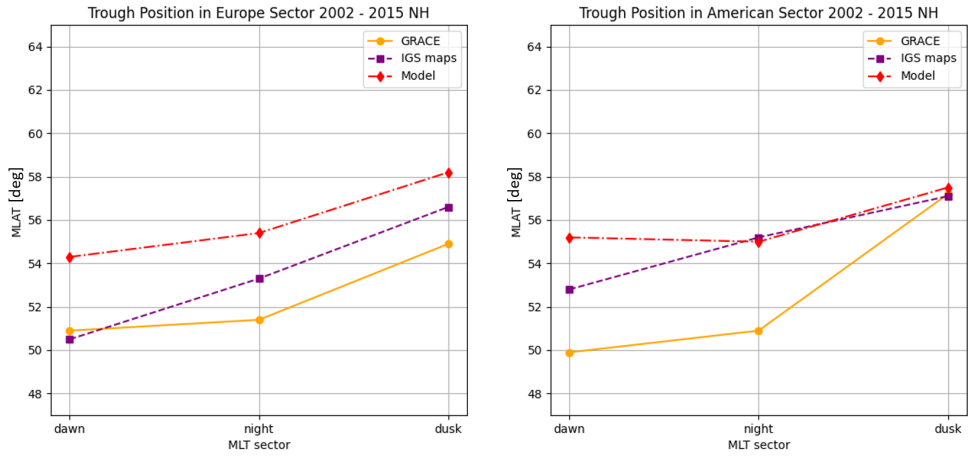

(A) Trough location



(B) Width

FIGURE 8.5: The trough minimum location (A) and trough width (B) mean plotted for different MLT sectors and for Europe and American sector separately using GRACE, IGS TEC maps and Model data.

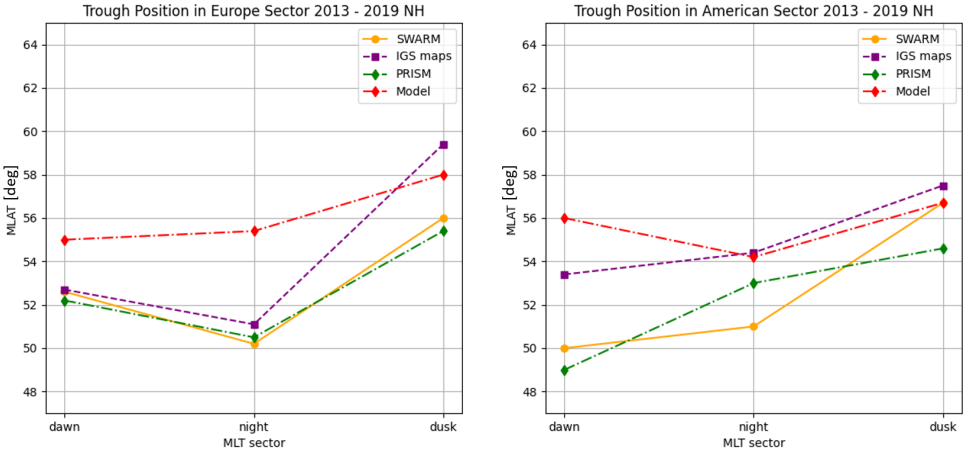

(A) Trough location

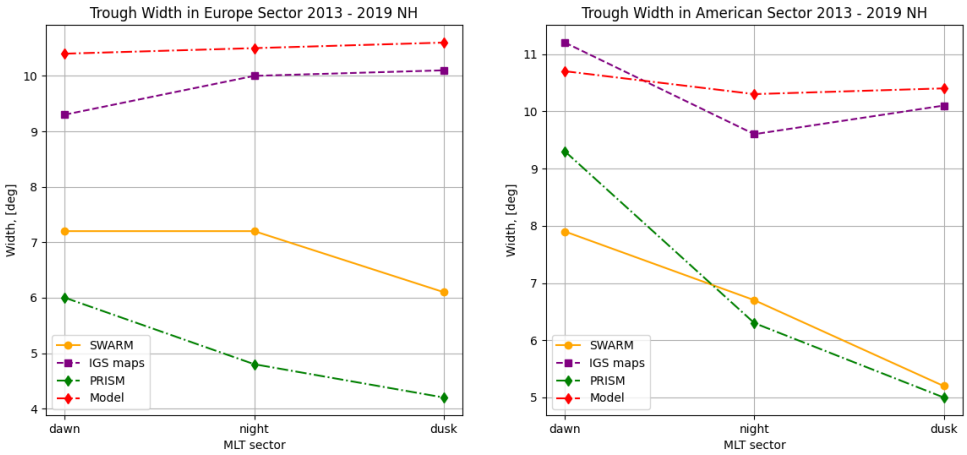

(B) Width

FIGURE 8.6: The trough minimum location (A) and trough width (B) mean plotted for different MLT sectors and for Europe and American sector separately using Swarm, IGS TEC maps, PRISM and Model data.

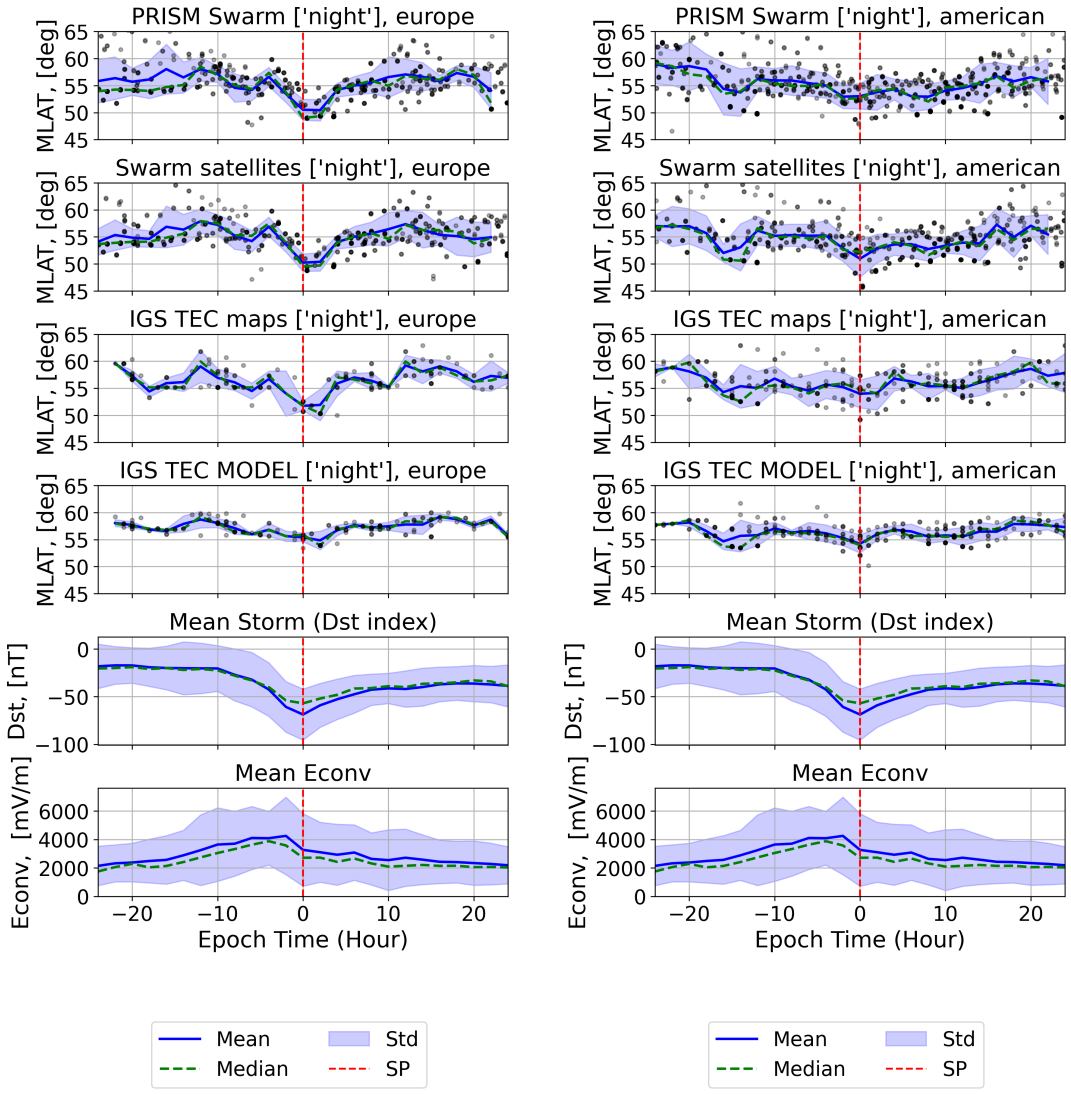

(A) European sector (B) American sector

FIGURE 8.7: Mean and median trough position during storms in the night magnetic local time sector (22 - 2 MLT) for the European (left column) and American (right column) sectors separately in the Northern Hemisphere for PRISM, Swarm, IGS TEC map observations and model values. The storm minimum is marked with a red dashed line and set to 0 epoch hour.

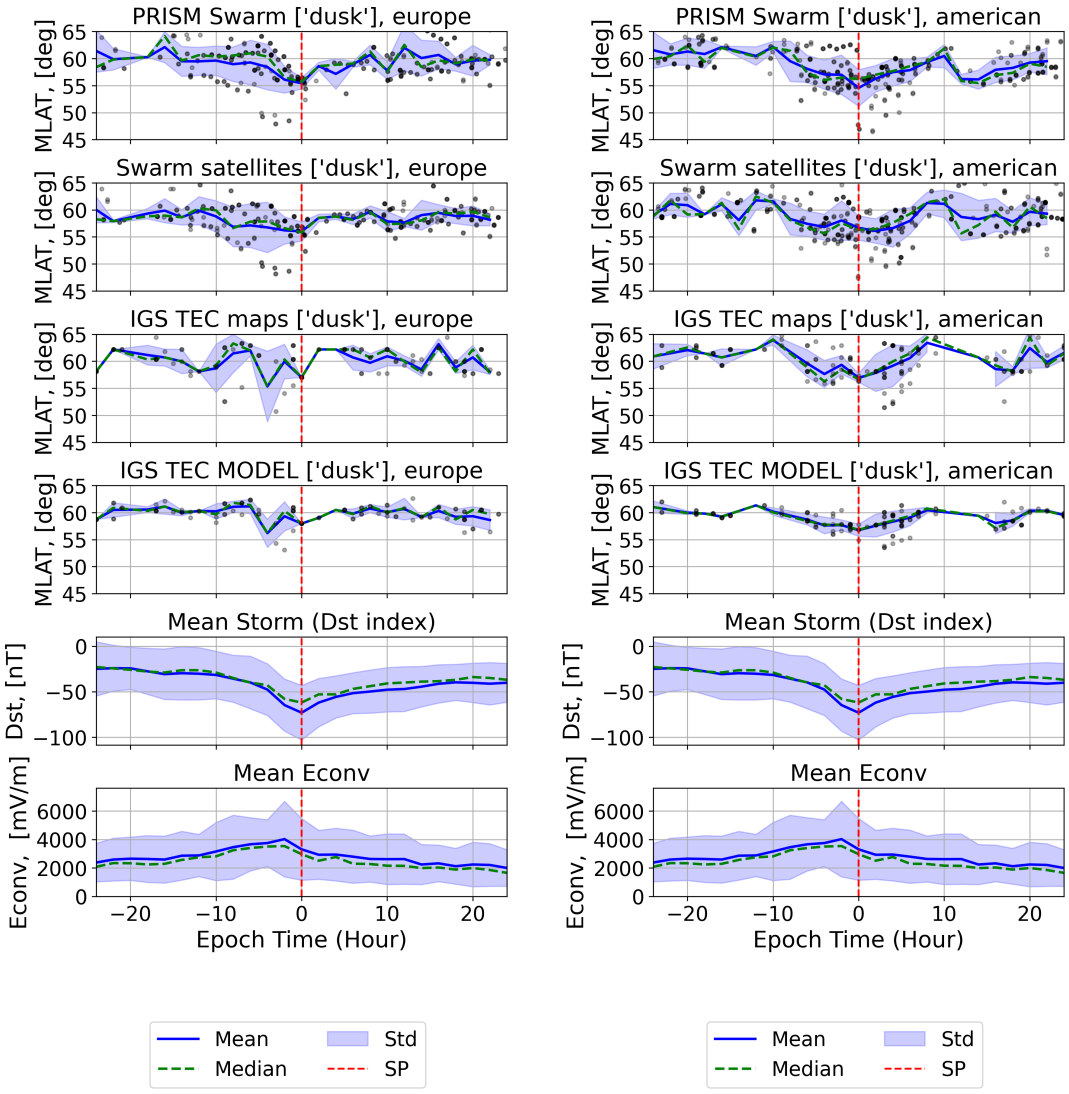

(A) European sector

(B) American sector

FIGURE 8.8: Mean and median trough position during storms in the dusk magnetic local time sector (18 - 21 MLT) for the European (left column) and American (right column) sectors separately in the Northern Hemisphere for PRISM, Swarm, IGS TEC map observations and model values. The storm minimum is marked with a red dashed line and set to 0 epoch hour.

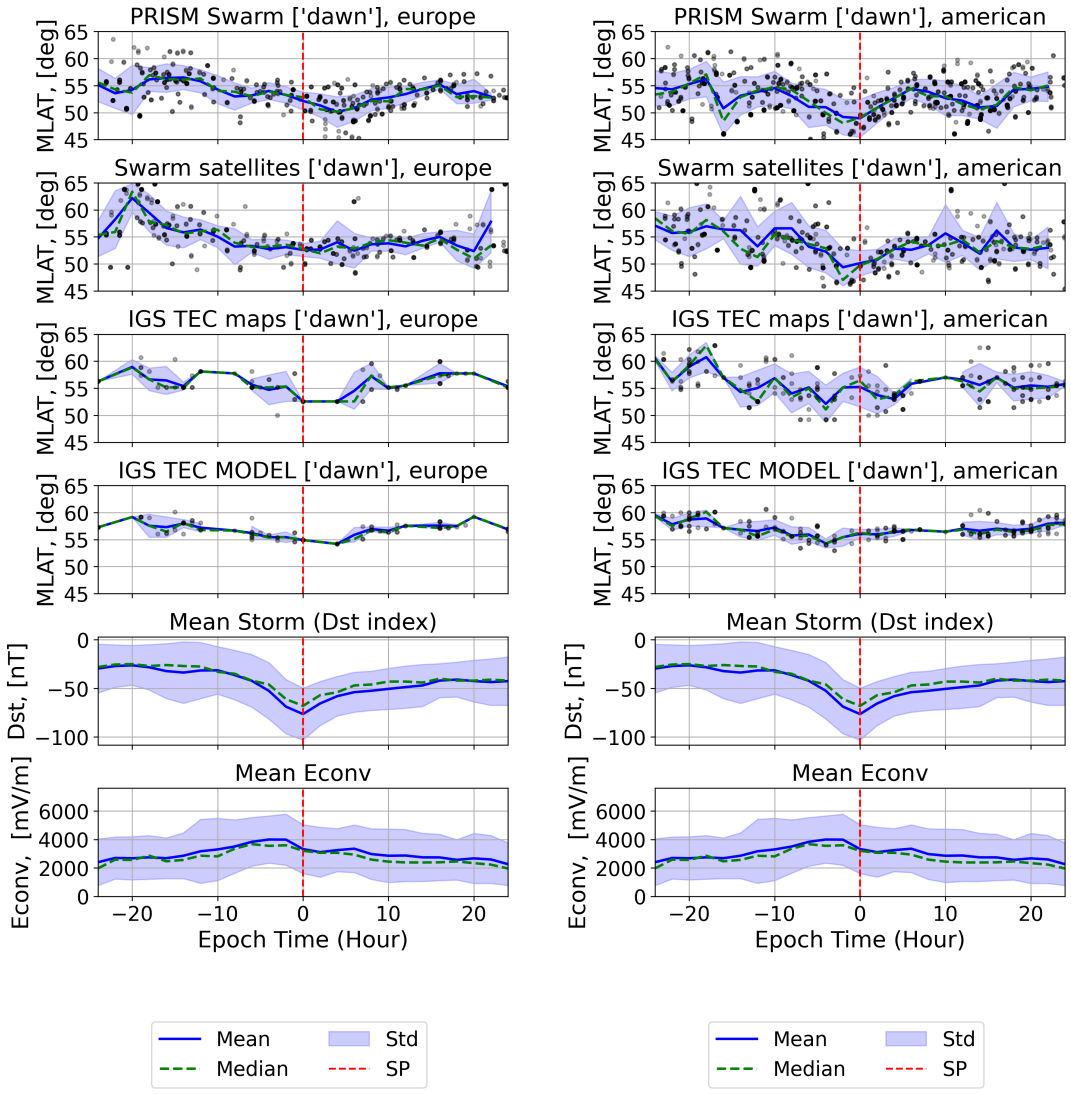

(A) European sector (B) American sector

FIGURE 8.9: Mean and median trough position during storms in the dawn magnetic local time sector (3 - 7 MLT) for the European (left column) and American (right column) sectors separately in the Northern Hemisphere for PRISM, Swarm, IGS TEC map observations and model values. The storm minimum is marked with a red dashed line and set to 0 epoch hour.

8.4 Case study: Mother's Day Storm 2024

To evaluate the trough model, Mother's Day Storm 2024, a severe geomagnetic activity event classified as a G5 class geomagnetic storm (Kp = 9), was examined. At 02:00 on 11 May, the Dst dropped to a minimum of -412 nT. The Mother's Day storm was the strongest geomagnetic storm since the Halloween storm of 2003. Two data sources were used for the study: troughs detected from IGS maps and troughs derived from the empirical model described in Chapter 7.

The analysis, shown in Figures 8.10 and 8.11, is an epoch analysis that examines the relationship between the trough position determined from the IGS UQRG maps and the trough position using the model values. The data are grouped into three

local time bins: dusk hours (18 - 21 MLT, marked with green color), night hours (22 - 2 MLT, marked with green-blue color) and dawn hours (3 - 7 MLT, marked with red color). The storm peak is marked by the vertical dashed line at epoch time 0, and the data are recalculated in epochs according to the storm minimum peak. The running average is also calculated using a window size of 8 points, which corresponds to 2 hours. The data point resolution is 15 minutes.

Both data show similar trends, although the model naturally shows more smoothed data. The model values also show minimal changes between local time groups. In contrast, the IGS TEC maps show the offset between local time groups and the position of the trough is shifted extremely equatorward around the storm minimum. The model also shows very smooth trough behaviour during the recovery phase. In general, the model is able to show smoothed changes in trough position during periods of intense geomagnetic activity. Each individual trough profile during the Mother Day storm is shown in the 3-dimensional Figure 8.12 for NH and Figure 8.13 for SH. The plots have 3 axes: the geographic latitude, which shows the position and width of the trough, the depth, and the epoch. It can be seen that the model generally overestimates the depth of the trough. Nevertheless, we can see that the trough derived from our model evolves similarly during the storm phases to the trough detected from the IGS TEC maps during the different phases of the storm.

8.5 Model performance during the Mother's Day Storm

The model performance for the Northern Hemisphere and Southern Hemisphere during the Mother's Day geomagnetic storm is shown in Figure 8.14. The trough minimum position derived by the empirical model, expressed in magnetic latitude, is compared with the trough minimum position obtained from IGS TEC maps. Since the empirical model database does not contain data for the year 2024, including the Mother's Day Storm, this event serves as an independent validation case. For the model performance evaluation, widely-used performance metrics were used, such as the Pearson correlation, were calculated for the night, dusk, and dawn sectors using the following equation:

$$r = \frac{\sum(x - m_x)(y - m_y)}{\sqrt{\sum(x - m_x)^2 \sum(y - m_y)^2}}, \tag{8.1}$$

where m_x is the mean of the vector x and m_y is the mean of the vector y.

The model demonstrates a high correlation in the Northern Hemisphere, especially at dusk (r = 0.77) and dawn (r = 0.72). In contrast, the Southern Hemisphere correlations are lower, showing a medium correlation and reaching their highest values at the dusk sector (r = 0.65). As previously pointed out, this is due to the low and uneven coverage of IGS stations.

Storm-time modeling remains a challenging task due to the complexity and rapid variability of ionospheric conditions. Nevertheless, the model shows promising capability in capturing storm-time behavior. Future work could focus on incorporating storm-specific drivers, such as solar wind parameters, to further enhance the predictive accuracy of the model.

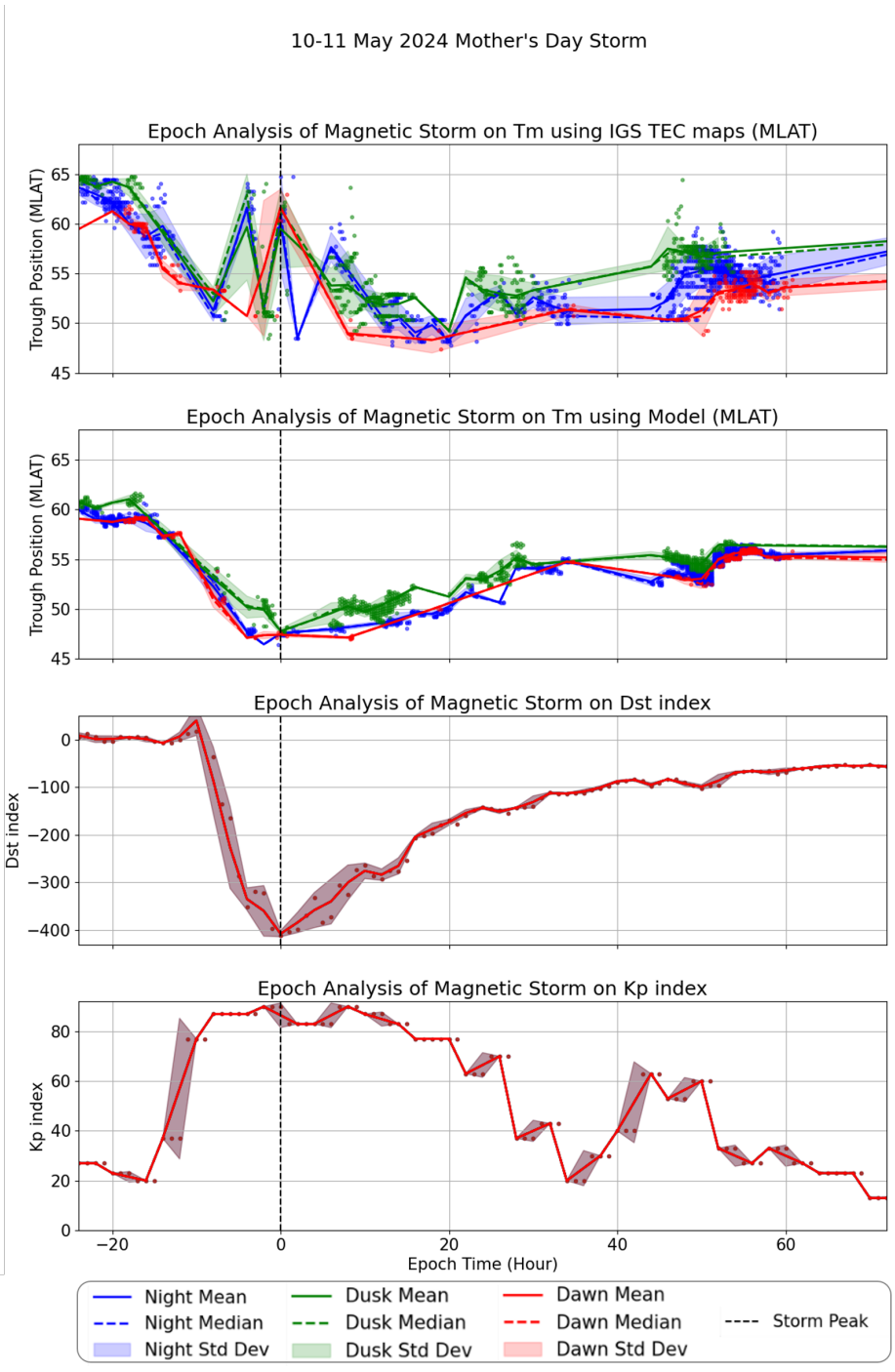

FIGURE 8.10: Epochal analysis of the trough position in NH during the Mother's Day storm event at different local times, such as dusk (green color), night (blue color), and dawn (red color). The top plot shows the trough position determined from the IGS UQRG maps, and the second plot below shows the trough position using the model values. The third plot displays the Dst index values, and the last plot shows the Kp index during the 24 hours before the storm peak, which occurred on 11.05.2024 at 02:00:00 (marked with a gray dashed line indicating the epoch time set to 0 hours) and 72 hours after.

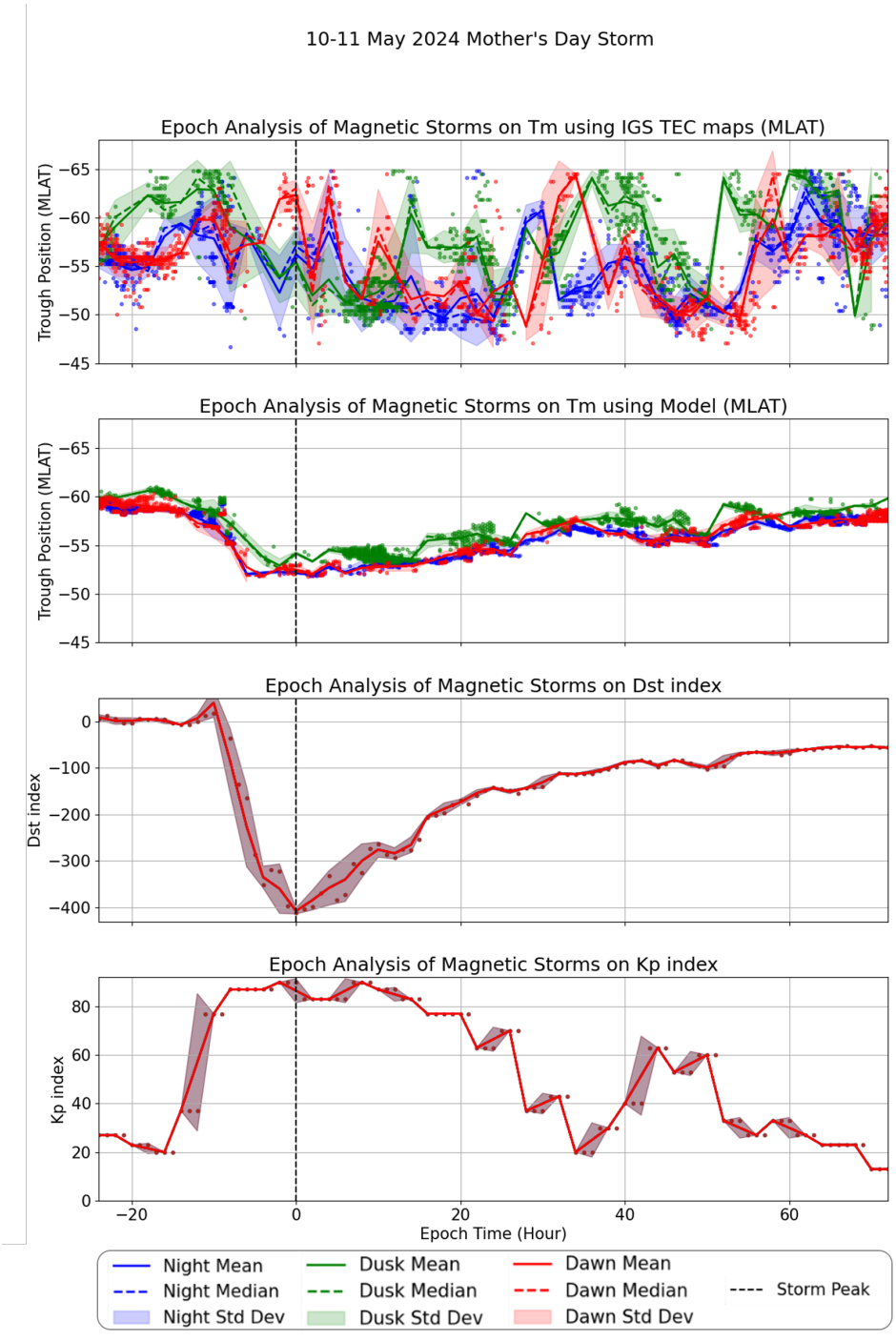

FIGURE 8.11: Epochal analysis of the trough position in SH during the Mother's Day storm event at different local times, such as dusk (green color), night (blue color), and dawn (red color). The top plot shows the trough position determined from the IGS UQRG maps, and the second plot below shows the trough position using the model values. The third plot displays the Dst index values, and the last plot shows the Kp index during the 24 hours before the storm peak, which occurred on 11.05.2024 at 02:00:00 (marked with a gray dashed line indicating the epoch time set to 0 hours) and 72 hours after.

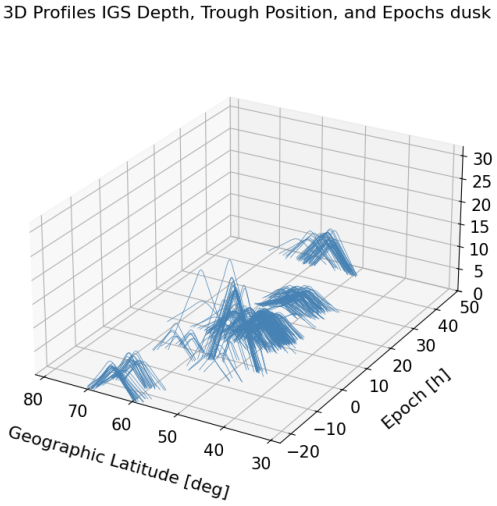

(A) Dusk trough, IGS TEC maps

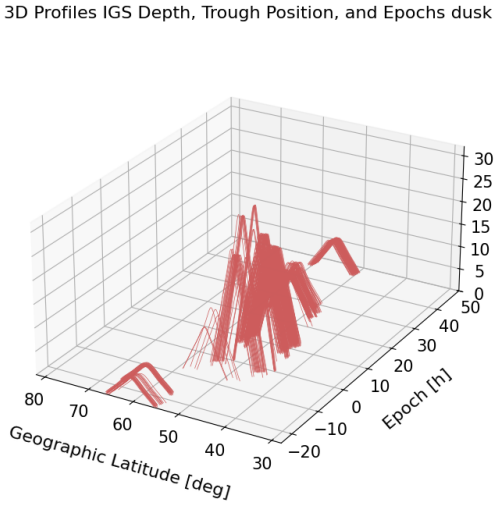

(B) Dusk trough, modelled

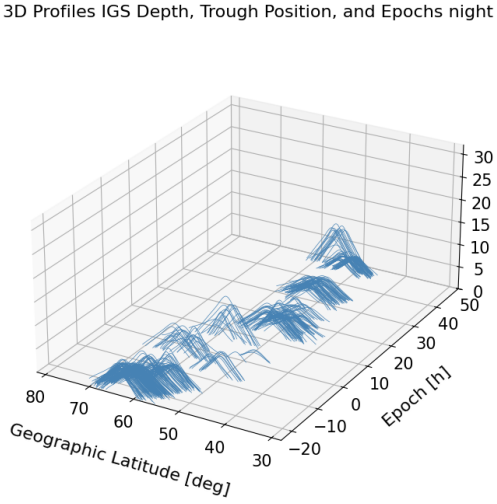

(C) Night trough, IGS TEC maps

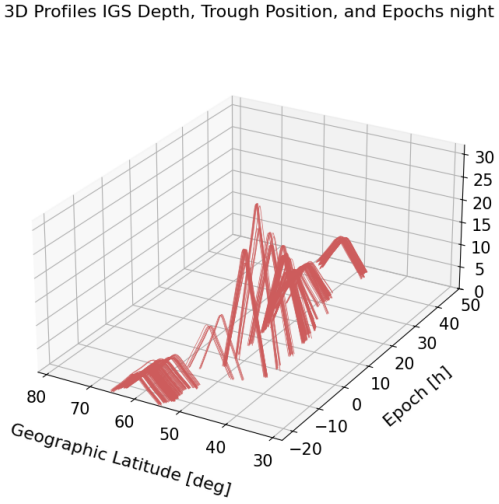

(D) Night trough, modelled

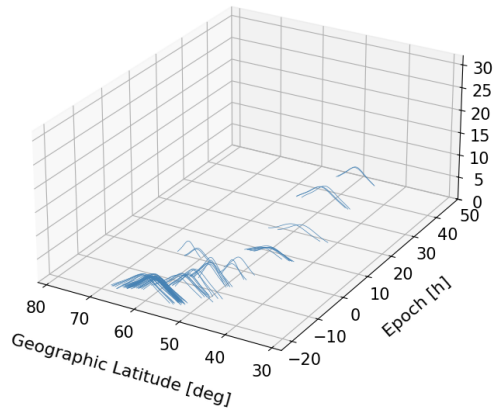

(E) Dawn trough, IGS TEC maps

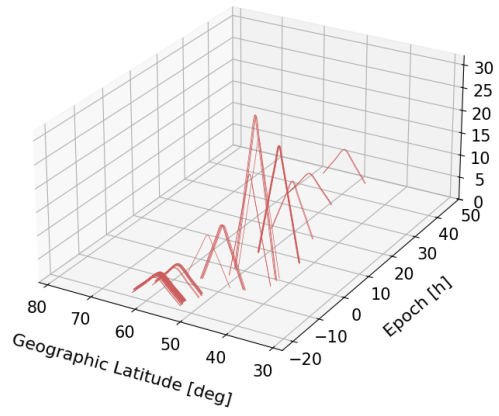

(F) Dawn trough, modelled

FIGURE 8.12: 3-Dimensional plot of trough profiles in NH detected during Mother day storm from IGS TEC maps (left column) and trough profiles derived using model (right columns).

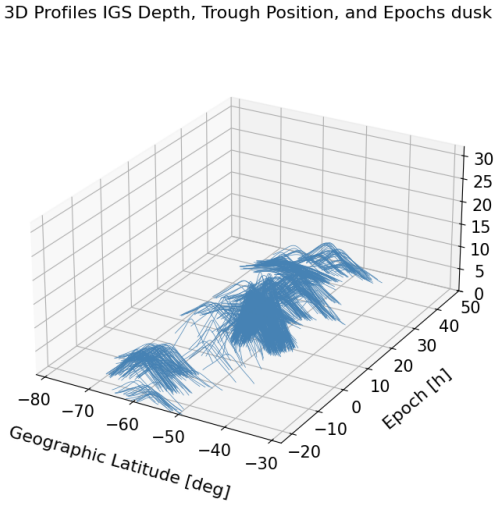

(A) Dusk trough, IGS TEC maps

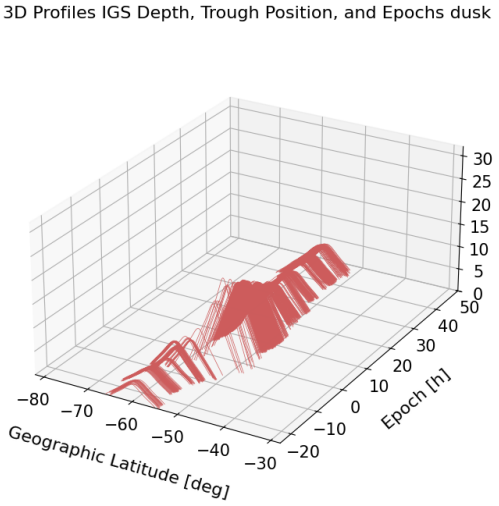

(B) Dusk trough, modelled

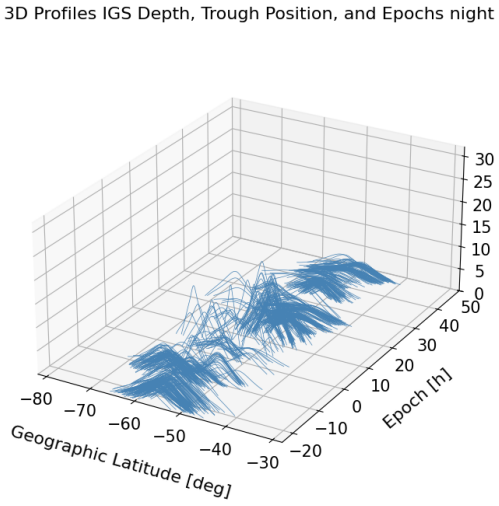

(C) Night trough, IGS TEC maps

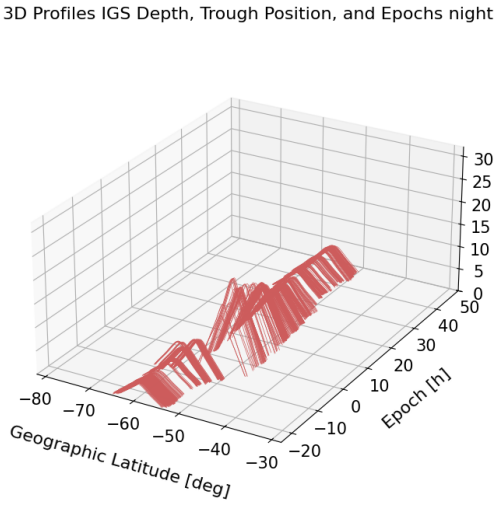

(D) Night trough, modelled

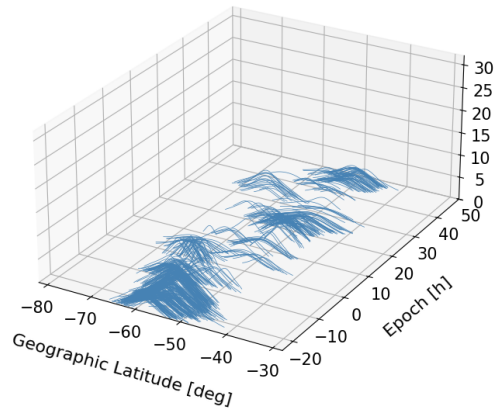

(E) Dawn trough, IGS TEC maps

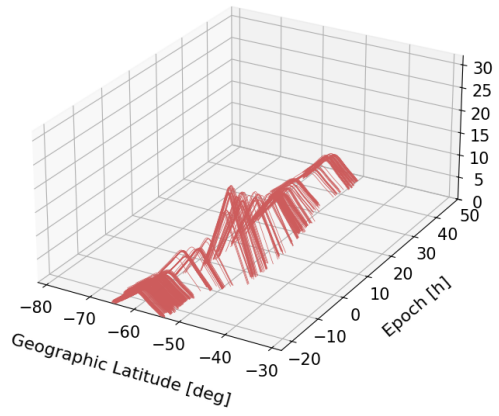

(F) Dawn trough, modelled

FIGURE 8.13: 3-Dimensional plot of trough profiles in SH detected during Mother day storm from IGS TEC maps (left column) and trough profiles derived using model (right columns).

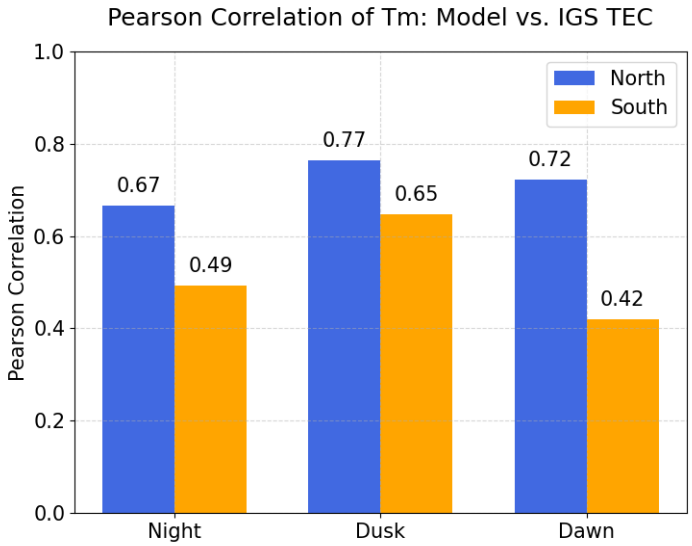

FIGURE 8.14: Model performance during the Mother's Day Storm event. Bar plots show the Pearson correlation between the observed trough minimum location from IGS TEC maps and our model predictions for geomagnetic latitude. Correlation in the Northern Hemisphere is marked with blue color, and the Southern Hemisphere is marked with yellow; results are separated by local time sectors (night, dusk, dawn).

Chapter 9

Summary and Outlook

This research has comprehensively studied the mid-latitude ionospheric trough. MIT is a critical feature of the ionosphere where plasma irregularities of the equatorward and poleward gradients can significantly affect radio communications, cause significant signal delays, making it a source of error for trans-ionospheric radio systems used in communications and navigation satellites such as GNSS. In particular, the L-band used by GNSS can experience signal scintillation due to small-scale irregularities at both the poleward and equatorward boundaries of the MIT. The resulting positioning errors can range from a minimum of 0.1 meters up to approximately 25 meters for GPS/Galileo L1 signals. For GLONASS, the mean frequency error that can cause the trough is 0.09 meters, and the maximum is about 24.29 meters. Such high errors emphasise the need for continued study and development of accurate ionospheric models of the mid-latitude trough and its inclusion in global ionospheric models, which was one of the main objectives of this study. To achieve this objective, the present study analyzed multiple data sources and developed the MIT model.

The mid-latitude ionospheric trough is not only related to various physical processes in the local ionosphere, but it is also influenced by geomagnetic perturbations from the Earth's magnetosphere. In order to study the morphological features and dynamic changes of the mid-latitude trough, this research investigates four different data sources. This study utilized Swarm, GRACE satellites, and ground-based data, such as IGS TEC map data. The ESA MIT product PRISM was also used to compare and evaluate the results obtained in this thesis. Each dataset varies in temporal and spatial coverage, and the inclusion of all of these data sources increases the confidence in the results.

By performing a statistical analysis of the detected mid-latitude trough using Swarm, GRACE, IGS TEC maps, and PRISM data, valuable insights into the location and dynamics of the ionospheric trough separately for the Northern and Southern Hemispheres were provided, including the following:

- **Changes in MIT Occurrence Rate**
  - MIT is observed more frequently at night and in the morning.
  - Troughs occur more frequently during equinoxes and winter months (Nov-Feb) than during summer (May-Aug) in NH. The trend in the SH is similar, mainly opposite, since the NH and SH have opposite seasons. Seasonal patterns are more pronounced in NH than in SH. This indicates a hemispheric asymmetry, namely with the offset of the geographic and magnetic poles.
  - The MIT occurred more frequently with increasing solar wind plasma speed in he Northern and Southern Hemispheres.

  - The trough occurred more frequently with increasing solar wind flow pressure in both hemispheres.
  - The IMF Bz component shows that the trough occurred more frequently in both hemispheres when the Bz component was negative, indicating periods of intense geomagnetic activity.
  - The trough occurred more frequently with increasing geomagnetic activity, as indicated mainly by the Hp 30 index, in both hemispheres.
  - Trough occurred more frequently with increasing ring current intensity, as indicated mainly by SYM-H index during geomagnetic storms in both hemispheres.
  - There is a negative correlation between the occurrence rate of MIT and the F10.7 index.

- **Changes in MIT Width**
  - Trough width becomes slightly narrower with increasing F10.7 index.
  - The average width of the troughs in all datasets varies between 6 and 13 degrees.
  - A slight increase in trough width is also observed from 7 to 14 MLT.
  - MIT width slightly decreases with increasing solar wind plasma speed.
  - Trough width changes with the Hp30 index; mainly, the trough is becoming wider with the increase of the Hp30 index.
  - When the SYM-H index decreases, the trough becomes narrower.

- **Changes in MIT Depth**
  - There is a strong positive correlation between the depth of the trough and the increase in the F10.7 index.
  - MIT depth is slightly increasing with increased solar wind plasma speed.
  - The trough becomes deeper with solar wind flow pressure increase.
  - The trough becomes deeper with the increase of the Hp30 index.
  - When the SYM-H index decreases, the trough gets deeper.

- **Changes in MIT Location**
  - The geographical distribution of the trough minimum position forms an approximate elliptical shape around the Earth's magnetic poles. All data show similar results, but the IGS TEC maps show some slight differences, especially in the SH, since the IGS TEC maps have a lower density of observing stations in the SH.
  - The position of the trough minimum shifts slightly equatorward during high solar activity conditions and poleward during low solar activity.
  - The trough minimum position moves slightly higher latitudes during the winter months compared to the summer months. In the Southern Hemisphere, the MIT is at a higher latitude during the summer.
  - Trough extends from dusk to dawn and widens at latitudes from about 60° to 50° MLAT.

  - In general, the trough is observed to be found around midnight, more equatorward being around 58° MLAT, and in the dusk and dawn, moving poleward around 63° MLAT.
  - There is a negative correlation between the solar wind plasma speed and the trough minimum location.
  - With an increase in solar wind flow pressure, the trough was observed to shift a bit to the lower latitudes.
  - Trough minimum location moves equatorward with an increasing Hp30 index in both hemispheres.
  - With the decrease of the SYM-H index, the trough position shifts equatorward.

- **Changes in Equatorward and Poleward MIT Slopes**
  - The poleward slopes of the trough are consistently sharper than the equatorward slopes.
  - With an increase in the F10.7 index, MIT has steeper slopes. The trough slopes become even sharper during the period of increased geomagnetic activity.
  - Equatorward and poleward slopes become exponentially sharper with the Kp index increase.
  - The poleward slope becomes significantly sharper during strong and extreme geomagnetic activity (8-9 Kp index).
  - Low Kp index (0-3) indicates that the poleward slope remains the same and the equatorward slope changes slightly.
  - As the Kp index becomes moderate (4-6), the poleward slope still shows no significant change, while the equatorward slope gradually increases.
  - With high geomagnetic activity (7-9), both equatorward and poleward slopes show very steep and very high slope increases.

Our analysis confirms previous MIT studies and provides new insights into its dependence on various geophysical conditions. Since the MIT is connected to magnetospheric processes, our results can be directly linked to and justified by the main physical processes and plasmaspheric dynamics.

In this work, it was found that trough occurrence is high around the evening and premidnight local time sectors and is located at more equatorward latitudes around 58° MLAT. This can be explained with the stagnation mechanism, which considers the conflicting effects of the Earth's rotation and auroral electric field-induced convection. In the evening sector eastward corotation drift (from Earth's rotation) and westward magnetospheric convection drift nearly cancel at certain latitudes, creating a stagnation zone where recombination dominates and a trough forms. At different magnetic local times such as from dusk to dawn troughs can be also observed, but different physical processes may dominate. In particular, troughs in the post-midnight sector are likely controlled by steady plasma depletion due to recombination. Toward morning, troughs shift poleward to roughly 65° MLAT and gradually fade as auroral convection weakens and increasing solar illumination reduces chemical losses.

High-speed solar wind enhances the potential for geomagnetic storms, which strongly affect MIT characteristics. During geomagnetically active periods, the main

trough is strongly influenced by subauroral electric fields and the development of SAPS. With increasing geomagnetic activity, the trough occurrence increases significantly compared to quiet-time period. During storm-time conditions trough (Hp30 $>$ 3 or SYM-H $\leq$ $-$50 nT) mean occurrence rates reach up to 50%, where during calm periods the occurrence is in range 10-30%. These changes reflect the coupled response of the magnetosphere–ionosphere system: storm-time ring current expansion modifies global convection patterns, storm-enhanced electric fields drive SAPS and SAID channels equatorward, and enhanced plasmaspheric erosion redistributes plasma to lower latitudes. As a result, troughs can move in average up to 6° latitude in equatorward direction, and become narrower up to 3° latitude and deeper. These findings are consistent with the expected behavior of the MIT derived from the continuity equation.

The continuity equation (Eq. 2.1, Section 2.2.2) gives us an excellent opportunity to understand how the mid-latitude trough and other ionospheric structures change with the seasons. With increasing solar activity level, quantified by F10.7 index, the MIT shifts slightly equatorward, becomes slightly narrower, and deepens. At the same time, its occurrence decreases as the ionisation production rate rises, driven by the enhanced solar extreme ultraviolet radiation associated with high solar activity. The deepening of a trough can be explained by dissociative recombination processes induced by higher ion temperatures, which correlate with elevated F10.7 levels. Higher EUV flux reduces the occurrence probability of troughs since enhanced photoionization makes it difficult to maintain the depletion. However, when a trough does form under such conditions (e.g. due to SAPS), elevated ion temperatures enhance recombination and make it deeper. This behaviour is consistent with the continuity-equation mechanism, where the seasonal and solar cycle dependence of the trough can be understood as the balance between plasma production q and recombination losses L.

Seasonally, the trough occurs most frequently during local winter and around the equinoxes. During the equinox trough occurrence rates are in range 10-30% in GRACE, IGS, Swarm datasets and reaching up to around 40% in PRISM dataset. By comparison, in local summer the occurrence rate reduces below 10%. There are several physical processes that influence these changes throughout the seasons. At mid-latitudes, the production term q is driven mainly by solar EUV radiation. In summer, when $q \gg \alpha N^2$ photo-ionization partly balances recombination, and plasma depletions are more easily restored, leading to shallower and shorter-lived troughs. In winter, however, reduced EUV radiation means $q \ll \alpha N^2$, while recombination losses remain significant. The plasma density therefore decays faster than it can be restored, resulting in deeper and longer-lasting depletions such as mid-latitude trough. On these seasonal timescales, the transport term $-\nabla \cdot (N\mathbf{v})$ plays only a secondary role compared to the balance between production and recombination.

Another important aspect is that the auroral particle precipitation leads to increase in plasma density and enhances the formation of the trough's poleward boundary making trough more clear to detect around equinox. Tilted magnetic field influencing plasma transport within the ionosphere by thermospheric neutral winds hence contribute to the hemispheric asymmetries observed in our results. The connections between our statistical results and the fundamental driving physics underscore that the MIT is not only an empirical feature but also a sensitive indicator of magnetosphere–ionosphere coupling.

A key novelty of this work lies in the comprehensive and simultaneous comparison of trough parameters — position, width, and depth — derived from long-term measurements from GRACE, Swarm, and ground-based IGS TEC maps for both Northern and Southern Hemispheres. These parameters were examined with respect to magnetic local time, geographic distribution, season, solar activity, and geomagnetic activity conditions, including solar wind plasma speed, interplanetary magnetic field components, and, for the first time, high-resolution geomagnetic indices such as SYM-H and Hp30 index. Furthermore, all these dependencies were compared with the PRISM product ("Plasmapause Related boundaries in the topside Ionosphere as derived from Swarm Measurements - Earth Online", n.d.) from the ESA's Swarm mission. The results obtained in this work confirm that the PRISM Swarm product *level-2 daily data - MIT* detection algorithm (European Space Agency (ESA), 2024) and the trough detection algorithm used in this work are showing, in most cases, very similar results. Moreover, our results are in agreement with the expected behavior of the MIT derived from the continuity equation.

This work provides the first detailed analysis of the dynamics of the trough's equatorward and poleward slopes in relation to the Kp and F10.7 indices during both calm and disturbed periods. It also introduces a newly developed empirical MIT model for the Northern and Southern hemispheres, based on troughs detected from IGS TEC maps over the period 1998–2023. Furthermore, a novel aspect of this study is the analysis of the MIT during 356 geomagnetic storms from 2002 to 2019. Finally, a case study was performed during the severe geomagnetic activity event known as the Mother's Day Storm (2024). The model's performance during this event was also examined.

The principal statistical findings outlined above provide a solid foundation for the MIT modeling. Based on the statistical dependencies of the MIT, the empirical model of the mid-latitude ionospheric trough for the NH and SH, representing its minimum location, width, and depth, has been built. Our developed MIT model is based on an extensive database of troughs detected from high-resolution 15-minute IGS TEC maps over the period 1998–2023, containing approximately 20 million trough profiles. The developed MIT model fits the data very well without significant bias. The distribution of the residuals is centered around 0. Our MIT model is easy to use and depends only on Kp, Dst, F10.7 index, day of the year, and local time.

The MIT model developed in this work was also run under perturbed geomagnetic conditions to verify its performance. The time series analysis of the trough behavior, as well as the developed MIT model during 356 geomagnetic storms, was performed. The dynamics of the trough during geomagnetic storms have been studied, differentiating between the Northern and Southern Hemispheres, as well as for the different local time groups, like dusk, night, and dawn. Among all the groups, it can be observed that there is a strong shift in the trough minimum position. The mean trough position shifts equatorward with a decreasing Dst index during the main phase of magnetic storms. As the Dst index increases during the storm recovery phase, the average trough position shifts poleward. The trough is located more poleward in the dusk local time sector, and it moves equatorward during the night and dawn sectors. The model is also able to reproduce the storm trend well, but slightly smoothed. In the European sector, the model overestimate the night and dawn sectors. In contrast, the American sector shows that the model performs better by slightly overestimating the trough position in the dawn sector. The trough detection in the Southern Hemisphere during storms is not as well performed because the IGS TEC maps are less accurate in the Southern Hemisphere,

as they are more smudged due to the lack of instrumentation. Therefore, it was not detected as many data points as for the Northern Hemisphere due to the lack of GNSS measurements in the Southern Hemisphere, and the storm correlation is not as well represented.

The strongest geomagnetic storm of the last decade, the Mother's Day Storm of 2024, was analyzed with respect to the trough detected from IGS TEC maps and model values. The model, of course, shows more smoothed results. The model values also show minimal changes between local time groups. In contrast, the IGS TEC maps show the offset between local time groups, and the position of the trough is shifted extremely equatorward around the storm minimum. The model also shows very smooth trough behavior during the recovery phase. In general, the model is able to show smoothed changes in trough position during periods of intense geomagnetic activity. Plotting the 3-dimensional plot of all trough profiles during the Mother's Day storm shows that the model generally overestimates the depth of MIT. However, it can be seen that the trough derived from our model evolves similarly to the trough detected from IGS TEC maps during the different phases of the storm. The performance of the model during the Mother's Day Storm event was evaluated using the Pearson correlation between the observed trough minimum location from IGS TEC maps and our model predictions for geomagnetic latitude. The model demonstrates a high correlation in the Northern Hemisphere, particularly at dusk (r = 0.77) and dawn (r = 0.72) local time sectors, with the lowest correlation occurring in the night sector (r = 0.67). In contrast, the Southern Hemisphere exhibits moderate to low correlations with the highest values at the dusk sector (r = 0.65) and lower correlations in the night (r=0.49) and dawn (r=0.42) sectors.

The developed mid-latitude trough model is planned to be included in the global TEC model, such as NTCM and NTCM-G. Later, it can also contribute to global empirical 3D electron density models such as IRI, NeQuick-G, NEDM, among others. Furthermore, several areas of future research could still be explored on the topic of the mid-latitude ionospheric trough. First, the presented work here could be expanded to include more data. For example, satellites that observe troughs at higher altitudes, such as the DMSP with an altitude of 830 km above the Earth's surface, can be included. TEC data from altimeter satellites (e.g., Jason, which flies at an altitude of approximately 1330 km) can also be utilized for trough research in the future. This would provide a more comprehensive view of trough morphology over a broader region. Additionally, other sources of data, such as the IMAGE (Imager for Magnetopause-to-Aurora Global Exploration) satellite (Yizengaw et al., 2005; Yizengaw & Moldwin, 2005), Van Allen Probe data, and others, could be incorporated to investigate the relationship between MIT and plasmapause location. Machine learning techniques, such as neural networks, could enhance the empirical model and capture more complex, nonlinear relationships between trough parameters and their drivers. Lastly, a more detailed investigation of MIT behavior during geomagnetic storms would provide deeper insights into the trough's dynamic response to space weather events.

Overall, the findings of this study contribute significantly to mid-latitude ionospheric trough knowledge and modeling with significant implications for future GNSS applications and space weather forecasting.

Bibliography

Aa, E., Zou, S., Erickson, P. J., Zhang, S.-R., & Liu, S. (2020). Statistical analysis of the main ionospheric trough using swarm in situ measurements. *Journal of Geophysical Research: Space Physics*, *125*(3), e2019JA027583.

Acharya, R. (2017). *Satellite signal propagation, impairments and mitigation*. Academic Press.

Anderson, P., Heelis, R., & Hanson, W. (1991). The ionospheric signatures of rapid subauroral ion drifts. *Journal of Geophysical Research: Space Physics*, *96*(A4), 5785–5792.

Bartels, J., Heck, N., & Johnston, H. (1939). The three-hour-range index measuring geomagnetic activity. *Terrestrial Magnetism and Atmospheric Electricity*, *44*(4), 411–454.

Baumjohann, W., & Treumann, R. A. (2012). *Basic space plasma physics*. World Scientific.

Bilitza, D. (2018). Iri the international standard for the ionosphere. *Advances in Radio Science*, *16*, 1–11.

Bilitza, D., Altadill, D., Zhang, Y., Mertens, C., Truhlik, V., Richards, P., McKinnell, L.-A., & Reinisch, B. (2014). The international reference ionosphere 2012–a model of international collaboration. *Journal of space weather and space climate*, *4*, A07.

Bilitza, D., McKinnell, L.-A., Reinisch, B., & Fuller-Rowell, T. (2011). The international reference ionosphere today and in the future. *Journal of Geodesy*, *85*, 909–920.

Bilitza, D., Pezzopane, M., Truhlik, V., Altadill, D., Reinisch, B. W., & Pignalberi, A. (2022). The international reference ionosphere model: A review and description of an ionospheric benchmark. *Reviews of Geophysics*, *60*(4), e2022RG000792.

Bilitza, D., Rawer, K., Bossy, L., Kutiev, I., Oyama, K.-I., Leitinger, R., & Kazimirovsky, E. (1990). *International reference ionosphere 1990* (tech. rep.).

Borovsky, J. E., & Shprits, Y. Y. (2017). Is the dst index sufficient to define all geospace storms? *Journal of Geophysical Research: Space Physics*, *122*(11), 11–543.

Cander, L. R. (2019). *Ionospheric space weather*. Springer.

Case, K., Kruizinga, G., & Wu, S. (2002). Grace level 1b data product user handbook. *JPL Publication D-22027*.

CDDIS | | archive | gnss | products |. (n.d.). Retrieved February 21, 2024, from https://cddis.nasa.gov/archive/gnss/products/ionex/

Chapman, S. (1918). An outline of a theory of magnetic storms. *Proceedings of the Royal Society of London. Series A, Containing Papers of a Mathematical and Physical Character*, *95*(666), 61–83.

Coley, W., & Heelis, R. (2012). Response of the equatorial topside ionosphere to 27-day variations in solar euv input during a low solar activity period using c/nofs. *Journal of Geophysical Research: Space Physics*, *117*(A3).

Collis, P., & Häggström, I. (1988). Plasma convection and auroral precipitation processes associated with the main ionospheric trough at high latitudes. *Journal of Atmospheric and Terrestrial Physics*, *50*(4-5), 389–404.

Davies, K. (1990). *Ionospheric radio*. IET.

Deminov, M., & Shubin, V. (2018). Empirical model of the location of the main ionospheric trough. *Geomagnetism and aeronomy*, *58*, 348–355.

Dominici, P., et al. (1998). My first fifty years in ionospheric research.

Dudeney, J., Rodger, A. S., & Jarvis, M. J. (1983). Radio studies of the main f region trough in antarctica. *Radio science*, *18*(06), 927–936.

ESA. (2023). *The structure of the sun: Cesar's booklet.* Retrieved February 7, 2024, from https://cesar.esa.int/upload/201809/booklet_the_suns_structure.pdf

European Space Agency. (2022). Swarm level-1b data – efix$_l p$(*entiremission*) [Accessed: 2025-07-15]. ftp://swarm-diss.eo.esa.int/Level1b/Entire_mission_data/EFIx_LP/

European Space Agency (ESA). (2024). Swarm level-2 daily data - mit [Accessed: 2024-12-05]. *European Space Agency*. https://swarm-diss.eo.esa.int/#swarm%2FLevel2daily%2FLatest_baselines%2FMIT

Feltens, J., & Schaer, S. (1998). Igs products for the ionosphere. *Proceedings of the 1998 IGS Analysis Center Workshop Darmstadt, Germany*, 3–5.

Foukal, P. V. (2008). *Solar astrophysics*. John Wiley & Sons.

Fratter, I., Léger, J.-M., Bertrand, F., Jager, T., Hulot, G., Brocco, L., & Vigneron, P. (2016). Swarm absolute scalar magnetometers first in-orbit results. *Acta Astronautica*, *121*, 76–87.

German Aerospace Center (DLR). (2024). Near real-time total electron content (tec) maps - global [Accessed: 2024-08-20].

GRACE (Gravity Recovery And Climate Experiment) - eoPortal. (n.d.). Retrieved May 23, 2024, from https://www.eoportal.org/satellite-missions/grace#grace-gravity-recovery-and-climate-experiment

Hargreaves, J. K. (1992). *The solar-terrestrial environment: An introduction to geospace-the science of the terrestrial upper atmosphere, ionosphere, and magnetosphere*. Cambridge university press.

He, M., Liu, L., Wan, W., & Zhao, B. (2011). A study on the nighttime midlatitude ionospheric trough. *Journal of Geophysical Research: Space Physics*, *116*(A5).

Heilig, B., & Lühr, H. (2013). New plasmapause model derived from champ field-aligned current signatures. *Annales Geophysicae*, *31*(3), 529–539.

Heilig, B., & Lühr, H. (2018). Quantifying the relationship between the plasmapause and the inner boundary of small-scale field-aligned currents, as deduced from swarm observations. *Annales Geophysicae*, *36*(2), 595–607.

Heilig, B., Stolle, C., Kervalishvili, G., Rauberg, J., Miyoshi, Y., Tsuchiya, F., Kumamoto, A., Kasahara, Y., Shoji, M., Nakamura, S., et al. (2022). Relation of the plasmapause to the midlatitude ionospheric trough, the sub-auroral temperature enhancement and the distribution of small-scale field aligned currents as observed in the magnetosphere by themis, rbsp, and arase, and in the topside ionosphere by swarm. *Journal of Geophysical Research: Space Physics*, *127*(3), e2021JA029646.

Hernández-Pajares, M., Lyu, H., Aragón-Àngel, À., Monte-Moreno, E., Liu, J., An, J., & Jiang, H. (2020). Polar electron content from gps data-based global ionospheric maps: Assessment, case studies, and climatology. *Journal of Geophysical Research: Space Physics*, *125*(6), e2019JA027677.

Hernández-Pajares, M., Roma-Dollase, D., Krankowski, A., García-Rigo, A., & Orús-Pérez, R. (2017). Methodology and consistency of slant and vertical assessments for ionospheric electron content models. *Journal of Geodesy*, *91*(12), 1405–1414.

Hoque, M. M., & Jakowski, N. (2012). A new global model for the ionospheric f2 peak height for radio wave propagation. *Annales Geophysicae*, *30*(5), 797–809.

Hoque, M., & Jakowski, N. (2015). An alternative ionospheric correction model for global navigation satellite systems. *Journal of Geodesy*, *89*, 391–406.

Hoque, M. M., & Jakowski, N. (2011). A new global empirical nmf2 model for operational use in radio systems. *Radio Science*, *46*(06), 1–13.

Hoque, M. M., Jakowski, N., & Berdermann, J. (2017). Ionospheric correction using ntcm driven by gps klobuchar coefficients for gnss applications. *GPS Solutions*, *21*, 1563–1572.

Hoque, M. M., Jakowski, N., & Berdermann, J. (2018). Positioning performance of the ntcm model driven by gps klobuchar model parameters. *Journal of Space Weather and Space Climate*, *8*, A20.

Hoque, M. M., Jakowski, N., & Orús-Pérez, R. (2019). Fast ionospheric correction using galileo az coefficients and the ntcm model. *GPS Solutions*, *23*(2), 41.

Hunsucker, R. D., & Hargreaves., J. K. (2003). *The high-latitude ionosphere and its effects on radio propagation*. Cambridge University Press.

ICD, O. (2010). European gnss galileo open service signal in space interface control document, sisicd-2006.

IGS Network. (n.d.). Retrieved February 21, 2024, from https://network.igs.org/

IRI, international reference ionosphere. (n.d.). Retrieved February 14, 2024, from https://irimodel.org/

Ishida, T., Ogawa, Y., Kadokura, A., Hiraki, Y., & Häggström, I. (2014). Seasonal variation and solar activity dependence of the quiet-time ionospheric trough. *Journal of Geophysical Research: Space Physics*, *119*(8), 6774–6783.

Iyemori, T. (1990). Storm-time magnetospheric currents inferred from mid-latitude geomagnetic field variations. *Journal of geomagnetism and geoelectricity*, *42*(11), 1249–1265.

Jakowski, N., Hoque, M., & Mayer, C. (2011). A new global tec model for estimating transionospheric radio wave propagation errors. *Journal of Geodesy*, *85*, 965–974.

Karpachev, A. (2003). The dependence of the main ionospheric trough shape on longitude, altitude, season, local time, and solar and magnetic activity. *GEOMAGNETISM AND AERONOMY C/C OF GEOMAGNETIZM I AERONOMIIA*, *43*(2), 239–251.

Karpachev, A. (2019). Variations in the winter troughs' position with local time, longitude, and solar activity in the northern and southern hemispheres. *Journal of Geophysical Research: Space Physics*, *124*(10), 8039–8055.

Karpachev, A., & Afonin, V. (1999). Longitudinal variations in the positions of daytime winter ionospheric troughs. *GEOMAGNETISM AND AERONOMY C/C OF GEOMAGNETIZM I AERONOMIIA*, *39*(2), 194–200.

Karpachev, A., Deminova, G., & Pulinets, S. (1995). Ionospheric changes in response to imf variations. *Journal of atmospheric and terrestrial physics*, *57*(12), 1415–1432.

Karpachev, A., Klimenko, M., Klimenko, V., & Pustovalova, L. (2016). Empirical model of the main ionospheric trough for the nighttime winter conditions. *Journal of Atmospheric and Solar-Terrestrial Physics*, *146*, 149–159.

Kelley, M. C. (2009). *The earth's ionosphere: Plasma physics and electrodynamics*. Academic press.

Knudsen, D., Burchill, J., Buchert, S., Eriksson, A., Gill, R., Wahlund, J.-E., Åhlén, L., Smith, M., & Moffat, B. (2017). Thermal ion imagers and langmuir probes in the swarm electric field instruments. *Journal of Geophysical Research: Space Physics*, *122*(2), 2655–2673.

Knudsen, W. (1974). Magnetospheric convection and the high-latitude f 2 ionosphere. *Journal of Geophysical Research*, *79*(7), 1046–1055.

Krankowski, A., Shagimuratov, I., Ephishov, I., Krypiak-Gregorczyk, A., & Yakimova, G. (2009). The occurrence of the mid-latitude ionospheric trough in gps-tec measurements. *Advances in Space Research*, *43*(11), 1721–1731.

Lang, K. R., & Lang, K. R. (2009). Space weather. *The Sun from Space*, 337–405.

Le, H., Yang, N., Liu, L., Chen, Y., & Zhang, H. (2017). The latitudinal structure of nighttime ionospheric tec and its empirical orthogonal functions model over north american sector. *Journal of Geophysical Research: Space Physics*, *122*(1), 963–977.

Lee, I.-T., Wang, W., Liu, J., Chen, C., & Lin, C. (2011). The ionospheric midlatitude trough observed by formosat-3/cosmic during solar minimum. *Journal of Geophysical Research: Space Physics*, *116*(A6).

Lilensten, J., & Bornarel, J. (2005). *Space weather, environment and societies*. Springer Science & Business Media.

Liu, Y., & Xiong, C. (2020). Morphology evolution of the midlatitude ionospheric trough in nighttime under geomagnetic quiet conditions. *Journal of Geophysical Research: Space Physics*, *125*(8), e2019JA027361.

Lu, L., Yu, Q., Jia, S., & Chang, Y. (2022). Energetic neutral atom (ena) imaging simulation of the distant planetary magnetosphere and ena emission discussion of the solar wind. *Astronomy*, *1*(3), 235–245.

Lubyk, K., Hoque, M. M., & Stolle, C. (2022). Evaluation of the mid-latitude ionospheric trough using grace data. *Remote Sensing*, *14*(17), 4384.

Mallis, M., & Essex, E. (1993). Diurnal and seasonal variability of the southern-hemisphere main ionospheric trough from differential-phase measurements. *Journal of atmospheric and terrestrial physics*, *55*(7), 1021–1037.

Mandea, M., & Korte, M. (2010). *Geomagnetic observations and models* (Vol. 5). Springer.

Matyjasiak, B., Przepiórka, D., & Rothkaehl, H. (2016). Seasonal variations of mid-latitude ionospheric trough structure observed with demeter and cosmic. *Acta Geophysica*, *64*, 2734–2747.

Matzka, J., Bronkalla, O., Tornow, K., Elger, K., & Stolle, C. (2021b). Geomagnetic Kp index. https://doi.org/10.5880/KP.0001

Matzka, J., Stolle, C., Yamazaki, Y., Bronkalla, O., & Morschhauser, A. (2021a). The geomagnetic kp index and derived indices of geomagnetic activity. *Space weather*, *19*(5), e2020SW002641.

Mayaud, P.-N. (1980). *Derivation, meaning, and use of geomagnetic indices* (Vol. 22). Wiley Online Library.

Mevius, M. (2018). Rmextract [Astrophysics Source Code Library, record [ascl:1806.024]].

Miteva, R., & Samwel, S. W. (2023). Catalog of geomagnetic storms with dst index ≤ -50 nt and their solar and interplanetary origin (1996–2019). *Atmosphere*, *14*(12), 1744.

Moldwin, M. (2008). *An Introduction to Space Weather*. Cambridge University Press. https://doi.org/10.1017/CBO9780511801365

Muldrew, D. (1965). F-layer ionization troughs deduced from alouette data. *Journal of Geophysical Research*, *70*(11), 2635–2650.

Nava, B., Coisson, P., & Radicella, S. (2008). A new version of the nequick ionosphere electron density model. *Journal of atmospheric and solar-terrestrial physics*, *70*(15), 1856–1862.

Nava, B., Coïsson, P., & Radicella, S. (2008). A new version of the NeQuick ionosphere electron density model. *Journal of Atmospheric and Solar-Terrestrial Physics*, *70*(15), 1856–1862. https://doi.org/10.1016/j.jastp.2008.01.015

Nilsson, H., Sergienko, T., Ebihara, Y., & Yamauchi, M. (2005). Quiet-time mid-latitude trough: Influence of convection, field-aligned currents and proton precipitation. *Annales geophysicae*, *23*(10), 3277–3288.

Nishimura, Y., Verkhoglyadova, O., Deng, Y., & Zhang, S.-R. (2021). *Cross-scale coupling and energy transfer in the magnetosphere-ionosphere-thermosphere system*. Elsevier.

Nlinfit. (n.d.). Retrieved April 8, 2025, from https://de.mathworks.com/help/stats/nlinfit.html#responsive_offcanvas

Oksman, J. (1982). Apparent diurnal movements of the trough in total electron content (tec) of the ionosphere. *Geophysica*, *19*(1), 13–22.

Olsen, N., Friis-Christensen, E., Floberghagen, R., Alken, P., Beggan, C. D., Chulliat, A., Doornbos, E., Da Encarnação, J. T., Hamilton, B., Hulot, G., et al. (2013). The swarm satellite constellation application and research facility (scarf) and swarm data products. *Earth, Planets and Space*, *65*, 1189–1200.

OMNIWeb Data Explorer. (n.d.). Retrieved May 2, 2024, from https://omniweb.gsfc.nasa.gov/form/dx1.html

Orús, R., Hernández-Pajares, M., Juan, J., & Sanz, J. (2005). Improvement of global ionospheric vtec maps by using kriging interpolation technique. *Journal of atmospheric and solar-terrestrial physics*, *67*(16), 1598–1609.

Parker, J. A., Pryse, S. E., Jackson-Booth, N., & Buckland, R. A. (2018). Modelling the main ionospheric trough using the electron density assimilative model (edam) with assimilated gps tec. *Annales Geophysicae*, *36*(1), 125–138.

Pierrard, V., & Voiculescu, M. (2011). The 3d model of the plasmasphere coupled to the ionosphere. *Geophysical Research Letters*, *38*(12).

Plasmapause Related boundaries in the topside Ionosphere as derived from Swarm Measurements - Earth Online. (n.d.). Retrieved July 26, 2024, from https://earth.esa.int/eogateway/activities/swarm-prism

Prölss, G. (2007). The equatorward wall of the subauroral trough in the afternoon/evening sector. *Annales Geophysicae*, *25*(3), 645–659.

Pryse, S., Kersley, L., Williams, M., & Walker, I. (1998). The spatial structure of the dayside ionospheric trough. *Annales Geophysicae*, *16*, 1169–1179.

Rishbeth, H., & Müller-Wodarg, I. (2006). Why is there more ionosphere in january than in july? the annual asymmetry in the f2-layer. *Annales Geophysicae*, *24*(12), 3293–3311.

Rodger, A. (2008). The mid-latitude trough—revisited. *Washington DC American geophysical union geophysical monograph series*, *181*, 25–33.

Rodger, A. S., Brace, L., Hoegy, W., & Winningham, J. (1986). The poleward edge of the mid-latitude trough—its formation, orientation and dynamics. *Journal of atmospheric and terrestrial physics*, *48*(8), 715–728.

Rodger, A., Moffett, R., & Quegan, S. (1992). The role of ion drift in the formation of ionisation troughs in the mid-and high-latitude ionosphere—a review. *Journal of Atmospheric and Terrestrial Physics*, *54*(1), 1–30.

Schunk, R. W., Banks, P. M., & Raitt, W. J. (1976). Effects of electric fields and other processes upon the nighttime high-latitude f layer. *Journal of Geophysical Research*, *81*(19), 3271–3282.

Schunk, R., & Nagy, A. (2000). *Ionospheres: Physics, plasma physics, and chemistry*. Cambridge Atmospheric; Space Science Series, Cambridge University Press.

Schunk, R. W., & Nagy, A. F. (2004, November). *Ionospheres: Physics, Plasma Physics, and Chemistry*. Cambridge University Press.

Southworth, G. C. (1945). Microwave radiation from the sun. *J. Franklin Inst.*, *239*, 285–297.

Spiro, R., Heelis, R., & Hanson, W. (1978). Ion convection and the formation of the mid-latitude f region ionization trough. *Journal of Geophysical Research: Space Physics*, *83*(A9), 4255–4264.

Sugiura, M. (1963). *Hourly values of equatorial dst for the igy* (tech. rep.).

Sugiura, M. (1991). Equatorial d_< st> index 1957-1986. *IAGA bulletin*, *40*, 17–38.

The Sun - NASA. (n.d.). Retrieved February 7, 2024, from https://www.nasa.gov/image-article/sun/

Swarm operations. (n.d.). Retrieved February 12, 2024, from https://www.esa.int/Enabling_Support/Operations/Swarm_operations

Tapping, K. F. (2013). The 10.7 cm solar radio flux (F10.7) [_eprint: https://onlinelibrary.wiley.com/doi/pdf/10.1002/swe.20064]. *Space Weather*, *11*(7), 394–406. https://doi.org/10.1002/swe.20064

Thomas, J. H., & Weiss, N. O. (2012). *Sunspots: Theory and observations* (Vol. 375). Springer Science & Business Media.

Tulunay, Y. K., & Sayers, J. (1971). Characteristics of the mid-latitude trough as determined by the electron density experiment on ariel iii. *Journal of Atmospheric and Terrestrial Physics*, *33*(11), 1737–1761.

Union, E. (2010). *European gnss (galileo) open service: Signal in space interface control document*. Office for Official Publications of the European Communities.

Vierinen, J., Coster, A. J., Rideout, W. C., Erickson, P. J., & Norberg, J. (2016). Statistical framework for estimating gnss bias. *Atmospheric Measurement Techniques*, *9*(3), 1303–1312. https://doi.org/10.5194/amt-9-1303-2016

Voiculescu, M., Nygrén, T., Aikio, A., & Kuula, R. (2010). An olden but golden eiscat observation of a quiet-time ionospheric trough. *Journal of Geophysical Research: Space Physics*, *115*(A10).

Voiculescu, M., Nygrén, T., Aikio, A., Vanhamäki, H., & Pierrard, V. (2016). Postmidnight ionospheric troughs in summer at high latitudes. *Journal of Geophysical Research: Space Physics*, *121*(12), 12–171.

Voiculescu, M., & Roth, M. (2008). Eastward sub-auroral ion drifts or asaid. *Annales Geophysicae*, *26*(7), 1955–1963.

Voiculescu, M., Virtanen, I., & Nygrén, T. (2006). The f-region trough: Seasonal morphology and relation to interplanetary magnetic field. *Annales geophysicae*, *24*(1), 173–185.

Voiculescu, M., & Nygrén, T. (2007). Imf effect on ionospheric trough occurrence at equinoxes. *Advances in Space Research*, *40*(12), 1935–1940.

Wanliss, J. A., & Showalter, K. M. (2006). High-resolution global storm index: Dst versus sym-h. *Journal of Geophysical Research: Space Physics*, *111*(A2).

Werner, S., & Prölss, G. (1997). The position of the ionospheric trough as a function of local time and magnetic activity. *Advances in Space Research*, *20*(9), 1717–1722.

Whalen, J. (1989). The daytime f layer trough and its relation to ionospheric-magnetospheric convection. *Journal of Geophysical Research: Space Physics*, *94*(A12), 17169–17184.

Xiong, C., Lühr, H., & Stolle, C. (2021). GRACE Electron Density derived from the K-Band Ranging System (KBR). https://doi.org/10.5880/GFZ.2.3.2021.003

Xiong, C., Stolle, C., & Park, J. (2018). Climatology of gps signal loss observed by swarm satellites. *Annales Geophysicae*, *36*(2), 679–693.

Yamazaki, Y., Matzka, J., Stolle, C., Kervalishvili, G., Rauberg, J., Bronkalla, O., Morschhauser, A., Bruinsma, S., Shprits, Y., & Jackson, D. (2022). Geomagnetic activity index hpo. *Geophysical Research Letters*, *49*(10), e2022GL098860.

Yang, N., Le, H., & Liu, L. (2015). Statistical analysis of ionospheric mid-latitude trough over the northern hemisphere derived from gps total electron content data. *Earth, Planets and Space*, *67*, 1–11.

Yang, N., Le, H., & Liu, L. (2016). Statistical analysis of the mid-latitude trough position during different categories of magnetic storms and different storm intensities. *Earth, Planets and Space*, *68*(1), 1–11.

Yang, N., Le, H., Liu, L., & Zhang, R. (2018). Statistical behavior of the longitudinal variations of the evening topside mid-latitude trough position in both northern and southern hemispheres. *Journal of Geophysical Research: Space Physics*, *123*(5), 3983–3997.

Yizengaw, E., Wei, H., Moldwin, M., Galvan, D., Mandrake, L., Mannucci, A., & Pi, X. (2005). The correlation between mid-latitude trough and the plasmapause. *Geophysical Research Letters*, *32*(10).

Yizengaw, E., & Moldwin, M. B. (2005). The altitude extension of the mid-latitude trough and its correlation with plasmapause position. *Geophysical Research Letters*, *32*(9).

Yu, T., Wan, W., Liu, L., & Zhao, B. (2004). Global scale annual and semi-annual variations of daytime nmf2 in the high solar activity years. *Journal of atmospheric and solar-terrestrial physics*, *66*(18), 1691–1701.

Zhang, S.-R., Erickson, P. J., Zhang, Y., Wang, W., Huang, C., Coster, A. J., Holt, J. M., Foster, J. F., Sulzer, M., & Kerr, R. (2017). Observations of ion-neutral coupling associated with strong electrodynamic disturbances during the 2015 st. patrick's day storm. *Journal of Geophysical Research: Space Physics*, *122*(1), 1314–1337.

Zhang, S.-R., Foster, J. C., Coster, A. J., & Erickson, P. J. (2011). East-west coast differences in total electron content over the continental us. *Geophysical Research Letters*, *38*(19).

Zhang, S.-R., Foster, J. C., Holt, J. M., Erickson, P. J., & Coster, A. J. (2012). Magnetic declination and zonal wind effects on longitudinal differences of ionospheric electron density at midlatitudes. *Journal of Geophysical Research: Space Physics*, *117*(A8).

Zolesi, B., & Cander, L. R. (2014). *Ionospheric prediction and forecasting*. Springer.

Zou, S., Moldwin, M. B., Coster, A., Lyons, L. R., & Nicolls, M. J. (2011). Gps tec observations of dynamics of the mid-latitude trough during substorms. *Geophysical Research Letters*, *38*(14).

Appendix A

List of Publications

A.1 Journal publications

Lubyk, Kateryna, Mohammed Mainul Hoque, and Claudia Stolle. “Evaluation of the Mid-Latitude Ionospheric trough Using GRACE Data”. In: Remote Sensing 14.17, p. 4384, 2022, https://doi.org/10.3390/rs14174384

A.2 Conference publications

Lubyk, Kateryna and Hoque, Mohammed Mainul and Stolle, Claudia (2022) Evaluation of the mid-latitude Ionospheric trough Using GRACE Data. International Workshop on GNSS Ionosphere (IWGI 2022), Neustrelitz (Germany), from 26 to 28 September 2022, (talk)

Lubyk, K., Hoque, M., Stolle, C. "Evaluation of mid-latitude ionospheric trough using GRACE data". In: XXVIII General Assembly of the International Union of Geodesy and Geophysics (IUGG), Berlin (Germany), from 11 to 20 July 2023, https://doi.org/10.57757/IUGG23-1881 (poster)

Lubyk, K., Hoque, M., Stolle, C., Wehrenpfennig A. "Evaluation of the mid-latitude ionospheric trough using high-resolution IGS GIMs maps". EGU General Assembly 2024, EGU24-19953, Vienna (Austria), from 14 to 19 April 2024, https://doi.org/10.5194/egusphere-egu24-19953 (poster)

A.3 Workshops

First PITHIA-NRF Training School, INGV headquarters, Rome (Italy), from 29 May to 1 June 2023

DLR Doctoral Theme and Poster Workshop, DLR Augsburg (Germany), 5 September 2023 (poster)

United Nations/Germany Workshop on the International Space Weather Initiative: Preparing for the Solar Maximum, Neustrelitz (Germany), from 10 to 14 June 2024 (poster)

Appendix B

Geomagnetic Storms

B.1 MIT during Geomagnetic storms using GRACE and IGS 2002-2015

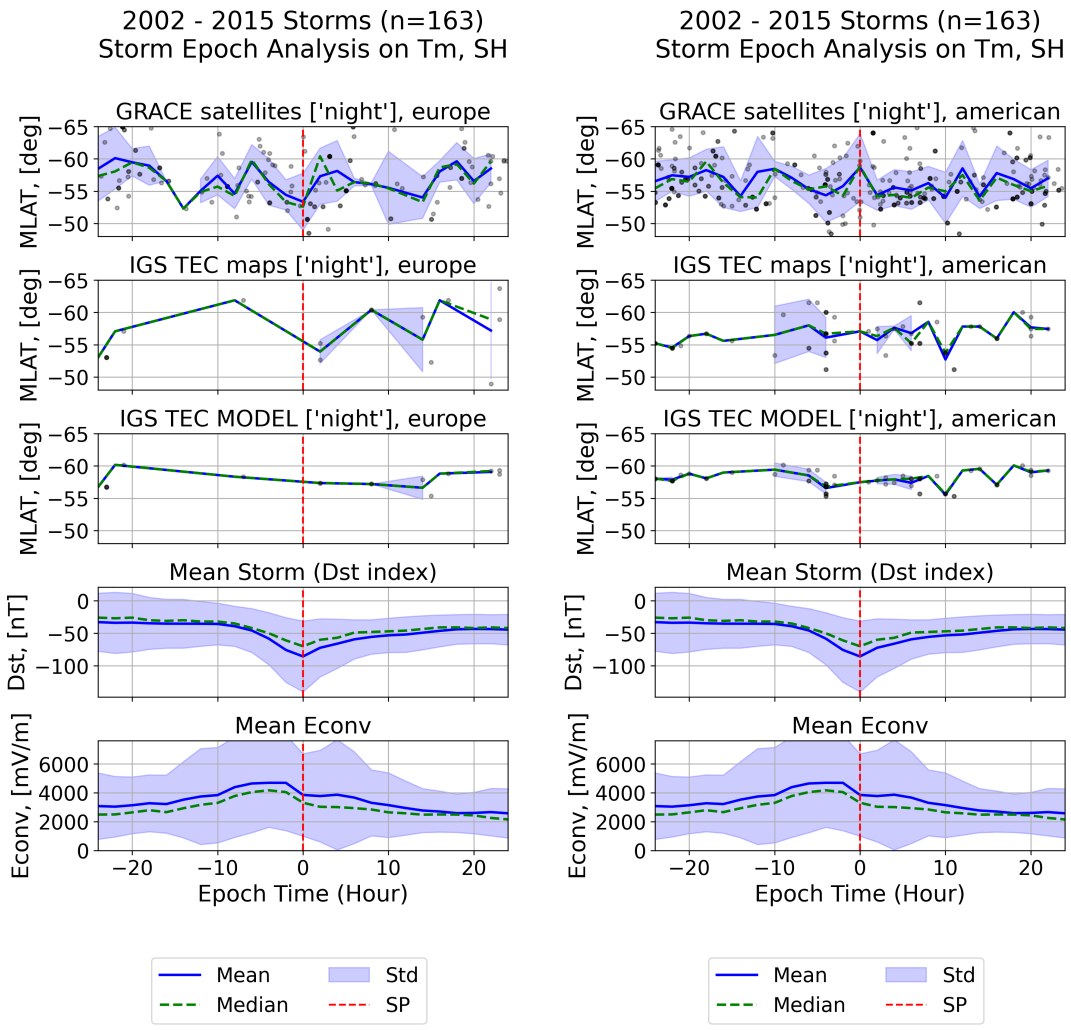

(A) European sector (B) American sector

FIGURE B.1: Mean and median trough position during storms in the night magnetic local time sector (22 - 2 MLT) for the European (left column) and American (right column) sectors separately in the Southern Hemisphere for GRACE, IGS TEC map observations and model values. The storm minimum is marked with a red dashed line and set to 0 epoch hour.

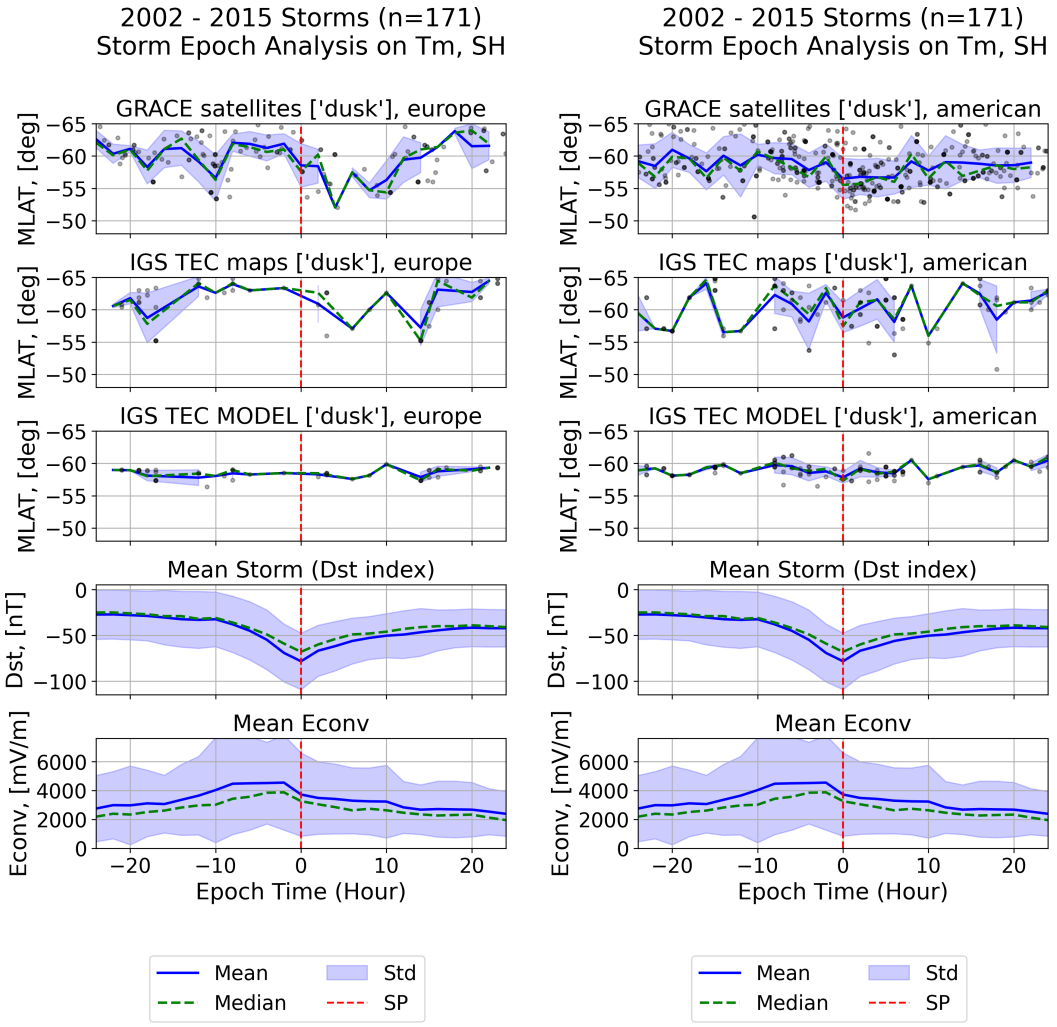

(A) European sector (B) American sector

FIGURE B.2: Mean and median trough position during storms in the dusk magnetic local time sector (18 - 21 MLT) for the European (left column) and American (right column) sectors separately in the Southern Hemisphere for GRACE, IGS TEC map observations and model values. The storm minimum is marked with a red dashed line and set to 0 epoch hour.

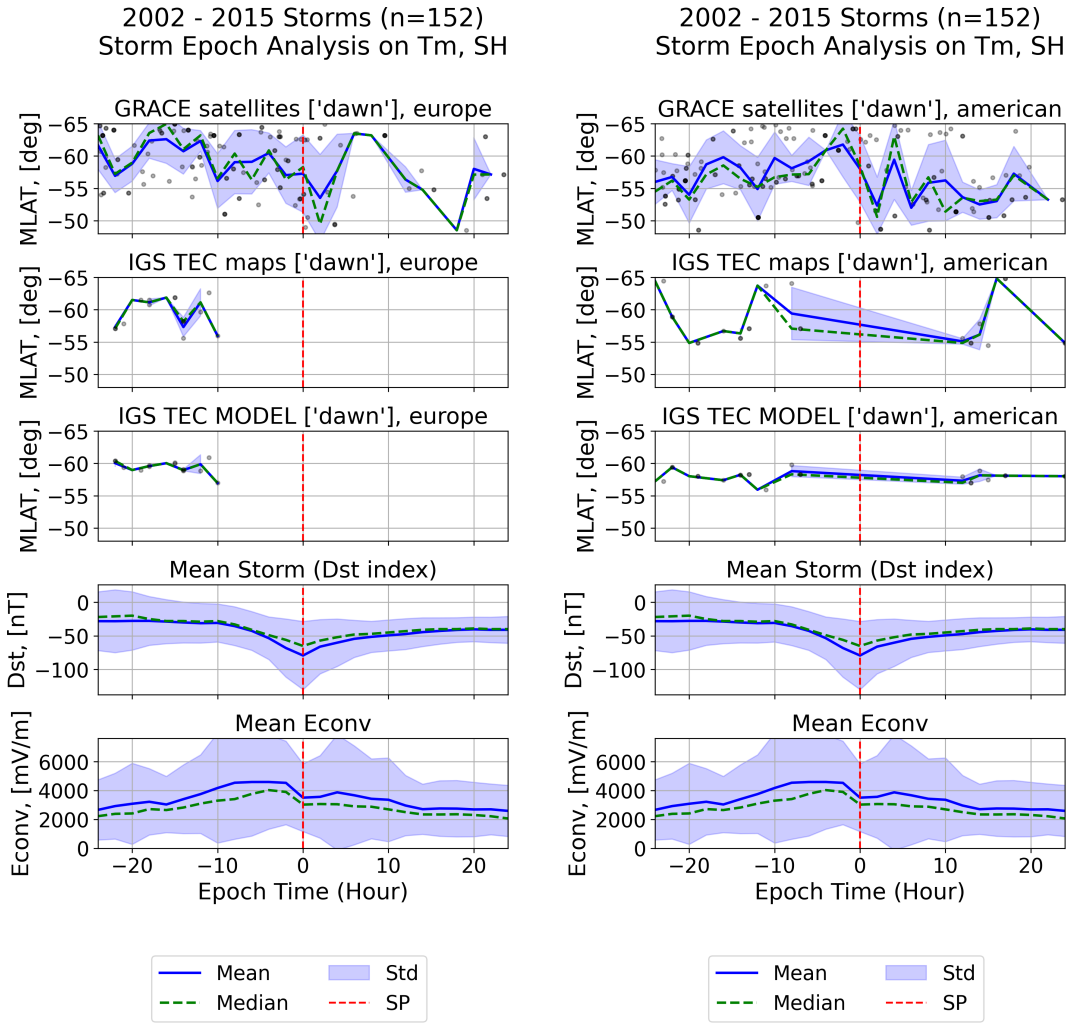

(A) European sector (B) American sector

FIGURE B.3: Mean and median trough position during storms in the dawn magnetic local time sector (3 - 7 MLT) for the European (left column) and American (right column) sectors separately in the Southern Hemisphere for GRACE, IGS TEC map observations and model values. The storm minimum is marked with a red dashed line and set to 0 epoch hour.

B.2 MIT during Geomagnetic storms 2013-2019: Swarm, PRISM and IGS

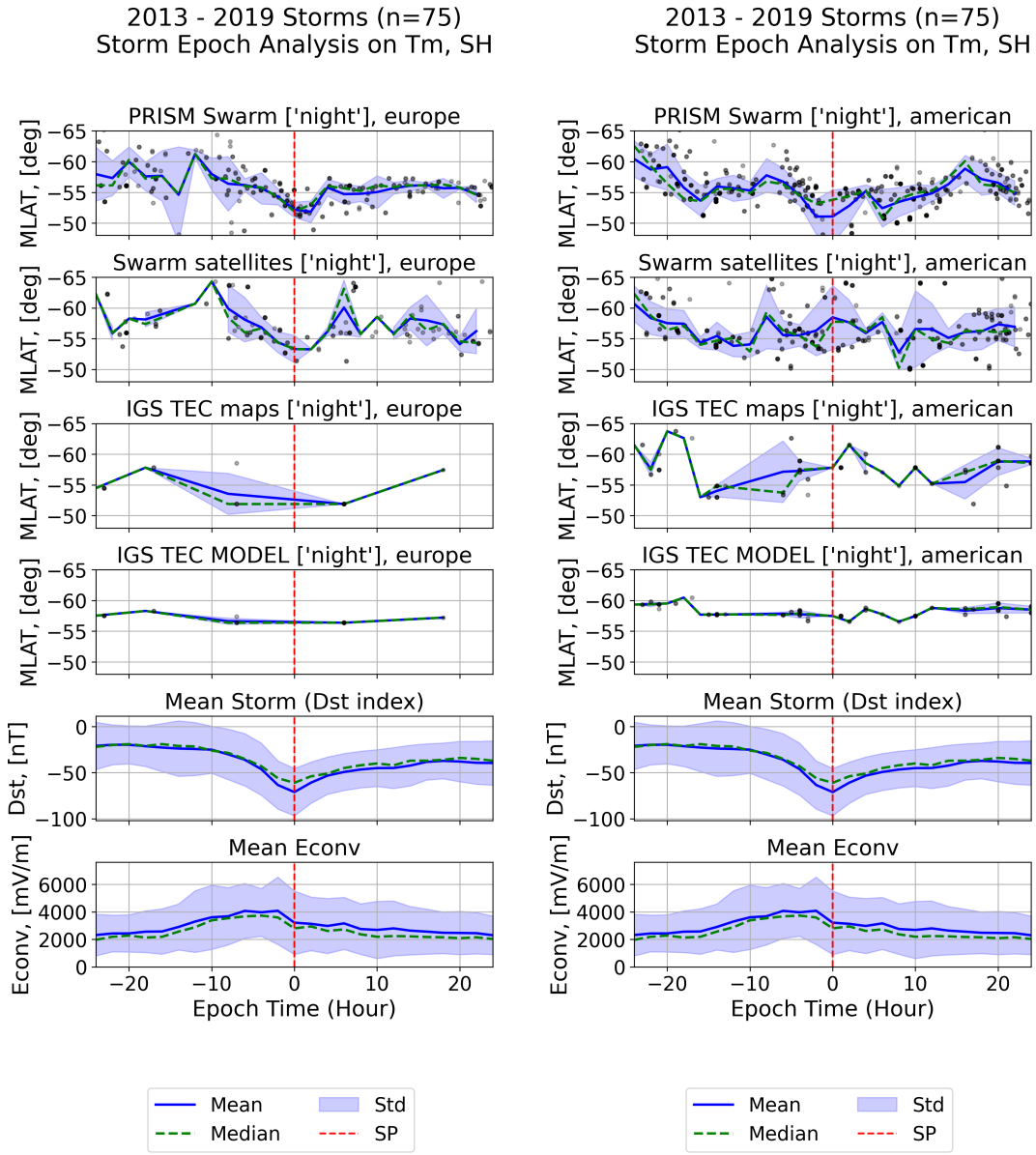

(A) European sector (B) American sector

FIGURE B.4: Mean and median trough position during storms in the night magnetic local time sector (22 - 2 MLT) for the European (left column) and American (right column) sectors separately in the Southern Hemisphere for PRISM, Swarm, IGS TEC map observations and model values. The storm minimum is marked with a red dashed line and set to 0 epoch hour.

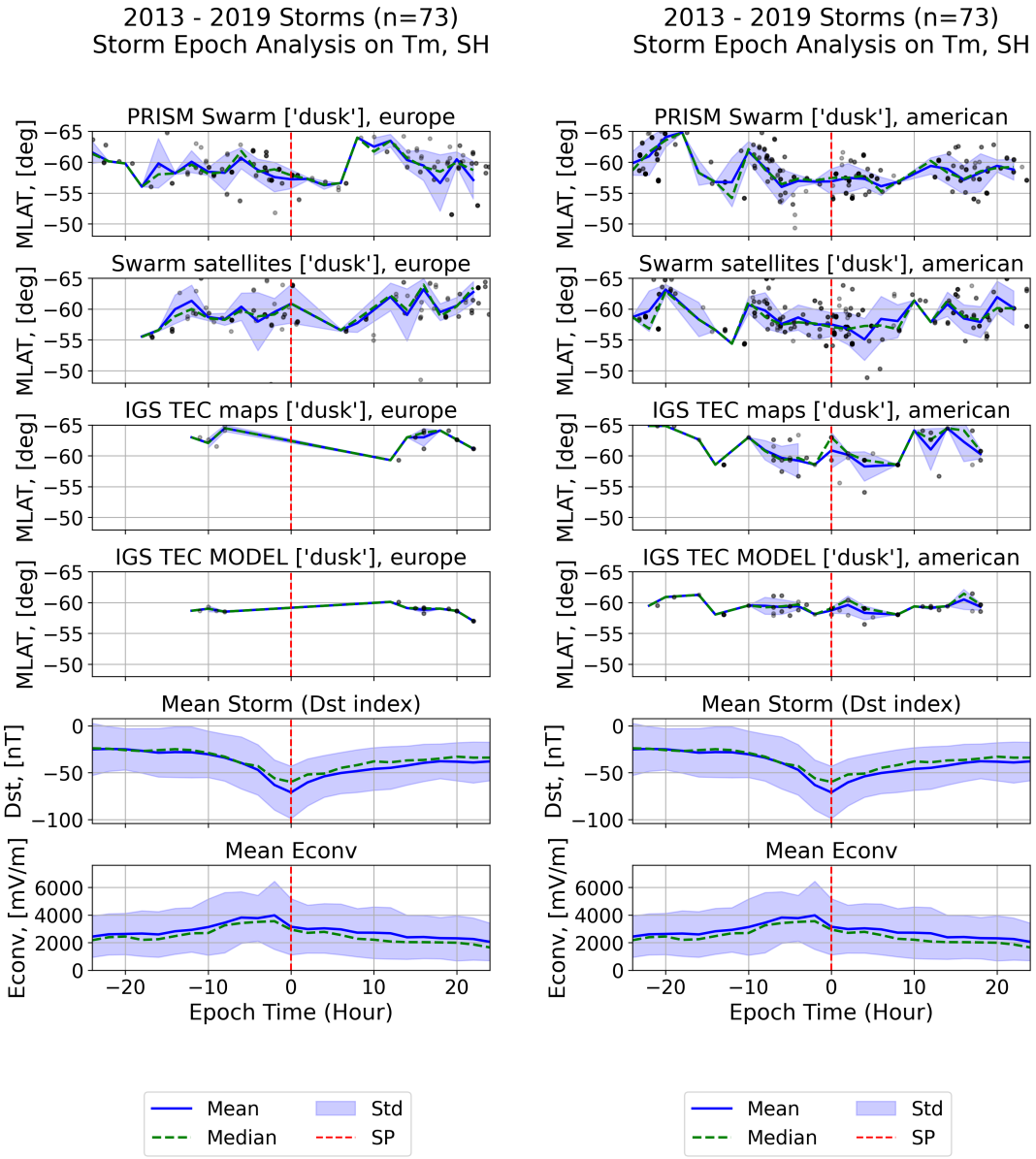

(A) European sector (B) American sector

FIGURE B.5: Mean and median trough position during storms in the dusk magnetic local time sector (18 - 21 MLT) for the European (left column) and American (right column) sectors separately in the Southern Hemisphere for PRISM, Swarm, IGS TEC map observations and model values. The storm minimum is marked with a red dashed line and set to 0 epoch hour.

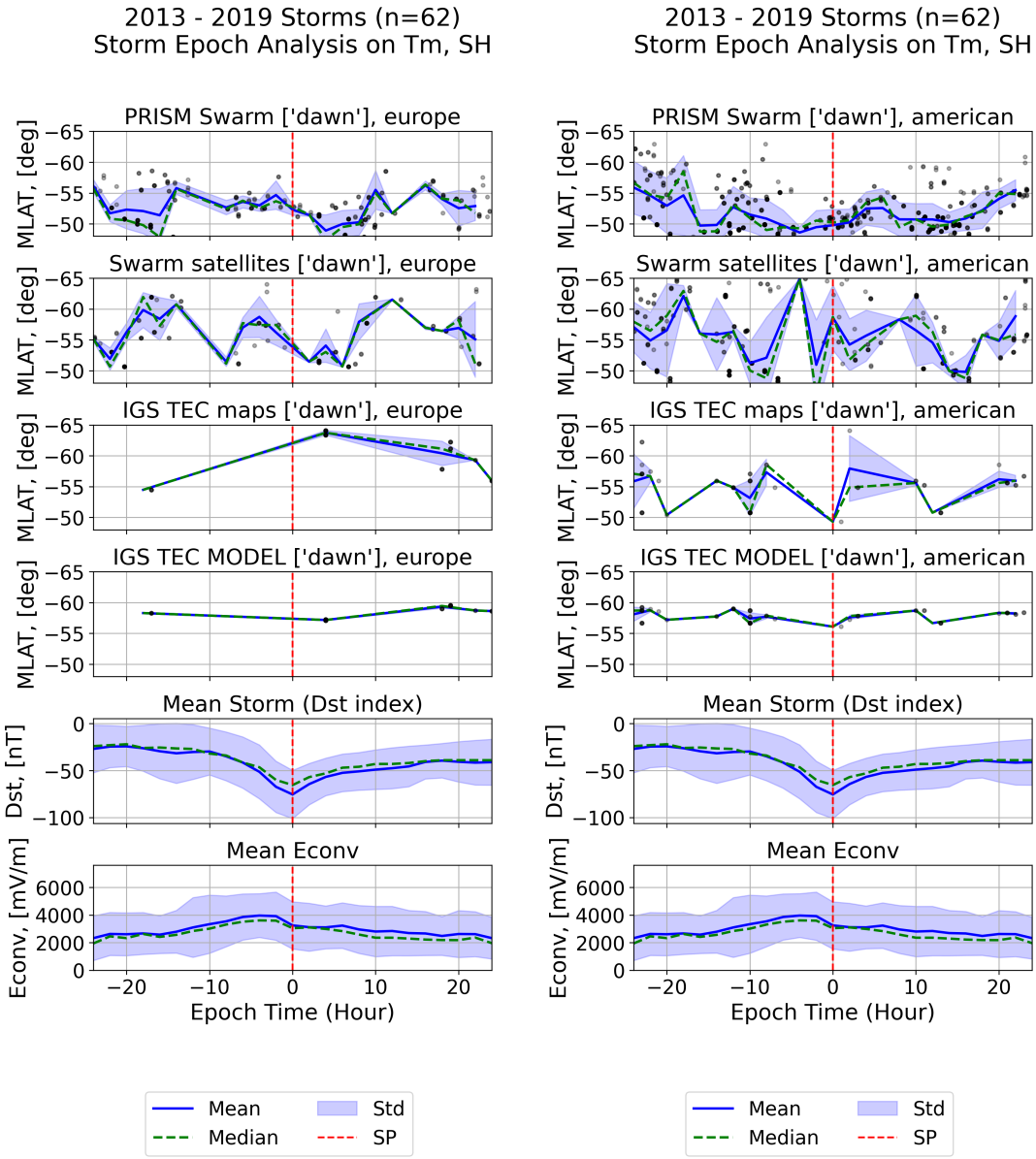

(A) European sector (B) American sector

FIGURE B.6: Mean and median trough position during storms in the dawn magnetic local time sector (3 - 7 MLT) for the European (left column) and American (right column) sectors separately in the Southern Hemisphere for PRISM, Swarm, IGS TEC map observations and model values. The storm minimum is marked with a red dashed line and set to 0 epoch hour.